

Regulation of Bone Morphogenetic growth factor bioavailability by the extracellular matrix

Inaugural-Dissertation

zur

Erlangung des Doktorgrades

der Mathematisch-Naturwissenschaftlichen Fakultät

der Universität zu Köln



vorgelegt von

Charikleia (Chara) Spanou

aus Kreta, Griechenland

Köln, 2022

Prüfungsvorsitzender: Prof. Dr. Siegfried Roth

Berichterstatter: Prof. Dr. Gerhard Sengle
(Gutachter)

Prof. Dr. Ulrich Baumann

Tag der mündlichen Prüfung: 2022-05-31

Abstract

Zusammenfassung

1. Introduction	1
1.1 TGF- β superfamily ligands	1
1.2 Discovery and biological role of BMPs	1
1.3 BMP biosynthesis and bioactivity	2
1.3.1 Biosynthesis of BMPs as prodomain-growth factor complexes	2
1.3.2 The conformation of BMP complexes defines their activation status	4
1.3.3 BMP type II receptors displace BMP prodomains from the growth factor	5
1.4 BMPs are targeted to the extracellular matrix components	6
1.4.1 Targeting to the extracellular component fibrillin-1	6
1.4.2 BMP activation mechanisms from FMF latent pools	8
1.4.2.1 Integrin mechanical pulling	9
1.4.3 The extracellular component heparin/HS	10
1.4.3.1 Heparin/HS controls growth factor signaling	10
1.4.3.2 BMPs are targeted to heparin/HS	10
1.5 Fibrillin and heparin/HS form extracellular microenvironments to control growth factor signaling	11
1.6 Dysregulated TGF- β signaling contributes to the fibrillinopathies	12
1.7 Goal of the thesis	13
2. Materials and methods	15
2.1 Instruments	15
2.2 Software	15
2.3 Online platforms	16
2.4 Purchased chemicals and solutions	16
2.5 Prepared buffers and solutions	18
2.6 Proteins, enzymes and antibodies	19
2.6.1 Proteins and enzymes	19
2.6.2 Antibodies	20
2.7 Oligonucleotides	21
2.7.1 Primers for generation of the BMP-7 prodomain truncations	21
2.7.2 Primers for generation of the fibrillin-1 FUN domain truncations	22
2.7.3 Primers for quantitative PCR	22
2.8 Plasmids	22
2.8.1 Mammalian expression	22
2.8.2 Bacterial expression	23
2.9 Expression organisms	24
2.9.1 Mammalian cells	24
2.9.2 Bacterial cells	24
2.10 Materials	24
2.10.1 Others	24
2.10.2 Kits	24
2.11 Mammalian cell culture work	25

2.11.1	Cell growth media and transfection.....	25
2.11.2	Clone selection and propagation.....	25
2.11.3	Freezing mammalian cells.....	25
2.11.4	Stimulation assays with C2C12 and HUVEC cells.....	26
2.11.5	Cell lysates of HEK293 cells.....	26
2.12	Biochemical methods.....	27
2.12.1	Protein expression and purification.....	27
2.12.1.1	Bacterial cells.....	27
2.12.1.1.1	Transformation.....	27
2.12.1.1.2	Clone selection, inoculation and collection of <i>E.coli</i> pellet.....	27
2.12.1.1.3	Urea purification.....	28
2.12.1.1.4	Protein extraction from <i>E.coli</i> cells.....	28
2.12.1.1.5	Protein purification from <i>E.coli</i> cells.....	29
2.12.1.2	Protein purification from mammalian cells.....	29
2.12.1.3	Size exclusion chromatography.....	29
2.12.1.4	Prodomain separation from BMP-7 complex.....	30
2.12.2	Protein quantification.....	30
2.12.3	Western blotting.....	30
2.12.4	Mass Spectrometry.....	31
2.13	Established protocols to study Bone Morphogenetic proteins.....	35
2.13.1	Wet lab techniques.....	35
2.13.2	<i>In silico</i> techniques.....	43
3.	Results.....	45
3.1.	Preface.....	45
3.2.	PPC processing renders BMPs bioactive.....	46
3.2.1	Manuscript in preparation #1.....	47
3.3.	Heparin/HS controls bioavailability of BMP growth factors.....	95
3.3.1	Manuscript in preparation #2.....	96
3.4.	Activation mechanisms to render fibrillin-bound BMPs bioavailable.....	146
3.4.1	Peer-reviewed manuscript.....	147
4.	Discussion.....	170
4.1.	Mechanisms controlling BMP bioavailability within the ECM.....	170
4.1.1	PPC processing impacts BMP bioavailability.....	170
4.1.2	MMP cleavage regulates the bioavailability of BMPs.....	172
4.1.3	Targeting of BMPs to glycosaminoglycans.....	172
4.1.4	Dysregulated ECM bioavailability mechanisms in disease onset and progression.....	174
4.1.4.1	BMPs in HHT.....	174
4.1.4.2	BMPs in cancer.....	175
4.1.4.3	BMPs in connective tissue disorders.....	176
4.2	Outlook.....	178
5.	References.....	179
6.	Abbreviations.....	200
7.	Acknowledgements.....	205

Curriculum Vitae.....

Erklärung.....

Abstract

Bone morphogenetic proteins (BMPs) belong to the TGF- β superfamily of pluripotent growth factors that exert several critical cellular functions such as proliferation, differentiation, and apoptosis during development and tissue homeostasis. Although originally discovered as extractable cytokines from bone matrix, it has not been investigated how the extracellular matrix controls their bioavailability. Gaining a better understanding about the molecular requirements controlling BMP activity within extracellular tissue microenvironments is crucial for new therapeutic advances in connective tissue disease and tissue regeneration. BMPs are synthesized as single chain precursors consisting of a prodomain (PD) and a growth factor (GF) moiety that are processed by proprotein convertases (PPCs) to form a non-covalently associated PD-GF complex (CPLX). By employing transmission electron microscopy (TEM) with single particle averaging, molecular docking and bioactivity assays, it was discovered that PPC processing induces a conformational change that renders BMP-10 CPLX signaling-competent. Since BMP-10 predominantly circulates in human plasma as an unprocessed variant, its bioactivity can thus be regulated by the availability of PPCs within the extracellular space.

In addition, the ECM can regulate BMP bioactivity by specific PD mediated targeting of BMP CPLXs to the microfibril component fibrillin-1. It was shown previously that the bioactive V-shape of BMP-7 CPLX assumes a latent, closed-ring conformation when targeted to fibrillin-1. In contrast, by employing negative staining EM and bioactivity assays on solid phase, it could be demonstrated that BMP-7 and BMP-9 CPLX targeting to heparin/ HS maintains their bioactive state. Molecular modeling, docking and heparin binding studies pointed towards conserved heparin/ HS binding epitopes residing within the PD arm regions.

In order to shed light into activation mechanisms of the fibrillin-bound BMPs, a cleavage screen using several matrix metalloproteinases (MMPs), combined with Edman sequencing and mutagenesis were employed that pointed towards a conserved PD cleavage consensus. By employing bioactivity assays, EM with single particle averaging and native PAGE it was found that MMP-13 releases bioactive GF leading to CPLX unfolding.

In summary, this thesis provides a comprehensive analysis of different mechanisms utilized by the ECM to control BMP bioactivity in distinct extracellular microenvironments.

Zusammenfassung

Knochenmorphogenetische Proteine (bone morphogenetic proteins: BMPs) gehören zur TGF- β -Superfamilie pluripotenter Wachstumsfaktoren, die während der Embryonalentwicklung und der Gewebshomöostase wichtige zelluläre Funktionen wie Proliferation, Differenzierung und Apoptose ausüben. Obwohl sie ursprünglich als extrahierbare Zytokine aus der Knochenmatrix entdeckt wurden, wurde bisher nicht untersucht, wie die extrazelluläre Matrix ihre Bioverfügbarkeit kontrolliert. Ein besseres Verständnis der molekularen Mechanismen, welche die BMP-Aktivität in der extrazellulären Mikroumgebung steuern, ist für neue therapeutische Fortschritte bei Bindegewbserkrankungen und Geweberegenerationsprozessen von entscheidender Bedeutung. BMPs werden als einkettige Vorläufer synthetisiert, die aus einer Prodomäne (PD) und einem Wachstumsfaktor (GF) bestehen und durch Proprotein-Konvertasen (PPCs) prozessiert werden. Dabei entsteht ein nicht-kovalent assoziierter PD-GF-Komplex (CPLX). Durch den Einsatz von Transmissions-Elektronenmikroskopie (TEM), molekularem Docking und Bioaktivitätstests wurde entdeckt, dass die PPC-Prozessierung eine Konformationsänderung hervorruft, die BMP-10 CPLX in den aktiven Zustand versetzt. Da BMP-10 überwiegend als unverarbeitete Variante im menschlichen Plasma zirkuliert, kann seine Bioaktivität durch die Verfügbarkeit von PPCs im Extrazellulärraum reguliert werden.

Darüber hinaus kann die ECM die Bioaktivität von BMP durch spezifische PD-vermittelte Interaktion von BMP-CPLXs an die Mikrofibrillen-Komponente Fibrillin-1 regulieren. Die bioaktive V-Form von BMP-7 CPLX nimmt dabei eine latente, geschlossene Ringkonformation an. Im Gegensatz dazu konnte durch den Einsatz von EM mit negativer Färbung und Bioaktivitätstests gezeigt werden, dass an Heparin/ HS gebundenes BMP-7 und BMP-9 CPLX, seinen bioaktiven Zustand beibehält. Molekulare Modellierung, Docking und Heparin-Bindungsstudien wiesen auf konservierte Heparin/ HS-Bindungsepitope in den jeweiligen PD-Arm-Regionen hin.

Um die Aktivierungsmechanismen der Fibrillin-gebundenen BMPs zu untersuchen, wurde ein Spaltungsscreening von BMP PDen mit verschiedenen Matrix-Metalloproteasen (MMPs) durchgeführt. Durch den Einsatz von Bioaktivitätstests, und EM wurde festgestellt, dass MMP-13 bioaktives GF freisetzt, das zur Entfaltung von CPLX führt.

Diese Arbeit zeigt verschiedene neue Mechanismen auf, die von der ECM zur Kontrolle der BMP Bioverfügbarkeit in der extrazellulären Mikroumgebungen genutzt werden.

1. Introduction

1.1 TGF- β superfamily ligands

The TGF- β superfamily consists of at least 35 cytokines and contains four subfamilies of growth factors which include TGF- β s, bone morphogenetic proteins (BMPs)/growth and differentiation factors (GDFs), activins/inhibins, and glial cell line-derived neurotrophic factors (GDNFs) (Weiskirchen et al., 2009). TGF- β superfamily members play important roles during embryonic development and postnatal homeostasis of various organs and tissues, (Shi Y and Massagué J, 2003; Wu and Hill, 2009). Currently, it is not well understood how the cellular microenvironment in tissues controls the activation status of TGF- β superfamily ligands in a contextual manner. Shedding light into these mechanisms is crucial in order to better understand why similar amounts of the same growth factor may be for instance latent in musculoskeletal tissues, but bioactive in the tumor microenvironment.

1.2 Discovery and biological role of BMPs

Bone morphogenetic proteins (BMPs) were firstly discovered in acid extracts of demineralized and lyophilized bone due to their ability to trigger the migration and proliferation of histiocytes and other specific cell types into an area of demineralized bone. (Urist, 1965). Subsequent studies confirmed this initial observation since cultivation of mesenchymal muscle cells together with demineralized bone matrix induced their differentiation into chondrocytes (Nogami and Urist, 1970; Urist and Strates, 1971). Since then, multiple other studies have demonstrated that BMPs function as pluripotent cytokines that regulate a multitude of biological functions such as embryonic patterning and organogenesis by controlling cell differentiation, migration, and apoptosis (Katlicheva et al., *Developmental Biology*. 2016; for review: Wang et al., *Genes and Diseases*. 2014). More specifically, deletion of BMP-2 in mice compromises viability due to amnion/chorion defects and cardiac abnormalities whereas concurrent deletion of BMP-6 and BMP-7 in mice results in death in early embryonic stages due to cardiac insufficiency (Zhang et al., 1996; Kim et al., 2001; for review: Zimmermann et al., 2021)

During postnatal life, BMPs maintain organ homeostasis and drive crucial tissue regeneration and repair processes. For example, BMP-2 has prominent roles in bone growth, regeneration and repair (Rosen et al., 2009). Apart from facilitating bone fracture healing

(Diwan et al., 2013), BMP-7 supports correct kidney function by counteracting the profibrotic TGF- β action to protect against kidney injury and fibrosis (Vukicevic et al., 1998; Zeisberg et al., 2003; Bramlage et al., 2010). BMP-9 and BMP-10 circulate in the blood stream to maintain vascular physiology and function by regulating proper capillary bed formation. This is illustrated by the consequences of deficient BMP-10 signaling which is causative for the genetic disease hereditary hemorrhagic telangiectasia (HHT) that is characterized by lack of vascular beds, abnormal connections between arteries and veins that lead to vascular rupture and internal bleeding as a consequence (Capasso et al., 2020; Roman et al., 2017).

Myostatin (also known as GDF-8) negatively regulates skeletal muscle mass by limiting satellite cell proliferation and maintaining their quiescent state (McCroscery et al., 2003). Studies in mice, cattle and humans revealed that myostatin inactivation leads to an overly-muscular phenotype accompanied by increased muscular strength (McPherron et al., 1997a, Grobet et al., 1997, McPherron et al., 1997b, Kambadur et al., 1997, Schuelke et al., 2004). This became more evident in the *mdx* mouse model of muscular dystrophy when myostatin inactivation improved the clinical muscle wasting phenotype of these mice (Wagner et al., 2002). Human *GDF8* ablation in a reported child whose mother was an athlete with several other family members resulted in unusual muscular strength for his age (Schuelke et al., 2004).

1.3 BMP biosynthesis and bioactivity

1.3.1 Biosynthesis of BMPs as prodomain-growth factor complexes

BMPs belong to TGF- β superfamily ligands which are all first produced as single chain precursors composed of an N-terminal prodomain (PD) and a C-terminal growth factor (GF) moiety. In a second step the PD is processed from the GF by proprotein convertases (PPCs) and a non-covalently associated PD-GF complex (CPLX) is formed. As long as both moieties are contained in a single chain, the PD needs to fold first or concurrently to the GF so that the resulting PD-GF complex (CPLX) can assume correct conformation (Gray and Mason, 1990; Shi et al., 2011). BMP single chain precursors are dimerized via exposed cysteines of the GF. Each GF moiety contains seven cysteines of which six fold into a 6-cysteine-knot while disulfide-bridging via the seventh cysteine allows the formation of a GF dimer (Griffith et al., 1996). In a final step, the family of proprotein convertases (PPC)

processes the carboxyl-end of the PD at the consensus sequence R/K-X_n-R/K↓ (Constam et al., 1999; Jaaks et al., PLOS. 2016) (Fig. 1.1).

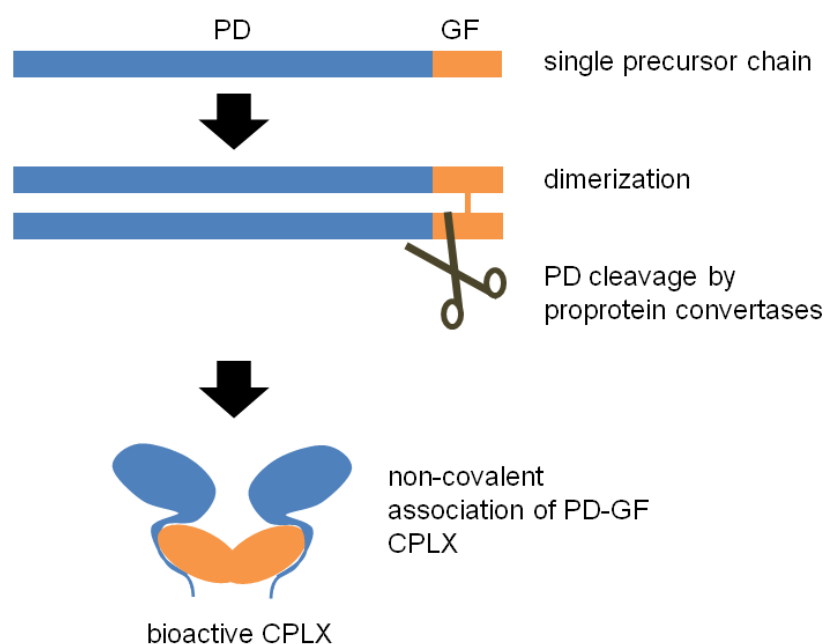


Figure 1.1: Schematic overview of BMP biosynthesis. BMPs are produced as single precursor chains that are dimerized via disulfide bridging of their GF moieties. The dimers are then subjected to proteolytic cleavage at the carboxyl end of the PD by proprotein convertases (PPCs) to yield a non-covalently associated PD-GF CPLX that is bioactive.

While in the most-widely accepted view PPC processing occurs intracellularly, also extracellular processing of TGF- β superfamily members has been proposed. For instance, it was found that Elastin microfibril interfacier 1 (EMILIN-1) can inhibit PPC processing of the secreted unprocessed TGF- β precursor within the extracellular space (Zacchigna et al., 2006). In addition, promyostatin was found in an unprocessed form extracellularly in skeletal muscle whereas the PPC-processed variant was abundant in serum (Anderson et al., 2008). Most BMP-10 in human plasma was detected in an unprocessed form (Hodgson et al, 2019), while quantitative intracellular processing by PPCs was demonstrated in cell culture (Susan-Resiga et al., 2011; Jiang et al., 2016).

The PPC family member furin requires an arginine or lysine in the P2 position of the PPC consensus along with positively-charged residues, preferably arginines in positions P1 and P4 to confer efficient cleavage (Hosaka et al. 1991; Henrich et al., 2003). Furin cleaves at the consensus sequence R-X-R/K-R and can thereby efficiently process the PDs of TGF- β (Shi et al., 2011), GDF-8 (Cotton et al., 2018; Le et al., 2018), proactivin (Wang et al., 2016), BMP-9 (Mi et al., 2015) and BMP-10 (Susan-Resiga et al., 2011; Jiang et al., 2016).

Intracellular or extracellular processing by PPC results in cleavage of the PD-GF covalent linkage of the precursor yielding a GF dimer that is now non-covalently associated to the two PDs. Hence after processing, BMPs form stable CPLXs consisting of two PDs that are non-covalently associated to the GF dimer as already demonstrated for proactivin (Wang et al., 2016), GDF-8 (Le et al., 2018), BMP-7 (Gregory et al., 2005), BMP-9 (Mi et al., 2015) and BMP-10 (Jiang et al., 2016).

1.3.2 The conformation of BMP complexes defines their activation status

The general positioning and functioning of distinct secondary structure elements of the PD is quite similar among TGF- β superfamily members. BMP-7, proactivin, GDF-8 and TGF- β CPLXs associate via their N-terminal PD α 1 helix with their cognate GFs and in addition receptor access is controlled via the PD latency lasso and the α 2 helix. Therefore, based on the structural arrangement of the PD and the GF within the CPLX, bioactivity or latency is manifested (Wohl et al., 2016; Furlan et al., 2021; Wang et al., 2016; Cotton et al., 2018; Le et al., 2018; Shi et al., 2011). For example, PPC processed BMP-7 and proactivin CPLXs both assume a V-shape that is bioactive in solution and allow cell surface receptor engagement with its GF epitopes (Wohl et al., 2016; Wang et al., 2016). Processed GDF-8 though assuming a similar V-shape, requires an additional PD proteolytic event by tolloid-like protein 2 (TLL2) in order to be rendered bioactive (Cotton et al., 2018; Le et al., 2018). Interestingly, after TLL2-cleavage the GDF-8 CPLX maintains its V-shape conformation (Le et al., 2018), that now permits receptor access. Though the PD α 1 helix associates to the GF similarly to BMP-7 and proactivin, the GDF-8 GF has a fundamentally different folding compared to other BMP GFs and may inadvertently get trapped into an inactive state when complexed to its PD (Cotton et al., 2018).

TGF- β GF on the other hand has been crystallized together with its PD called latency-associated peptide (LAP) in a closed-ring CPLX conformation called small latent complex (SLC) that requires further activation mechanisms in order to render the GF accessible to receptors (Shi et al., 2011). A stable PD-GF closed-ring conformation is maintained by intra PD disulfide bridges within the C-terminal region of LAP. The TGF- β GF also assumes different folding than the free, bioactive, uncomplexed TGF- β GF (Shi et al., 2011) which means that the structure of the LAP must be altered or compromised so that the receptors can interact with the TGF- β GF (Le et al., 2018; Shi et al., 2011).

Processed BMP-9 CPLX assumes a slightly more open V-shape (termed “open-arm”) that is bioactive in solution (Mi et al., 2015) whereas its unprocessed counterpart is latent (Kienast et al., 2016). BMP-9 has a surprisingly low PD-GF affinity in comparison to other BMP CPLXs that renders it less stable as evidenced by isothermal titration calorimetry (ITC) measurements (Mi et al., 2015). In agreement with the above, BMP-9 CPLX is structured differently and has thereby a different PD-GF interface compared to other BMP CPLXs. More specifically, it is the PD $\alpha 5$ helix that associates with the GF (Mi et al., 2015) instead of the $\alpha 1$ helix that is utilized in all other investigated BMP CPLXs and TGF- β (Wohl et al., 2016; Furlan et al., 2021; Wang et al., 2016; Cotton et al., 2018; Le et al., 2018; Shi et al., 2011).

For BMP-10 CPLX, the closest relative of BMP-9, little structural information is available. A recent study showed that the unprocessed BMP-10 dimer assumes an open-arm conformation similar to the processed BMP-9 CPLX (Le et al., 2022), however, without investigating the structure of BMP-10 CPLX after PPC processing.

1.3.3 BMP type II receptors displace BMP prodomains from the growth factor

For non-covalently associated PD-GF CPLXs of BMP-7, -9, and -10 after processing it has been shown that the PD is “displaceable” after receptor binding to the GF. More specifically, type II receptors can spontaneously remove BMP-7 (Sengle et al., 2008b), BMP-9 (Kienast et al., 2016) or BMP-10 PDs (Jiang et al., 2016) to gain GF access. In the case of BMP-9 the co-receptor endoglin is also able to spontaneously remove the BMP-9 PD in order to make contact with the GF (Salmon et al., 2020). This notion is also supported from a structural perspective based on the atomic model of the BMP-9 GF/endoglin (Saito et al., 2017). Comparison of this model with the BMP-9 CPLX structure clearly showed that the PD masks the endoglin binding site on the GF (Mi et al., 2015; Saito et al., 2017). However, not for all receptors PD displacement is required. For instance, type I receptors require access to different regions within the GF that are already available within its PD-complexed form as evidenced from the BMP-9 CPLX/ALK-1 atomic model (Salmon et al., 2020).

Generally to initiate BMP signaling, BMPs form a ternary complex with type II and type I receptors. For canonical pSMAD pathway activation, type II receptors phosphorylate type I receptors (Allendorph et al., 2006) that transduce signaling by further phosphorylating the SMADs (small mothers against decapentaplegic): SMAD1, SMAD5 and SMAD8. After association with the co-SMAD SMAD4, the SMAD complex translocates to the nucleus to trigger gene expression of downstream BMP gene targets such as the inhibitor of

differentiation 3 (*Id3*) (Sengle et al., 2008b). Apart from the canonical pSMAD, BMPs can also activate the non-canonical pSMAD that signals via mitogen activated protein kinases (MAPK-ERK) (Horbelt et al., 2012).

1.4 BMPs are targeted to extracellular matrix components

1.4.1 Targeting to the extracellular component fibrillin-1

Fibrillin-1 is a large multi-domain, extracellular glycoprotein that is assembled into fibrillin microfibrils (FMF) in a staggered conformation (Lee et al., 2004). Thereby the N-terminal part of a single fibrillin-1 molecule (domains: FUN until EGF3) interacts with the C-terminal part of another fibrillin-1 molecule (domains: cbEGF41 until cbEGF43) to form beads-on-a-string FMF (Fig. 1.2 and El-Hallous et al., 2007; Hubmacher et al., 2008; Yadin et al., 2013; Sakai et al., 1991; for review: Zigrino and Sengle 2019) that serve as scaffolds for the deposition of other extracellular matrix (ECM) components during elastogenesis (Olivieri et al., 2010). Apart from their structural role within the ECM architecture, FMF actively control the bioavailability of ligands of the TGF- β superfamily (Sengle et al., 2015b). BMPs were shown to be targeted to the FMF scaffold via direct PD interactions with the N-terminal region of fibrillin-1 (Isogai et al., 2003; Sengle et al., 2008a). The closed-ring SLC that is comprised of LAP and the TGF- β GF is targeted to fibrillin-1 via latent TGF- β binding proteins (LTBPs). More specifically, the TB domains of LTBPs interact with LAP to form the large latent complex (LLC) whereas LTBPs C-terminal moieties bind to the first hybrid and following cbEGF-like domains of the fibrillin-1 N-terminus to anchor the LLC to the FMF (Isogai et al., 2003; Ono et al., 2009; Shi et al., 2011 and Fig. 1.2).

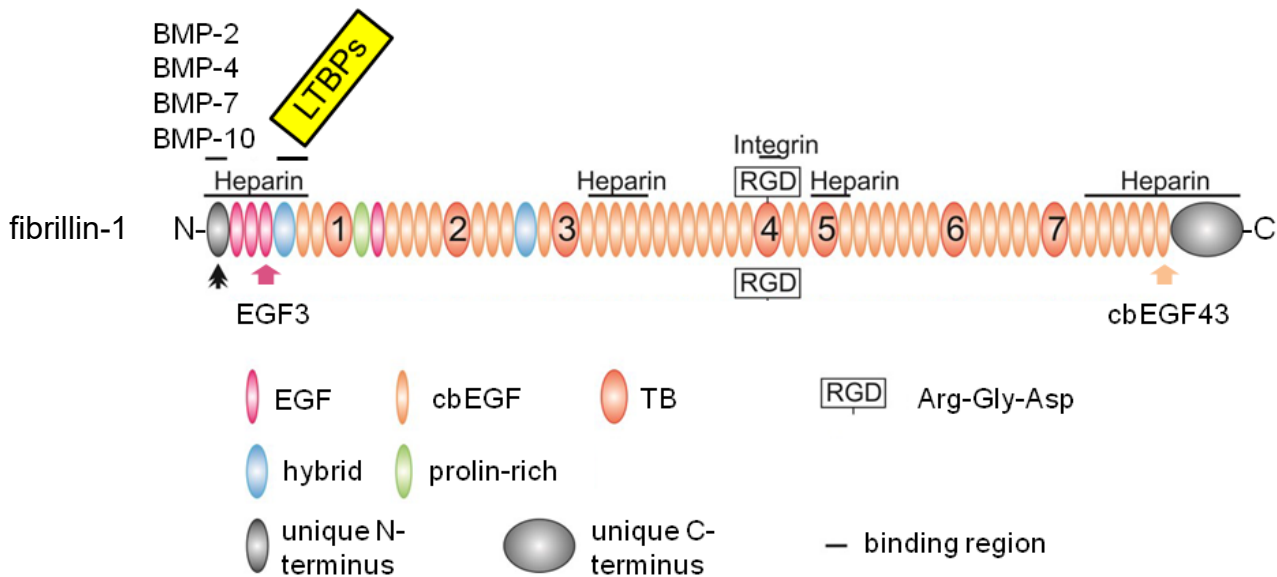
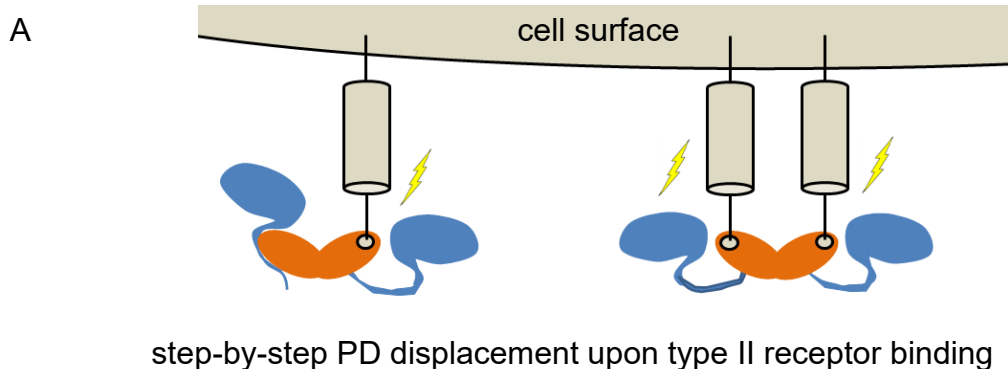


Figure 1.2: TGF- β superfamily ligands are targeted to fibrillin-1. Scheme showing fibrillin-1 domains. BMPs bind at the unique N-terminus domain (FUN) whereas LTBPs bind further down at the hybrid and the following cbEGF-like domains (modified after Piha-Gossack et al., 2012).

BMP CPLXs are targeted via their PDs to a different N-terminal region of fibrillin-1 called the FUN domain (Sengle et al., 2008a; Fig. 1.2). The PD-FUN interaction has profound consequences for the BMP-7 CPLX conformation that is altered from an open V-shape to a closed-ring similar to SLC (Wohl et al., 2016; Shi et al., 2011). This induced conformation is stabilized by additional interactions between the C-terminal ends of both PDs that lock the inhibitory $\alpha 2$ helix of the PD in position so that PD displacement cannot take place anymore and receptor access to the GF is blocked (Wohl et al., 2016). Hence, for BMP-7 CPLX, transition from the in solution V-shape to the fibrillin-bound closed-ring is also accompanied by a change in the bioactivity status from bioactive to latent (Wohl et al., 2016 and Fig. 1.3A and B). Such a sequestration mechanism has been also hypothesized for BMP-9 CPLX since it seems able to undergo a similar conformational change from open-arm to closed-ring as evidenced from *in silico* studies (Mi et al., 2015 and Fig. 1.3A and B).



B

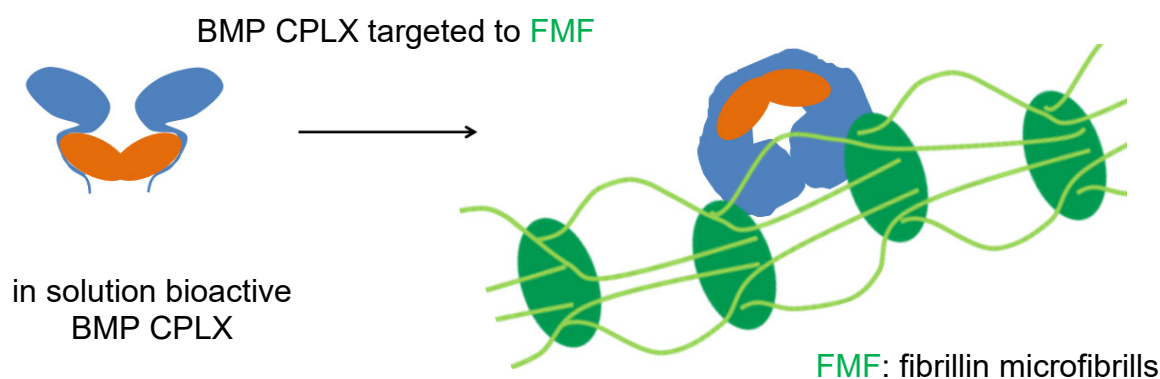


Figure 1.3: BMP CPLXs assume a closed-ring shape conformation when bound to FMF.

(A) Type II receptors displace BMP PDs to render the GF accessible in the in-solution bioactive BMP CPLX structure (Sengle et al., 2008b; Kienast et al., 2016; Jiang et al., 2016). Activated receptor is marked with a thunder sign. (B) Receptor access is blocked when BMP CPLXs are bound to fibrillin microfibrills in closed-ring shape conformation (Wohl et al., 2016) (modified after Wohl et al., 2016).

1.4.2 BMP activation mechanisms from FMF latent pools

Several activation mechanisms have been described to activate and utilize TGF- β growth factors from their ECM-bound state. Most studies have focused on the activation of TGF- β GF that involves LAP removal via mechanical integrin pulling, or proteolytic degradation. So far five activation mechanisms to release TGF- β GF have been described. First, mechanical pulling of LAP via its RGD binding site by integrins within the LLC has been reported to result in the release of bioactive GF (Fontana et al., 2005; Buscemi et al., 2011; Shi et al., 2011). Second, proteolytic degradation of LAP by MMP-2 and -9 renders the GF accessible by TGF- β receptors (Yu et al., 2000). Third, a combination of activation mechanisms was also proposed with integrin pulling of LAP within the LLC followed by MMP-14-mediated LAP degradation (Mu et al., 2002). Fourth, sequential proteolytic events such as LTBP-1 cleavage by BMP-1 to release the LLC from the ECM followed by MMP-2 mediated degradation of LAP (Ge et al., 2006). Fifth, TGF- β GFs can also be activated within the SLC via the interaction of thrombospondin-1 with LAP that results in LAP re-arrangement within the SLC to activate TGF- β GF without SLC disintegrating (Solange et al., 1999).

1.4.2.1 Integrin mechanical pulling

The SLC is composed of two processed LAP molecules that non-covalently associate to the GF dimer via the $\alpha 1$ helix. Activation of the TGF- β GF by integrin pulling cannot take place unless the SLC is LTBP-bound at a stoichiometry SLC: LTBP 1:1 (Shi et al., 2011). This makes sense since the application of mechanical integrin forces at the exposed integrin binding epitopes (RGDs) on the LAP arms is resisted by LTBP that is disulfide-linked to LAP (shown as bottom in figure 1.4). Exerting mechanical integrin forces on LAP of the LLC, unfastens the LAP straightjacket within the LLC structure and renders the TGF- β GF dimer receptor-accessible. The LLC structure seems to extend like a spring so that association of the straightjacket to the GF is lost thereby leading to disintegration of the SLC (Fig. 1.4). Furthermore, while effective integrin pulling requires its tethering as LLC to the ECM, it is not clear whether the thrombospondin-1/SLC ternary complex is targeted to the ECM or follows a different receptor engagement mechanism (Solange et al., 1999). Although not yet investigated, similar potential activation mechanisms of fibrillin-bound BMP CPLXs can be considered.

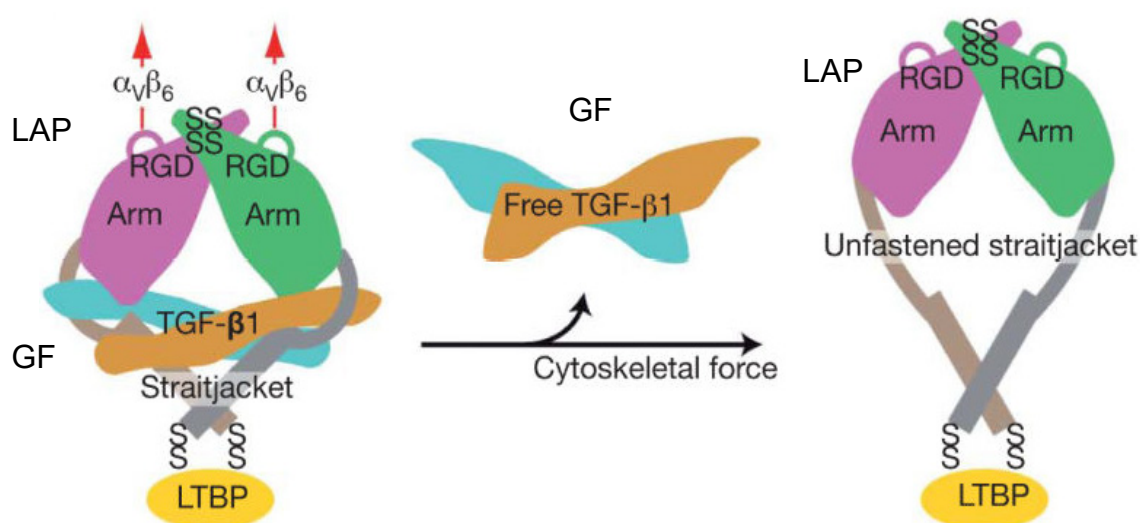


Figure 1.4: Scheme showing activation of TGF- β GF upon integrin mechanical pulling of LAP.

In this figure, a simplified model of the LLC is presented. The model shows that LAP straightjacket masks the GF and additionally establishes disulfide-bonding with the LTBP. Integrin mechanical forces (indicated as red arrows) are applied at the exposed integrin binding sites (RGDs) of the LAP arm regions. The outcome of the cytoskeletal forces is the liberation of the TGF- β GF by unfastening the straightjacket to render the GF available to receptors. The LLC seems to extend like a spring due to the mechanical pulling so that association of the straightjacket to the GF is lost. LAP monomer: purple/green, GF monomer: brown/blue straightjacket: grey, LTBP: yellow (modified after Shi et al., 2011).

1.4.3 The extracellular component heparin/HS

1.4.3.1 Heparins/ HS controls growth factor signaling

It has been an established concept that heparin/ HS regulates GF availability and signaling by interacting with receptors and co-receptors on the cell surface such as the receptors of the vascular endothelial growth factor (VEGF) and the fibroblast growth factor (FGF) (Allen et al., 2003; Teran et al., 2015). Indeed, presence of heparin/ HS can facilitate VEGF binding to its receptors and can even assist in receptor selection thus fine-tuning VEGF signaling to endothelial cells (Teran et al., 2015). In addition, heparin/ HS acts as reservoir that concentrates GFs locally as a sink, protects GFs against proteolytic degradation or quenches GF signal capability (Bishop et al., 2007). Rendering heparin/HS-bound GFs available to cells is thought to involve the action of heparinases that cleave away the disaccharide chains to free the GFs thereby allowing these cytokines to signal locally (Vlodavsky et al., 2001; Li et al., 2010).

1.4.3.2 BMPs are targeted to heparin/ HS

Spatial concentration of GFs to heparin/ HS in embryonic tissues is thought to be required for the establishment of FGF, VEGF, and BMP morphogen gradients that are critical for embryonic patterning. Indeed, deletion of the BMP-4 heparin/HS binding site disturbed BMP-4 gradient formation in the *Xenopus* embryo during development (Ohkawara et al., 2002) (Rider et al., 2017). Since fibrillin-1 contains four heparin binding sites (Cain et al., 2005 and Fig. 1.2A), BMPs may also be targeted to FMF via interactions with fibrillin-bound heparin/ HS or fibrillin-bound heparan sulfate proteoglycans (HSPGs) such as perlecan (Tiedemann et al., 2005). One prominent example for such an indirect targeting mechanism to FMF is GDF-8, since its PD interacts with the HS side-chains of the perlecan but not with fibrillin-1 itself (Tiedemann et al., 2005; Sengle et al., 2011).

Ionic protein-heparin/ HS contacts are mediated by secondary structure elements which form tunnels or pockets that allow the insertion of long heparin chains to stabilize the interaction. Thereby, the affinity of proteins to the negatively charged heparin chain with its densely sulfated disaccharides depends on the positively charged patches available on the protein surface (Gandhi et al., 2012). So far, only the aminoacid sequences of proactivin CPLX that bind heparin/ HS have been identified without mapping them within the CPLX

atomic model. These heparin/HS aminoacid sequences are contained within the proactivin PD while the proactivin GF alone failed to bind heparin/ HS (Li et al., 2010). It was further shown that the proactivin CPLX binds to the HS side-chains of perlecan and that same CPLX can be targeted to specific ECM components such as perlecan or agrin suggesting therefore BMP spatial concentration within heparin/ HS-enriched ECM microenvironments (Li et al., 2010). However, BMP-2, BMP-4, BMP-7, BMP-5 and BMP-6 GFs do interact with heparin/ HS with characterized binding epitopes that contain the general consensus motifs: XBBXB or XBBBXXBX (with X: uncharged amino acid and B: basic amino acid) (Billings et al., 2018). Apart from harboring such motifs, cooperative binding with other interacting partners can additionally enhance heparin binding. Such an example is the interaction of GDF-8 to the heparin-binding antagonist follistatin 288 that creates a strong positive surface charge to confer more efficient heparin binding when GDF-8 is complexed (Cash et al., 2009; for review: Rider et al., 2017). Overall, heparin/ HS serves as an ECM scaffold that concentrates GFs in free or PD-complexed form locally with unknown consequences for bioactivity. So far, it has only been shown that specifically concentrating BMP-2 GF on grafted heparin/HS surfaces maintains its signaling competency (Migliorini et al., 2017).

1.5 Fibrillin and heparin/ HS form extracellular microenvironments to control growth factor signaling

Within the staggered conformation of FMF, epitopes for heparin, LTBP, and BMP binding localize to the bead region that locally controls GF signaling (Zigrino and Sengle, 2019; Fig. 1.5). Since it was shown that TB5 contains heparin binding sites that are abolished by WMS causing mutations (Cain et al., 2005, Fig. 1.5), it is conceivable that BMP GFs may be concentrated to FMF via the binding of GAGs. Concentrating bioactive BMP GFs locally allows to maintain physiologically relevant levels of BMP signaling that are required for tissue homeostasis. On the other hand, spatial concentration of BMPs in a latent state via heparin/ HS or extracellular protein scaffolds such as FMF may allow to activate them as soon as the tissue integrity is compromised. Activation of sequestered TGF- β s and BMPs underlies tight regulation involving heparinases (Vlodavsky et al., 2001; Li et al., 2010), integrins (Shi et al., 2011), or proteases (Zimmermann et al., 2021).

fibrillin-1 is assembled into
fibrillin microfibrils (FMF)

FMF microenvironment
that controls GF signaling
locally

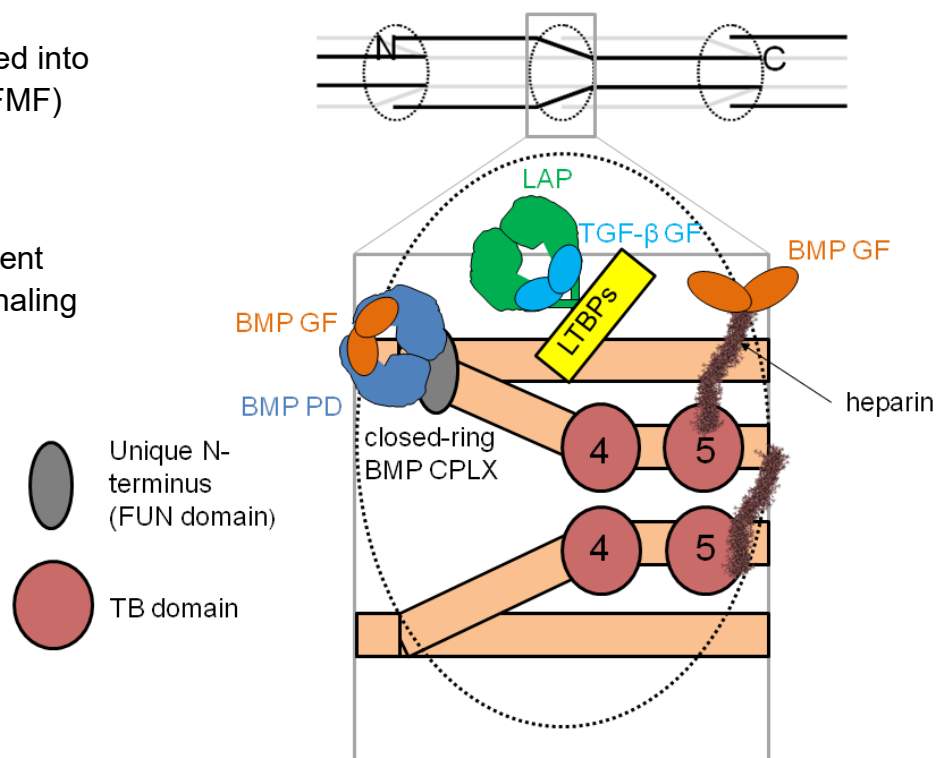


Figure 1.5: FMF forms an extracellular microenvironment that controls GF signaling locally. Fibrillin-1 is assembled into FMF in staggered conformation with the fibrillin-1 N-terminus of one molecule interacting with the fibrillin-1 C-terminus of another molecule to form the beads-on-a-string ultrastructure (bottom). Heparin binds at the TB5 domain (Cain et al., 2012) and may attract BMP GFs. BMP CPLXs bind FUN (shown in grey) and LLCs bind the first hybrid domain (not indicated). BMP GF: orange, TGF- β GF: light blue, BMP PD: blue, LAP: green, LTBPs: yellow (modified after Zigrino, Sengle, 2019).

1.6 Dysregulated TGF- β signaling contributes to the fibrillinopathies

The regulation of TGF- β superfamily growth factor bioavailability by FMF is illustrated by diseases caused by fibrillin-1, or -2 mutations (fibrillinopathies). Patients with fibrillin-1 mutations show a significant clinical overlap with patients with mutations in TGF- β type I or II receptors or TGF- β -3 (Loeys et al., 2005; Bertoli-Avella et al., 2015). Fibrillin-1 mutations are causative for Marfan Syndrome (MFS) that is characterized by long bone overgrowth, muscle wasting, and aortic aneurysm formation (Lee et al., 1991; Dietz et al., 1991). Part of the disease pathology can be attributed to dysregulated TGF- β signaling since administration of losartan to inhibit TGF- β signaling together with β -blockers to lower blood pressure had a beneficial effect (Andel et al., 2020). Similarly, mutations in the TGF- β I and II receptors lead to Loeys-Dietz syndrome (LDS) that is characterized by skeletal defects, aortic aneurysms, decreased mental function and dysregulated TGF- β signaling (Loeys et al.,

2005). Interestingly, mutations in TB5 or genetic deletion of three fibrillin-1 domains (TB1, proline-rich, and EGF4-like domains) is causative for the Weill-Marchesani Syndrome (WMS) that is characterized by clinical features opposite to MFS such as short stature, hypermuscularity, thick skin, stiff joints, and brachydactyly (Faivre et al., 2003; Sengle et al., 2012). Interestingly, a genetic mutation in GDF-5 that abolishes PPC processing results in the synthesis of latent GDF-5 causing a WMS-like phenotype (Plöger et al., 2008). A similar phenotype was also reported in patients carrying a single missense mutation within the GDF-5 PD (Farooq et al., 2013) or the receptor epitope of the GDF-5 GF (Kjaer et al., 2006). GDF-5 GF is also predicted to bind heparin (Gandhi et al., 2012, for review: Rider et al., 2017) suggesting that targeting of GDF-5 to FMF via TB5-bound heparin is conceivable. Since the GDF-5 PD interacts with fibrillin-1, it seems plausible that not only GDF-5 CPLX can be directly targeted to FMF, but also GDF-5 GF indirectly via heparin.

Further, it was shown that disintegrin and metalloprotease with thrombospondin-like motif proteins like (ADAMTSL) proteins can be targeted to the WMS deletion site in fibrillin-1. ADAMTSL proteins also interact with the disintegrin and metalloprotease with thrombospondin motif 10 (ADAMTS-10) protease and mutations in ADAMTSL-2 or ADAMTS-10 were shown to be causative for WMS-like clinical manifestations (Dagoneau et al., 2004; Goff et al., 2008). ADAMTSL proteins are thought to anchor ADAMTS-10 enzymes at the three-domain deletion site to activate BMPs or TGF- β s that are targeted in close proximity within the FMF ultrastructure (Sengle et al., 2012; for review: Zimmermann et al., 2021). These findings indicate that FMF serve as critical scaffolds not only for growth factor sequestration, but also for their proper activation in the right physiological context.

1.7 Goal of the thesis

Currently, it is not clear how the ECM controls the bioavailability of BMPs. It was previously shown that BMP-7 is targeted to the ECM via the interaction of its PD with fibrillin-1. This interaction induces a conformational change in the BMP-7 CPLX which renders the GF latent. Such a mechanism not only suggests that the ECM is capable to spatially concentrate BMP CPLXs in latent state, but also that activation mechanisms for their context-dependent activation must exist. Interactions of BMP growth factors with the ECM have been already described, but almost exclusively in absence of the PD. For instance, a conserved heparin/HS binding motif in the BMP GF region was identified. Since it is known

that BMPs are secreted as PD-GF CPLXs it remains so far unknown how BMP CPLX binding to GAGs such as heparin/HS impacts their bioavailability.

Therefore, the overall goal of the thesis was to investigate the general mechanisms controlling BMP bioavailability within the ECM.

The first aim of the thesis was to understand how exactly PPC processing converts latent BMP precursors into signaling-competent, bioactive molecules.

The second aim was to investigate the binding mechanism of BMP CPLXs to heparin/HS and how this impacts their bioactivity.

The third aim was to investigate the activation mechanisms of fibrillin-bound, sequestered BMP CPLXs to release the bioactive GF.

2. Materials and Methods

2.1 Instruments

Name	Manufacturer
ÄKTA purifier 100 plus	<i>GE Healthcare (Little Chalfont, USA)</i>
Biacore® 2000	<i>GE Healthcare (Little Chalfont, USA)</i>
Cell culture incubator	<i>Heraeus Instruments, Thermo Fisher Scientific (MA, USA)</i>
Centrifuge 5424 (microcentrifuge)	<i>Eppendorf</i>
Compact S/M Gel electrophoresis chamber	<i>Analytik Jena (Jena, DE)</i>
FEI Tecnai 12 twin TEM	<i>FEI Company (Oregon, USA)</i>
FEI Tecnai G2 Polara TEM	<i>FEI Company (Oregon, USA)</i>
Flexcycler Duo	<i>Analytik Jena (Jena, DE)</i>
Glacios Cryo Transmission Electron Microscope	<i>Thermo Fisher Scientific (MA, USA)</i>
Gradient Mixer	<i>Topac (Massachusetts, USA)</i>
Infors HT Unitron incubator Plus AJ252	<i>Infors HT (Annapolis, USA)</i>
J-715 spectropolarimeter	<i>Jasco (Umstadt, DE)</i>
Microplate Reader Sunrise™	<i>Tecan (Männedorf, CH)</i>
Mini-PROTEAN® Tetra Cell System	<i>Bio-Rad Laboratories (Hercules, USA)</i>
Mini Trans-Blot® Cell	<i>Bio-Rad Laboratories (Hercules, USA)</i>
Nanodrop Spektralphotometer 2000	<i>Thermo Fisher Scientific (MA, USA)</i>
Odyssey CLx Imaging System	<i>LI-COR (Nebraska, USA)</i>
Peristaltic pump, HP model	<i>MDX Biotechnik (Nörten-Hardenberg, DE)</i>
qPCR Cycler StepOnePlus	<i>Applied Biosystems, Thermo Fisher Scientific (Schwerte, DE)</i>
Röntgenfilmentwicklermaschine Optimax (AGFA developing instrument)	<i>Protec Processor Technology (Oberstenfeld, DE)</i>
SDS-Gel Mini-PROTEAN Tetra Cell Casting Module	<i>Bio-Rad Laboratories (Hercules, USA)</i>
Sierra SPR-32	<i>Bruker (Hamburg, DE)</i>
Sorvall LYNX 6000 centrifuge	<i>Thermo Fisher scientific (MA, USA)</i>
Talos L120C G2 TEM	<i>Thermo Fisher scientific (MA, USA)</i>
Zetasizer Nano-S	<i>Malvern (Herfordshire, UK)</i>

2.2 Software

Name	Manufacturer
BIAevaluation Software 3.0	<i>GE Healthcare (Little Chalfont, USA)</i>
cryosparc software	<i>Punjani et al., 2017</i>
Epson Scan	<i>Epson Deutschland GmbH (Meerbusch, DE)</i>
Graph Pad Prism	<i>GraphPad (California, USA)</i>
ImageJ	<i>National Institute of Health (USA)</i>
Image Studio 5.2	<i>LI-COR (Nebraska, USA)</i>

Sierra Analyser	<i>Bruker (Hamburg, DE)</i>
Spectra Manager	<i>Jasco (Tokio, Japan)</i>
Swiss-PdbViewer 4.1.0	<i>(Guex und Peitsch, 1997)</i>
Tecan software	<i>Tecan Software Competence Center GmbH (Essen, DE)</i>
UCSF Chimera	<i>(Pettersen et al., 2004)</i>

2.3 Online platforms

Name	Link
Cluspro 2.0	https://cluspro.bu.edu/publications.php
Clustal Omega	https://www.ebi.ac.uk/Tools/msa/clustalo/
Dichroweb	http://dichroweb.cryst.bbk.ac.uk
ExPASy: Protparam tool	https://web.expasy.org/protparam/
Phyre2	http://www.sbg.bio.ic.ac.uk/phyre2/html/page.cgi?id=index
Swiss model	https://swissmodel.expasy.org/

2.4 Purchased chemicals and solutions

Name	Manufacturer
1-Step Ultra TMB ELISA	<i>Thermo Fisher Scientific (MA, USA)</i>
Acetone	<i>VWR (Darmstadt, DE)</i>
Acetic acid	<i>VWR (Darmstadt, DE)</i>
Acrylamide/ Bis-acrylamide	<i>National diagnostics (Atlanta, USA)</i>
AG 501-X8 Mixed Bed Resin, molecular biology grade (beads for urea purification)	<i>Bio-Rad, München (DE)</i>
Agarose	<i>Biozym (Wien, AUT)</i>
Animal-free blocker	<i>Vector Labs (California, USA)</i>
APS (Ammonium persulfate)	<i>Sigma-Aldrich (St. Luis, USA)</i>
Ampicillin	<i>Carl Roth (Karlsruhe, DE)</i>
Biotinylated heparin	<i>Nanocs (MA, USA) and Koch Lab</i>
Benchmark protein ladder	<i>Thermo Fisher Scientific (MA, USA)</i>
Benchmark prestained protein ladder	<i>Thermo Fisher Scientific (MA, USA)</i>
BSA (Bovine Serum Albumine)	<i>Serva (Heidelberg, DE)</i>
B-PER™ Bacterial Protein Extraction Reagent	<i>Thermo Fisher Scientific (MA, USA)</i>
Bromophenol Blue	<i>VWR International (Langenfeld, DE)</i>
Buffer BXT (10 ×)	<i>Iba lifesciences (Göttingen, DE)</i>
cOmplete, EDTA-free protease inhibitor cocktail	<i>Sigma-Aldrich (St. Luis, USA)</i>
Coomassie Brilliant Blue G250 pure	<i>Serva (Heidelberg, DE)</i>
Coomassie Brilliant Blue R250 pure	<i>Serva (Heidelberg, DE)</i>
DMEM Glutamax (Dulbecco's modified Eagle's medium)	<i>Thermo Fisher Scientific (MA, USA)</i>
DMSO	<i>Sigma-Aldrich, (St. Luis, USA)</i>
Di-Sodium tetraborate decahydrate for analysis ACS, ISO	<i>AppliChem GmbH, (Darmstadt, DE)</i>

DNA-Marker Gene Ruler	<i>BioLabs, (Frankfurt a.M., DE)</i>
DTT (dithiothreitol)	<i>Sigma-Aldrich, (St. Luis, USA)</i>
EDC (1-Ethyl-3-(3-dimethylaminopropyl) carbodiimide)	<i>Cytiva (MA, USA)</i>
EDTA	<i>Sigma-Aldrich (St. Luis, USA)</i>
Ethanol (bulk-96.5%)	<i>Bergchemie (Wuppertal, DE)</i>
Ethanol ROTIPURAN (99.8 %)	<i>Carl Roth (Karlsruhe, DE)</i>
Ethanolamine-HCl, pH=8.5	<i>Cytiva (MA, USA)</i>
Endothelial cell growth medium 2	<i>Promocell (Heidelberg, DE)</i>
FBS (fetal bovine serum)	<i>Merck (Darmstadt, DE)</i>
FuGENE® HD transfection reagent	<i>Promega (Madison, USA)</i>
Geneticin (G418 sulfate)	<i>Thermo Fisher Scientific (MA, USA)</i>
Glycerol 99.5%	<i>VWR International (Langenfeld, DE)</i>
Glycine	<i>VWR International (Langenfeld, DE)</i>
HEPES	<i>VWR (Darmstadt, DE)</i>
HBS-EP buffer for Biacore	<i>Cytiva (MA, USA)</i>
Hydrochloric acid	<i>Merck (Darmstadt, DE)</i>
Imidazole	<i>Carl Roth (Karlsruhe, DE)</i>
IPTG	<i>Carl Roth (Karlsruhe, DE)</i>
Methanol	<i>VWR (Darmstadt, DE)</i>
Milk powder	<i>Heirler (Radolfzell, DE)</i>
NHS (N-Hydroxysuccinimide)	<i>Cytiva (MA, USA)</i>
Nickel sulfate	<i>Sigma-Aldrich (St. Luis, USA)</i>
Nuclease-free water	<i>Qiagen (Hilden, DE)</i>
PBS (10 ×), pH 7.4	<i>Thermo Fisher Scientific (MA, USA)</i>
Pen/Strep (Penicillin/Streptomycine)	<i>Life technologies (Carlsbad, CA, USA)</i>
Perchloric acid ACS reagent, 70% (liquid form)	<i>Merck (Darmstadt, DE)</i>
PMSF (Phenylmethylsulfonylfluorid)	<i>Sigma-Aldrich (St. Luis, USA)</i>
Ponceau S	<i>Applichem (Darmstadt, DE)</i>
PureCube 100 Ni-NTA Agarose	<i>Cube Biotech (Monheim, DE)</i>
Puromycin	<i>Sigma-Aldrich (St. Luis, USA)</i>
RIPA lysis and extraction buffer	<i>Thermo Fisher Scientific (MA, USA)</i>
TEMED (N,N,N',N'-Tetramethyl ethylenediamine)	<i>Sigma-Aldrich (St. Luis, USA)</i>
Trypsin/EDTA solution (10 ×)	<i>Biochrom AG (Berlin, DE)</i>
SDS (Sodium dodecyl sulfate)	<i>VWR International (Langenfeld, DE)</i>
Sodium Chloride	<i>Carl Roth (Karlsruhe, DE)</i>
Sodium hydroxide	<i>VWR (Darmstadt, DE)</i>
Sodium phosphate monobasic dihydrate	<i>Thermo Fisher Scientific (MA, USA)</i>
Strep-Tactin®XT 4Flow® resin	<i>Iba lifesciences (Göttingen, DE)</i>
Sulfuric acid	<i>VWR (Darmstadt, DE)</i>
TEMED	<i>Sigma-Aldrich (St. Luis, USA)</i>
Trichloroacetic acid (TCA)	<i>VWR (Darmstadt, DE)</i>
Trichlormethan/Chloroform	<i>Carl Roth (Karlsruhe, DE)</i>
Triton™ X-100	<i>Sigma-Aldrich (St. Luis, USA)</i>
Trizma Base	<i>Applichem (Darmstadt, DE)</i>
Trizol	<i>Thermo Fisher Scientific (MA, USA)</i>

Trypan blue	<i>Sigma-Aldrich (St. Luis, USA)</i>
Trypsin	<i>Invitrogen (Karlsruhe, DE)</i>
Tween® 20	<i>Sigma-Aldrich (St. Luis, USA)</i>
Urea	<i>VWR (Darmstadt, DE)</i>
Urea > 99.5%	<i>Carl Roth (Karlsruhe, DE)</i>
Water for LC-MS via Th. Geyer (used for SEC buffers)	<i>Chemsolute (Stuttgart, DE)</i>

2.5 Prepared buffers and solutions

All protein buffers used in this work were prepared with MilliQ water and filter-sterilized through a 0.2 µm filter. The protein buffers used for SEC were prepared with liquid chromatography-mass spectrometry (LC-MS) water that was filtered through a 0.2 µm filter and degassed. All materials and solutions used for cell culture work or cultivation of *E.coli* cells were purchased sterile-packed or autoclaved at 121 °C.

Buffer/ Solution	Composition
LB medium	tryptone 10 g, yeast extract 5 g, NaCl 10 g, double-distilled water to 1 l final
LB ampicillin plates	17 g bacto-agar in 1 l LB medium. Addition of 0.5 ml 100 mg/ml ampicillin prior pouring the plates
1 × PBS	For 1 × PBS, solution is prepared by 10-fold dilution of the 10 × PBS stock in MilliQ water
1 × Trypsin/ EDTA	For 1 × Trypsin/ EDTA, solution is prepared by 10-fold dilution of the 10 × trypsin/ EDTA stock in sterile 1 × PBS
1 × TBS	50 mM Tris, 150 mM NaCl, pH 7.4
1 × TBS-T	50 mM Tris, 150 mM NaCl, 0.025 % Tween-20, pH 7.4
TAE	0.04 M Tris-Acetate, 0.001 M EDTA, pH 8.0
DNA gel loading dye	250 mM EDTA, 25 % sucrose, 1.2 % SDS, 0.01 % xylencyanol, 0.01 % bromophenol blue
1 × SDS-running buffer	25 mM Tris, 250 mM glycine, 0.1 % SDS
1 × Laemmli sample buffer (non-reducing)	50 mM Tris-HCl (pH 6.8), 2 % SDS, 10 % glycerol, 0.1% bromophenol blue
1 × Laemmli sample buffer (reducing)	50 mM Tris-HCl (pH 6.8), 2 % SDS, 10 % glycerol, 0.1 % Bromophenol blue, 125 mM DTT (DTT is freshly added)

Coomassie Brilliant Blue	50 % methanol, 10 % acetic acid 2 g/l Coomassie Blue R250 0.5 g/l Coomassie Blue G250
Fixative solution	10 % acetic acid, 40 % ethanol
Coomassie R-250 staining solution	10 % acetic acid, 60 mg/l Coomassie Blue R250
Destaining solution	10 % acetic acid, 50 % methanol
Blotting buffer	10 mM di-sodium-tetraborate-decahydrate
5 % milk blocking buffer	5 % skimmed milk in 1 × TBS
3 % BSA	3 % BSA in 1 × TBS
Buffer for the affinity purification of proteins extracted from bacteria	8 M urea, 1 M NaCl, 20 mM NaH ₂ PO ₄ × 2 H ₂ O, pH = 7.4
Buffer for the nickel affinity chromatography of cell culture-derived proteins (buffer M)	1 M NaCl, 20 mM NaH ₂ PO ₄ × 2H ₂ O, pH = 7.4
Buffer for the streptavidin affinity chromatography (buffer W)	1 M NaCl, 20 mM Tris-HCl, pH 8.0
Calibration buffer	8 M urea, 20 mM NaH ₂ PO ₄ × 2 H ₂ O, pH = 7.4
Native calibration buffer	150 mM NaCl, 20 mM NaH ₂ PO ₄ × 2 H ₂ O, pH = 7.4
Buffers for anion exchange chromatography and gradient elution (HiTrap Q HP column)	Buffer A1: 100 mM NaCl, 20 mM Tris-HCl, pH 7.6 Buffer B1: 2 M NaCl, 20 mM Tris-HCl, pH 7.6
Buffers for cation exchange chromatography and gradient elution (HiTrap heparin HP column)	Buffer A2: 150 mM NaCl, 20 mM NaH ₂ PO ₄ × 2 H ₂ O, pH = 7.4 Buffer B2: 2 M NaCl, 20 mM NaH ₂ PO ₄ × 2 H ₂ O, pH = 7.4
Glycine regeneration buffer	10 mM glycine-HCl, pH 1.7

2.6 Proteins, enzymes and antibodies

2.6.1 Proteins and enzymes

Protein and enzymes	Manufacturer
BMP-7 GF	<i>R&D Systems (Minneapolis, MN, USA)</i>
BMP-9 GF	<i>Biolegend (California, USA)</i>
BMP-9 CPLX	<i>R&D Systems (Minneapolis, MN, USA)</i>
BMP-10 GF	<i>R&D Systems (Minneapolis, MN, USA) and the Hinck Lab (Structural Biology, University of Pittsburgh)</i>
Neutravidin protein	<i>Thermo Fisher Scientific (MA, USA)</i>
DNase I grade II from bovine pancreas	<i>Sigma-Aldrich (St. Luis, USA)</i>

All MMP proteinases used in the study Furlan, Spanou et al., 2021 were provided by the Koch Lab, Center for Biochemistry, University of Cologne.

2.6.2 Antibodies

Primary antibodies

Antigen	Host	Western	ELISA	Manufacturer/research laboratory
BMP-7 GF	rabbit	1:2000	1:2000	<i>Peprotech (Hamburg, DE)</i>
BMP-7 PD (mab33)	mouse	1:1000	1:1000	<i>Sakai Lab, Shriners Hospital, Portland (USA)</i>
BMP-7 PD (mab2)	mouse	1:1000	1:1000	<i>Sakai Lab, Shriners Hospital, Portland (USA)</i>
BMP-9 GF	mouse	1:500	1:1000	<i>R&D Systems (Minneapolis, MN, USA)</i>
BMP-9 PD	goat	1:2000	1:2000	<i>R&D Systems (Minneapolis, MN, USA)</i>
BMP-10 GF	mouse	1:1000	1:1000	<i>R&D Systems (Minneapolis, MN, USA)</i>
BMP-10 PD	goat	1:2000	1:2000	<i>R&D Systems (Minneapolis, MN, USA)</i>
His ₆ (HRP conjugate)	mouse	1:2000	1:2000	<i>Miltenyi Biotec (Bergisch Gladbach, DE)</i>
His ₆ (MAB050)	mouse	1:2000	-	<i>R&D Systems (Minneapolis, MN, USA)</i>
Strep-tag [®] II and Twin-Strep-tag [®] (HRP conjugate)	mouse	1:5000	1:10000	<i>Iba lifesciences (Göttingen, DE)</i>
Biotin (HRP conjugate)	goat	-	1:10000	<i>Biozol (Eching, DE)</i>
phospho-Smad 1/5/9	rabbit	1:1000	-	<i>Cell Signaling Technology (Danvers, MA, USA)</i>
GAPDH	mouse	1:10000	-	<i>Abcam (Cambridge, UK)</i>
Fibrillin-1	rabbit	1:2000	1:5000	Home made (Sengle lab), Furlan, Spanou et al. 2021

The antibody against fibrillin-1 was used at dilution 1:1000 for immunofluorescence.

Secondary antibodies

Antigen	Host	Conjugate	ELISA	Western	Manufacturer
Rabbit	Goat	HRP	1:2000	1:2000	<i>Dianova (Hamburg, DE)</i>

Mouse	Goat	HRP	1:2000	1:2000	<i>Dianova (Hamburg, DE)</i>
Goat	Donkey	HRP	1:2000	1:2000	<i>Dianova (Hamburg, DE)</i>
Rabbit	Donkey	IRDye 800CW	-	1:12000	<i>LI-COR (Nebraska, USA)</i>
Mouse	Goat	IRDye 680LT	-	1:12000	<i>LI-COR (Nebraska, USA)</i>

2.7 Oligonucleotides

All oligonucleotides were purchased from Sigma-Aldrich (St. Luis, USA).

2.7.1 Primers for generation of the BMP-7 prodomain truncations

BMP-7 PD	Sequence 5' - 3'
5BMP7ppN-his ₆ (forward)	5'-ggaattccatatgcaccatcaccatcaccatgacttcagcctggacaacgaggt-3'
5BMP7ppNterm (forward)	5'-ggaattccatatggacttcagcctggacaacgaggt-3'
3'BMP7ppC-his ₆ (reverse)	5'-catgggatcctcagtgatggtgatggtgatgccggatgctgcggaagtgg-3'
5BMP7pp185 (forward, primer 1)	5'-ggaattccatatgtccacggggagcaaacagcgc-3'
5BMP7pp185 (forward, primer 2)	5'-ggaattccatatggacaatgagacgtccggatcagc-3'
3BMP7PP184 (reverse)	5'-catgggatcctcagcgttcccggatgtagtccttcta-3'
5BMP7pp74 (forward)	5'-ggaattccatatgggcaagcacaactcggcacc-3'
5BMP7pp74N-his ₆ (forward)	5'-ggaattccatatgcaccatcaccatcaccatggcaagcacaactcggcacc-3'
5BMP7pp166N-his ₆ (forward)	5'-ggaattccatatgcaccatcaccatcaccatggggaagctgtcacggcagc-3'
5BMP7pd166 (forward)	5'-ggaattccatatgggggaagctgtcacggcagc-3'
3BMP7pp217C-his ₆ (reverse)	5'-catgggatcctcagtgatggtgatggtgatgccagagggtacggctgtcag-3'

The 2- or 3-digit numbers in the name of the primers correspond to BMP-7 PD amino acid positions with the 29 aa signal peptide included.

The fragments A) 30-72 aa, B) 63-102 aa, C) 236-292 aa were provided by the Sengle Lab, Center for Biochemistry, University of Cologne.

2.7.2 Primers for generation of the fibrillin-1 FUN domain truncations

FUN	Sequence 5' - 3'
5rF87pCepPuCstrep (forward)	5'-gtcagctagcgtcctacacgagccatg-3'
3rF87pCepPuCstrep (reverse)	5'-tcgactcgagtatgcatctggtaccatctggagaggtg-3'
5rF87V152GPN (forward)	5'-gtcagctagcgggacccaatgtctgtggatcacg-3'
5rF87V152RYN (forward)	5'-gtcagctagcgcgttataatgcttactgttgcctggatg-3'
5rF87V152GWK (forward)	5'-gtcagctagcgggatggaaaaccttacctggcgg-3'
5rF87V152GNQ (forward)	5'-gtcagctagcgggaaatcagtgtattgtccccattgcccgg-3'

The fibrillin-1 fragments startEGF4 and rF11 were provided by the Sengle Lab, Center for Biochemistry, University of Cologne.

2.7.3 Primers for quantitative PCR

Gene	Name	Sequence 5' - 3'
Acidic ribosomal binding protein (ARBP)	<i>Arbp F</i>	TATCCAAAATGCTTCATTGTGGGAG
	<i>Arbp R</i>	CGGATGTGAGGCAGCAGTTTCT
Inhibitor of differentiation 3 (Id3)	<i>Id3 F</i>	GCATGGATGAGCTTCGATCT
	<i>Id3 R</i>	ACCAGCGTGTGCTAGCTCTT

The primers used to detect the expression levels of MMPs are described in Furlan, Spanou et al., 2021.

2.8 Plasmids

2.8.1 Mammalian expression

pCEP-PU backbone vector was from IBA GmbH (Göttingen, DE)

The pCEP-PU backbone vector contains an N-terminal BM-40 signal peptide for secretion to cell culture media and a C-terminal double StrepII-tag downstream of the restriction sites.

For the cloning of the BMP-10 cDNA processing variants:

1. Human BMP-10 tag-free cDNA sequence was flanked with the restriction sites NheI at the 5' end and BamHI at the 3' end. A stop codon was introduced right before the BamHI restriction site to block the incorporation of the Strep-tag into the protein sequence. The described cDNA fragment was generated by gene synthesis (Genewiz, South Plainfield, NJ, USA) and cloned into the pCEP-PU vector.
2. The human cDNA sequences encoding for the N-terminal his-tagged BMP-10 or BMP-10 I314S/R315I mutant were flanked with the restriction sites NheI at the 5' end and BamHI at the 3' end. A stop codon was introduced right before the BamHI restriction site to block the incorporation of the strep-tag into the protein sequences. The described cDNA fragments were generated by gene synthesis (Genewiz, South Plainfield, NJ, USA) and cloned into the pCEP-PU vector.

For the cloning of the rF87 and its N-terminal truncations, the respective human cDNA sequences were generated by PCR using the primers listed in section 2.7.2 and cloned into the pCEP-PU vector.

For all cloning experiments into the pCEP-PU vector the same restriction sites NheI and BamHI were utilized.

2.8.2 Bacterial expression

pET11a backbone vector was from EMD Millipore (Billerica, USA)

The cDNA fragments were generated by PCR using the respective primer pair shown in section 2.7.1 or by gene synthesis from Genewiz (South Plainfield, NJ, USA) or from Life Technologies (Carlsbad, California, USA) and cloned into the pET11a via the restriction sites NdeI/ BamHI.

All plasmids used were generated with the methods explained in the section 2.8 of this thesis and provided by the Sengle Lab, Center for Biochemistry, University of Cologne.

2.9 Expression organisms

2.9.1 Mammalian cells

The immortalized cell line: HEK293 EBNA (provided by Sakai Lab, Shriners Hospital, Portland, USA) was employed.

2.9.2 Bacterial cells

The bacterial cells: *E.coli* BL21-CodonPlus(DE3)-RIPL and *E.coli*XL1Blue (Agilent Technologies, Santa Clara, USA) were employed.

2.10 Materials

2.10.1 Others

Material	Manufacturer
Nunc™ Cell Culture Treated TripleFlasks™	<i>Sigma-Aldrich (St. Luis, USA)</i>
Cell culture flasks T25 / T75	<i>Sarstedt (Nümbrecht, DE)</i>
Cell culture 6 well plates	<i>Corning Costar (Corning, USA)</i>
Cell culture 96 well plates	<i>Corning Costar (Corning, USA)</i>
pipettes 2 ml, 5 ml, 10 ml, 25 ml	<i>Greiner (Kremsmünster, Austria)</i>
Cell Scraper, 28cm length	<i>Greiner (Kremsmünster, Austria)</i>
Nunc MaxiSorp® flat-bottom 96 well plates	<i>VWR (Darmstadt, DE)</i>
Cryo vials for cell culture	<i>Greiner (Kremsmünster, Austria)</i>
Millex-GP syringe filter, PES, 0,22 µm, 33 mm	<i>Merck (Darmstadt, DE)</i>
Sterile 500 mL Steritop Quick Release with 0.22 µm pore size	<i>Sigma-Aldrich (St. Luis, USA)</i>
Amicon Ultra-0.5 ml MWCO 3kDa and 10 kDa cut-off	<i>Merck (Darmstadt, DE)</i>
Slide-A-Lyzer™ MINI 0.1 ml 2 kDa and 10 kDa cut-off	<i>Thermo Fisher Scientific (MA, USA)</i>
Sensor Chip CM5	<i>Cytiva (MA, USA)</i>
Sensor Chip PEG	<i>XanTec bioanalytics (Düsseldorf, DE)</i>
Superose 12 10/300 GL	<i>Cytiva (MA, USA)</i>
Protan Nitrocellulose Blotting Membrane 0.45µm	<i>VWR (PA, USA)</i>
X-ray film, Fujifilm	<i>Dinker, Düsseldorf (DE)</i>
BRAND® Parafilm® M sealing film	<i>Sigma-Aldrich (St. Luis, USA)</i>

2.10.2 Kits

Amine coupling kit	<i>Cytiva (MA, USA)</i>
Supersignal West pico Plus Chemiluminescent substrate	<i>Thermo Fisher Scientific (MA, USA)</i>
Immun-Blot® Opti-4CN™ Colorimetric Kit	<i>Bio-Rad, München (DE)</i>

iScript cDNA Synthesis Kit	<i>Bio-Rad, München (DE)</i>
SensiFAST™ SYBR® Hi-ROX Kit	<i>Bioline, Luckenwalde (DE)</i>
Pierce BCA Protein Assay Kit	<i>Thermo Fisher Scientific (MA, USA)</i>

2.11 Mammalian cell culture work

Cells were grown at 37 °C incubator with 5 % CO₂ under sterile conditions.

All cell culture work was performed under sterile conditions.

2.11.1 Cell growth media and transfection

These are described in the materials and methods parts of the manuscripts: “Spanou et al., in preparation#1” in *cell culture* and *protein expression and purification* sections and “Spanou et al., in preparation#2” in *cell culture* and *transfection* sections.

Further details of clone selection are provided in section 2.11.2 below.

2.11.2 Clone selection and propagation

Cells were propagated under puromycin or geneticin antibiotic selection in DMEM Glutamax supplemented with 10 % FBS. Pen./ strep. at 1 % was added only when cells were under puromycin selection. Puromycin at 1 µg/ml was applied 24 h post transfection to facilitate selection and then reduced to 0.5 µg/ml to maintain proliferation of positive clones. Media was removed and cells were transferred by trypsinization to several T75 flasks at constant 0.5 µg/ml puromycin selection in serum-containing media. In the end, at 80 % confluency, cells from three T75 flasks were transferred to a single triple flask. When confluency reached 80 %, the serum-containing media was discarded and serum-free media with 1 % pen./ strep. was added to collect the secreted protein of interest in the cell culture supernatant.

2.11.3 Freezing mammalian cells

Cells were maintained under stable antibiotic selection and grown to 70 % confluency in T75 flasks, followed by trypsin treatment and resuspension in DMEM Glutamax containing 20 % FBS and 10 % DMSO without any antibiotics. The cell suspension was then distributed to cryo vials and stored at -80 °C inside styrofoam boxes for two overnights. Next, the cryo vials were transferred to the liquid nitrogen container.

2.11.4 Stimulation assays with C2C12 and HUVEC cells

These techniques were performed as explained in the “materials and methods” part of each manuscript depending on the experiment pursued.

- For the HUVEC and C2C12 cells in-solution stimulation with BMP-10 processing variants please refer to: Spanou et al., in preparation#1, materials and methods, “*Stimulation assays with HUVEC and C2C12 cells*”. For result assessment of the stimulation experiments please refer to: Spanou et al., in preparation#1, materials and methods, “*Western blotting*”.
- For the C2C12 cells stimulation experiment of BMPs immobilized to heparin to measure the *Id3* mRNA levels please refer to: Spanou et al., in preparation#2, materials and methods: “*Bioactivity assays on heparin*”.

For RNA extraction and cDNA synthesis of the stimulated C2C12 cells with heparin-bound BMPs please refer to: Furlan, Spanou et al., 2021, materials and methods, section 2.10 “*BMP bioactivity assay*”. Briefly, 0.1 ml Trizol per well was added to the adherent C2C12 cells after discarding the media followed by phenol/chloroform RNA extraction according to the manufacturer’s protocols. RNA was subsequently air-dried and resuspended in RNase-free water followed by reverse transcription using the iScript cDNA Synthesis Kit according to manufacturer’s protocol. The resulting cDNA was then subjected to qPCR using the primers for *Id3* and *ARBP* and the SensiFAST™ SYBR® Hi-ROX Kit according to manufacturer’s protocols. Analysis of the results of the qPCR was performed by employing the $2^{-\Delta\Delta Ct}$ method (Livak et al., 2001) and quantitation of the *Id3* transcripts was performed relative to the housekeeping *ARBP* transcripts. The primers for *Id3* and *ARBP* are listed in section 2.7.3 of the materials and methods section of this thesis.

2.11.5 Cell lysates of HEK293 cells

For HEK293 cell lysis, the RIPA lysis and extraction buffer product information sheet was followed (Thermo scientific, cat.no.: 89900). Briefly, HEK293 cells were grown to 75 % confluency in T75 flask, media was discarded and 5 ml of ice-cold 1 × PBS was carefully added to wash the cells and then discarded. A second 1 × PBS washing

step followed and then 1 ml of cold RIPA was added supplemented with EDTA-free protease inhibitor cocktail (Sigma, cat.no.: 11873580001). The inhibitor was used as 1 tablet that was resuspended in 2 ml MilliQ water to prepare a 25 × concentrated stock. 60 µl of the 25 × inhibitor concentrated stock was applied to 1.5 ml of cold RIPA that was subsequently used for cell lysis. Cells were detached using a cell scraper into the added cold RIPA solution and flask was kept on ice for 5 min. Next the lysate was gathered to one side of the flask using cell scraper and was subsequently placed to a microcentrifuge tube. Material was centrifuged at 14000 rcf for 15 min to remove the cell debris and the resulting supernatant was aliquoted in new tubes and stored at -20 °C freezer for further analysis.

2.12 Biochemical methods

2.12.1 Protein expression and purification

2.12.1.1 Bacterial cells

2.12.1.1.1 Transformation

Plasmid DNA at 50 ng was incubated with *E.coli* BL21-CodonPlus(DE3)-RIPL competent cells for 10 min on ice. Next, cells were heat-shocked at 42 °C for 45 seconds, followed by incubation on ice for 2 min. LB without antibiotics was provided at 0.4 ml to the cells and cells were incubated for 1 h at 37 °C. Next, cells were plated to LB plates containing 50 µg/ml ampicillin and plates were placed in a 37 °C incubator, O/N.

2.12.1.1.2 Clone selection, inoculation and collection of *E.coli* pellet

A single clone was selected from the ampicillin-containing LB plate and was propagated in LB media containing 50 µg/ml ampicillin O/N, shaking at 220 rpm/min. The following day, the desired volume of LB media containing 50 µg/ml ampicillin was inoculated at a 1:50 dilution of the O/N culture. At OD₆₀₀ = 0.6, IPTG at 1 mM final was administered and the culture was incubated shaking at 220 rpm/min at 37 °C for 4 h. Next, the *E.coli* pellet was collected by centrifugation at 6000 rpm for 30 min at 4 °C. Then the *E.coli* pellet was resuspended in 1 × PBS, centrifuged at 13000 rpm at 4 °C for 30 min, supernatant was discarded and the pellet was stored at -20 °C.

2.12.1.1.3 Urea purification

8M urea was dissolved in MilliQ water at RT without addition of NaCl or phosphates. Urea solutions usually contain ions that attack and degrade protein samples over time. Hence, to preserve protein quality, urea solutions were purified. The most efficient method to purify liters of urea is by employing the on-column purification approach as described in manuals of mixed bed resins. To that end, 2.6 g of AG 501-X8 mixed bed resin was resuspended in 10 ml MilliQ water. A column with dimensions 0.5×20 cm was selected and resuspended beads were poured into the column slowly only every 0.5 ml by introducing equal volumes of anion and cation exchanger beads from the mixed resin in each pipetting step so that after pouring column bed had a “tiger-stripes” appearance. Alternation of anion and cation exchangers in the column bed facilitates efficient ion removal. After bed column assembly, the mixed resin was washed with MilliQ water for 3 column volumes. The dissolved urea (no more than 1 l) was filtered through a $0.2 \mu\text{m}$ filter and run over the column. The eluate of the first 30 ml was collected separately and discarded. The remaining eluate was collected and assessed for efficient ion removal by measuring conductivity before and after the on-column purification. The urea purification procedure took place at RT. After purification, the conductivity of the 8 M urea solution was reduced 6-fold. Then the 8 M urea buffer was prepared by addition of NaCl and phosphates into the purified 8 M urea solution and pH was adjusted to $\text{pH} = 7.4$. The urea buffer was then filtered and kept in the dark in cold temperature.

2.12.1.1.4 Protein extraction from *E.coli* cells

The bacterial pellet was resuspended in 20 ml B-PER with 2 mM PMSF added. Next, $50 \mu\text{l}$ DNase I (5000 Units/ml) were administered and resuspended cells were incubated for 30 min at RT. Centrifugation followed at 13000 rpm at 4°C for 30 min. Supernatant was removed and pellet was washed with 10 % B-PER in double-distilled water. A second centrifugation step followed in same conditions, supernatant was discarded and pellet was resuspended in 40 ml of 8 M urea buffer. A final centrifugation step followed in same conditions and supernatant was filtered through a $0.2 \mu\text{m}$ filter.

2.12.1.1.5 Protein purification from *E.coli* cells

To purify the filtered supernatant containing His₆-tagged proteins, 2 ml of 50 % Ni-NTA agarose suspension was applied on a column with dimensions 1 × 10 cm. Resin was washed with MilliQ water for 3 column volumes (1 column volume = 10 bed volumes) and calibrated with 1 column volume of the 8 M urea buffer. Next, the filtered supernatant was applied to the nickel resin, and the resin was washed with 2 column volumes of the 8 M urea buffer, followed by elution in 5 ml fractions of 5 mM, 10 mM, 20 mM and 30 mM imidazole in 8M urea buffer. After that, elution was continued by applying 2 × 1 ml of 40 mM , 50 mM , 100 mM , 150 mM , 200 mM and 250 mM imidazole in 8M urea buffer to the nickel resin. Elution fractions were kept at 4 °C until analysis.

2.12.1.2 Protein purification from mammalian cells

Serum-free media containing the protein of interest was collected from HEK293 cells and filtered through a 0.2 µm filter. Depending on the affinity purification method employed, the pH of the media was calibrated to pH = 7.4 for nickel affinity chromatography, or pH = 8.0 for streptavidin affinity chromatography. Columns with either Ni-NTA or streptavidin resin were prepared as described in section 2.12.1.1.5, washed with MilliQ water and calibrated with 1 column volume of buffer M (1 M NaCl, 20 mM NaH₂PO₄ × 2 H₂O, pH = 7.4) or buffer W (1 M NaCl, 20 mM Tris-HCl, pH 8.0) respectively. Half liter of the filtered cell culture supernatant was run over either column and resins were washed with 2 column volumes of buffer M or buffer W. Next, elution took place using the 1 × biotin buffer for the streptavidin resin or the previously described imidazole gradient (5 - 250 mM) prepared in buffer M for the nickel resin. Elution fractions were kept at 4 °C for analysis.

For the purification of the tag-free BMP-10 expressed in HEK293 EBNA cells, the procedure is explained thoroughly in Spanou et al., in preparation#1, materials and methods, “*Protein expression and purification*”.

2.12.1.3 Size exclusion chromatography

ÄKTA purifier was calibrated with LC-MS water and a Superose 12 10/300 GL tricorncolumn (Cytiva) was connected to the system. After washing with LC-MS water for at least 2 bed volumes (1 bed volume=24 ml) to remove all 20 % ethanol

that is contained in the column, column was calibrated with buffer M or buffer W depending on the buffer of the protein sample to be injected. For SEC purification of BMP-7 CPLX, buffer M was supplemented with 0.15 M imidazole to prevent aggregation during the run. Sample injection onto the column was performed with 1 ml of loop-volume and elution took place at RT in serpentine row for 2 bed volumes with 0.5 ml per fraction. After the run was complete, column was washed with 2 bed volumes of buffer M or buffer W and then LC-MS water was applied to remove buffer M or buffer W completely before 20 % ethanol was pumped into the column. Flow rates were as follows: 0.25 ml/min when ethanol was used, 0.5 ml/min when LC-MS water, buffer M or buffer W was used. For an overnight run, LC-MS water at 0.050 ml/min flow rate was applied.

2.12.1.4 Prodomain separation from BMP-7 complex

BMP-7 CPLX was dialyzed into 8 M urea buffer using a 3 kDa cut-off membrane for two overnights in the cold room and was subjected to nickel affinity chromatography as explained previously. Nickel column flow through was applied on same nickel resin 10 times, followed by direct elution of BMP-7 PD at 250 mM imidazole in 8M urea buffer. For testing the running behavior of the separated BMP-7 PD on native gels, the PD was dialyzed into TC buffer for an O/N at 4 °C using a 10 kDa cut-off membrane to remove the urea and was subsequently loaded on native gel.

2.12.2 Protein quantification

For quantifying proteins, the instructions in the Pierce BCA protein assay kit (Thermo Fisher Scientific, cat.no.: 23227) were followed for applying BSA standard and samples on microplates using the standard or enhanced protocols as appropriate. Protein concentrations were also verified via nanodrop measurements.

2.12.3 Western blotting

Western blotting was performed as explained in Spanou et al., in preparation#1, materials and methods, "*Western blotting*". Samples were TCA-precipitated prior loading to SDS-gels and antibodies were used as explained in Spanou et al., in preparation#1, materials and methods, "*Antibodies and proteins*" and "*Western blotting*". For detecting BMP PD fragments after MMP cleavage, samples were again TCA-precipitated prior loading to 10-20% gradient SDS-gels and blotted to PROTAN

nitrocellulose membranes using 10 mM di-sodium-tetraborate-decahydrate at 400 mA for 1.5 h. Membranes were blocked with 5% milk/ 1 × TBS for 1h at RT and incubated with primary antibody for O/N at 4 °C. Next, membranes were washed 3 × for 10 min with 1 × TBS-Tween and secondary antibody incubation followed for 1h at RT. All antibody incubation steps were performed in 2% milk/ 1 × TBS. Antibody dilutions were as described in Furlan, Spanou et al., 2021, materials and methods, section 2.2 “*Antibodies*”. Additional information about antibody suppliers and working dilutions are contained in section 2.6.2 of the materials and methods part of this thesis. Signals were developed using chemiluminescence detection by employing the Supersignal West Pico kit (Thermo Fisher Scientific, cat.no.: 34580), the X-ray films and the AGFA developing instrument.

2.12.4 Mass Spectrometry

To analyze the peptide composition of the strong heparin-binding BMP-7 fragment after heparin affinity chromatography and gradient elution, gel bands were excised so that a single gel slice contained a single protein band and placed into individual microcentrifuge tubes. The “in gel digestion” protocol of the CECAD Proteomics Core Facility was followed that is available online:

<https://proteomics.cecad-labs.uni-koeln.de/protocols>.

The protocol enables digestion of the gel slice that contains the protein fragment of interest by the proteolytic enzymes Trypsin and LysC. The resulting peptides after the digest were extracted from the gel slice and dried by using a speedvac to remove the organic solvent. Finally, the stage tip purification protocol was applied that is also available online on same website. After calibration of the stage tips with the required buffers, the acidified peptides post speedvac drying from a single gel slice were loaded after centrifugation onto a single stage tip followed by purification with the necessary solutions prior to storage at 4 °C. The detailed steps followed for both protocols are presented below:

1. In gel digestion protocol:

All solutions and buffers required for the “in gel digestion” protocol steps were provided by the CECAD Proteomics Core Facility.

Solutions/ Reagents
Dithiothreitol (DTT), 100 mM stocks
Chloroacetamide (CAA), 550 mM stocks
Acetonitrile (ACN)
Ammoniumbicarbonate (ABC), 50 mM
50 mM ABC/50% ACN
Trypsin protease, 1 µg/µL or 0.1 µg/µL
Lysyl Endopeptidase (Lys-C), 0.5 µg/µL
Peptide extraction buffer: 30% Acetonitrile / 3% Trifluoroacetic acid in water
Formic acid, 10% in water

After the SDS-PAGE run under reducing conditions, the gel slices were placed in 1.5 ml microcentrifuge tubes and 100 µlit of 50 mM ABC/50% ACN per tube was added. The sample was vortexed and incubated for 20 min at RT. The supernatant was discarded and procedure was repeated. Since the samples were not alkylated prior the SDS-PAGE run, the gel slices were placed in 10 mM DTT, vortexed and incubated for 30 min at 55 °C with mild shaking. Supernatant was discarded and gel slices were placed in ACN, vortexed for 1 min and incubated for 15 min at RT. The supernatant was discarded and gel slices were placed in 55 mM CAA, vortexed and incubated for 30 min at RT in the dark. The supernatant was discarded and gel slices were placed in ACN, vortexed for 1 min and incubated for 15 min at RT. Supernatant was discarded and previous step was repeated by adding 100 µlit ACN and incubating for 10 min at RT. Supernatant was discarded and gel slices were dried in speedvac for 5 min.

To destain the Coomassie-stained gel slices, 100 µlit of 50 mM ABC was added and sample was vortexed and incubated for 15 at RT. Next the supernatant was discarded and gel slices were placed in ACN, vortexed for 1 min and incubated for 15 min at RT. Supernatant was discarded and destaining steps were repeated until gel slices were completely decolorized. Next gel slices were dried in the speedvac for 5 min. After the drying step, gel slices were placed in 100 µlit of 50 mM ABC solution that contained 9 µlit of 0.1 µg/µlit Trypsin and 1 µlit of 0.1 µg/µlit LysC. The gel

slices were allowed to swell for 30 min at 4 °C. Next the supernatant was discarded, 100 µlit of 50 mM ABC was added and O/N incubation at 37 °C, 750 rpm shaking followed.

The following day, the supernatant of the gel slices was transferred to new 1.5 ml tubes. To release the peptide fragments still present inside the gel slices, these were placed in 100 µlit of 30% ACN/3% TFA, vortexed and incubated for 20 min at RT. The supernatant was then merged to the supernatant that was kept after the overnight step for each sample individually. To release the remaining peptides still trapped inside the gel slices, 100 µlit of 100% ACN were added to the gel slices that were subsequently vortexed and incubated for 20 min at RT. The supernatant was then merged with the supernatant that was kept from previous steps for each sample individually. The resulting merged supernatants were then dried in speedvac until volume was less than 50 µlit. After the drying step, formic acid was added to 1% final.

2. Stage tip purification protocol

All solutions, buffers and materials required for the stage tip purification protocol were provided by the CECAD Proteomics Core Facility.

Solutions/ Reagents
Buffer <i>A</i> : 0.1% formic acid in water
Buffer <i>B</i> : 0.1% formic acid in 80% Acetonitrile
Formic acid, 10% in water
100% Methanol
Key materials
SDB-RP StageTips, packed in 200 µL pipette tips
2 mL Eppendorf collection tubes
Centrifugal adaptors for StageTips

Stage tips were calibrated with 20 μ lit of methanol and centrifugation followed at 2600 rpm for 1 min. Next 20 μ lit of Buffer *B* were loaded on the stage tips and centrifugation followed at 2600 rpm for 1 min. Then 20 μ lit of Buffer *A* were loaded on stage tips and centrifugation followed at 2600 rpm for 1.5 min. Finally, 20 μ lit of Buffer *A* were loaded on stage tips and centrifugation followed at 2600 rpm for 2 min. The collection tubes were emptied after calibration was complete.

The acidified peptides were centrifuged at full speed for 5 min. Supernatants were loaded on stage tips and centrifugation followed at 2600 rpm for 5 min. Stage tips were washed sequentially with 30 μ lit of Buffer *A* and 30 μ lit of Buffer *B* twice, each time for 3 min at 2600 rpm. Finally, stage tips were air-dried with a syringe and placed at 4 °C.

Data analysis was performed by the CECAD Proteomics Core Facility.

At the end of the “Materials and methods” part of this thesis (following pages) a special section termed “**Established protocols to study Bone Morphogenetic proteins**” is included. In this section the new methodology used in the manuscripts is explained by providing gel examples.

All other techniques and methodologies employed are explained in detail in the manuscripts, materials and methods. The closed-ring BMP-7 CPLX model building method is described in Furlan, Spanou et al., 2021, materials and methods, section 2.13, "Molecular docking experiments".

2.13 Established protocols to study Bone Morphogenetic proteins

2.13.1 Wet lab techniques

Native PAGE

Problem: The Blue native stain method relies on the concept that the stain adds a negative charge upon incorporation into the amino acid side chains hence forcing a migration through the native gel that is charge-based. Attempts to run BMP-7 CPLX using the SERVAGEL™ N native starter kit (Serva, cat.no.: 4320401) with the Blue Native stain method yielded variable results after several runs, possibly due to the stain interfering with the stability of the CPLX during the native run. Attempts to run BMP-7 CPLX at pH = 7.4 without the native stain resulted in failed migration of the protein. Due to the isoelectric point of the BMP-7 precursor at pH = 6.9, pH values for gels near this range for BMP-7 CPLX should therefore be avoided since uncharged proteins cannot migrate in native gels.

Protocol establishment: In general, it is expected that using a slightly basic native running buffer will add negative charge to amino acid residues at the protein surface without compromising the overall protein structure. Proteins can then migrate through the native gel. To examine the possibility of running protein samples in slightly basic pH without compromising protein structure, two different native PAGE protocols were merged:

1. available online from IMBB, FORTH, Crete, Greece

chrome-

extension://efaidnbmnnnibpcajpcglclefindmkaj/viewer.html?pdfurl=https%3A%2F%2Fwww.imbb.forth.gr%2FProFI%2Fmethods%2Fpdf%2FNATIVE_Page.pdf&clen=58982&chunk=true

2. A second native PAGE protocol was provided by the Roman Lab (University of Pittsburgh). The two protocols were merged with the final protocol running at pH=8.4. The accuracy of this protocol was assessed by running the native marker (SERVA, cat.no.: 39219) at pH = 8.4 and its migration pattern was not found compromised when compared to the expected migration pattern at neutral pH = 7.0 as provided by SERVA (Fig. 2.1).

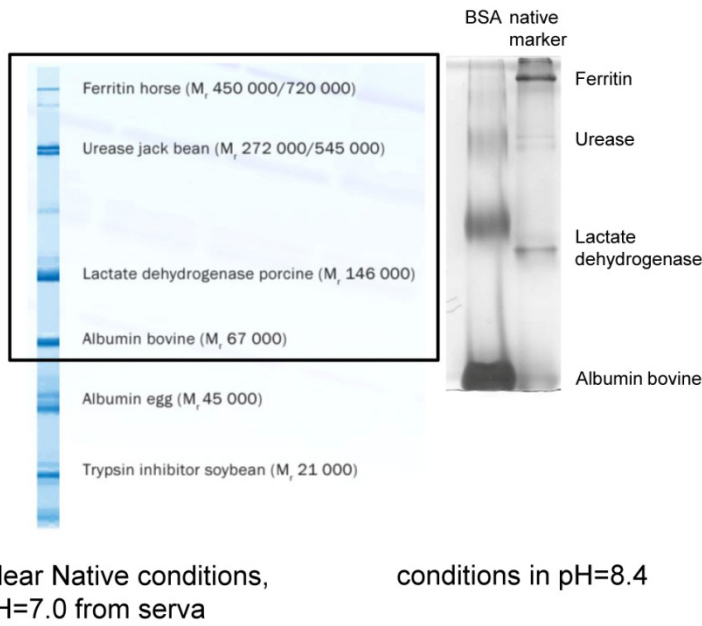


Figure 2.1: Migration pattern of the SERVA native marker utilizing the new native PAGE protocol. Native marker from SERVA was run at pH = 8.4 on a 4 % native stacking gel followed by 10 % native running gel for 5 h total running time to test for protein stability at these conditions. The SERVA native marker migration pattern was then compared to the pattern as provided by the SERVA company (available online) run at native conditions, pH = 7.0 on SERVAGel 4-16 %. BSA shown on gel on the right was from SERVA (M_r : 67 000) but due to the high quantity loaded BSA oligomers running at higher positions are also visible. This migration pattern already shows good promise for BMP CPLXs and PD dimers with molecular weights at ~110 kDa and ~90 kDa, respectively.

In addition, the 4 % native stacking gel of the newly established native PAGE has the ability to prevent aggregated proteins from entering the gel. More specifically, aggregated proteins are trapped within the native stacking gel and at the border to the native running gel. This was assessed by running the same protein sample with or without a boiling step and assessing the band pattern (Fig. 2.2).

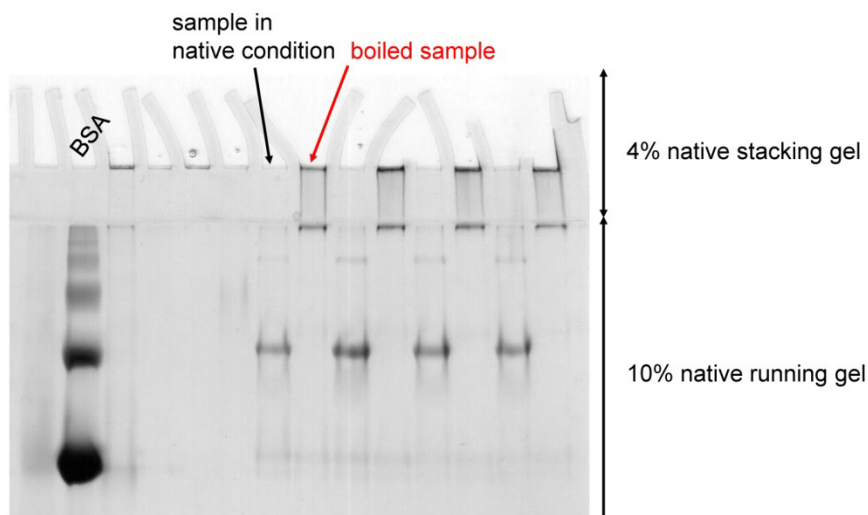


Figure 2.2: Native and denatured protein sample runs utilizing the new native PAGE protocol. Same protein sample was subjected to the new native PAGE protocol before and after boiling. Running time was 1.5 h.

Applying the same protocol allowed to accurately detect BMP-7 CPLX aggregates trapped in the 4 % native stacking gel and at the border to the native running gel. Furthermore, separated BMP-7 PD was also detected after keeping BMP-7 CPLX for weeks at 4 °C without SEC (Fig. 2.3).

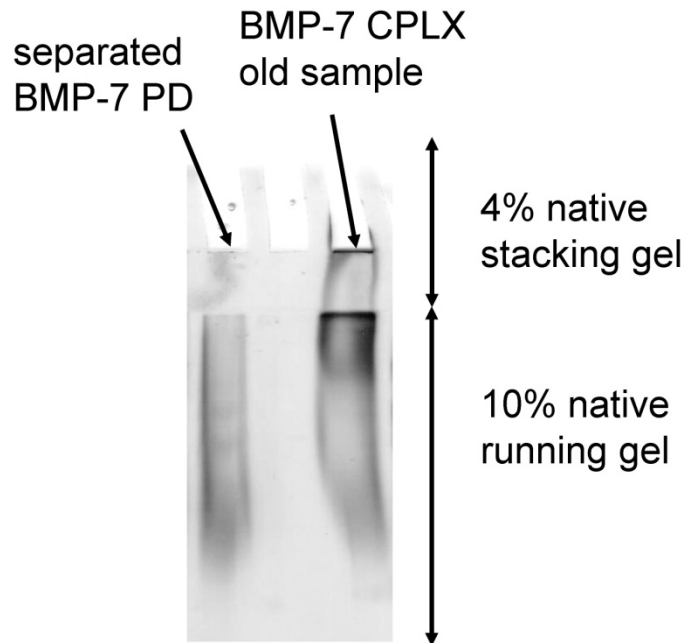


Figure 2.3: Quality check of aggregated BMP-7 CPLX using the newly established native PAGE protocol. BMP-7 CPLX was kept for weeks at 4 °C without SEC to induce aggregation and spontaneous PD-GF separation followed by native PAGE analysis. Running time was approximately 2.5 h.

BMP-10 was also subjected to native PAGE analysis. The isoelectric point of BMP-10 precursor is at pH = 4.9 which means that at pH = 8.4 its surface charge is negative. As expected, BMP-10 CPLX readily migrated to the bottom of the gel yielding a band pattern consistent with published reports (Jiang et al., 2016 and Spanou et al., in preparation#1, Figs. 2A5 and 2B) after a running time of approximately 2.5 h. Interestingly, after the same running time following the same native PAGE protocol, BMP-7 CPLX lingered at the top of the gel consistent with its higher isoelectric point (Furlan, Spanou et al., 2021, Fig. 9A).

Solution: Hence, native PAGE for BMP-7 CPLX can only be conducted in 1 × Tris-glycine buffer at pH 8.4 following the protocol as provided below. For native PAGE

of BMP-10 CPLX, the same protocol was found to be working based on similar band pattern shown by Jiang et al., 2016. The provided protocol is compatible with BIORAD devices and is as follows:

Native PAGE gels

	10 % running (2 gels)	4 % stacking (2 gels)
H ₂ O	12.9 ml	4 ml
40 % acrylamide	5 ml	0.62 ml
1.5 M Tris-HCl, pH 8.4	1.7 ml	0.416 ml
APS 10 %	200 μ l	50 μ l
TEMED	20 μ l	5 μ l

The gels can be stored in wet paper soaked with 1 \times native running buffer at 4 °C and should be cooled before the run.

The composition of 10 \times native running buffer (Tris-glycine) was: 25 mM Tris, 193 mM glycine with pH adjusted to 8.4. The buffer was filter-sterilized prior use. The 1 \times native running buffer was again filter-sterilized and stored in the cold room to cool down for 2 h minimum prior to the run. The 5 \times native loading dye composition is presented below. The dye was aliquoted and stored in -20 °C freezer for future use.

5 \times native loading dye (8.5 ml)	
1.5 M Tris pH 8.4	1.67 ml
Glycerol 100 %	4.0 ml
Bromophenol blue	0.005 g
H ₂ O	2.83 ml

Running conditions were at 150 V constant in the cold room. When loading dye diffused, the gel was allowed to run for 10 min in addition.

Sensitive Coomassie staining for BMPs on native gels

Problem: BMP-10 CPLX does not stain convincingly at 0.1 mg/ml in native gels. Since purification of BMP-10 CPLX involves 3 chromatographic steps, the end concentration after SEC usually does not exceed 0.1 mg/ml. So far it was unclear

whether BMP-10 CPLX can be condensed without compromising its structure. Therefore more sensitive methods for BMP-10 detection were evaluated.

Protocol establishment: The information that Coomassie Blue R-250 is more sensitive for protein detection on gels compared to Coomassie Blue G-250 is available in online protocols (interchim manual, “Coomassie Blue (R-250, G-250)”). Hence, the staining efficiency of Coomassie Blue R-250 solution was compared to the staining efficiency of the conventional, Coomassie Brilliant Blue solution (composition: 50% methanol, 10% acetic acid, 2 gr/L Coomassie Blue R250, 0.5 g/L Coomassie Blue G250) that is used for SDS-gel staining by many labs. Indeed, the Coomassie R-250 solution alone convincingly stained BMP-10 CPLX in native gels when ~0.1 mg/ml of protein was loaded (Spanou et al., in preparation#1, Figs. 2A5 and 2B).

Solution: A new staining method was developed using Coomassie R-250 that stained SEC purified BMP-10 CPLX yielding sharp, well defined bands in native gels at a concentration of ~0.1 mg/ml.

The new staining method was developed from the interchim protocol (interchim manual, “Coomassie Blue (R-250, G-250)”) as follows:

After MilliQ washes of the native gel after PAGE, a separate fixation step was performed by applying the fixative solution: 10 % acetic acid, 40 % ethanol in MilliQ water. Fixation step was for 1 h at RT.

After subsequent MilliQ washes, application of Coomassie R-250 staining solution followed. The solution was prepared as follows: 10 % acetic acid, 60 mg/L Coomassie Blue R-250 (SERVA) in MilliQ water. Incubation was until sharp bands appeared within 30-60 min. Then the solution was removed and 5% acetic acid in MilliQ water was applied for destaining the gel.

Production protocol for detecting MMP-13 cleaved BMP-7 CPLX after DLS

Problem: DLS requires protein amounts in the range of 0.2-0.3 mg/ml for reliable detection (Baldock lab, University of Manchester). BMP-7 CPLX purification yields 2 aliquots of 0.5 mg/ml each from a total of 0.5 l cell culture supernatant. After the SEC purification step, BMP-7 CPLX is obtained at 0.1 mg/ml compared to 0.5 mg/ml

as starting concentration. Hence, a condensation step had to be introduced before the SEC step. However, BMP-7 CPLX is known to readily aggregate and stick to membranes due to its hydrophobic nature. Freezing BMP-7 CPLX serum-free cell culture supernatants results in loss of protein yield as well as shockfreezing of affinity purified BMP-7 CPLX without the SEC step. Hence, it was unclear what condensation step should be used.

Protocol establishment: Hence, exclusively for the needs of this purification experiment, BMP-7 CPLX was affinity-purified fresh from HEK293 cells. For the condensation step, a 10 kDa cut-off centrifugation unit filter with 0.5 ml volume capacity (Amicon ultra cell) was used to ensure BMP-7 CPLX does not severely stick to the membrane that would result in loss of protein yield. Next, BMP-7 CPLX was briefly centrifuged as follows:

- 1) 9500 rcf for 1 min at 4 °C
- 2) 9500 rcf for 1 min at 4 °C
- 3) 9500 rcf for 30 sec at 4 °C

The condensed BMP-7 CPLX was re-solubilized with addition of 150 mM imidazole final in the established buffer M (1 M NaCl, 20 mM NaH₂PO₄ × 2 H₂O, pH = 7.4) that is known to keep BMP-7 CPLX more soluble based on existing knowledge in the Sengle Lab. Next, the condensed BMP-7 CPLX was carefully pipetted away from the 10 kDa cut-off membrane to homogeneity. Sample was immediately injected to the SEC column at 1 mg/ml final for a total of 1 ml in presence of 0.15 M imidazole in buffer M. SEC column specifications and the hydrophobic nature of BMP-7 CPLX do not allow injection of larger volumes or higher concentrations that would result either in incomplete separation of the CPLX from the PD dimer or in aggregation of the CPLX within the ÄKTA tubings possibly leading to system clogging. Imidazole at a final concentration of 0.15 M was freshly added followed by shockfreezing right after SEC elution. Protein quality was assessed both with SDS- and native gels prior to shipping. Concentration of SEC purified BMP-7 CPLX was at 0.25-0.5 mg/ml as estimated by running 1:2 dilutions of BSA standard (Thermo Fisher Scientific, cat.no.: 23227) on the same gel (Spanou et al., in preparation#1, Fig. S1C and see Fig. 2.4 below for full gel, stained with Coomassie Brilliant Blue and fully destained). In addition, the ÄKTA purifier UV detector showed a peak at 480 mAU at the expected

fraction numbers during the SEC elution (Spanou et al., in preparation#1, Fig. S1C and for comparison: Wohl et al., 2016, Fig. 1B).

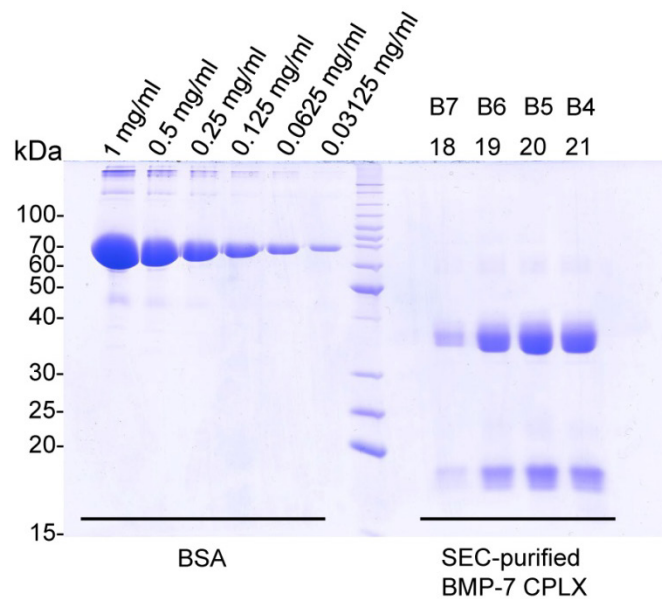


Figure 2.4: Quantification of SEC-purified BMP-7 CPLX before shipping. SEC-purified BMP-7 CPLX was run on SDS-gels together with BSA as standard under reducing conditions and stained using Coomassie Brilliant Blue. BSA (Thermo Fisher Scientific, cat.no.: 23227) was prepared in 1:2 dilutions from 1 mg/ml to 0.03125 mg/ml as shown and 12.5 μ l from each sample was loaded.

Solution: A protocol was established that can reliably condense BMP-7 CPLX after 3 brief centrifugation steps using the 10 kDa cut-off Amicon ultra centrifugation units followed by resuspension in 0.15 M imidazole in buffer M and direct SEC elution. The protocol works provided BMP-7 CPLX over-expressing HEK293 cells are propagated in presence of at least 250 μ g/ml geneticin (G418) without Pen/ Strep because it interferes with geneticin selection (User guide: Geneticin, Thermo Fisher). BMP-7 CPLX should be purified fresh from cell culture media, strictly no later than 48 h serum-free due to its hydrophobic nature and the presence of proteolytic cleavage events (Furlan, Spanou et al., 2021, Fig. 1A). In addition, BMP-7 CPLX either in media or affinity-purified should not be frozen or shockfrozen before the SEC step. BMP-7 CPLX generated with this methodology gave convincing results after MMP-13 cleavage and DLS as shown in Furlan, Spanou et al., 2021, Fig. S3.

NaCl gradient elution of the BMP-7PD truncation variants after heparin affinity chromatography

After thorough washing of the heparin column in calibration buffer: 8 M urea, 20 mM $\text{NaH}_2\text{PO}_4 \times 2 \text{H}_2\text{O}$, pH = 7.4 for 10 ml at RT, the NaCl gradient elution was performed using the ÄKTA purifier as described below:

Buffer A: calibration buffer

Buffer B: calibration buffer with 1 M NaCl

The gradient elution was performed within 100 fractions at RT. Fraction 1 corresponded to 2.5 % buffer B in total and for subsequent fractions the percentage of buffer B rose by 2.5 % per fraction until fraction 40. From fraction 41 until fraction 100, there is no gradient and the ÄKTA eluted with plain buffer B.

NaCl gradient elutions of the tag-free processed BMP-10 CPLX from the HiTrapQ HP and HiTrap heparin HP columns

After thorough washing of the HiTrap Q HP or the HiTrap heparin HP columns using the buffers: 100 mM NaCl, 20 mM Tris-HCl, pH 7.6 or 150 mM NaCl, 20 mM $\text{NaH}_2\text{PO}_4 \times 2 \text{H}_2\text{O}$, pH = 7.4 respectively for 10 ml, NaCl gradient elution followed using a single protocol.

For the HiTrap Q HP column the specific elution buffer was used:

2 M NaCl, 20 mM Tris-HCl, pH 7.6 (buffer B1)

For the HiTrap heparin HP column the specific elution buffer was used:

2 M NaCl, 20 mM $\text{NaH}_2\text{PO}_4 \times 2 \text{H}_2\text{O}$, pH = 7.4 (buffer B2)

The gradient elution was performed within 100 fractions at 4 °C. Fraction 1 contained 1.25 % buffer B1 or B2 in total and for subsequent fractions the percentage of buffer B1 or B2 increased by 1.25 % per fraction until fraction 80. From fraction 81 until fraction 100, there is no gradient and the ÄKTA eluted with plain buffer B1 or B2.

The eluates of the HiTrap Q HP column after condensation of media of over-expressing BMP-10 CPLX HEK293 EBNA cells collected after the first 4 days serum-free, required no purification over a heparin column (Spanou et al., in preparation#1, Fig. 2A2). For serum-free media containing BMP-10 CPLX over-

expressed by HEK293 EBNA cells collected after the second 4-day-incubation, the heparin affinity chromatography step is beneficial. Thereby the different biochemical properties of BMP-7 and BMP-10 CPLXs have to be considered: BMP-7 CPLX can only be reliably purified after 48 h of serum-free collection at the latest not only due to its sensitivity to proteolytic cleavage (Furlan, Spanou et al., 2021, Fig. 1A) but also due to its highly hydrophobic nature. BMP-10 CPLX is more soluble and can be purified after 4 days in serum-free media (Spanou et al., in preparation#1, Fig. 2).

Storage of BMP CPLXs

BMP-7 CPLX is safely stored shockfrozen in -80 °C after the SEC step is performed in presence of 0.15 M imidazole final in buffer M and can be thawed and shockfrozen multiple times to maintain its biological function over the course of ongoing experiments. However, the same is not true for BMP-10 CPLX. Due to material loss after a second shockfreezing step, BMP-10 CPLX is aliquoted after SEC and stored shockfrozen in -80 °C only once. Hence, after thawing, it can only be kept at 4 °C. In the 4 °C condition, SEC-purified BMP-10 CPLX can signal potently for 5 months (B. Roman, personal communication). In sharp contrast, SEC-purified BMP-7 CPLX loses its signaling competency after 1 week at 4 °C.

2.13.2 *In silico* techniques

Problem: Established techniques to identify heparin binding sites rely on *in silico* techniques such as molecular docking of heparin chains to structural models of BMPs and electrostatic surface coloring that can only be applied reliably when an atomic structural model of the BMP CPLX is available in the protein data bank (PDB). Hence, to identify the BMP-7 CPLX heparin binding site, a different methodology needed to be employed since BMP-7 CPLX is not crystallized and hence no atomic model is available.

Protocol establishment: My research approach was based on the hypothesis that the heparin-binding stretches within PDs are partially conserved but not necessarily a strict motif as already described for GFs (Billings et al., 2018). In order to identify the heparin-binding site of the BMP-7 CPLX, a new approach was tried based on

sequence and structural homology of heparin-binding GFs to BMP-7 PD. More specifically, chain-by-chain alignments of several heparin-binding GFs to the structural model of the BMP-7 PD using the UCSF chimera command “MatchMaker” and subsequent sequence alignment of the matched structures using the same software were attempted. The only heparin-binding GF structure that yielded alignment results agreeing with the BMP-7 CPLX negative staining EM images (Fig. 4A) was the NMR solution structure of the VEGF heparin-binding domain (PDB: 2VGH). Due to the scarce distribution of the positive charge within BMP-7 PD, the approach needed to be tested on a heparin-binding BMP for which an atomic model is available, such as the BMP-9 CPLX (Spanou et al., in preparation#2, Fig. 10). Indeed, successful identification of the heparin binding site of BMP-9 CPLX was also possible using the same *in silico* method.

Solution: The chain-by-chain alignment of the VEGF heparin binding domain to the structural model of BMP PD followed by sequence alignment of the two using the UCSF chimera software accurately identified the heparin/HS binding sites of the processed proactivin, BMP-7, and BMP-9 CPLXs (Spanou et al., in preparation#2, Figs. 6, 10 and S6). It remains to be tested whether the same approach can be applied for the identification of heparin-binding sites of other BMPs. In order to obtain reliable results, the structural models of processed BMP PDs must be utilized and not their crystallized unprocessed counterparts.

3. Results

3.1 Preface

The results section contains 1 peer-reviewed manuscript and 2 manuscripts in preparation. The manuscripts are referred to in text as follows:

1. “Prodomain processing defines shape and bioactivity of bone morphogenetic protein 10” is referred to as: Spanou et al., in preparation #1
2. “Regulation of BMP bioactivity by heparin/heparan sulfate glycosaminoglycans ” is referred to as: Spanou et al., in preparation #2
3. “A new MMP-mediated prodomain cleavage mechanism to activate bone morphogenetic proteins from the extracellular matrix ” is referred to as : Furlan, Spanou et al., 2021.

3.2 PPC processing renders BMPs bioactive

The conserved PPC cleavage consensus sequence localized at the C-terminal ends of BMP PDs suggests a general substrate recognition mechanism by several PPC family members and not just furin (Constam et al., 1999; Jaaks et al., 2016a). In addition, it was reported that only PPC-processed BMP CPLXs are signaling-competent since unprocessed GDF-5 (Plöger et al., 2008), unprocessed proactivin (Wang et al., 2016) and unprocessed BMP-9 (Kienast et al., 2016) do not show any biological activity. In addition, it was found that BMP-10 circulates in human plasma predominantly in unprocessed form (Hodgson et al., 2019). In this manuscript the nanoscale structure of BMP-10 was elucidated before and after PPC processing. *In silico* methods enabled structural refinement for both processing variants, and provided insight into the PD-GF interface.

The following manuscript was written by Chara E.S. Spanou and Gerhard Sengle.

The experiments in figures 1, 2, 6, 7, S1B, S1C, S2, S5, S6, S7 and S8 were performed and analyzed by Chara E.S. Spanou.

S4 was conceived by Chara E.S. Spanou.

The overview figure 8 was done by Chara E.S. Spanou based on molecular docking results of the closed-ring BMP-10 and BMP-7 CPLX models to the NMR solution structure of the FUN domain (Yadin et al., 2013).

Prodomain processing defines shape and bioactivity of bone morphogenetic protein 10

Chara E.S. Spanou^{1,2}, Alan R.F. Godwin^{3,4}, Stefanie Morosky^{5#}, Arulselvi Anbalagan^{5#}, Alexander P. Wohl¹, Beth L. Roman^{5,6}, Clair Baldock^{3,4}, Gerhard Sengle^{1,2,7,8*}

From the ¹Center for Biochemistry, Faculty of Medicine, University Hospital of Cologne, Joseph-Stelzmann-Street 52, 50931 Cologne, Germany; ²Department of Pediatrics and Adolescent Medicine, Faculty of Medicine and University Hospital Cologne, University of Cologne, Cologne, Germany; ³Division of Cell Matrix Biology and Regenerative Medicine, School of Biological Sciences, Faculty of Biology, Medicine and Health, Manchester Academic Health Science Centre, University of Manchester, Manchester, UK; ⁴Wellcome Centre for Cell-Matrix Research, School of Biological Sciences, Faculty of Biology, Medicine and Health, Manchester Academic Health Science Centre, University of Manchester, Manchester, UK; ⁵Department of Human Genetics, Graduate School of Public Health, University of Pittsburgh, Pittsburgh, PA, 15261, USA; ⁶Heart, Lung, Blood and Vascular Medicine Institute, University of Pittsburgh, Pittsburgh, PA, 15261, USA; ⁷Center for Molecular Medicine Cologne (CMMC), University of Cologne, Robert-Koch-Street 21, 50931 Cologne, Germany; ⁸Cologne Center for Musculoskeletal Biomechanics (CCMB), 50931 Cologne, Germany Running title: Prodomain processing defines shape and bioactivity of the prodomain-bound form of BMP-10

#contributed equally

*To whom correspondence should be addressed: Gerhard Sengle, Center for Biochemistry, Medical Faculty, University of Cologne, Joseph-Stelzmann-Street 52, D-50931 Cologne, Germany, phone: +49 (0)221 47897260, fax: +49 (0)2214786977, email: gsengle@uni-koeln.de

Keywords: Bone morphogenetic protein, growth factor, complex, proprotein convertases (PPCs), furin, conformational change, single particle analysis, cryo-electron microscopy, molecular modeling

Abstract

1 Activin receptor-like kinase 1 (ALK1) -mediated endothelial cell signaling in response to bone
2 morphogenetic protein 10 (BMP-10) is of significant importance in cardiovascular disease and cancer.
3 BMP-10 biosynthesis and folding involves processing by proprotein convertases (PPCs) leading to the
4 formation of a prodomain-growth factor (PD-GF) complex (CPLX), as already described for most TGF-
5 β superfamily ligands. However, the molecular requirements regulating BMP-10 bioactivity are
6 unknown. To better understand the conformational requirements for BMP-10 bioactivity, we examined
7 the nanoscale structure and bioactivity of BMP-10 in the presence and absence of PPC processing.
8 Single-particle transmission electron microscopy revealed that PD processing converts BMP-10 from a
9 latent conformation with wider angle between PD arms to a bioactive V-shape CPLX. Moreover,
10 processed BMP-10 showed enhanced potency in HUVEC and C2C12 cells compared to free BMP-10
11 growth factor, whereas the unprocessed variant was latent. Our data suggest that PD processing induces
12 specific folding events at the PD-GF interface that are required to render the CPLX into a bioactive
13 state.

14 **Introduction**

15 BMPs belong to the TGF- β superfamily of growth factors (GFs) and participate in a multitude of
16 biological events such as proliferation, differentiation, adhesion, and organogenesis [1]. Similar to other
17 TGF- β family members, BMPs are secreted as complexes (CPLXs) consisting of a GF dimer that is
18 non-covalently associated with two cognate prodomains (PDs) [2-6]. Both BMP moieties originate from
19 a single precursor polypeptide chain. These precursors form dimers via disulfide bridges between
20 distinct cysteines of two GF moieties. Processing by proprotein convertases (PPCs) results in C-terminal
21 PD cleavage right before the GF moiety at the consensus site: R/K-X_n-R/K↓ [7] to render the dimer into
22 a PD-GF CPLX.

23 In recent years, several studies have demonstrated that the conformation of TGF- β ligand PDs
24 defines the bioactivity of their GFs, acting as a protective shell to prevent the GF from triggering
25 unwanted signaling events [8]. Interestingly, some members, such as GDF-8 and TGF- β , are cleaved by
26 furin intracellularly and secreted in a latent precursor protein form that requires additional extracellular
27 proteolytic PD processing for GF activation [9-12]. For these proteins, the conformational difference
28 between bioactive and latent CPLXs was suggested to play a decisive role in activity. For example, the
29 small latent PD-GF TGF- β CPLX (SLC) was crystallized in a closed ring-shape conformation, with
30 both PD arms being disulphide-linked within their C-terminal regions [11]. This so called cross-armed
31 conformation prevents access of TGF- β receptors to the GF. TGF- β GF activation involves several
32 mechanisms to remove the PD (also known as latency associated peptide: LAP) such as proteolytic
33 degradation [10, 13, 14], mechanical displacement via thrombospondin [15], or RGD-site mediated
34 integrin-pulling [11, 16].

35 Other TGF- β superfamily members such as BMP-7 and BMP-9 are secreted in a bioactive V-
36 shape conformation, in which the PD competes with the BMP type II receptor ectodomain for the same
37 GF binding sites, but is freely displaced upon receptor binding [6, 17-19]. However, we previously
38 showed that the BMP-7 CPLX is converted from a bioactive open V-shape into a latent closed ring
39 shape upon binding to the extracellular microfibril component, fibrillin-1 [19]. Recently, we
40 demonstrated an effective activation mechanism for BMP CPLXs from extracellular matrix (ECM)
41 stored pools that is mediated by specific matrix metalloproteinase (MMP) degradation of the PD [8, 20].

42 However, not all V-shaped CPLXs are bioactive in solution. Unprocessed and furin-processed
43 GDF-8 CPLXs are both latent and adopt a V-shape conformation [12]. Processed GDF-8 CPLX can be
44 activated by tolloid-like protein 2 (TLL2) cleavage of the PD (primed GDF-8) and this active complex
45 retains a V-shape conformation [9].

46 The molecular nature of secreted BMP-10 remains unclear. Recent data suggest that BMP-10 is
47 a predominantly soluble CPLX expressed by hepatic stellate cells and cardiomyocytes that circulates in
48 the bloodstream in association with the PD [21]. However, it is not known whether BMP-10 is secreted
49 in a processed or unprocessed form. Furthermore, BMP-10 is capable of forming a heterodimer with
50 BMP-9 [22]. This GF heterodimer is found in blood and has similar signaling potency to BMP9 or
51 BMP10 homodimers [22], but the nature of the heterodimer CPLX has not been investigated.

52 While it seems clear that BMP10 PD associates with the GF in circulation, it is not clear how
53 the PD affects signaling competency [21]. Cell-based assays showed that PD addition to the BMP-10
54 GF results in a cell-type specific inhibition of its bioactivity: while BMP-10 PD addition at
55 supraphysiological ratios led to quantitative inhibition of GF bioactivity towards C2C12 myoblasts [5,
56 23], this effect was not observed for human umbilical vein endothelial cells (HUVEC) [5]. However, it
57 remains possible that the PD may confer latency *in vivo*. Like BMP-7, the BMP-10 PD was shown to
58 interact with fibrillin-1, suggesting that fibrillin microfibrils may also target BMP-10 CPLXs to the
59 ECM and thereby confer latency [21, 24].

60 Gaining a better understanding of the molecular requirements for BMP-10 activity may lead to
61 improved therapeutic approaches to cancer and vascular disease. BMP-10 is essential for cardiac
62 development in mice and is therefore thought to be implicated in the pathogenesis of congenital heart
63 defects [25-27]. Downregulation of BMP-10 has been linked to cancer onset and progression, whereas
64 its overexpression limits metastasis and prolongs survival [28-31]. Additionally, mutations in *BMP-9* or
65 the genes encoding BMP-9/-10 receptors, *ACVRL1* (encoding ALK1) and *ENG* (encoding endoglin),
66 lead to hereditary hemorrhagic telangiectasia (HHT), a rare genetic disease that is characterized by
67 arteriovenous malformations (AVMs) and internal bleeding [32, 33]. Recently, we delineated the roles
68 of BMP-9 and -10 in AVM development using zebrafish genetic models. While we found no
69 requirement for *bmp9*, combined loss of duplicate *BMP10* paralogs, *bmp10* and *bmp10-like*, results in

70 embryonic lethal cranial AVMs indistinguishable from *acvr11* mutants. Additionally, *bmp10* loss alone
71 resulted in a later-onset HHT-like phenotype characterized by skin and liver vascular malformations and
72 high-output heart failure [34]. These data strongly suggest that BMP10 is an indispensable ALK1 ligand
73 necessary for vascular homeostasis and AVM prevention.

74 In this work, we aimed to determine the nanoscale structure of BMP-10 in processed and
75 unprocessed forms and assess their respective bioactivities.

76 **Results**

77 *Reconstitution of stable BMP-10 CPLX from separate BMP-10 PD and GF components.*

78 Our previous protein interaction studies showed a high molecular affinity between the BMP-10 GF and
79 its cognate PD ($K_D = 7$ nM) [23], thereby suggesting the possibility of stable CPLX formation in
80 solution. To test this assumption, we performed reconstitution experiments using the *E.coli*-derived C-
81 terminally His₆-tagged BMP-10 PD and the commercially available HEK293 cell culture-derived BMP-
82 10 GF in the presence of 0.1% BSA. The reconstituted sample was subjected to size exclusion
83 chromatography (SEC) followed by dot blot analysis (Fig. S1A). The analyses identified peak fractions
84 showing parallel signals for PD and GF, suggesting the presence of successfully reconstituted BMP-10
85 CPLX molecules (Fig. S1A). Successful BMP-10 CPLX formation could be also demonstrated in the
86 presence of 0.8 M urea by sandwich ELISA (capture: anti-GF, detector: anti-PD) indicating robust and
87 stable PD-GF assembly (Fig. S1B). Interestingly, reconstituted BMP-10 CPLX was detected in the same
88 peak elution fractions as BMP-7 CPLX after SEC (Fig. S1C), suggesting that similar hydrodynamic
89 shapes of both CPLXs can be assumed.

90 *N-terminally placed His₆-tag interferes with BMP-10 CPLX assembly*

91 Next, we attempted to overexpress BMP-10 CPLX with a His₆-tag at the N-terminal end of the PD in
92 HEK293 cells. For the generation of the overexpression construct, we were guided by our experience
93 with BMP-7 CPLX, which can be readily purified from the conditioned media in processed form when
94 an N-terminal His₆-tag is placed after the BM40 signal peptide [19] (Fig. S1C). To our surprise, non-
95 reducing SDS-PAGE analysis of elution fractions after Ni-chelate affinity chromatography of the

96 conditioned media only showed the presence of the processed BMP-10 PD, while the mature GF was
97 not detected (Fig. 1A). This suggests that, in contrast to BMP-7 CPLX (Fig. S1C), an N-terminally
98 placed His₆-tag strongly interfered with stable BMP-10 CPLX assembly.

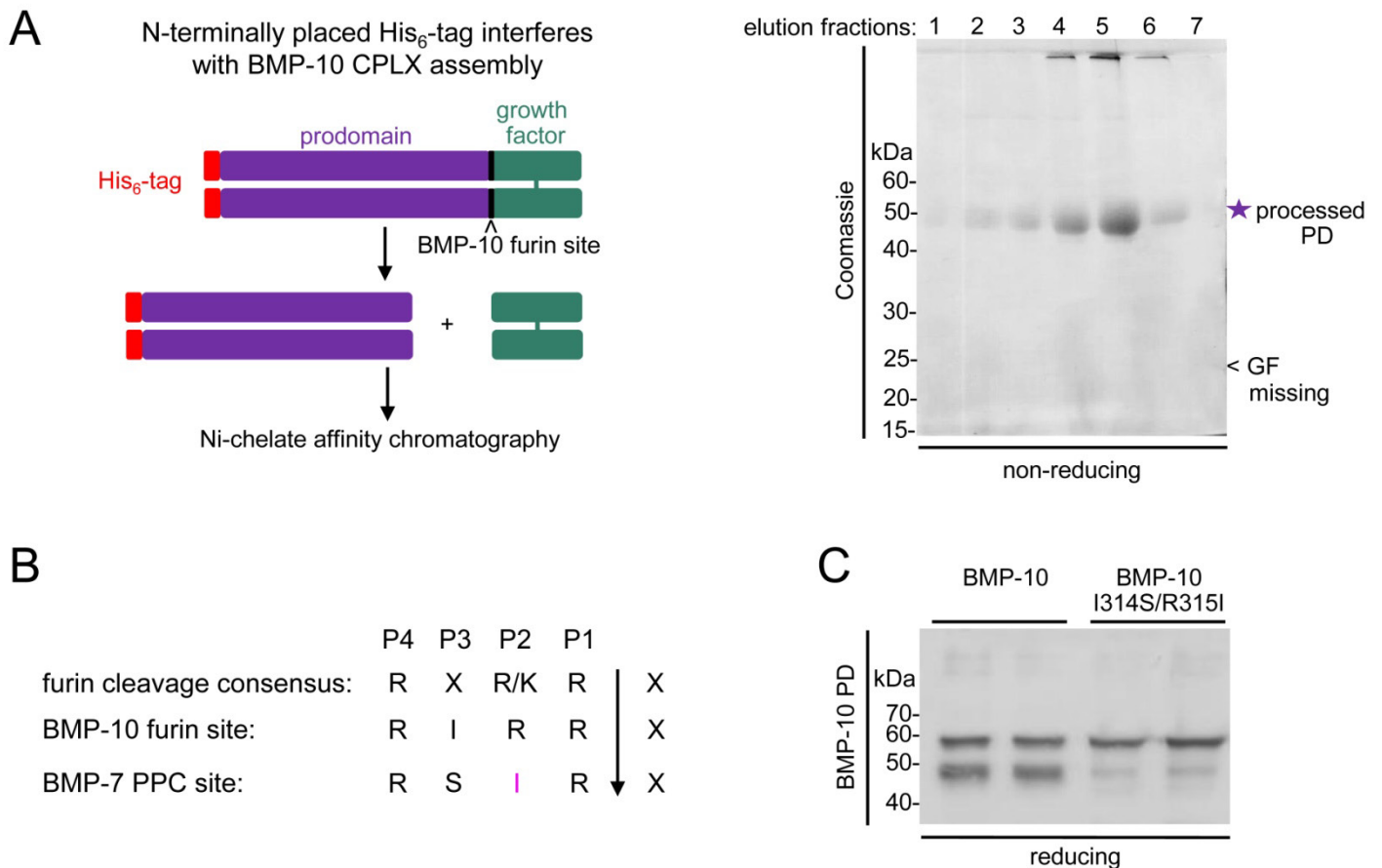
99 *Generation of unprocessed BMP-10 dimer*

100 N-terminal His₆-tag placement did not affect BMP-10 processing in HEK293 cells since no secreted
101 unprocessed protein could be detected by SDS-PAGE under non-reducing conditions (Fig. 1A).
102 However, there is strong *in vivo* evidence that unprocessed BMP-10 is secreted and transported, as
103 shown in human plasma where most BMP-10 was detected in unprocessed form [35]. This suggests that
104 BMP-10 processing is mediated in a cell type-specific manner by intracellular or extracellular (“shed”)
105 furin or other extracellular proprotein convertases (PPCs) that all cleave near a lysine/arginine-enriched
106 consensus site [7]. That is, depending on the cell type, BMP-10 may be intracellularly folded, secreted
107 and then processed or intracellularly folded, processed, and then secreted. Accordingly, unprocessed
108 BMP-10 may be transported in an inactive form to target cells where it can be activated via membrane-
109 associated or extracellular PPCs. The conformation of BMP-10 may therefore change during the
110 transition from an unprocessed to a processed state.

111 To investigate whether the order of this sequence of events impacts the BMP-10 conformation,
112 we generated an overexpression construct that blocks intracellular processing in HEK293 cells but
113 allows it to occur post-secretion. We were guided by our experience with BMP-7 CPLX production in
114 HEK293 cells that leads to more than 95 % of processing [2, 19]. WB analysis of cell lysates obtained
115 from stably transfected cells showed that BMP-7 processing does not occur intracellularly (Fig.S2A),
116 suggesting exclusively extracellular processing on the cell surface. Therefore, in order to facilitate
117 secretion of unprocessed BMP-10 CPLX in HEK293 cells, we switched the endogenous BMP-10 PD
118 furin cleavage site (RIRR↓) to the BMP-7 PD PPC cleavage site (RSIR↓) (BMP-10 I314S/R315I
119 mutant) (Fig. 1B). Western blot analysis of conditioned media one day after transfection confirmed that
120 intracellular processing was quantitatively blocked in the BMP-10 I314S/R315I mutant compared to the
121 control (Fig. 1C). Molecular modeling suggested that substitution of the positively charged arginine in
122 position P2 of the furin cleavage consensus by the uncharged isoleucine affects the negatively charged

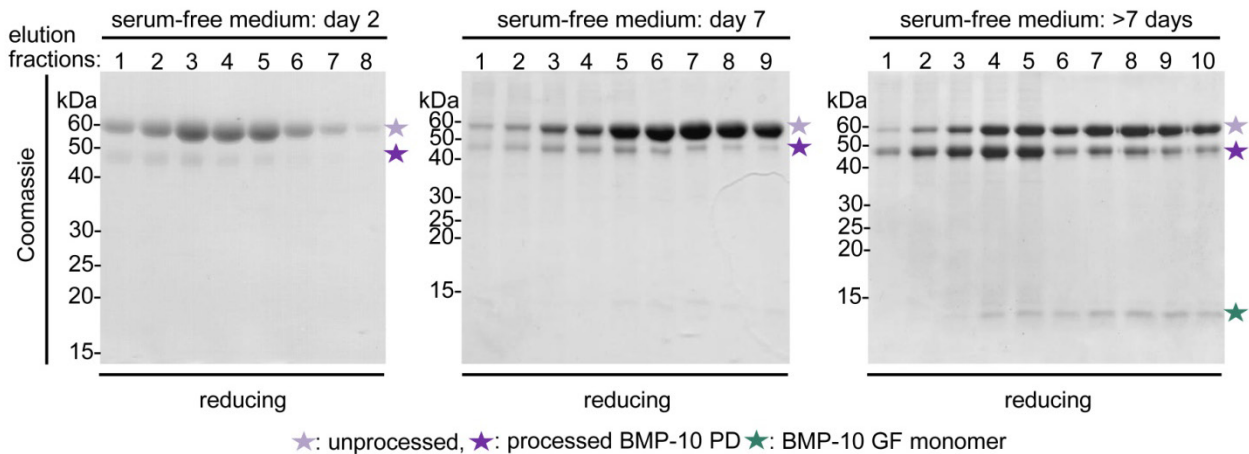
123 catalytic triad (Ser368, His194, Asp153) of the enzyme (Fig. S2B). Therefore, our experimental and *in*
 124 *silico* results suggested that furin cannot efficiently process substrates that lack a positive charge in the
 125 P2 position of the consensus sequence (Fig. 1C and Fig. S2B).

126 Consistent with the extracellular processing requirement of the BMP-7 CPLX cleavage site,
 127 prolonged contact of the BMP-10 I314S/R315I variant with the cell layer resulted in some processing of
 128 BMP-10 that increased over time, thus yielding a mixed population of unprocessed and partially
 129 processed BMP-10 molecules (Fig. 1D). Non-reducing SDS-PAGE analysis of affinity purified
 130 unprocessed BMP-10 collected after 2 days of contact with the cell layer allowed detection of the most
 131 abundant band at 120 kDa, indicating the formation of unprocessed disulfide-linked dimers between the
 132 cysteines of the precursor GF moieties (Fig. 1E). Indicative of the partial processing taking place is the
 133 observation that BMP-10 GF monomers appear on gel when the BMP-10 I314S/R315I variant is
 134 incubated with the cell layer for more than a week thus potentially generating BMP-10 dimers with only
 135 one GF monomer cleaved and the other still covalently-bound to the PD (Fig. 1D, right)



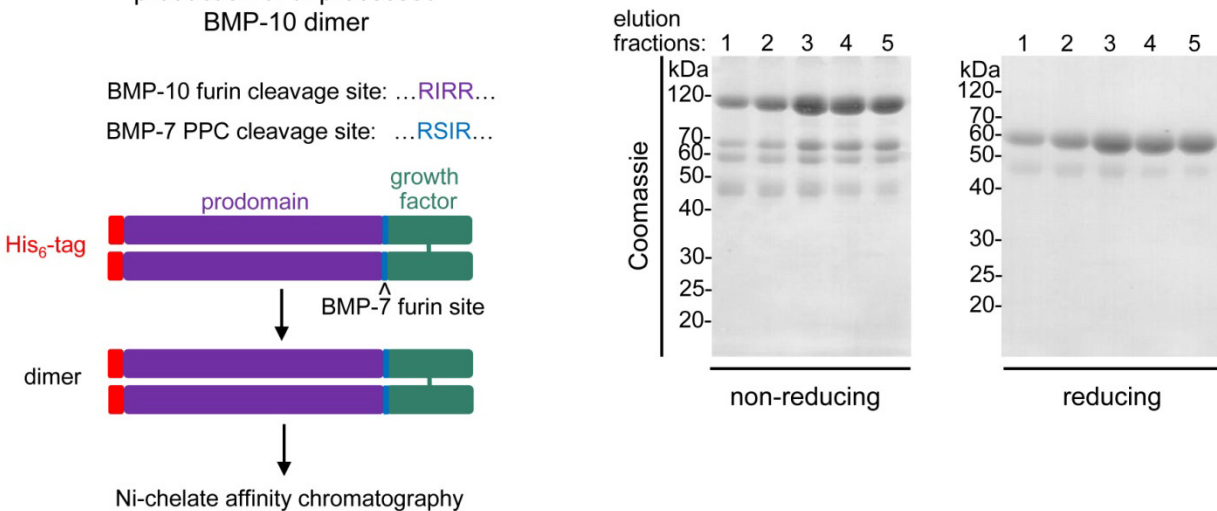
D

progressive extracellular processing of BMP-10 I314S/R315I



E

production of unprocessed BMP-10 dimer

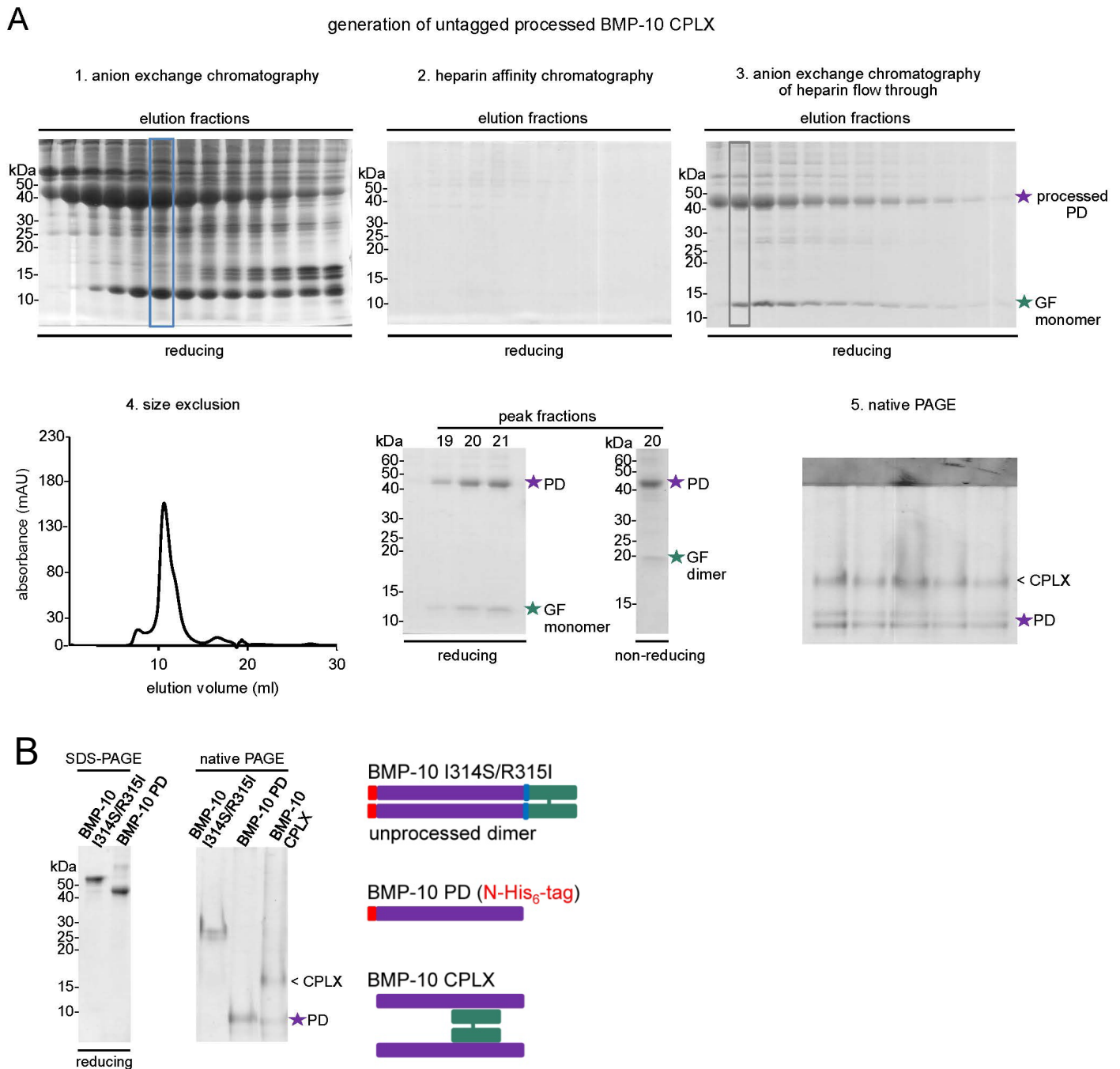


136 **Figure 1: N-terminally placed His₆-tag interferes with BMP-10 CPLX assembly.** (A) (left) Scheme
 137 illustrating His₆-tag placement at the N-terminus of the BMP-10 PD. (right) Coomassie stained gel of
 138 elution fractions after non-reducing SDS-PAGE of N-terminally His₆-tagged full length BMP-10. (B)
 139 Scheme explaining the BMP-10 and -7 PPC cleavage sites together with the furin cleavage consensus
 140 site. (C) Western blot analysis of BMP-10 PD in HEK293 supernatants transfected with full length
 141 BMP-10 (no-tag), or the BMP-10 I314S/R315I mutant construct. (D) Progressive extracellular
 142 processing of the BMP-10 I314S/R315I mutant after prolonged contact (2-7 days) with the cell layer in
 143 serum-free conditioned media. Coomassie-stained SDS-PAGE gels under reducing conditions after Ni-
 144 NTA affinity chromatography of 500 ml media collected after 2 days, 7 days and more than 7 days in
 145 contact with the cell layer. (E) (left) Scheme illustrating the substitution of the endogenous BMP-10
 146 furin site with the BMP-7 PPC site. (right) Coomassie-stained SDS gels under non-reducing and
 147 reducing conditions after Ni-NTA affinity chromatography of 500 ml of conditioned media from
 148 HEK293 cells overexpressing the BMP-10 I314S/R315I mutant.

149 *Generation of the processed BMP-10 CPLX in mammalian cells*

150 To recombinantly produce processed BMP-10 CPLX, we generated a construct encoding for the tag-
151 free BMP-10 CPLX containing the endogenous furin site. Conditioned media from stably transfected
152 HEK293 cells was condensed over anion and cation exchange columns (HiTrap Q and heparin)
153 followed by salt gradient elution (Fig. 2A1-3). Peak fractions were subjected to SEC to remove high
154 molecular weight aggregates from intact BMP-10 CPLX eluting in fractions 19-21 (Fig. 2A4), as
155 expected from the SEC elution profile of the reconstituted BMP-10 CPLX (Fig. S1A). The purified and
156 processed BMP-10 CPLX was composed of the glycosylated PD running at 45 kDa and the GF running
157 at 12 kDa under reducing conditions (monomeric form) or at 20 kDa under non-reducing conditions
158 (dimeric form) due to the formation of disulfide bonds between GF monomers (Fig. 2A4, right). In
159 agreement with previous reports, the SEC-purified BMP-10 CPLX yielded multiple bands after native-
160 PAGE with the upper band corresponding to the fully processed BMP-10 CPLX, whereas the lower
161 bands indicated the presence of separated BMP-10 PD that could not be removed by SEC [5] (Fig.
162 2A5).

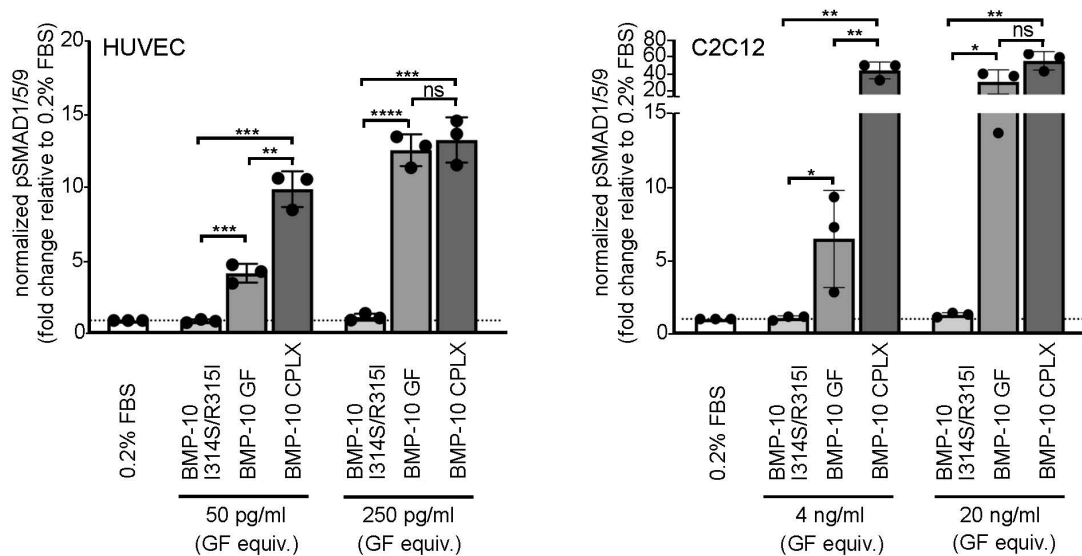
163 To further investigate the native-PAGE band pattern of obtained BMP-10 species, different
164 BMP-10 processing variants were purified. The unprocessed BMP-10 I314S/R315I dimer, the N-
165 terminally His₆-tagged BMP-10 PD, and the tag-free BMP-10 CPLX were analyzed by SDS-PAGE and
166 native-PAGE (Fig. 2B). The unprocessed BMP-10 dimer and the fully processed tag-free BMP-10
167 CPLX migrated to different positions in native-PAGE suggesting that they assume different
168 conformations due to their processing status. The processed BMP-10 CPLX showed two bands after
169 SEC in native-PAGE, as shown previously [5]. However, the lower bands migrated to the same position
170 as the N-terminally His₆-tagged BMP-10 PD, suggesting that the upper band corresponds to the fully
171 processed non-covalently associated BMP-10 CPLX (Fig. 2B and [5]).



172 **Figure 2: Generation of untagged, processed BMP-10 CPLX.** (A) 1. Coomassie stained SDS-PAGE
 173 gel of elution fractions containing BMP-10 CPLX from condensed conditioned media after HiTrap Q
 174 HP anion exchange chromatography, 2. Coomassie stained SDS-PAGE gel of elution fractions (fraction
 175 highlighted in blue in (1.) was loaded) after HiTrap heparin HP cation exchange chromatography, 3.
 176 SDS-PAGE and Coomassie staining of elution fractions after HiTrap Q HP anion exchange
 177 chromatography of condensed flow through from heparin column, 4. (left) SEC elution profile of
 178 processed BMP-10 CPLX, (right) Coomassie stained SDS-PAGE gel after SEC purification of the
 179 fraction highlighted in grey in (3) under reducing and non-reducing conditions, 5. Native-PAGE of the
 180 SEC purified material from (4). (B) Coomassie stained-SDS-PAGE and native PAGE gels of His₆-
 181 tagged BMP-10 PD, the unprocessed BMP-10 dimer, and the processed BMP-10 CPLX.

182 *Processed but not unprocessed BMP-10 signals to both HUVEC and C2C12 cells*

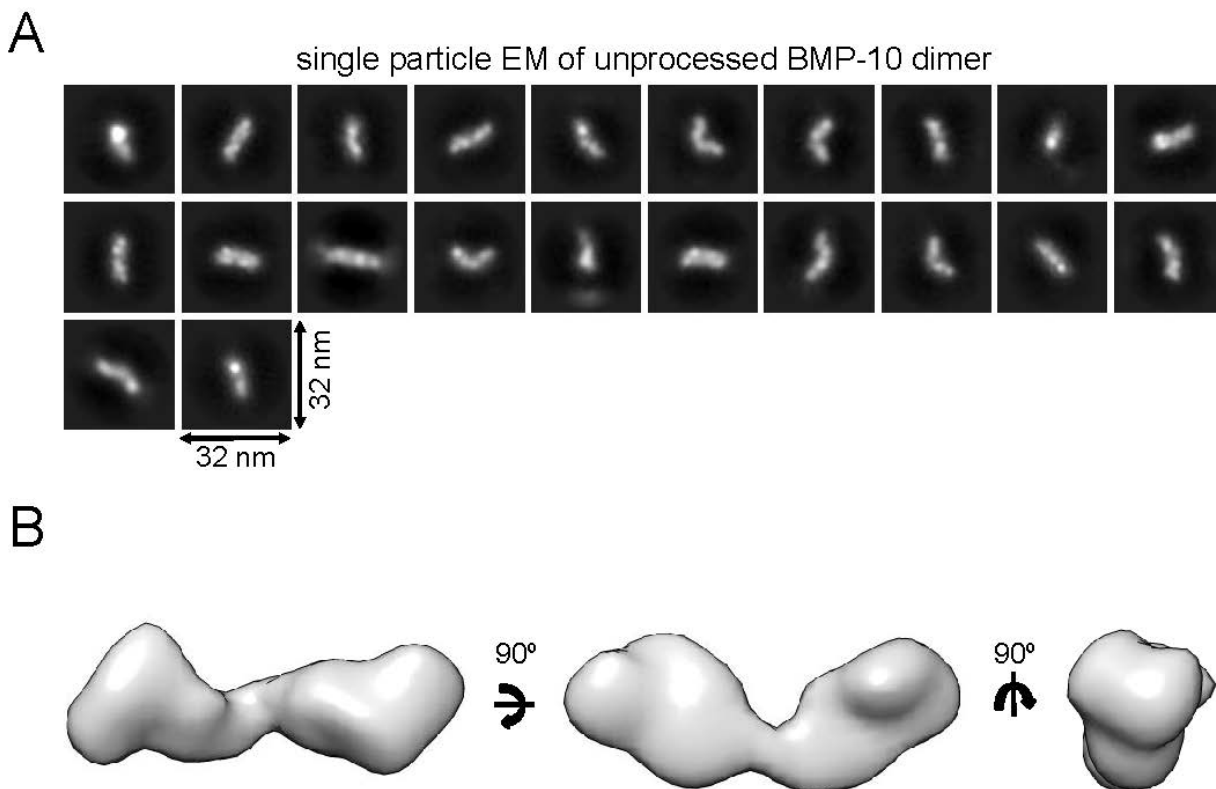
183 To assess the bioactivity of unprocessed and processed BMP-10, HUVEC and C2C12 cells were
 184 stimulated with purified proteins followed by quantification of pSMAD1/5/9 via Western blotting. The
 185 unprocessed BMP-10 dimer failed to signal above baseline in HUVECs and C2C12 cells, whereas the
 186 processed BMP-10 CPLX potently induced pSMAD1/5/9. At 50 pg/mL, representing the approximate
 187 EC₅₀ of free BMP-10 GF dimer, the BMP-10 CPLX was more active than the free GF dimer, whereas
 188 potency was similar at higher concentrations (Fig. 3). The unprocessed and processed BMP-10 showed
 189 similar results in C2C12 cells. The unprocessed BMP-10 dimer failed to signal, whereas, compared to
 190 the free BMP-10 GF dimer, the processed BMP-10 CPLX exhibited higher potency near the EC₅₀ (4
 191 ng/mL) and similar potency at higher concentrations. These results suggest the previously observed PD
 192 inhibition of BMP-10 GF activity on C2C12 [5, 23] was a consequence of supraphysiological PD
 193 concentrations, and that the BMP-10 PD does not inhibit GF activity at a physiologically relevant 2:1
 194 ratio on HUVEC or C2C12 (Fig. 3).



195 **Figure 3: The processed BMP-10 CPLX is bioactive towards HUVEC and C2C12 cells while the**
 196 **unprocessed BMP-10 dimer is latent.** Quantification of Western blot of HUVEC or C2C12 cells
 197 treated for 45 minutes with indicated BMP-10 proteins. pSMAD1/5/9 intensity was normalized to
 198 GAPDH intensity, and values expressed as fold change relative to 0.2% FBS control. Each data point is
 199 the mean value of duplicate samples from a single experiment, N = 3 experiments. Bars represent
 200 overall mean \pm SD. Unpaired *t*-test. * $P \leq 0.05$; ** $P \leq 0.01$; *** $P \leq 0.001$; **** $P \leq 0.0001$.

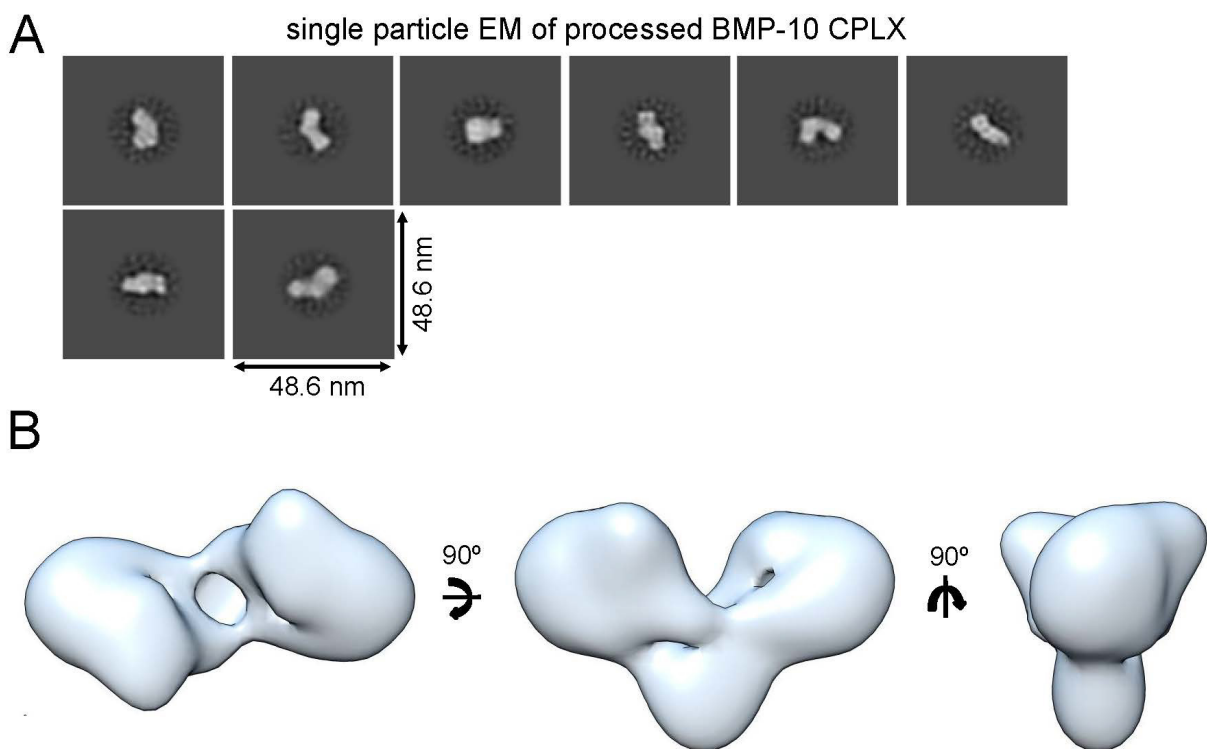
201 *Unprocessed BMP-10 dimer assumes an open-arm conformation while processed BMP-10 CPLX*
 202 *assumes a V-shape conformation*

203 To gain further structural insight on the conformational requirements to ensure BMP-10 bioactivity we
 204 aimed to determine the nanoscale structures of unprocessed and processed BMP-10. Single particle
 205 transmission electron microscopy (TEM) followed by 3D classification as well as cryo-TEM analysis
 206 revealed that the unprocessed BMP-10 dimer assumes an open-arm conformation with maximum
 207 dimension of 14.7 nm (Fig. 4A, B and Fig. S3). Molecular docking identified processed BMP-9 CPLX
 208 (PDB: 4YCG) as the atomic model with the best fitting parameters for the unprocessed BMP-10 dimer
 209 EM envelope (Table 1) in comparison to all available CPLX structures (Fig. S4).

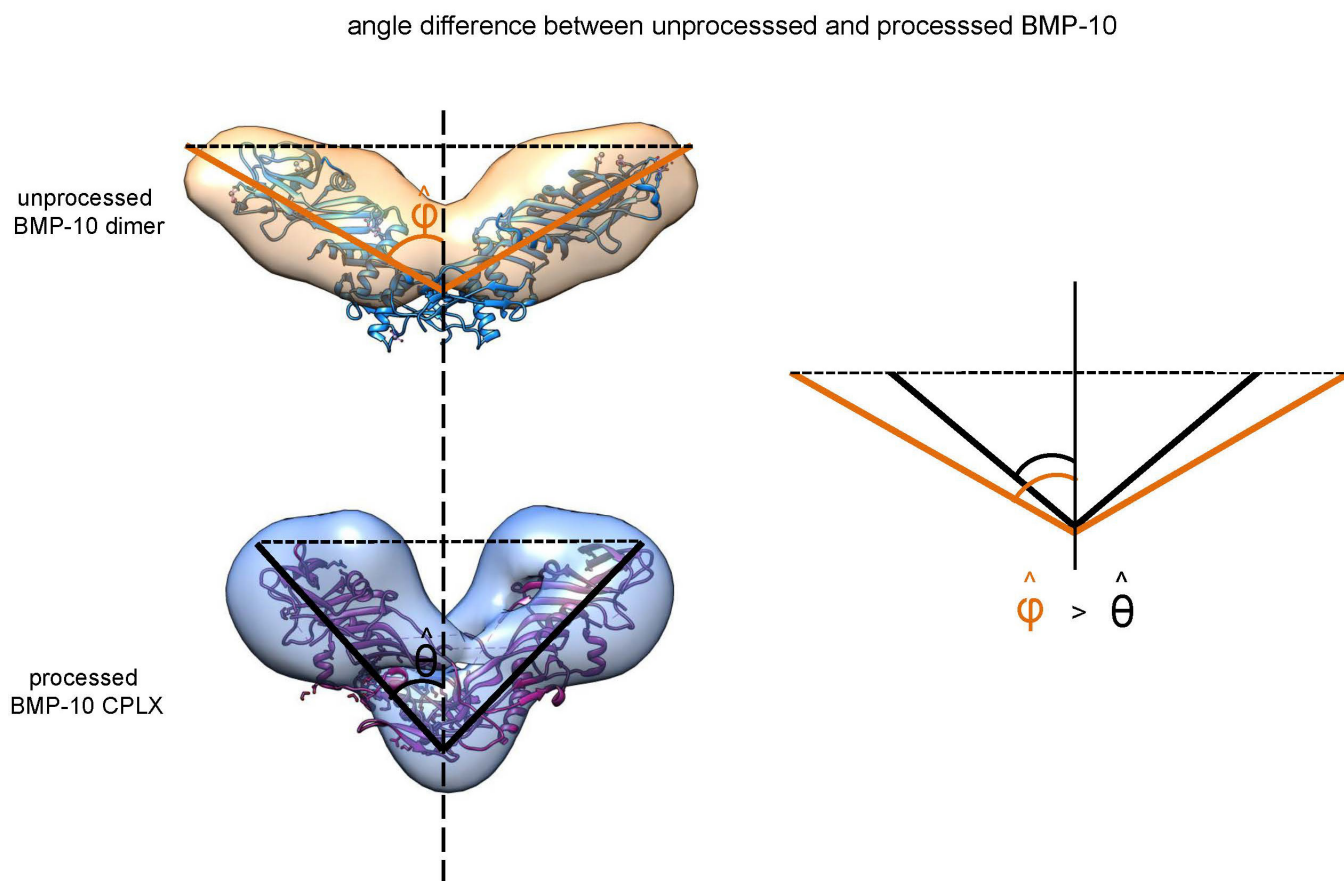


210 **Figure 4: The unprocessed BMP-10 dimer assumes an open-arm conformation and is not**
 211 **bioactive.** (A) Single particle transmission EM class averages of the unprocessed BMP-10 dimer from
 212 negatively stained images. (B) EM envelope of the 3D reconstruction of the unprocessed BMP-10
 213 dimer.

214 Single particle TEM of the processed BMP-10 CPLX followed by 3D classification revealed
 215 that it assumes a more compact V-shape conformation with maximum dimension of 13 nm (Fig. 5A and
 216 B). Molecular docking of several published atomic models into the measured EM envelope of the fully
 217 processed BMP-10 CPLX (Fig. 5B) revealed that the best molecular fit was accomplished for the
 218 promyostatin atomic model (Table 1 and Fig. S4). Identification of the symmetry axis of both EM
 219 envelopes and fitted models showed that in the fully processed BMP-10 CPLX, the angle between the
 220 prodomain arms is smaller than in the unprocessed, latent BMP-10 dimer (Fig. 6).



221 **Figure 5: The processed BMP-10 CPLX assumes a V-shape conformation.** (A) Single particle
 222 transmission EM class averages of the tag-free processed BMP-10 CPLX from negatively stained
 223 images. (B) EM envelope of the 3D reconstruction of processed tag-free BMP-10 CPLX.



224 **Figure 6: Processed BMP-10 CPLX assumes a tighter V-shape than unprocessed dimer.** Angle
 225 difference between PD arms in processed and unprocessed EM envelopes. The published atomic models
 226 with the best fit into the EM envelopes are depicted.

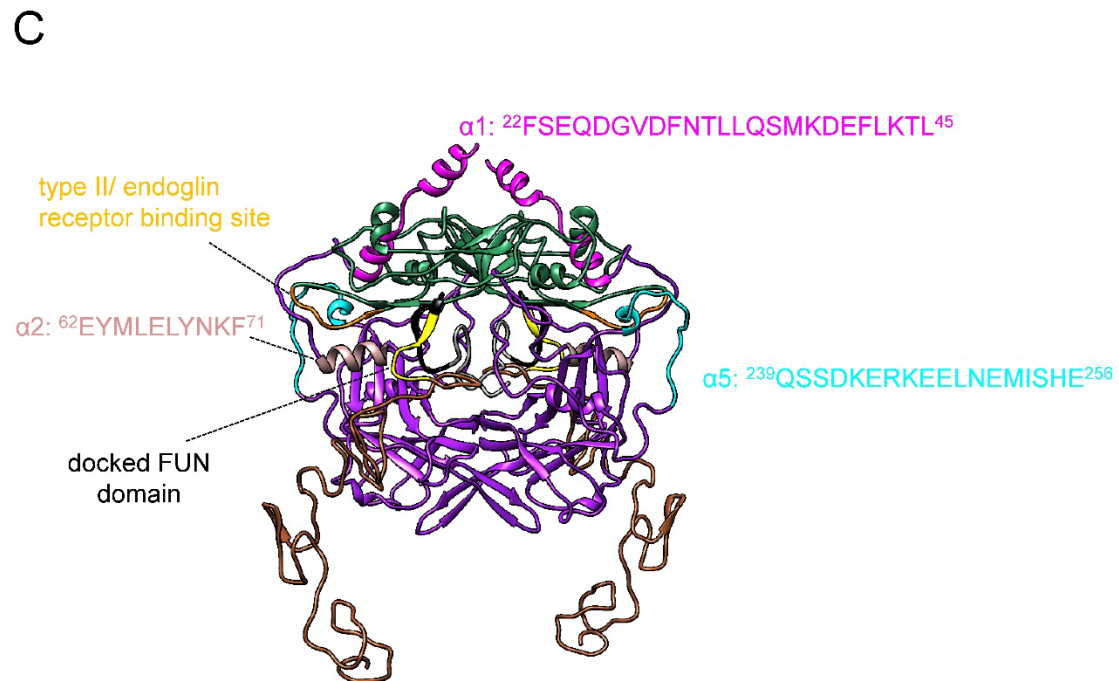
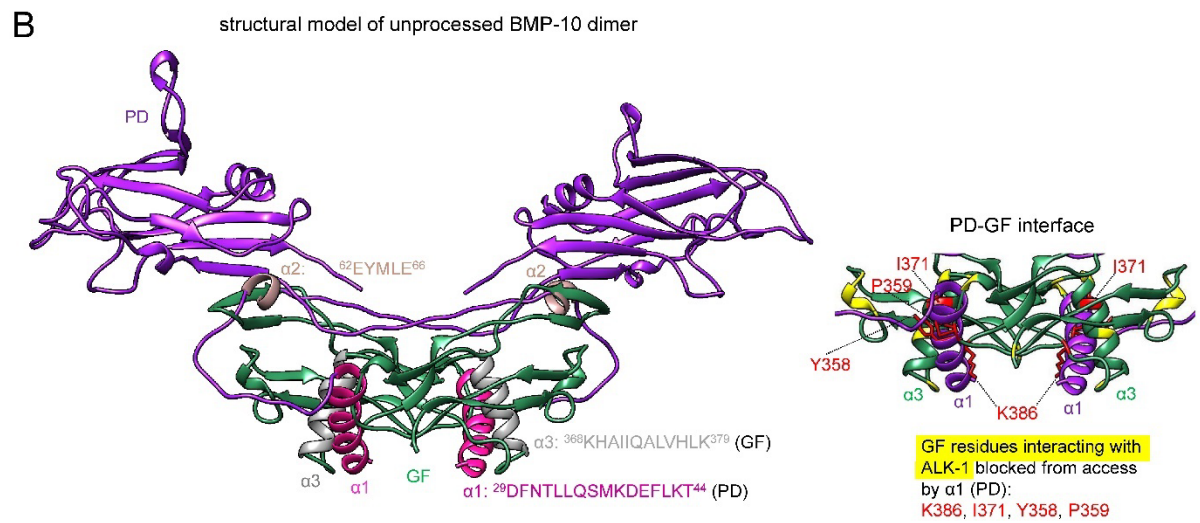
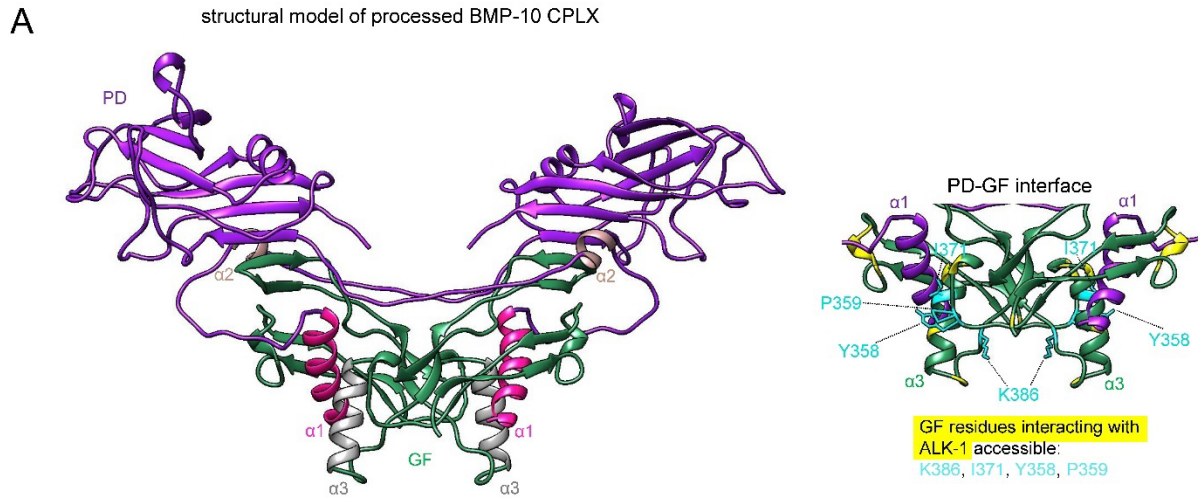
227 *New structural models of unprocessed BMP-10 dimer and processed BMP-10 CPLX*

228 Guided by our fitting results of known CPLX structures into the determined EM envelopes, we
 229 generated corresponding atomic models for both BMP-10 variants. We first generated a structural
 230 model of the processed bioactive BMP-10 CPLX by building the BMP-10 PD single chain model on the
 231 promyostatin crystal structure and aligning chain-by-chain the modeled PDs and the crystal structure of
 232 the BMP-10 GF (PDB: 6SF3, with receptor deleted) to the promyostatin crystal (PDB: 5NTU) (Fig.
 233 7A). In this model, the PD-GF interaction is mainly mediated by residues within the $\alpha 1$ -helix of the PD
 234 and the GF (Fig. S6C). Similar PD-GF interfaces also exist in other CPLXs to assure their assembly and
 235 stability [11, 12, 19, 36-38]. However, building the BMP-10 PD single chain model on the BMP-9 PD
 236 crystal structure of the processed BMP-9 CPLX atomic model (PDB: 4YCG) and aligning both modeled

237 PDs and the crystal structure of the BMP-10 GF (PDB: 6SF3, receptor deleted) chain-by-chain to the
238 promyostatin template resulted in a compromised PD-GF interface with a reduced number of potential
239 molecular interactions between the $\alpha 5$ -helix of the PD and the $\alpha 3$ -helix of the GF when compared to the
240 processed BMP-9 CPLX structure (Fig. S5A,B; Fig.S6A,B). Due to the predicted weakened PD-GF
241 interaction in this model, the processed BMP-10 CPLX would be even less stable than the BMP-9
242 CPLX which shows a molecular binding affinity between the PD and its cognate GF of 0.8 μM [6].
243 However, previously we determined the BMP-10 PD-GF affinity in the low nanomolar range ($K_D = 7$
244 nM) [23] indicating a stable interaction also suggested by our reconstitution assays (Fig. S1A, B).
245 Therefore, we considered the model built on the BMP-9 CPLX template as less likely.

246 To better understand how latency occurs in the unprocessed BMP-10 dimer, we built the BMP-
247 10 PD single chain model on the promyostatin crystal structure which covers the $\alpha 1$ -helix of the PD that
248 is known to be required for conferring GF latency and CPLX stability [11, 12, 19, 37] and is not present
249 in the processed BMP-9 CPLX atomic model [6]. We next aligned the modeled PDs and the crystal
250 structure of the BMP-10 GF (PDB: 6SF3 with receptor deleted) chain-by-chain to the BMP-9 CPLX
251 atomic model due to the best obtained fitting results into the determined EM envelope of the
252 unprocessed BMP-10 dimer (Table 1, Fig. S4). Visualization of the PD-GF interface in this model
253 shows that the $\alpha 1$ -helix of the PD provides steric hindrance to the $\alpha 3$ -helix of the GF thereby blocking
254 access of crucial GF residues required for ALK-1 binding (Fig. 7B). This is different to the model of the
255 processed BMP-10 CPLX in which the same GF residues appear to be accessible for ALK-1
256 engagement (Fig. 7A).

257 Since processed BMP-10 CPLX is bioactive in solution, extracellular control mechanisms may
258 exist that restrict its signaling capability in a contextual manner. For the processed BMP-7 CPLX we
259 found that its bioactivity can be controlled by PD targeting to fibrillin-1 microfibrils which renders the
260 CPLX into a latent, closed-ring conformation [19]. A similar mechanism may be plausible for processed
261 BMP-10, since we previously found that BMP-10 PD interacts with fibrillin-1 [23]. We therefore
262 assessed *in silico* whether BMP-10 CPLX can theoretically also assume a closed ring-shape. Our
263 modeling suggested that the BMP-10 CPLX can indeed be rendered into a closed ring-shape that was
264 also predicted to exist for processed BMP-9 CPLX (Fig. 7C) [6].



Fibrillin-1 FUN domain epitopes:
SARGGGGHDALKGPNVCGSRYNAYCCPGWK

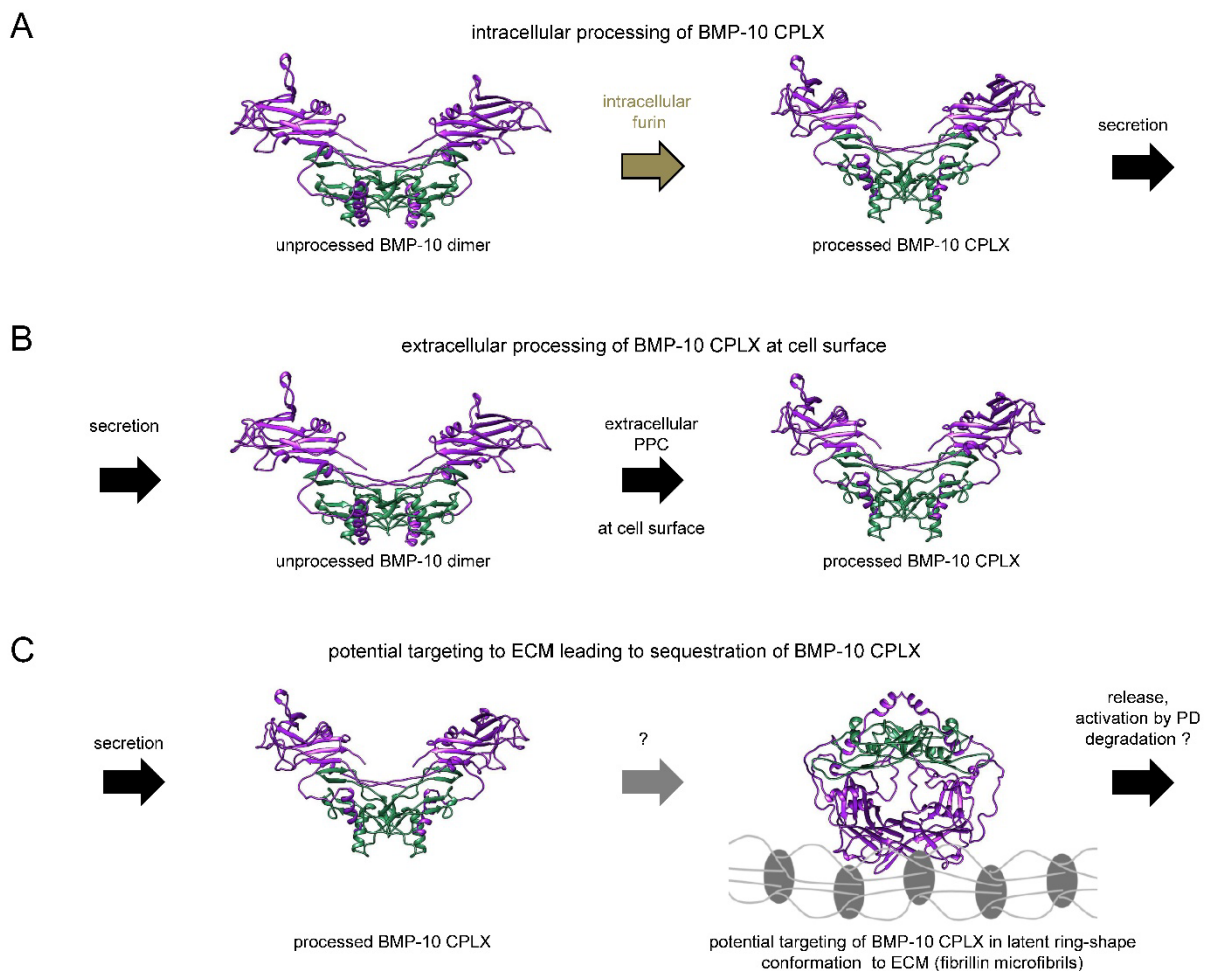
265 **Fig. 7: Atomic models generated for bioactive BMP-10 CPLX in open and closed ring shape**
 266 **conformation, and for the unprocessed BMP-10 dimer.** (A) (left) Structural model of processed
 267 BMP-10 CPLX generated by building the BMP-10 PD single-chain model on the promyostatin template
 268 (5NTU) followed by chain-by-chain alignment of the modeled PDs and the crystal structure of the
 269 BMP-10 GF to the promyostatin atomic model. (right) PD-GF interface in processed BMP-10 CPLX
 270 model. GF residues interacting with ALK-1 are accessible (marked in cyan). (B) (left) Atomic model of
 271 the unprocessed BMP-10 dimer generated by building the BMP-10 PD single-chain model on the
 272 promyostatin template (5NTU) and aligning chain-by-chain the modeled PDs and the crystal structure
 273 of the BMP-10 GF to the BMP-9 CPLX template (4YCG). (right) PD-GF interface in unprocessed
 274 BMP-10 dimer model. Access of GF residues interacting with ALK-1 is blocked (marked in red). GF
 275 residues participating in the BMP-10 GF/ALK-1 interface [45] are highlighted in yellow for both BMP-
 276 10 models. Please note that the BMP-10 signal peptide (21 aa) has been added to the BMP-10 GF amino
 277 acid positions. (C) Model of BMP-10 CPLX in closed-ring shape conformation docked to the NMR
 278 solution structure of the FUN domain of fibrillin-1 (2M74) [54]. In this conformation, the BMP-10 GF
 279 interacts with the α 1- and α 5-helices of the PD similar as in the closed-ring BMP-9 CPLX hypothetical
 280 model [6]. The generated docking model agrees with experimental results obtained after dialysis of
 281 BMP-7 CPLX with FUN of fibrillin-1 followed by TEM analysis [19]. In this model, the position of the
 282 BMP-10 PD α 2 helix is stabilized by the FUN domain thus masking the predicted type II/ endoglin
 283 receptor binding site on the BMP-10 GF (marked in orange) [45] [44]. This is different to the processed
 284 BMP-10 CPLX in open V-shape conformation where the PD can be spontaneously displaced by the
 285 type II/ endoglin receptors to gain BMP-10 GF access [5] [44] and Fig. S8.

286 Discussion

287 In this study, we present for the first time the nanoscale structures of the unprocessed BMP-10 dimer as
 288 well as the processed non-covalently associated BMP-10 PD-GF CPLX. We further show that furin
 289 processing alters the shape of BMP-10 from a latent open-arm conformation to a signaling competent
 290 tighter V-shape.

291 Our results suggest a new working model of how BMP-10 bioactivity is controlled by intra- or
 292 extracellular processing (Fig. 8). Depending on the cell type, BMP-10 may be first intracellularly
 293 processed and secreted in bioactive conformation (Fig. 8A). Thereafter, other extracellular cues may be
 294 required to control its activity. Based on our previous findings that the BMP-10 PD interacts directly
 295 with the extracellular microfibril component fibrillin-1 [24], and that the BMP-7 CPLX changes its
 296 conformation from a bioactive open V-shape into a latent, closed ring-shape upon binding to fibrillin-1

297 [19], we speculate that matrix binding may control BMP-10 activity. Indeed, our modeling results
 298 suggest that a latent ring-shape is possible in which PD displacement may be hindered due to PD
 299 interactions with fibrillin-1 (Fig. 7C, Fig. 8C). From these sequestered pools, BMP-10 GF may be
 300 liberated by proteolytic cleavage of the PD (Fig. 8C). Our previous work suggests BMP-1 [23] and
 301 matrix metalloproteinases (MMPs) such as MMP-2, -3, and -7 as likely candidates [20]. Alternatively,
 302 it is also possible that BMP-10 is secreted as latent, open-arm dimer that can be activated on the surface
 303 of target cells by extracellular PPCs (Fig. 8B).



304 **Figure 8: Model on control mechanisms of BMP-10 bioactivity.** (A) Intracellular processing of
 305 BMP-10 CPLX by furin results in the secretion of bioactive BMP-10 CPLX. (B) The secreted latent,
 306 unprocessed BMP-10 dimer undergoes processing at the cell surface of target cells leading to the
 307 generation of bioactive BMP-10 CPLX. (C) Secreted and/or circulating bioactive BMP-10 CPLXs may
 308 get targeted to the ECM via interactions of their PD with fibrillin microfibrils. Molecular modeling of

309 the BMP-10 CPLX suggests the possibility of a closed-ring shape conformation which was shown to be
310 latent for TGF- β and BMP-7.

311 We found that an N-terminal His₆-tag on the PD interferes with proper CPLX assembly. On the
312 other hand, C-terminal His₆-tag placement does not affect BMP-10 CPLX formation (Fig. S1A and B).
313 Our data even suggest that the C-terminal His₆-tag may stabilize the interaction with the GF and
314 interfere with rapid PD displacement, thereby explaining the previously reported inhibitory effect of
315 BMP-10 PD administration in C2C12 cultures [5, 23]. This effect was not only observed with C-
316 terminally His₆-tagged *E.coli*-derived BMP-10 PD lacking glycosylation, but also by using
317 commercially available (3956-BP, R&D systems) mammalian cell culture-derived BMP-10 PD [5].
318 Interestingly, R&D System reports that at a molar ratio of 1:5-19 over the GF, the mammalian cell
319 culture-derived BMP-10 PD inhibits 50 % alkaline phosphatase (ALP) production by mouse
320 preosteoblast MC3T3-E1 cells. Similar to our data, it was also reported in other studies that introduction
321 of a His₆-tag may either interfere with or promote protein-protein interaction events [39, 40].
322 Interestingly, assessing the position of the N- and C-terminal ends of the PD within our BMP-10 CPLX
323 model lends insight into why an N-terminally placed His₆-tag may interfere with the PD-GF interface
324 (Fig. S8A). Whereas the C-terminal end of the PD does not interact with the GF, an N-terminally placed
325 His₆-tag may interfere with the interaction of the α 1-helix of the PD with the GF.

326 In a physiological context, processing of BMP-10 CPLX by extracellular PPCs cleaving within
327 a lysine/arginine enriched consensus R/K-X_n-R/K↓ [7] could be a novel mechanism to regulate
328 bioavailability to different cells and tissues (Fig. 8B). Since most BMP-10 in human plasma has been
329 detected in unprocessed form [35], PPCs may convert unprocessed molecules into signaling competent
330 bioactive CPLXs in distinct endothelial subtypes or vascular beds in order to fine tune vascular
331 homeostasis. Thereby, BMP-10 may have different modes of processing by different extracellular PPCs
332 in different tissue resident cells. For example, PACE4 is activated intracellularly and exerts its function
333 within the extracellular space [41, 42]. This may also be relevant for HHT since the tissue-specific
334 availability and activity of extracellular PPCs could modify the severity of HHT by rendering distinct
335 tissues more prone for AVM development due to misbalanced BMP-10 signaling. Therefore, a
336 comprehensive screen to identify the tissue specific expression patterns of extracellular PPCs may be

337 informative to predict in which tissues AVMs will more likely develop. Moreover, furin-mediated
338 processing of BMP-10 may also play a role in hepatocellular carcinoma (HCC), which may be caused
339 by liver-specific inactivation of furin [43] and may be suppressed by administration of BMP-10 [31].

340 Furin processing converts the latent BMP-10 dimer into a signaling competent BMP-10 CPLX
341 that, at the EC_{50} for the GF, was even more bioactive than the free GF towards HUVEC (~2.4-fold) and
342 C2C12 cells (~6.7-fold) (Fig. 3). This suggests that the presence of the PD at the physiological relevant
343 2:1 ratio with GF may enhance proper targeting to the receptors via interactions with unknown cell
344 surface molecules. For example, both HUVEC and C2C12 express the co-receptor, endoglin (ENG) (A.
345 Anbalagan and B. Roman, data not shown). We speculate that ENG association with the BMP-10 PD
346 may be involved in accelerated CPLX recruitment or enhanced positioning towards cellular BMP
347 signaling receptor complexes. ENG has a high affinity binding site for BMP-9 GF that is also conserved
348 in the BMP-10 GF sequence [44], and is able to displace the BMP-9 PD [45]. According to our
349 structural model of processed BMP-10 CPLX, ENG binding to the GF would also likely lead to PD
350 displacement, as the predicted ENG binding region and the PD interaction site overlap on the BMP-10
351 GF (Fig. S8B). Interestingly, the residues identified to mediate ENG binding significantly differ in
352 BMPs that either fail to bind ENG or interact only weakly [46, 47]. This may explain our findings that
353 the bioactivity of BMP-10 and BMP-7 CPLXs significantly differs in C2C12 cells (Fig. 3 and [18]).
354 Moreover, C2C12 cells may express lower ALK-1 levels than HUVECs which will result in a
355 requirement of higher ligand concentrations for the activation of a different type I receptor. At higher
356 required BMP-10 concentrations, the presence of the PD in the BMP-10 CPLX may enhance signaling
357 further compared to the GF only treatment in C2C12 versus HUVEC cells (Fig. 3), since it may prolong
358 the GF in bioactive state and enhance spatial concentration on the cell surface.

359 Single particle transmission electron microscopy followed by molecular docking of
360 representative published atomic models with different angles between the PD arms revealed that the
361 processed, bioactive BMP-10 CPLX generated in HEK293 cells assumes a V-shape (Fig. 5 and S4) with
362 smaller angle than the widened conformation characteristic of the processed BMP-9 CPLX [6]. This
363 confirms a recent report of an open-arm conformation of the unprocessed BMP-10 dimer in which the
364 furin site was mutationally inactivated [48]. However, in this study the unprocessed BMP-10 dimer was

365 termed “non-latent” without showing any experimental proof of its bioactivity [48]. Also in the same
366 study, an atomic model was generated based on the BMP-9 CPLX structure [48]. In the processed
367 BMP-9 CPLX, a unique PD-GF interface was described in which the C-terminally located $\alpha 5$ -helix of
368 the PD interacts with the GF [6]. However, this PD-GF interface is different from all other structurally
369 studied CPLXs, in which the N-terminally located $\alpha 1$ -helix of the PD is required to maintain strong
370 interactions with the GF. Such a PD-GF interface was found for proactivin [36], promyostatin [12, 38],
371 TGF- β [11, 37], and was also functionally tested by us for BMP-7, previously [19]. Our previous
372 interaction studies illustrated a strong PD-GF interface for BMP-7, promyostatin, and BMP-10 with
373 binding affinities in the low nanomolar range (7-20 nM) [19, 23]. However, the strength of the PD-GF
374 interaction for BMP-9 was measured to be two orders of magnitude lower (0.8 μ M) [6] than for BMP-
375 10 (7 nM) [23]. This suggests a less stable PD-GF interface for the processed BMP-9 CPLX and
376 therefore reduced CPLX stability compared to the processed BMP-10 CPLX. In the atomic model of
377 processed BMP-10 based on the BMP-9 CPLX structure, the PD-GF interface is compromised with less
378 predicted interactions compared to that of the BMP-9 CPLX (Fig. S5, 6). This disagrees with a high PD-
379 GF affinity for BMP-10 [23] and stable BMP-10 CPLX reconstitution even in the presence of 0.8 M
380 urea (Fig. S1A, B). We therefore favor our model based on the promyostatin structure which was guided
381 by the best fitting results to the determined EM envelope of the processed, bioactive BMP-10 CPLX
382 (Fig. 7A). In this model, the PD-GF interface is mediated by interactions of the $\alpha 1$ -helix of the PD with
383 the GF (Fig. 7A, Fig. S6C).

384 Since the $\alpha 1$ -helix in the BMP-9 PD is not present in the crystal structure of the processed
385 BMP-9 CPLX, it is still possible that an additional interaction with the $\alpha 1$ -helix of the PD occurs as
386 already previously suggested [6]. Also, in a modeled closed conformation of the BMP-9 CPLX both the
387 $\alpha 1$ - and the $\alpha 5$ -helices interact with the GF [6]. In the closed-ring model generated for BMP-10 CPLX,
388 we obtained coverage for both $\alpha 1$ - and $\alpha 5$ -helices of the PD that seem to interact with the BMP-10 GF.
389 Therefore, it is plausible that PD interactions with ECM proteins such as fibrillin-1 help to preserve the
390 closed ring-shape conformation in which both the $\alpha 1$ - and $\alpha 5$ -helices interact with the GF and thereby
391 inhibit PD displacement and confer latency.

392 To better understand how GF latency is maintained in the unprocessed BMP-10 (Fig. 3), we
393 generated a model of the unprocessed BMP-10 dimer. We built the BMP-10 PD model on the
394 promyostatin crystal structure followed by chain-by-chain alignment of the modeled PDs to the BMP-9
395 CPLX structure (Fig. 7B). Visualization of the BMP-10 GF crystal structure aligned chain-by-chain on
396 the BMP-9 GF of the BMP-9 CPLX crystal in this model of the latent dimer (Fig. 7B) showed that the
397 PD α 1-helix provides steric hindrance to the α 3-helix of BMP-10 GF so that crucial GF residues
398 required for ALK-1 binding are no longer accessible. This agrees with SPR binding studies of the
399 unprocessed, latent BMP-9 dimer to the immobilized ALK-1 receptor showing a profound reduction in
400 affinity in comparison to the processed, bioactive BMP-9 CPLX or bioactive BMP-9 GF [17].
401 Furthermore, the covalent PD-GF linkage in the unprocessed BMP-10 dimer makes PD displacement by
402 BMP type II receptors and ENG impossible [5, 44]. In agreement with this, also unprocessed, latent
403 BMP-9 failed to associate to the immobilized type II receptors in SPR binding studies [17]. However, in
404 the PD-GF interface of the processed, bioactive BMP-10 CPLX, GF residues are accessible for ALK-1
405 binding (Fig. 7A) and PD displacement upon receptor engagement with the GF is possible.

406 Interestingly, our finding that processing of the latent BMP-10 dimer results in a smaller angle
407 between the PD arms in the bioactive CPLX was also previously reported for proactivin [36]. However,
408 GDF-8 appears to be latent after processing and does not change its V-shape conformation [12]. Further
409 proteolytic processing of the PD at the inhibitory α 2-helix renders the CPLX in a conformation that is
410 primed to be bioactive [9]. The fact that latency persists in the processed myostatin CPLX suggests that
411 receptor binding sites on the GF are still not accessible. This may be caused by a GF conformation
412 within the myostatin CPLX that is not signaling-competent. Interestingly, by assessing different
413 myostatin structures, we observed that the angle between myostatin GF monomers of the dimer in free,
414 bioactive (PDB: 5J11) [49] or PD-complexed (PDB: 5NTU) [12] conformation differs by about 50
415 degrees. This suggests that the PD serves as a molecular clamp that wedges the GF into an inactive
416 conformation. The clamp still persists after processing, but is primed for disintegration or receptor
417 mediated displacement after subsequent PD degradation [9, 38]. This is different to BMP-7, -9, -10
418 CPLXs for which type II receptor mediated PD displacement without PD cleavage could be
419 demonstrated [5, 17, 18]. It can therefore be assumed that GF dimers in CPLXs with displaceable PDs

420 are already in signaling-competent conformations. Indeed, by comparing the conformations of the
421 BMP-9 GF dimer when free (PDB: 1ZKZ) [3], PD-complexed (PDB: 4YCI) [6], bound to ENG (PDB:
422 5HZW) [44], or ALK1 (PDB: 6SF2) [45] no angle difference between the two monomers of the GF
423 dimer can be observed. Based on these considerations we conclude that the angle change between the
424 PD arms upon BMP-10 processing occurs due to PD rearrangement, thereby allowing access of type I
425 receptor binding sites on the GF and simultaneously priming the PD for displacement.

426 Overall, our data provide new insight into the molecular requirements for BMP-10 CPLX
427 bioactivity. Therefore, our findings may inform development of new therapeutics for BMP-10-
428 associated diseases like HHT and cancer.

429 **Experimental procedures**

430 *Antibodies and proteins*

431 For western blot and sandwich ELISAs the following antibodies were used: anti-His₆-HRP (130-092-
432 785, Miltenyi Biotec, Germany), goat anti-human BMP-10 propeptide (AF3956-SP, R&D Systems,
433 Minneapolis, MN, USA), mouse anti-human BMP-10 GF (MAB2926, R&D Systems), rabbit anti-
434 human phospho-Smad 1/5/9 (13820, Cell Signaling Technology, Danvers, MA, USA), and mouse anti-
435 rabbit GAPDH (ab8245, Abcam, Cambridge, UK). Recombinant BMP-10 GF was kindly provided by
436 Andrew Hinck (Structural Biology, University of Pittsburgh).

437 *Expression constructs*

438 The cDNA sequences coding for the human BMP-10 I314S/R315I variant with N-terminal His₆-tag, full
439 length BMP-10 with N-terminal His₆-tag, and full length tag-free BMP-10 were generated by gene
440 synthesis (Genewiz, South Plainfield, NJ, USA), and cloned via NheI/ BamHI sites into a pCEP-Pu
441 vector containing the signal peptide of BM40 [2].

442 *Cell culture*

443 HEK293 EBNA cells were cultivated in DMEM GlutaMAX media (31966047, Thermo Fisher
444 Scientific, Waltham, MA, USA) supplemented with 10% fetal bovine serum (FBS; F7524-500ML,

445 Merck, Germany) and 1% penicillin-streptomycin (Pen/ Strep) (15140-130, Life technologies, Carlsbad,
446 CA, USA). HUVECs (C-12208, PromoCell, Heidelberg, Germany) were cultured in complete
447 endothelial cell growth medium 2 (EGM-2, C-22111, PromoCell, Heidelberg, Germany) containing 2%
448 FBS. C2C12 cells were cultured in DMEM (D5796, Sigma-Aldrich, St. Luis, USA) supplemented with
449 10% FBS (A3160401, Gibco, Massachusetts, USA) and antibiotic/antimycotic solution (SV30079.01,
450 HyClone, Logan, UT, USA). All cells were maintained at 37°C in a 5% CO₂, humidified incubator
451 under sterile conditions.

452 *Transient transfections and protein precipitation*

453 cDNA constructs were transfected in HEK293 EBNA cells (Portland, Oregon, USA) at 60% confluency
454 in duplicates in 6-well plates (3516, Corning Costar, Corning, NY, USA) using the Fugene®
455 transfection reagent (E2312, Promega, Madison, USA) according to the protocol provided by the
456 manufacturer at a ratio of 3 µl FuGENE® to 1 µg DNA. After 24 h of incubation, the
457 FuGENE®/vector-containing medium was exchanged for serum-free DMEM high glucose medium
458 containing 1% v/v Pen/ Strep. 2 ml of media was collected after 24 h in the serum-free DMEM and
459 TCA-precipitated. Protein pellet was resuspended in 8 M ultrapure urea, 1 M NaCl in 20 mM NaH₂PO₄
460 × 2H₂O, pH = 7.4 after 2 × ice-cold acetone washes.

461 *Protein expression and purification*

462 The BMP-7 CPLX over-expressing clone 77 (Portland, Oregon, USA) was propagated in 250 µg/ml
463 geneticin without Pen/ Strep. Next, BMP-7 CPLX from media collected at 48 h serum-free was purified
464 as previously described [2, 19]. The His₆-tagged BMP-10 I314S/R315I mutant, the BMP-10 tag-free
465 and the His₆-tagged BMP-10 constructs were all transfected into HEK293 EBNA cells grown in 6-well
466 plates at 75% confluency using Fugene® according to the protocol provided by the manufacturer at a
467 ratio of 3 µl FuGENE® to 1 µg DNA. Cells were grown into triple flasks in DMEM supplemented with
468 10% v/v FBS, 1% v/v Pen/ Strep under 0.5 µg/mL puromycin selection (P7255, Sigma-Aldrich, St.
469 Luis, USA) at 85% confluency. For purification of His₆-tagged BMP-10 variants, typically 500 mL of
470 conditioned media were filtered, pH adjusted to 7.4 and subjected to Ni-NTA affinity chromatography

471 (74105, PureCube 100 Ni-NTA Agarose, Cube Biotech, Germany). Elution fractions contained 5 - 250
472 mM imidazole concentration in 1 M NaCl, 20 mM NaH₂PO₄ × 2 H₂O, pH = 7.4. The purification of tag-
473 free BMP-10 CPLX was already described elsewhere [5]. A revised version of that protocol was
474 followed in this study: Briefly, half liter of media was filtered and adjusted to pH=7.6 and condensed
475 over a HiTrap Q HP column (29051325, Cytiva, Marlborough, MA, USA). The column was washed
476 with 20 mM Tris-HCl, pH=7.6 and additionally with 100 mM NaCl, 20 mM Tris-HCl, pH 7.6 until the
477 column wash came out transparent. Next, elution took place at a gradient of NaCl for 100 fractions from
478 100 mM NaCl to 2M NaCl in buffer: 20 mM Tris-HCl, pH 7.6. The fraction containing BMP-10 was
479 subjected to heparin affinity chromatography over a HiTrap heparin HP column (17040601, Cytiva,
480 Marlborough, MA, USA) using the binding buffer: 150 mM NaCl, 20 mM NaH₂PO₄ × 2H₂O, pH=7.4 to
481 remove contaminating peptides. Heparin flow through was condensed over HiTrap Q a second time and
482 gradient elution took place for another 100 fractions as described previously using same buffers.
483 Detailed NaCl gradient elution protocol used for the previously described runs is provided in the
484 “Established protocols to study Bone Morphogenetic proteins” section of the materials and methods part
485 of this thesis. The fraction containing the pure BMP-10 was subjected to size exclusion chromatography
486 using a superose 12 10/300 GL column (GE17-5173-01, Cytiva, Marlborough, MA, USA) and the
487 buffer: 1M NaCl, 20 mM NaH₂PO₄ × 2H₂O, pH=7.4. Full length protein of the human BMP-10 PD
488 sequence with a C-terminal his₆-tag was expressed in *E.coli* BL21-CodonPlus Competent Cells (Agilent
489 Technologies, Santa Clara, CA, USA) and purified by Ni-NTA affinity chromatography similarly to
490 *E.coli*-derived BMP-7 PD [50].

491 *Reconstitution assays*

492 BMP-10 PD and GF (C-67317, Promocell) were placed in a microcentrifuge tube at a molar ratio 2 PD:
493 1 GF in 20 mM HEPES, 0.8 M urea, pH=7.4 using 0.1% BSA as carrier and allowed to reconstitute in
494 the presence of 2% casein with mild shaking at RT for 1.5 h. In a different experimental setup, BMP-10
495 PD and GF (2926-BP-025/CF, R&D Systems) were placed in a mini dialysis device with a 2 kDa cut-
496 off (69553, Thermo Fisher Scientific, Waltham, MA, USA) at a molar ratio 3 PD: 1 GF in presence of
497 0.1% BSA and dialyzed stepwise into 4M, 2M, 1M urea in 1 × PBS and plain 1 × PBS for 4 h per

498 dialysis step before an overnight dialysis into plain $1 \times$ PBS in the cold. Next, the reconstituted material
499 was subjected to size exclusion chromatography (SEC) on a superose 12 column in 1M NaCl, 20 mM
500 $\text{NaH}_2\text{PO}_4 \times 2 \text{H}_2\text{O}$, pH=7.4 buffer to separate the PD-GF species from aggregated material or the PD
501 dimer. Same dialysis procedure and SEC of a PD sample without addition of GF served as a control.

502 *Sandwich ELISA*

503 Sandwich ELISA assays were performed as described previously. Complex formation after
504 reconstitution was assessed by sandwich ELISA using the mouse monoclonal BMP-10 GF antibody as
505 capture and the goat polyclonal BMP-10 PD antibody as detector. The capture antibody was coated at 4
506 $\mu\text{g}/\text{ml}$ to Nunc MaxiSorp flat-bottom 96-well plates (735-0083, VWR, Germany) in $1 \times$ PBS overnight
507 in the cold. Coated surfaces were blocked in 5% casein in 20 mM HEPES, pH=7.4 for 1h at RT after 5
508 \times washes with 20 mM HEPES, pH=7.4. Incubation of the reconstituted material in 2% casein in 20 mM
509 HEPES, pH=7.4 for 2h at RT followed and wells were washed 5 \times with 20 mM HEPES, pH=7.4,
510 followed by consecutive 1h incubations of detector and secondary antibodies in 2% casein in 20 mM
511 HEPES, pH=7.4 at RT. Between antibody incubations, plate was washed 5 \times with 20 mM HEPES,
512 pH=7.4. Signal was developed by adding 50 μlit 1-step ultra TMB ELISA (34028, Thermo Fisher
513 Scientific, MA, USA), reaction was quenched by adding 50 μlit 10% sulfuric acid and OD measured at
514 450 nm. All washing steps were performed by adding 200 μlit of solution per well, antibody incubation
515 steps were performed by adding 100 μlit of solution per well whereas reconstituted material was added
516 at 50 μlit per well.

517 *Stimulation assays with HUVEC and C2C12 cells*

518 Cells were seeded in 6-well plates and grown for two days to 90% confluency. HUVECs (passage 4-6)
519 were serum-deprived for 4 h in 0.2% FBS-supplemented endothelial cell basal medium 2 (EBM-2; C-
520 22211, PromoCell) and treated for 45 minutes with 50 or 250 pg/mL growth factor equivalents of
521 BMP10 GF, unprocessed BMP10 dimer (BMP-10 I314S/R315I), processed BMP10 CPLX, or EBM2 +
522 0.2% FBS. C2C12 cells were serum-deprived for 4 h in 0.2% FBS-supplemented DMEM and treated
523 for 45 minutes with 4 or 20 ng/ml GF equivalents of BMP10 GF, unprocessed BMP10 dimer (BMP-10

524 I314S/R315I), processed BMP10 CPLX, or 0.2% FBS + DMEM. In each experiment, treatments were
525 applied in duplicate, and experiments were repeated 3 times.

526 *Dot blot analysis*

527 To examine the relevant fractions of reconstituted BMP-10 CPLX after SEC for concurrent
528 presence of BMP-10 PD and GF, fractions 17-33 were dot blotted on a nitrocellulose membrane, 0.45
529 μm (10600002, VWR, Radnor, PA, USA), blocked with 5% milk in $1 \times$ TBS for 1h at RT and blotted
530 with the goat polyclonal BMP-10 PD primary antibody or the mouse monoclonal primary BMP-10 GF
531 antibody for 1h at RT in 2% milk/ $1 \times$ TBS. After $3 \times$ washes with $1 \times$ TBS-Tween, anti-goat or anti-
532 mouse secondary antibody incubation followed in 2% milk/ $1 \times$ TBS for 1h at RT. After $3 \times$ washes
533 with $1 \times$ TBS-Tween, signal was developed with the Bio-Rad Opti 4CN Substrate kit (1708235, Bio-
534 Rad, Hercules, CA, USA). The intensity of obtained signals was determined by employing ImageJ. All
535 washing steps were performed for 10 min.

536 *Western blotting*

537 HUVEC or C2C12 cells were lysed in RIPA buffer (89900, Thermo Fisher Scientific) with Halt
538 Protease and Phosphatase Inhibitor Cocktail (78440, Thermo Fisher Scientific, MA, USA) and frozen at
539 -80°C . Just before use, thawed samples were sonicated and centrifuged. Cleared supernatants were
540 collected and the protein concentrations were determined by Pierce BCA Protein Assay (23227, Thermo
541 Fisher Scientific, MA, USA). Ten micrograms of protein was separated by 10% reducing SDS-PAGE
542 and transferred to nitrocellulose membrane (1620115, Bio-Rad, München, Germany). Membranes were
543 dried for 1 h, rehydrated in water, and blocked in Intercept (TBS) Blocking Buffer (92760001, LI-COR,
544 Lincoln, NE, USA) for 1 h. Antibodies were diluted in blocking buffer with 0.1% Tween 20.
545 Membranes were probed with a 1:1000 dilution of rabbit phospho-Smad 1/5/9 antibody overnight at
546 4°C and a 1:10,000 dilution of mouse GAPDH antibody for 1 h at room temperature the following day.
547 Membranes were washed in TBS-Tween and probed with 1:12,000 dilutions of IRDye 800CW donkey
548 anti-rabbit IgG (925-32213, LI-COR, Lincoln, NE, USA) and IRDye 680LT goat anti-mouse IgG (926-
549 68020, LI-COR, Lincoln, NE, USA) secondary antibodies for 1 h at room temperature, protected from

550 light. Membranes were washed with TBS-Tween while protected from light and imaged using the
551 Odyssey CLx Imaging System (LI-COR). pSMAD1/5/9 intensities were measured using Image Studio
552 5.2 software (LI-COR) and normalized to GAPDH, according to manufacturer's instructions. The
553 normalized signal values were then averaged for the technical replicates and divided by the 0.2% FBS
554 media control value to determine the fold-change for each condition. This fold-change was then graphed
555 for each condition across each of three independent assays using GraphPad Prism 8 (San Diego, CA,
556 USA).

557 To evaluate the inhibition of intracellular furin processing, equal protein amounts of untagged
558 BMP-10 or BMP-10 I314S/R315I were subjected to SDS-PAGE using 15 % gels, followed by western
559 blot transfer to nitrocellulose membrane in 10 mM di-sodium-tetraborate-decahydrate buffer (131644,
560 AppliChem, Darmstadt, Germany). Membrane was blocked with 5 % milk in 1 × TBS overnight in the
561 cold and next the polyclonal goat BMP-10 PD primary antibody was applied overnight in 2 % milk in 1
562 × TBS in the cold. After 5 × washes with 1 × TBS, the anti-goat secondary was applied in 2% milk in 1
563 × TBS for 1h at RT and signals were developed with the Bio-Rad Opti 4CN Substrate kit after 5 ×
564 washes with 1 × TBS. Same procedure was followed to assess BMP-7 processing in HEK293 cell
565 lysates and cell culture supernatants. In that case, the monoclonal mouse anti-BMP-7 PD mab2 and
566 mab33 primary antibodies were applied in 1:1000 in "1-1" mixture in 2% milk/ 1x TBS O/N in the cold
567 followed by 5x washes with 1x TBS and incubation of anti-mouse secondary in 2% milk/ 1x TBS for 1h
568 at RT. Detection was with the Bio-Rad Opti 4CN Substrate kit after 5 × washes with 1 × TBS. All
569 washing steps were performed for 10 min.

570 *Statistical analysis*

571 For quantitative Western blot, *t*-tests were performed using GraphPad Prism 8.

572 *Single particle transmission electron microscopy*

573 His-tagged BMP-10 dimer was concentrated over a Q HP column and purified further over an s200i
574 column twice in 1M NaCl, in 1 × PBS pH=7.4. The peak fraction was then used to prepare negative
575 stain EM grids as described in [20]. All images were collected on a Talos L120C G2 TEM at 120 keV at

576 57,000 × magnification with a 1 second exposure at ~ -1 μm defocus on a Ceta 16M Camera.
577 Automated particle picking using a circular template with a Gaussian drop off “blob picker” picked
578 16125 particles between 100-200 Å in size. 2D classification excluded poor quality particles. 9181
579 particles were selected and used to generate ab initio models. 2D class images of good quality classes
580 were then used as templates for template-based particle picking. 87068 particles were picked with that
581 approach and were 2D-classified to exclude poor quality classes. 43320 particles were used to refine the
582 best 3D ab initio model. To obtain class averages of the processed BMP-10 CPLX, the sample was
583 diluted 1:10 in buffer: 1M NaCl 20 mM NaH₂PO₄, pH=7.4 before adsorption to negative stain EM
584 grids. The same automated particle picking technique picked 25205 particles sized 100-200 Å. Three
585 rounds of 2D classification excluded poor quality particles and BMP-10 PD dimers. 9181 particles were
586 selected and used to generate the ab initio models which were used as starting models for 3D
587 classification of the full particle set. The structure and specific particle set from 3D classification was
588 used for further 3D refinement. Particles were picked and processed with the cryosparc software.

589 *Cryo transmission electron microscopy*

590 His₆-tagged BMP-10 unprocessed dimer was concentrated to 0.5 mg/ml and 3 μl applied to a Copper
591 Quantifoil R1.2/1.3 grid and blotted for 3 seconds using a vitrobot. Images were collected on a Glacios
592 Cryo Transmission Electron Microscope at 200 keV at 190,000 x magnification (0.77Å/pixel) using a
593 Falcon III detector in counting mode. 4796 movies were collected and 291000 particles were picked
594 using crYOLO neural network and 2D classified. Particles were used for 3D reconstruction and 3D
595 classification. Particle picking and processing was performed with the cryosparc software.

596 *Molecular docking*

597 To understand which atomic model describes best the structures of the unprocessed BMP-10 dimer and
598 the processed bioactive BMP-10 CPLX, the templates of the unprocessed pro-activin (PDB code:
599 5HLY), the processed pro-activin (PDB code: 5HLZ), the BMP-9 CPLX (PDB code: 4YCG), the
600 unprocessed pro-myostatin (PDB code: 5NTU) and the TGF-β (PDB code: 3RJR) were docked into the
601 EM envelopes of the unprocessed BMP-10 dimer and the processed BMP-10 CPLX. To assess the

602 validity of the performed molecular fits, the parameters “correlation”, “average” and “inside” were
603 measured for each docking experiment. “Correlation” is the cross-correlation score between the model
604 and the density. “Average” is the average map value at fit atom positions and “inside” is the proportions
605 of fit atoms inside the reference map contour surface. All *in silico* experiments were performed using
606 the UCSF Chimera software.

607 *Molecular modeling*

608 The structure of the activated human furin (PDB: 4RYD) [51] was visualized using the UCSF chimera
609 software [52] together with the tetrabasic inhibitor MI-1148 that resides at the negatively-charged
610 catalytic cleft of the enzyme. To understand the potential effect of the elimination of the positive charge
611 (arginine) in P2 position for furin processing, the arginine in the respective position was switched to the
612 isoleucine to mimic the BMP-7 PPC cleavage site using the “swapaa” command of the UCSF chimera
613 software.

614 To generate the unprocessed BMP-10 dimer model, the BMP-10 precursor single chain model
615 was built on the promyostatin crystal structure (PDB: 5NTU) [12] using the swiss model server [53].
616 Next, the BMP-10 precursor single chain model was aligned to the BMP-10 PD of a BMP-10 CPLX
617 model that was built on and aligned to the BMP-9 CPLX crystal structure (PDB: 4YCG) [6]. Next, the
618 BMP-10 PDs of the BMP-10 CPLX model that were built on and aligned chain-by-chain to the BMP-9
619 CPLX crystal structure were hidden, the GF of the BMP-10 precursor model built on promyostatin was
620 hidden, and the BMP-10 GF (PDB: 6SF3, with the receptor deleted) [45] that was aligned chain-by-
621 chain to the BMP-9 GF of the BMP-9 CPLX template was visualized. The resulting model constituted
622 of the modeled BMP-10 PDs of the BMP-10 precursor (built on promyostatin) and the crystal structure
623 of the BMP-10 GF. This approach ensured that the angle between PD arms in the unprocessed BMP-10
624 dimer is similar to that found in the atomic model of the processed BMP-9 CPLX, which gave the best
625 molecular fit to the EM envelope of the unprocessed BMP-10 dimer.

626 To generate the V-shaped model of the processed bioactive BMP-10 CPLX, the BMP-10 PD
627 single chain model was built on the promyostatin crystal structure using the swiss model server, and
628 modeled PDs were aligned chain-by-chain to the promyostatin template. The BMP-10 GF crystal

629 structure (PDB: 6SF3, with the receptor deleted) was also aligned chain-by-chain again to the
630 promyostatin template. The promyostatin template was hidden to visualize the resulting model.

631 To generate the closed-ring model of BMP-10, the BMP-10 precursor single chain model was
632 built on the proTGF- β crystal structure (PDB: 5VQF) [11] using the swiss model server, and was
633 subsequently aligned chain-by-chain to the closed-ring model of the BMP-7 CPLX [20]. The closed-
634 ring BMP-7 CPLX model was hidden to visualize the resulting closed-ring BMP-10 CPLX model. For
635 the generation of the BMP-10 GF/ ENG interaction model the BMP-9 GF/ ENG interaction model
636 (PDB: 5HZW) was unified in a single file. Using the processed BMP-10 CPLX model, the BMP-9 GF/
637 ENG single model was overlaid on the BMP-10 GF, the BMP-9 GF was hidden and the five crucial
638 residues of the BMP-10 GF were highlighted. To generate the model of the processed BMP-10 using the
639 atomic models of BMP-9 CPLX and promyostatin as templates, the BMP-10 PD single chain model
640 was built on the crystal structure of the BMP-9 PD of the BMP-9 CPLX atomic model. Next, the
641 modeled BMP-10 PDs and the BMP-10 GF crystal structure (PDB: 6SF3, with the receptor deleted)
642 were aligned chain-by-chain to the promyostatin template. The promyostatin template was hidden to
643 visualize the resulting model.

644 Sequence coverage for all models is provided in Fig. S7. All model manipulations were
645 performed with the UCSF Chimera software unless indicated otherwise. All chain-by-chain alignments
646 between models were performed using the “MatchMaker” tool of the same software.

647 **Acknowledgments**

648 We thank Marina Tauber (University of Cologne) and Teresa Rosato (University of Pittsburgh) for
649 excellent technical assistance. We also thank staff of The University of Manchester EM Core Facility
650 (RRID:SCR_021147) for their assistance and BBSRC for funding the Glacios cryoEM
651 (BB/T017643/1). Further, we are grateful to Andrew Hinck (Structural Biology, University of
652 Pittsburgh) for providing recombinant BMP-10 GF protein. Funding for this study was provided by the
653 Deutsche Forschungsgemeinschaft (DFG, German Research Foundation) project number 73111208
654 (SFB 829/B12) and 397484323 (TRR259/B09) to G.S. and NIH R01 HL133009 to B.L.R. The

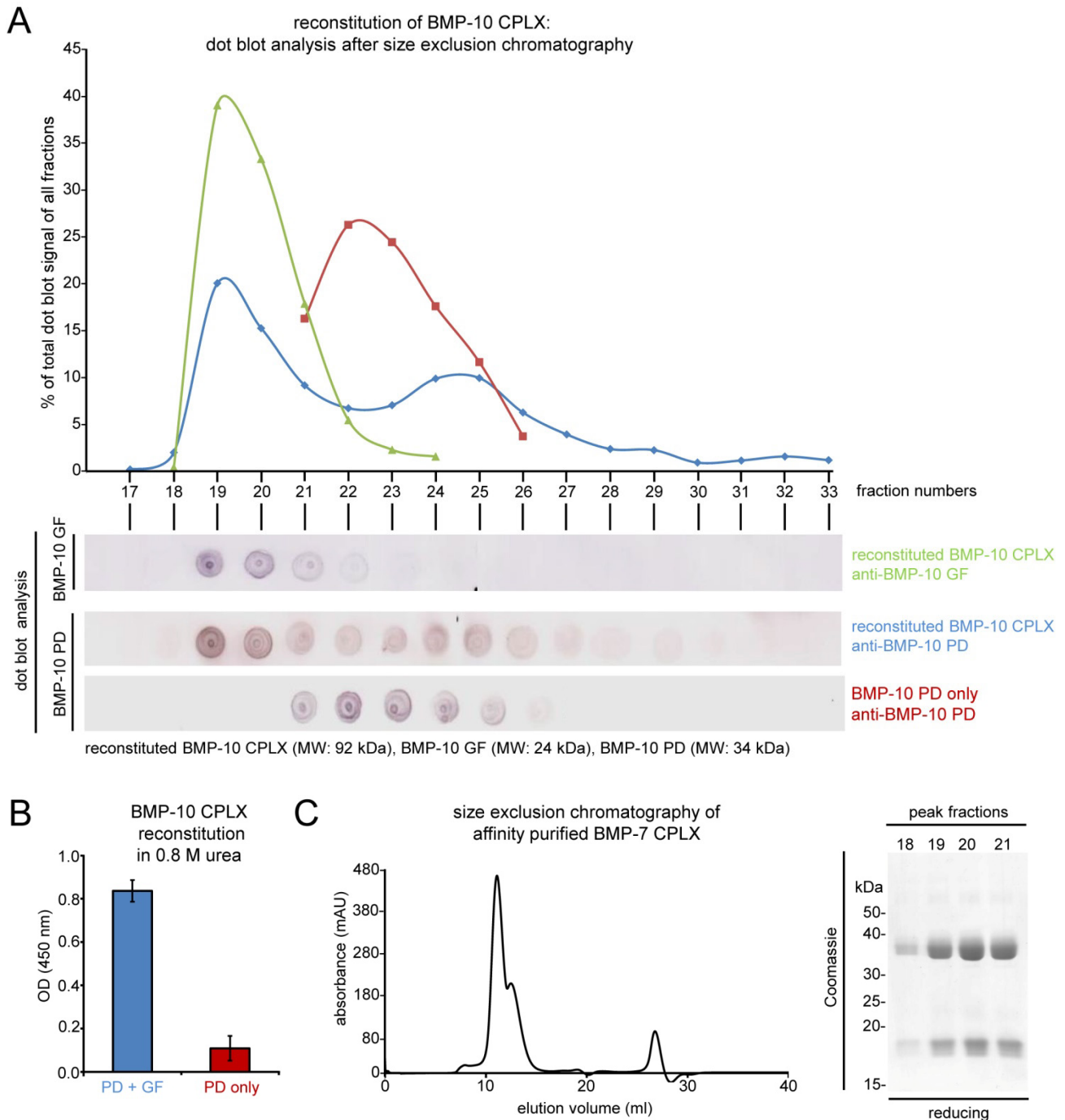
655 Wellcome Centre for Cell-Matrix Research is supported by funding from the Wellcome Trust
656 (203128/Z/16/Z). A.R.F.G. is supported by BBSRC funding (Ref: BB/S015779/1). Molecular graphics
657 and analyses were performed with the UCSF Chimera package. Chimera was developed by the
658 Resource for Biocomputing, Visualization, and Informatics at the University of California (San
659 Francisco, CA) (supported by NIGMS, National Institutes of Health, Grant P41-GM103311).

660 **Author contribution statement**

661 C.E.S.S. and G.S. conceived the study. C.E.S.S., A.R.F.G., S.M., A.A., A.P.W. performed research and
662 analyzed data. A.R.F.G., and C.B. conducted and evaluated EM analysis. S.M., A.A., and B.L.R.,
663 designed, performed, and evaluated bioactivity assays. B.L.R. and C.B. provided expert advice and
664 edited the manuscript. C.E.S.S., and G.S. wrote and edited the manuscript. B.L.R., C.B., and G.S.
665 acquired funding for this study.

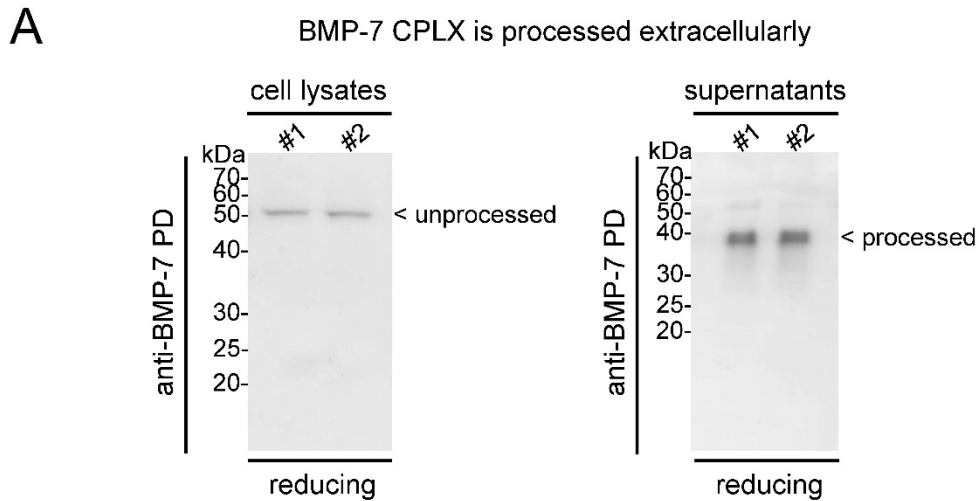
666 **Conflict of interest**

667 The authors declare no conflict of interest.

668 **Supplementary material**

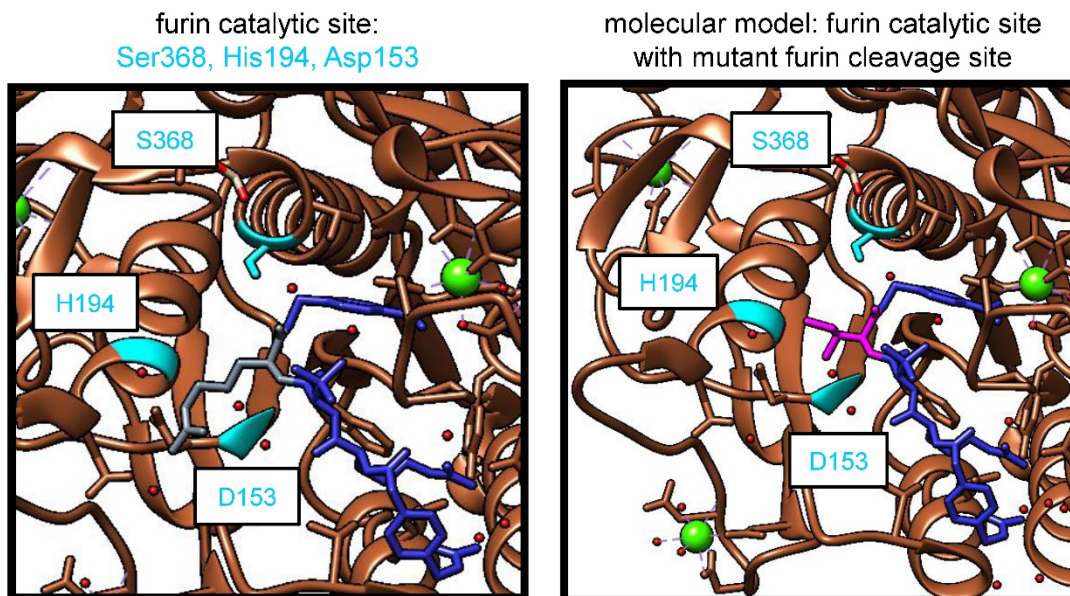
669 **Figure S1: Reconstitution of BMP-10 CPLX by dialyzation of C-terminally His6-tagged PD (*E***
 670 ***coli*. expressed) together with GF dimer (commercially available, overexpressed in HEK293 cell**
 671 **culture). (A) Dot blot analysis of size exclusion chromatography (SEC) elution fractions after**
 672 **reconstitution (molar ratio PD:GF at 3:1) showed presence of reconstituted BMP-10 CPLX in fractions**
 673 **19-21 as indicated by parallel detection of BMP-10 PD and GF signals. SEC of purified BMP-10 PD**
 674 **only served as reference. (B) Sandwich ELISA detection of reconstituted BMP-10 CPLX (in HEPES**

675 buffer/ 0.8 M urea in presence of 0.1% BSA) using anti-BMP-10 GF antibody as capture and anti-BMP-
 676 10 PD antibody as detector. (C) SEC of BMP-7 CPLX after affinity purification. (left) Elution fractions
 677 showed highest absorbance in peak fractions around 11 ml. (right) SDS-PAGE analysis (reducing
 678 conditions) of peak fractions followed by Coomassie staining



B

	P5	P4	P3	P2	P1	
furin cleavage consensus:		R	X	R/K	R	X
modeled inhibitor sequence:	X	R	X	R	X	
BMP-10 furin site:		R	I	R	R	X
BMP-7 PPC site:		R	S	I	R	X



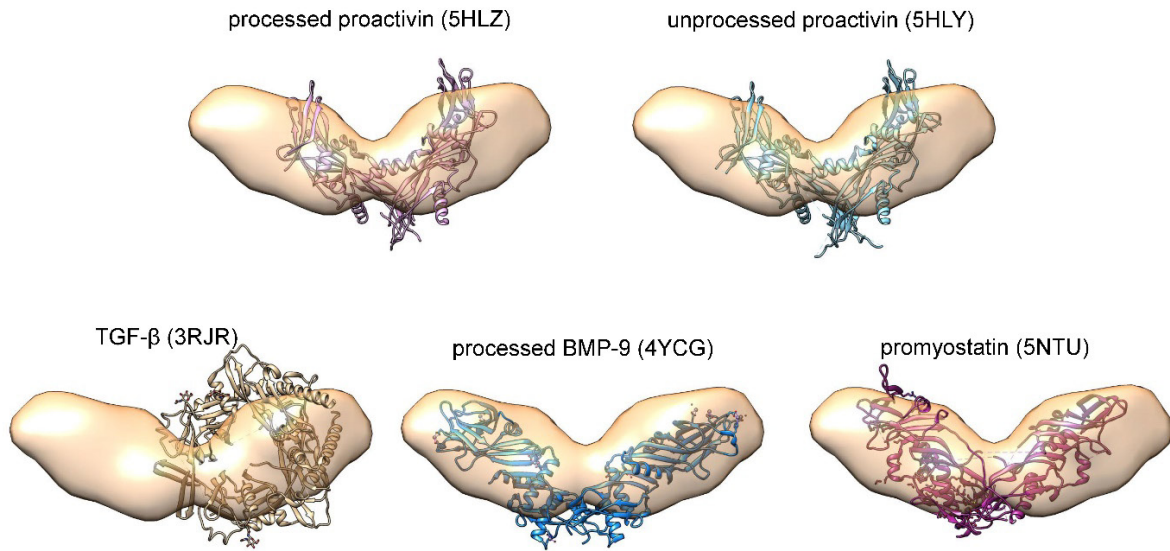
679 **Figure S2: Extracellular processing of BMP-7 CPLX and modeling of BMP-7 RSIR cleavage site at**
 680 **furin catalytic site.** (A) Transfection of HEK293 cells with full length BMP-7 CPLX construct shows
 681 extracellular processing of BMP-7 PD. Western blot analysis of cell lysates and conditioned media was
 682 performed with monoclonal anti-BMP-7 PD mab2 and mab33 (1:1 mixture). (B) (top) PPC cleavage sites
 683 of BMP-10 and BMP-7 together with consensus and modeled inhibitor sequence. (bottom, left)
 684 Visualization of human furin (PDB code: 4RYD) in ribbon representation (brown) together with the
 685 tetrabasic inhibitor MI-1148 (19) highlighted in blue with the P2 position (Arg) of the furin cleavage
 686 consensus shown in grey. The negatively-charged catalytic triad (Ser368, His194, Asp153) of the furin
 687 enzyme is depicted in cyan. (bottom, right) Same structure is visualized but arginine in P2 position of the
 688 inhibitor is switched into isoleucine (magenta) to mimic the BMP-7 PPC cleavage site.



689 **Figure S3: Cryo-TEM analysis of unprocessed BMP-10 dimer.**

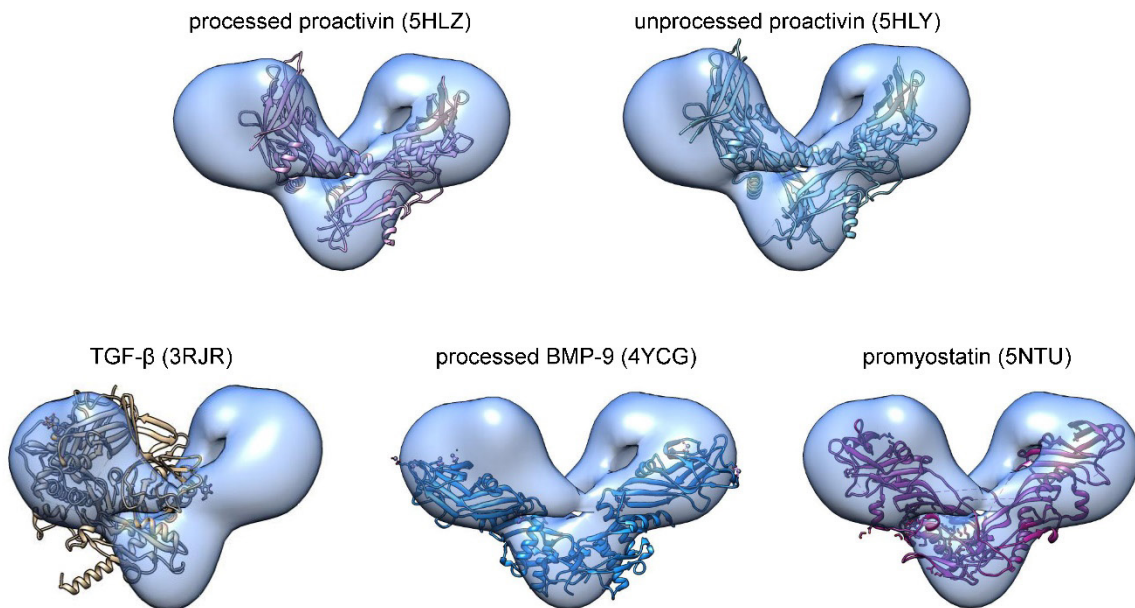
A

unprocessed BMP-10 dimer

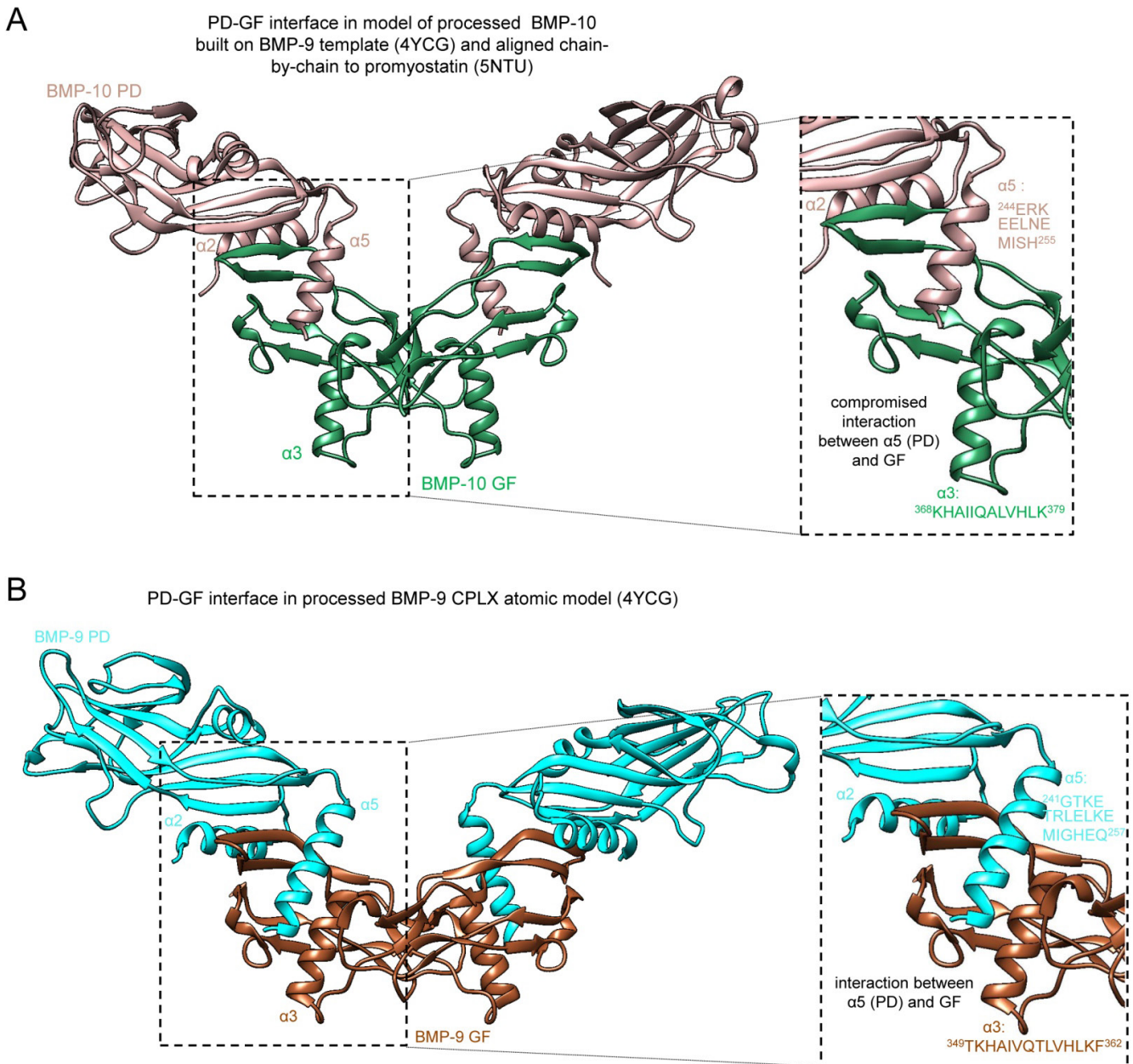


B

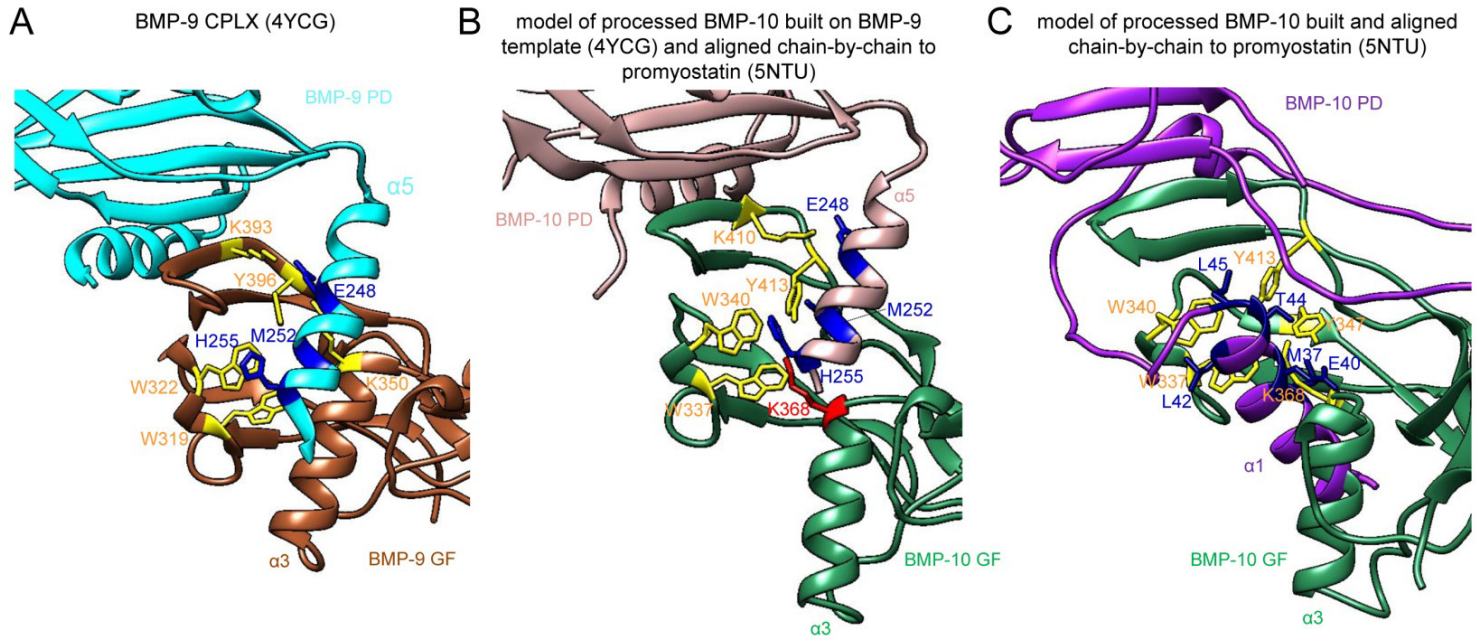
processed BMP-10 CPLX



690 **Figure S4: Molecular docking of published atomic models into the EM envelopes of unprocessed and**
 691 **processed BMP-10.** The atomic models of the processed proactivin (5HLZ), unprocessed proactivin
 692 (5HLY), TGF- β (3RJR), processed BMP-9 (4YCG), and promyostatin (5NTU) were docked into the EM
 693 envelopes of (A) BMP-10 unprocessed dimer, and (B) processed BMP-10 CPLX.



694 **Figure S5: Comparison of PD-GF interface in processed BMP-10 CPLX model based on BMP-9**
 695 **template and BMP-9 CPLX atomic model.** (A) Predicted compromised interaction between $\alpha 5$ -helix of
 696 PD and GF observed in BMP-10 CPLX model built on BMP-9 template (4YCG) and aligned chain-by-
 697 chain to promyostatin (5NTU). (B) Apparent interaction between $\alpha 5$ -helix of PD and GF in processed
 698 BMP-9 CPLX atomic model (4YCG). Please note that the BMP-10 signal peptide (21 aa) has been added
 699 to the BMP-10 GF aminoacid positions.



700 **Figure S6: Comparison of PD-GF interface in BMP-9 CPLX (4YCG) and BMP-10 CPLX models.**

701 (A) In the BMP-9 CPLX atomic model (4YCG) the PD-GF interface is mainly composed by amino acid
 702 interactions between the $\alpha 5$ -helix of the PD and the GF: E248 interacts with K393 and K350 (salt-bridge),
 703 M252 interacts with Y396, and H255 interacts with W322 (PMID: 25751889). (B) In the model of
 704 processed BMP-10 built on BMP-9 template (4YCG) and aligned chain-by-chain to promyostatin
 705 (5NTU) the predicted PD-GF interaction interface allows only a reduced number of molecular
 706 interactions between the $\alpha 5$ -helix of the PD and the GF: E248 is unable to make a salt bridge with K368
 707 (marked in red) but interacts with K410, M252 interacts with Y413, and H255 with W340. (C) In the
 708 model of processed BMP-10 built and aligned chain-by-chain to promyostatin (5NTU) the predicted PD-
 709 GF interface allows a strong interaction mainly between the $\alpha 1$ of the PD and the GF: M37 shows a
 710 methionine-aromatic interaction with Y347, T44 shows hydrogen bonding with Y413, E40 forms a
 711 potential salt bridge with K368, L42 interacts with W337 and respectively L45 with W340 via
 712 hydrophobic interactions. In all shown PD-GF interfaces, interacting residues are labeled (PD: blue, GF:
 713 yellow). Please note that the BMP-10 signal peptide (21 aa) has been added to the BMP-10 GF amino
 714 acid positions.

A unprocessed BMP-10 dimer in open-arm conformationcoverage of **BMP-10 PD** in unprocessed dimer model

Score	Expect	Method	Identities	Positives	Gaps
439 bits(1130)	3e-163	Compositional matrix adjust.	213/213(100%)	213/213(100%)	0/213(0%)
Query 1	DFNTLLQSMKDEFLKTLNLSDIPTQDSAKVDPPEYMLELYNKFATDRTSMPANIIRSFK				60
Sbjct 29	DFNTLLQSMKDEFLKTLNLSDIPTQDSAKVDPPEYMLELYNKFATDRTSMPANIIRSFK				88
Query 61	NEDLFSQPVSNGLRKYPLLFNVSIPHHEEVIMAEALRLYTLVQRDRMIYDGVDRKITIFE				120
Sbjct 89	NEDLFSQPVSNGLRKYPLLFNVSIPHHEEVIMAEALRLYTLVQRDRMIYDGVDRKITIFE				148
Query 121	VLESKGDNEGERNMLVLSGIEYGTNSEWETFVDVDAIRRWQKSGSSTHQLVHIESKHD				180
Sbjct 149	VLESKGDNEGERNMLVLSGIEYGTNSEWETFVDVDAIRRWQKSGSSTHQLVHIESKHD				208
Query 181	EADASSGRLEIDTSAQNKHNPLLVFSDQSS		213		
Sbjct 209	EADASSGRLEIDTSAQNKHNPLLVFSDQSS		241		

query: aa sequence of *in silico* built BMP-10 PD (swiss model server)
subject: human BMP-10 PD aa sequence (uniprot database)

coverage of **BMP-10 GF** in unprocessed BMP-10 dimer model

Score	Expect	Method	Identities	Positives	Gaps
218 bits(554)	1e-80	Compositional matrix adjust.	104/104(100%)	104/104(100%)	0/104(0%)
Query 1	NYCKRTPLYIDFKEIGWDSWIIAPPGEAYEYCRGVCNPLAEHLTPTKHAIQALVHLKN				60
Sbjct 5	NYCKRTPLYIDFKEIGWDSWIIAPPGEAYEYCRGVCNPLAEHLTPTKHAIQALVHLKN				64
Query 61	SQKASKACCVPTKLEPISILYLDKGVVTKFYEGMAVSECGR		104		
Sbjct 65	SQKASKACCVPTKLEPISILYLDKGVVTKFYEGMAVSECGR		108		

query: aa sequence of the BMP-10 GF crystal structure (6SF3)
subject: human BMP-10 GF aa sequence (uniprot database)

B BMP-10 CPLX in open V-shape conformationcoverage of **BMP-10 PD** in BMP-10 CPLX model

Score	Expect	Method	Identities	Positives	Gaps
438 bits(1127)	1e-162	Compositional matrix adjust.	212/212(100%)	212/212(100%)	0/212(0%)
Query 1	DFNTLLQSMKDEFLKTLNLSDIPTQDSAKVDPPEYMLELYNKFATDRTSMPANIIRSFK				60
Sbjct 29	DFNTLLQSMKDEFLKTLNLSDIPTQDSAKVDPPEYMLELYNKFATDRTSMPANIIRSFK				88
Query 61	NEDLFSQPVSNGLRKYPLLFNVSIPHHEEVIMAEALRLYTLVQRDRMIYDGVDRKITIFE				120
Sbjct 89	NEDLFSQPVSNGLRKYPLLFNVSIPHHEEVIMAEALRLYTLVQRDRMIYDGVDRKITIFE				148
Query 121	VLESKGDNEGERNMLVLSGIEYGTNSEWETFVDVDAIRRWQKSGSSTHQLVHIESKHD				180
Sbjct 149	VLESKGDNEGERNMLVLSGIEYGTNSEWETFVDVDAIRRWQKSGSSTHQLVHIESKHD				208
Query 181	EADASSGRLEIDTSAQNKHNPLLVFSDQSS		212		
Sbjct 209	EADASSGRLEIDTSAQNKHNPLLVFSDQSS		240		

query: aa sequence of *in silico* built BMP-10 PD (swiss model server)
subject: human BMP-10 PD aa sequence (uniprot database)

coverage of **BMP-10 GF** in BMP-10 CPLX model

Score	Expect	Method	Identities	Positives	Gaps
218 bits(554)	1e-80	Compositional matrix adjust.	104/104(100%)	104/104(100%)	0/104(0%)
Query 1	NYCKRTPLYIDFKEIGWDSWIIAPPGEAYEYCRGVCNPLAEHLTPTKHAIQALVHLKN				60
Sbjct 5	NYCKRTPLYIDFKEIGWDSWIIAPPGEAYEYCRGVCNPLAEHLTPTKHAIQALVHLKN				64
Query 61	SQKASKACCVPTKLEPISILYLDKGVVTKFYEGMAVSECGR		104		
Sbjct 65	SQKASKACCVPTKLEPISILYLDKGVVTKFYEGMAVSECGR		108		

query: aa sequence of the BMP-10 GF crystal structure (6SF3)
subject: human BMP-10 GF aa sequence (uniprot database)

C BMP-10 CPLX in closed ring-shape conformationcoverage of **BMP-10 PD** in closed ring-shape BMP-10 CPLX model

Score	Expect	Method	Identities	Positives	Gaps
563 bits(1450)	0.0	Compositional matrix adjust.	274/274(100%)	274/274(100%)	0/274(0%)
Query 1	FSEQDGVDFNTLLQSMKDEFLKTLNLSDIPTQDSAKVDPPEYMLELYNKFATDRTSMPA				60
Sbjct 22	FSEQDGVDFNTLLQSMKDEFLKTLNLSDIPTQDSAKVDPPEYMLELYNKFATDRTSMPA				81
Query 61	NIRSFKNEDLFSQPVSNGLRKYPLLFNVSIPHHEEVIMAEALRLYTLVQRDRMIYDGV				120
Sbjct 82	NIRSFKNEDLFSQPVSNGLRKYPLLFNVSIPHHEEVIMAEALRLYTLVQRDRMIYDGV				141
Query 121	RKITIFEVLESKGDNEGERNMLVLSGIEYGTNSEWETFVDVDAIRRWQKSGSSTHQLV				180
Sbjct 142	RKITIFEVLESKGDNEGERNMLVLSGIEYGTNSEWETFVDVDAIRRWQKSGSSTHQLV				201
Query 181	HIESKHDEADASSGRLEIDTSAQNKHNPLLVFSDQSSDKERKEELNEMISHEQLPEL				240
Sbjct 202	HIESKHDEADASSGRLEIDTSAQNKHNPLLVFSDQSSDKERKEELNEMISHEQLPEL				261
Query 241	DNLGLDSFSSGPEEALLQMRSNIIYDSTARIRR		274		
Sbjct 262	DNLGLDSFSSGPEEALLQMRSNIIYDSTARIRR		295		

query: aa sequence of *in silico* built BMP-10 PD model (swiss model)
subject: human BMP-10 PD aa sequence (uniprot database)

coverage of **BMP-10 GF** in closed ring-shape BMP-10 CPLX model

Score	Expect	Method	Identities	Positives	Gaps
246 bits(629)	1e-87	Composition-based stats.	108/108(100%)	108/108(100%)	0/108(0%)
Query 275	NAKGNYCKRTPLYIDFKEIGWDSWIIAPPGEAYEYCRGVCNPLAEHLTPTKHAIQALV				334
Sbjct 1	NAKGNYCKRTPLYIDFKEIGWDSWIIAPPGEAYEYCRGVCNPLAEHLTPTKHAIQALV				60
Query 335	HLKNSQKASKACCVPTKLEPISILYLDKGVVTKFYEGMAVSECGR		382		
Sbjct 61	HLKNSQKASKACCVPTKLEPISILYLDKGVVTKFYEGMAVSECGR		108		

query: aa sequence of the BMP-10 GF crystal structure (6SF3)
subject: human BMP-10 GF aa sequence (uniprot database)

D BMP-10 CPLX built on BMP-9 and aligned to promyostatincoverage of **BMP-10 PD** in BMP-10 CPLX model

Score	Expect	Method	Identities	Positives	Gaps
411 bits(1057)	2e-152	Compositional matrix adjust.	199/199(100%)	199/199(100%)	0/199(0%)
Query 1	VDPPEYMLELYNKFATDRTSMPANIIRSFKNEDLFSQPVSNGLRKYPLLFNVSIPHHE				60
Sbjct 58	VDPPEYMLELYNKFATDRTSMPANIIRSFKNEDLFSQPVSNGLRKYPLLFNVSIPHHE				117
Query 61	EVIMAEALRLYTLVQRDRMIYDGVDRKITIFEVLESKGDNEGERNMLVLSGIEYGTNSEW				120
Sbjct 118	EVIMAEALRLYTLVQRDRMIYDGVDRKITIFEVLESKGDNEGERNMLVLSGIEYGTNSEW				177
Query 121	ETFVDVDAIRRWQKSGSSTHQLVHIESKHDEADASSGRLEIDTSAQNKHNPLLVFSD				180
Sbjct 178	ETFVDVDAIRRWQKSGSSTHQLVHIESKHDEADASSGRLEIDTSAQNKHNPLLVFSD				237
Query 181	DQSSDKERKEELNEMISHE		199		
Sbjct 238	DQSSDKERKEELNEMISHE		256		

query: aa sequence of *in silico* built BMP-10 PD model (swiss model)
subject: human BMP-10 PD aa sequence (uniprot database)

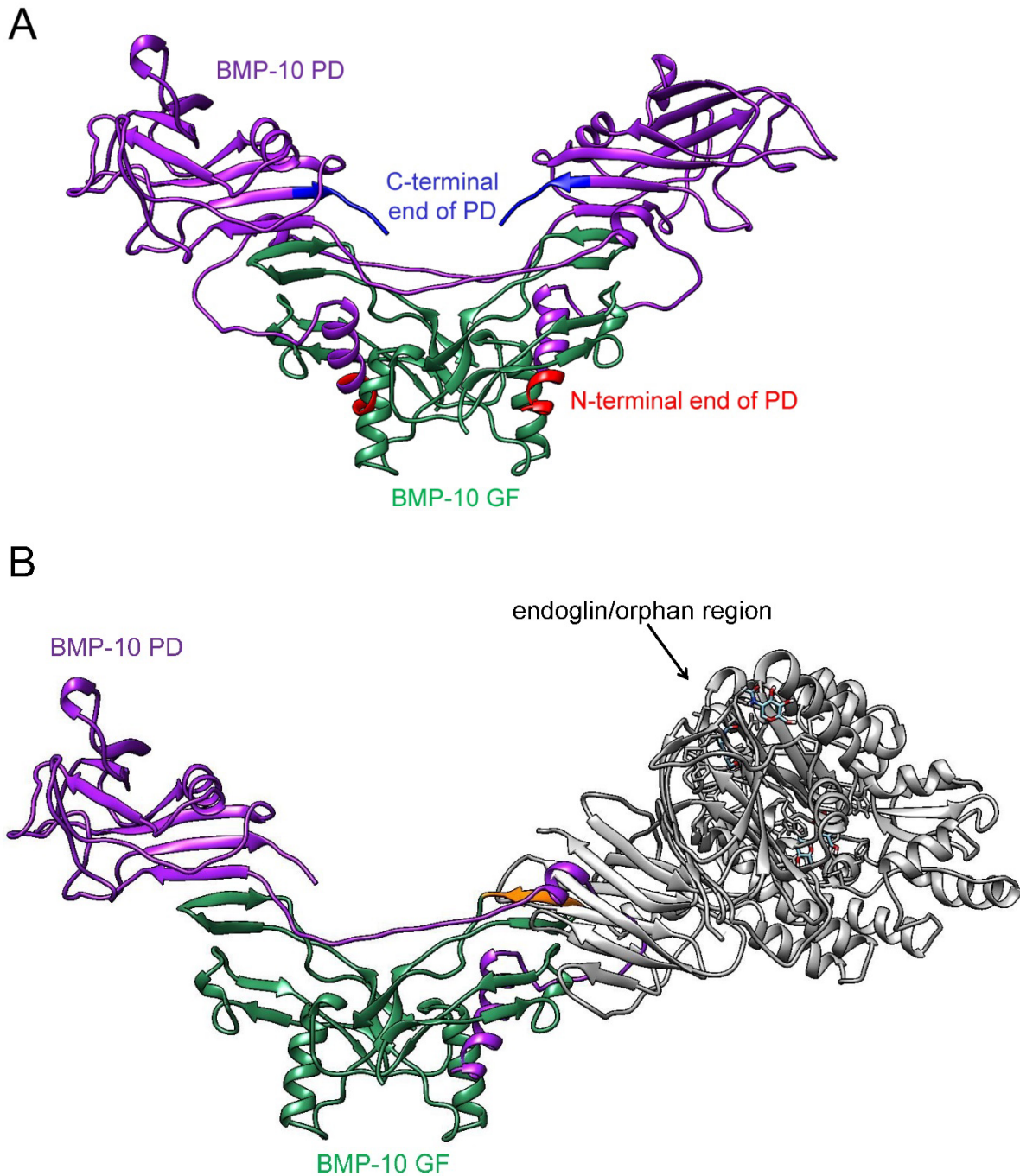
coverage of **BMP-10 GF** in BMP-10 CPLX model

Score	Expect	Method	Identities	Positives	Gaps
218 bits(554)	1e-80	Compositional matrix adjust.	104/104(100%)	104/104(100%)	0/104(0%)
Query 1	NYCKRTPLYIDFKEIGWDSWIIAPPGEAYEYCRGVCNPLAEHLTPTKHAIQALVHLKN				60
Sbjct 5	NYCKRTPLYIDFKEIGWDSWIIAPPGEAYEYCRGVCNPLAEHLTPTKHAIQALVHLKN				64
Query 61	SQKASKACCVPTKLEPISILYLDKGVVTKFYEGMAVSECGR		104		
Sbjct 65	SQKASKACCVPTKLEPISILYLDKGVVTKFYEGMAVSECGR		108		

query: aa sequence of the BMP-10 GF crystal structure (6SF3)
subject: human BMP-10 GF aa sequence (uniprot database)

715 Figure S7: Amino acid sequence coverage of PD and GF in generated BMP-10 structural models.

716 (A) Sequence coverage of BMP-10 PD and GF moieties in unprocessed dimer model in open-arm
717 conformation. (B) Sequence coverage of PD and GF in BMP-10 CPLX model in open V-shape
718 conformation. (C) Sequence coverage of PD and GF in BMP-10 CPLX model in closed ring-shape
719 conformation. (D) Sequence coverage of BMP-10 PD and GF in BMP-10 CPLX model built on BMP-9
720 and aligned chain-by-chain to promyostatin.



⁴⁰⁵GVV⁴¹¹TYKF⁴¹¹: predicted conserved BMP-10 GF interaction site with type II receptor/ endoglin

721 **Figure S8: Generated model of bioactive BMP-10 CPLX predicts interaction interface with type II**
 722 **receptor/ endoglin and allows a better understanding of His6-tag interference with CPLX stability.**
 723 (A) Marking the position of the N-terminal and C-terminal ends of the PD in the BMP-10 CPLX model
 724 shows that N-terminal His6-tag placement may interfere with the PD-GF interface. Marked in red: first 6
 725 residues of the modeled N-terminal end, marked in blue: last 6 residues of the modeled C-terminal end.
 726 (B) The processed, bioactive BMP-10 CPLX model illustrates that the PD interaction site on the GF
 727 overlaps with the predicted type II receptor/ endoglin binding site on the GF (marked in orange) [45] [44].

728 In the open V-shape conformation of the processed BMP-10 CPLX, PD is displaced so that type II/
729 endoglin receptors can signal [5] [44]. In this graph, only the orphan region of the endoglin receptor is
730 shown (in grey).

731 **References**

- 732 [1] Shi Y, Massague J. Mechanisms of TGF-beta signaling from cell membrane to the nucleus. *Cell*.
733 2003;113:685-700.
- 734 [2] Gregory KE, Ono RN, Charbonneau NL, Kuo CL, Keene DR, Bachinger HP, et al. The prodomain of
735 BMP-7 targets the BMP-7 complex to the extracellular matrix. *J Biol Chem*. 2005;280:27970-80.
- 736 [3] Brown MA, Zhao Q, Baker KA, Naik C, Chen C, Pukac L, et al. Crystal structure of BMP-9 and
737 functional interactions with pro-region and receptors. *J Biol Chem*. 2005;280:25111-8.
- 738 [4] Ge G, Hopkins DR, Ho WB, Greenspan DS. GDF11 forms a bone morphogenetic protein 1-activated
739 latent complex that can modulate nerve growth factor-induced differentiation of PC12 cells. *Mol Cell*
740 *Biol*. 2005;25:5846-58.
- 741 [5] Jiang H, Salmon RM, Upton PD, Wei Z, Lawera A, Davenport AP, et al. The Prodomain-bound Form
742 of Bone Morphogenetic Protein 10 Is Biologically Active on Endothelial Cells. *J Biol Chem*.
743 2016;291:2954-66.
- 744 [6] Mi LZ, Brown CT, Gao Y, Tian Y, Le VQ, Walz T, et al. Structure of bone morphogenetic protein 9
745 procomplex. *Proc Natl Acad Sci U S A*. 2015;112:3710-5.
- 746 [7] Jaaks P, D'Alessandro V, Grob N, Buel S, Hajdin K, Schafer BW, et al. The Proprotein Convertase
747 Furin Contributes to Rhabdomyosarcoma Malignancy by Promoting Vascularization, Migration and
748 Invasion. *PLoS One*. 2016;11:e0161396.
- 749 [8] Zimmermann LA, Correns A, Furlan AG, Spanou CES, Sengle G. Controlling BMP growth factor
750 bioavailability: The extracellular matrix as multi skilled platform. *Cell Signal*. 2021;85:110071.
- 751 [9] Le VQ, Iacob RE, Tian Y, McConaughy W, Jackson J, Su Y, et al. Tolloid cleavage activates latent
752 GDF8 by priming the pro-complex for dissociation. *EMBO J*. 2018;37:384-97.
- 753 [10] Ge G, Greenspan DS. BMP1 controls TGFbeta1 activation via cleavage of latent TGFbeta-binding
754 protein. *J Cell Biol*. 2006;175:111-20.
- 755 [11] Shi M, Zhu J, Wang R, Chen X, Mi L, Walz T, et al. Latent TGF-beta structure and activation.
756 *Nature*. 2011;474:343-9.
- 757 [12] Cotton TR, Fischer G, Wang X, McCoy JC, Czepnik M, Thompson TB, et al. Structure of the human
758 myostatin precursor and determinants of growth factor latency. *EMBO J*. 2018;37:367-83.

- 759 [13] Yu Q, Stamenkovic I. Cell surface-localized matrix metalloproteinase-9 proteolytically activates
760 TGF-beta and promotes tumor invasion and angiogenesis. *Genes Dev.* 2000;14:163-76.
- 761 [14] Mu D, Cambier S, Fjellbirkeland L, Baron JL, Munger JS, Kawakatsu H, et al. The integrin
762 alpha(v)beta8 mediates epithelial homeostasis through MT1-MMP-dependent activation of TGF-beta1. *J*
763 *Cell Biol.* 2002;157:493-507.
- 764 [15] Ribeiro SM, Poczatek M, Schultz-Cherry S, Villain M, Murphy-Ullrich JE. The activation sequence
765 of thrombospondin-1 interacts with the latency-associated peptide to regulate activation of latent
766 transforming growth factor-beta. *J Biol Chem.* 1999;274:13586-93.
- 767 [16] Buscemi L, Ramonet D, Klingberg F, Formey A, Smith-Clerc J, Meister JJ, et al. The single-
768 molecule mechanics of the latent TGF-beta1 complex. *Curr Biol.* 2011;21:2046-54.
- 769 [17] Kienast Y, Jucknischke U, Scheiblich S, Thier M, de Wouters M, Haas A, et al. Rapid Activation of
770 Bone Morphogenic Protein 9 by Receptor-mediated Displacement of Pro-domains. *J Biol Chem.*
771 2016;291:3395-410.
- 772 [18] Sengle G, Ono RN, Lyons KM, Bachinger HP, Sakai LY. A new model for growth factor activation:
773 type II receptors compete with the prodomain for BMP-7. *J Mol Biol.* 2008;381:1025-39.
- 774 [19] Wohl AP, Troilo H, Collins RF, Baldock C, Sengle G. Extracellular Regulation of Bone
775 Morphogenetic Protein Activity by the Microfibril Component Fibrillin-1. *J Biol Chem.* 2016;291:12732-
776 46.
- 777 [20] Furlan AG, Spanou CES, Godwin ARF, Wohl AP, Zimmermann LA, Imhof T, et al. A new MMP-
778 mediated prodomain cleavage mechanism to activate bone morphogenetic proteins from the extracellular
779 matrix. *FASEB J.* 2021;35:e21353.
- 780 [21] Desroches-Castan A, Tillet E, Bouvard C, Bailly S. BMP9 and BMP10: two close vascular
781 quiescence partners that stand out. *Dev Dyn.* 2021.
- 782 [22] Tillet E, Ouarne M, Desroches-Castan A, Mallet C, Subileau M, Didier R, et al. A heterodimer
783 formed by bone morphogenetic protein 9 (BMP9) and BMP10 provides most BMP biological activity in
784 plasma. *J Biol Chem.* 2018;293:10963-74.

- 785 [23] Sengle G, Ono RN, Sasaki T, Sakai LY. Prodomains of transforming growth factor beta (TGFbeta)
786 superfamily members specify different functions: extracellular matrix interactions and growth factor
787 bioavailability. *J Biol Chem.* 2011;286:5087-99.
- 788 [24] Sengle G, Charbonneau NL, Ono RN, Sasaki T, Alvarez J, Keene DR, et al. Targeting of bone
789 morphogenetic protein growth factor complexes to fibrillin. *J Biol Chem.* 2008;283:13874-88.
- 790 [25] Neuhaus H, Rosen V, Thies RS. Heart specific expression of mouse BMP-10 a novel member of the
791 TGF-beta superfamily. *Mech Dev.* 1999;80:181-4.
- 792 [26] Chen H, Shi S, Acosta L, Li W, Lu J, Bao S, et al. BMP10 is essential for maintaining cardiac
793 growth during murine cardiogenesis. *Development.* 2004;131:2219-31.
- 794 [27] Shou W, Aghdasi B, Armstrong DL, Guo Q, Bao S, Charng MJ, et al. Cardiac defects and altered
795 ryanodine receptor function in mice lacking FKBP12. *Nature.* 1998;391:489-92.
- 796 [28] Ye L, Kynaston H, Jiang WG. Bone morphogenetic protein-10 suppresses the growth and
797 aggressiveness of prostate cancer cells through a Smad independent pathway. *J Urol.* 2009;181:2749-59.
- 798 [29] Ye L, Bokobza S, Li J, Moazzam M, Chen J, Mansel RE, et al. Bone morphogenetic protein-10
799 (BMP-10) inhibits aggressiveness of breast cancer cells and correlates with poor prognosis in breast
800 cancer. *Cancer Sci.* 2010;101:2137-44.
- 801 [30] Zhang N, Ye L, Wu L, Deng X, Yang Y, Jiang WG. Expression of bone morphogenetic protein-10
802 (BMP10) in human urothelial cancer of the bladder and its effects on the aggressiveness of bladder cancer
803 cells in vitro. *Anticancer Res.* 2013;33:1917-25.
- 804 [31] Yuan YM, Ma N, Zhang EB, Chen TW, Jiang H, Yin FF, et al. BMP10 suppresses hepatocellular
805 carcinoma progression via PTPRS-STAT3 axis. *Oncogene.* 2019;38:7281-93.
- 806 [32] McDonald J, Wooderchak-Donahue W, VanSant Webb C, Whitehead K, Stevenson DA, Bayrak-
807 Toydemir P. Hereditary hemorrhagic telangiectasia: genetics and molecular diagnostics in a new era.
808 *Front Genet.* 2015;6:1.
- 809 [33] Roman BL, Hinck AP. ALK1 signaling in development and disease: new paradigms. *Cell Mol Life*
810 *Sci.* 2017;74:4539-60.

- 811 [34] Capasso TL, Li B, Volek HJ, Khalid W, Rochon ER, Anbalagan A, et al. BMP10-mediated ALK1
812 signaling is continuously required for vascular development and maintenance. *Angiogenesis*.
813 2020;23:203-20.
- 814 [35] Hodgson J, Swietlik EM, Salmon RM, Hadinnapola C, Nikolic I, Wharton J, et al. Characterization
815 of GDF2 Mutations and Levels of BMP9 and BMP10 in Pulmonary Arterial Hypertension. *Am J Respir*
816 *Crit Care Med*. 2020;201:575-85.
- 817 [36] Wang X, Fischer G, Hyvonen M. Structure and activation of pro-activin A. *Nat Commun*.
818 2016;7:12052.
- 819 [37] Walton KL, Makanji Y, Chen J, Wilce MC, Chan KL, Robertson DM, et al. Two distinct regions of
820 latency-associated peptide coordinate stability of the latent transforming growth factor-beta1 complex. *J*
821 *Biol Chem*. 2010;285:17029-37.
- 822 [38] Walker RG, McCoy JC, Czepnik M, Mills MJ, Hagg A, Walton KL, et al. Molecular characterization
823 of latent GDF8 reveals mechanisms of activation. *Proc Natl Acad Sci U S A*. 2018;115:E866-E75.
- 824 [39] Beitzinger C, Stefani C, Kronhardt A, Rolando M, Flatau G, Lemichez E, et al. Role of N-terminal
825 His6-Tags in binding and efficient translocation of polypeptides into cells using anthrax protective
826 antigen (PA). *PLoS One*. 2012;7:e46964.
- 827 [40] Majorek KA, Kuhn ML, Chruszcz M, Anderson WF, Minor W. Double trouble-Buffer selection and
828 His-tag presence may be responsible for nonreproducibility of biomedical experiments. *Protein Sci*.
829 2014;23:1359-68.
- 830 [41] Tsuji A, Sakurai K, Kiyokage E, Yamazaki T, Koide S, Toida K, et al. Secretory proprotein
831 convertases PACE4 and PC6A are heparin-binding proteins which are localized in the extracellular
832 matrix. Potential role of PACE4 in the activation of proproteins in the extracellular matrix. *Biochim*
833 *Biophys Acta*. 2003;1645:95-104.
- 834 [42] Mayer G, Hamelin J, Asselin MC, Pasquato A, Marcinkiewicz E, Tang M, et al. The regulated cell
835 surface zymogen activation of the proprotein convertase PC5A directs the processing of its secretory
836 substrates. *J Biol Chem*. 2008;283:2373-84.

- 837 [43] Declercq J, Brouwers B, Pruniau VP, Stijnen P, Tuand K, Meulemans S, et al. Liver-Specific
838 Inactivation of the Proprotein Convertase FURIN Leads to Increased Hepatocellular Carcinoma Growth.
839 Biomed Res Int. 2015;2015:148651.
- 840 [44] Saito T, Bokhove M, Croci R, Zamora-Caballero S, Han L, Letarte M, et al. Structural Basis of the
841 Human Endoglin-BMP9 Interaction: Insights into BMP Signaling and HHT1. Cell Rep. 2017;19:1917-28.
- 842 [45] Salmon RM, Guo J, Wood JH, Tong Z, Beech JS, Lawera A, et al. Molecular basis of ALK1-
843 mediated signalling by BMP9/BMP10 and their prodomain-bound forms. Nat Commun. 2020;11:1621.
- 844 [46] Castonguay R, Werner ED, Matthews RG, Presman E, Mulivor AW, Solban N, et al. Soluble
845 endoglin specifically binds bone morphogenetic proteins 9 and 10 via its orphan domain, inhibits blood
846 vessel formation, and suppresses tumor growth. J Biol Chem. 2011;286:30034-46.
- 847 [47] Gregory AL, Xu G, Sotov V, Letarte M. Review: the enigmatic role of endoglin in the placenta.
848 Placenta. 2014;35 Suppl:S93-9.
- 849 [48] Le VQ, Iacob RE, Zhao B, Su Y, Tian Y, Toohey C, et al. Protection of the prodomain alpha1-helix
850 correlates with latency in the transforming growth factor-beta family. J Mol Biol. 2022:167439.
- 851 [49] Walker RG, Czepnik M, Goebel EJ, McCoy JC, Vujic A, Cho M, et al. Structural basis for potency
852 differences between GDF8 and GDF11. BMC Biol. 2017;15:19.
- 853 [50] Kuo CL, Isogai Z, Keene DR, Hazeki N, Ono RN, Sengle G, et al. Effects of fibrillin-1 degradation
854 on microfibril ultrastructure. J Biol Chem. 2007;282:4007-20.
- 855 [51] Harges K, Becker GL, Lu Y, Dahms SO, Kohler S, Beyer W, et al. Novel Furin Inhibitors with
856 Potent Anti-infectious Activity. ChemMedChem. 2015;10:1218-31.
- 857 [52] Pettersen EF, Goddard TD, Huang CC, Couch GS, Greenblatt DM, Meng EC, et al. UCSF Chimera--
858 a visualization system for exploratory research and analysis. J Comput Chem. 2004;25:1605-12.
- 859 [53] Bertoni M, Kiefer F, Biasini M, Bordoli L, Schwede T. Modeling protein quaternary structure of
860 homo- and hetero-oligomers beyond binary interactions by homology. Sci Rep. 2017;7:10480.
- 861 [54] Yadin, D. A., Robertson, I. B., McNaught-Davis, J., Evans, P., Stoddart, D., Handford, P. A., Jensen,
862 S. A., and Redfield, C. (2013) Structure of the fibrillin-1 N-terminal domains suggests that heparan
863 sulfate regulates the early stages of microfibril assembly. *Structure* **21**, 1743-1756

Tables

Table 1: Molecular docking results of published atomic models into the determined EM envelopes of BMP-7 CPLX, BMP-10 unprocessed dimer and processed BMP-10 CPLX.

atomic model	PDB code	cross correlation score between model and density	average map value at atomic model positions	proportion of atomic models inside EM envelope	determined envelope
unprocessed proactivin:	5HLY	0.8984	1.271	0.558	BMP7
	5HLY	0.865	7.874	0.445	BMP-10 unprocessed
	5HLY	0.7833	2.877	0.539	BMP-10 processed
processed proactivin:	5HLZ	0.8968	1.272	0.557	BMP7
	5HLZ	0.8705	7.917	0.449	BMP10 unprocessed
	5HLZ	0.7728	2.911	0.548	BMP10 processed
processed BMP-9	4YCG	0.8854	1.238	0.542	BMP7
	4YCG	0.9063	8.933	0.551	BMP10 unprocessed
	4YCG	0.7667	2.278	0.407	BMP10 processed
promyostatin	5NTU	0.8958	1.288	0.579	BMP7
	5NTU	0.8909	8.695	0.532	BMP10 unprocessed
	5NTU	0.7974	3.493	0.656	BMP10 processed
processed TGF- β	3RJR	0.9077	1.162	0.452	BMP7

3RJR	0.8786	6.774	0.33	BMP10 unprocessed
3RJR	0.7694	2.322	0.409	BMP10 processed

3.3 Heparin/HS controls bioavailability of BMP growth factors

It was published previously that BMP-7 CPLX assumes a closed-ring, latent conformation when targeted to the extracellular matrix protein fibrillin-1 (Wohl et al., 2016). In addition, it is well known that BMP GFs can be bound and spatially concentrated to the ECM via GAGs such as heparin/HS. However, it is currently not understood whether GAG binding to BMP CPLXs renders them latent, which would represent an additional sequestration mechanism by the ECM. Previous studies showed that the proactivin CPLX binds heparin/HS via the PD but the identified binding site was not localized within the structure of the CPLX nor the bioactivity of the heparin-bound proactivin CPLX was measured (Li et al., 2010). Hence, the aim of this study was to identify the molecular requirements for BMP CPLX interactions with GAGs and to investigate how these interactions affect their bioactivity. To that end, the heparin binding sites for BMP-7 and BMP-9 CPLX were determined. Further, it was investigated by employing both *in vitro* and *in silico* approaches whether heparin binding to BMP-7 or BMP-9 CPLX induces a conformational change and thereby affects their bioactivity.

The following manuscript was written by Chara E.S. Spanou and Gerhard Sengle.

The experiments in figures 1A, 2, 4B, 5, 6, 7A, 7B, 7D, 7E, 8C, 8D, 9, 10B, 10C, 11A, 11B, 11D, 11E, S1, S2, S3, S4, S6 were performed and analyzed by Chara E.S. Spanou.

The overview figure 12 was designed by Chara E.S. Spanou.

Regulation of BMP bioactivity by heparin/heparan sulfate glycosaminoglycans

Chara E.S. Spanou^{1,2}, Annkatrin Correns^{1,2#}, Sandra Doherr^{1#}, Alexander Wohl^{1#}, Matthias Mörgelin³, Steffen Lütke^{1,2}, Thomas Imhof^{1,4}, Manuel Koch^{1,4}, Gerhard Sengle^{1,2,5,6*}

From the ¹Center for Biochemistry, Faculty of Medicine, University Hospital of Cologne, Joseph-Stelzmann-Street 52, 50931 Cologne, Germany; ²Department of Pediatrics and Adolescent Medicine, Faculty of Medicine and University Hospital Cologne, University of Cologne, Cologne, Germany; ³Division of Infection Medicine, Department of Clinical Sciences, Lund University, Lund, Sweden; Colzyx AB, Lund, Sweden; ⁴Medical Faculty, Institute for Dental Research and Oral Musculoskeletal Biology, University of Cologne, 50923 Cologne, Germany; ⁵Center for Molecular Medicine Cologne (CMMC), University of Cologne, Robert-Koch-Street 21, 50931 Cologne, Germany; ⁶Cologne Center for Musculoskeletal Biomechanics (CCMB), 50931 Cologne, Germany

Running title: Molecular requirements for regulating the bioactivities of the prodomain-bound forms of BMP-7 and BMP-9 by the extracellular component heparin/HS

#contributed equally

*To whom correspondence should be addressed: Gerhard Sengle, Center for Biochemistry, Medical Faculty, University of Cologne, Joseph-Stelzmann-Street 52, D-50931 Cologne, Germany, phone: +49 (0)221 47897260, fax: +49 (0)2214786977,

email: gsengle@uni-koeln.de

Keywords: Bone morphogenetic protein (BMP), vascular endothelial growth factor (VEGF), heparan sulfate proteoglycans (HSPGs), heparin, heparan sulfate (HS), growth factor (GF), complex (CPLX), prodomain (PD), ELISA-style bioactivity assay, negative-staining transmission electron microscopy, heparin affinity chromatography, molecular modeling, surface plasmon resonance (SPR)

1 Abstract

2 Bone morphogenetic proteins (BMP) are powerful regulators of cellular processes including
3 proliferation, differentiation, and apoptosis. However, the specific molecular requirements
4 controlling the bioavailability of BMPs in the extracellular matrix (ECM) are not yet fully
5 understood. Our previous work showed that BMPs are targeted to the ECM as growth factor-
6 prodomain (GF-PD) complexes (CPLXs) via specific interactions of their PDs. We showed that
7 BMP-7 PD binding to the extracellular microfibril component fibrillin-1 renders the CPLXs from an
8 open, bioactive V-shape into a closed, latent ring-shape. Here, we show that specific PD interactions
9 with heparin/ heparan sulfate glycosaminoglycans (GAGs) allow to target and spatially concentrate
10 BMP-7 and BMP-9 CPLXs in bioactive V-shape conformation. However, targeting to GAGs may be
11 BMP specific, since BMP-10 GF and CPLX do not interact with heparin. Bioactivity assays on solid
12 phase in combination with interaction studies showed that the BMP-7 PD protects the BMP-7 GF
13 from inactivation by heparin. By using transmission electron microscopy, molecular docking, and
14 site directed mutagenesis we determined the BMP-7 PD binding site for heparin. Further, fine-
15 mapping of the fibrillin-1 binding site within the BMP-7 PD and molecular modeling showed that
16 both binding sites are mutually exclusive in the open V- versus closed ring-shape conformation.
17 Together, our data suggest that targeting of exquisite BMP PD epitopes by extracellular protein and
18 GAG scaffolds integrates BMP GF bioavailability in a contextual manner in development, postnatal
19 life, and connective tissue disease.

20 **Introduction**

21 Bone morphogenetic proteins (BMPs) are pluripotent growth factors of the TGF- β superfamily that
22 drive a multitude of biological programs during embryogenesis and tissue regeneration (1, 2). Due to
23 their high potency as cellular morphogens tightly regulated extracellular control mechanisms of their
24 bioavailability are mandatory. BMPs are stored and sequestered by the extracellular matrix (ECM)
25 microenvironment of tissues from which they are specifically activated upon cellular utilization (3-
26 5). This view is supported by the original discovery of BMPs as cytokines extractable from bone
27 matrix under denaturing conditions (6). These extracts contain the liberated, bioactive growth factor
28 (GF) moiety since injection into tissues induces strong ectopic bone formation (7, 8).

29 Currently, it is not fully understood how the ECM regulates the bioavailability of GFs of the
30 TGF- β superfamily. However, this question is not only important to better understand how
31 embryonic patterning occurs, but also how remodeling and regeneration processes are regulated in
32 tissues. TGF- β and BMP growth factors are known to play crucial roles in growth and differentiation
33 processes, but the specific molecular requirements to fine tune their bioactivity within the respective
34 cellular microenvironment remain elusive. So far the impact of the ECM on BMP GF activity has
35 been mostly studied in absence of their prodomains (PDs) that are proteolytically cleaved from the
36 GF and non-covalently associate with them to form PD-GF complexes (CPLXs) before secretion (9).
37 Thereby, several interactions of TGF- β GFs to ECM components such as procollagen II (10, 11),
38 oligomeric matrix protein (COMP) (12), and glycosaminoglycan (GAG) carrying heparin sulfate
39 proteoglycans (HSPG) such as decorin (13, 14) have been investigated. However, depending on the
40 investigated physiological context, GF binding to ECM proteins seems to either promote or limit
41 their bioactivity (15-19).

42 Until now, it is not clear how BMP targeting to ECM proteins versus GAGs integrates their
43 bioavailability. GAGs are supramolecular oligomers consisting of sulfated disaccharides that can
44 strongly associate with several other GFs such as VEGF or FGF and were suggested to act as general
45 sinks or reservoirs for GFs required for their spatial concentration (20). A more active role for GAGs
46 has been described by their function as co-receptors thereby assisting in the presentation of GFs to
47 their cell surface signaling receptors (21, 22). Generally, BMP GFs are predicted to interact with

48 their basic, electropositive surface epitopes with the long-sulfated negatively charged disaccharides
49 of GAGs (23). The GAG heparin is chemically similar to heparin sulfate (HS), but contains more
50 fully sulfated sequences resulting often times in increased binding affinity to heparin/ HS binding
51 proteins (24). Several studies have shown that BMP GF signaling and gradient formation is
52 controlled by HS during developmental processes (25, 26). Thereby, HS traps BMP GFs within the
53 ECM by binding to the basic core of four to three amino acids in the N- or C-terminal region (26).
54 This way GFs of BMP-2, -4, -5, -6, -7, -15 and GDF-5 were shown to bind to heparin and HS (27-
55 31).

56 To better understand how targeting of BMPs by the ECM control their bioavailability, the
57 presence of BMPs as PD-GF CPLXs has to be considered (32-36). Three modes have been proposed
58 how PDs may regulate GF activity (34). For BMP-2 it was shown that it does not form stable CPLXs
59 with its cognate PD (33). Therefore studying BMP-2 GF bioactivity in absence of the PD may be
60 still relevant for physiological processes. However, other TGF- β superfamily members form stable
61 CPLXs with their PDs of which some are bioactive and some remain latent when soluble. For
62 instance BMP-7, -9, and -10 form stable, bioactive CPLXs in solution (35-37), while TGF- β s, GDF-
63 8 (myostatin), and GDF-11 are latent (38-40). For bioactive CPLXs such as BMP-7 targeting of the
64 PD to the ECM protein fibrillin-1 was shown to confer latency to the GF. Thereby, BMP-7 CPLX
65 changes its conformation from a bioactive V-shape into a latent ring-shape similar to the latent TGF-
66 β 1 CPLX (40, 41). Recently, we demonstrated that bioactive BMP GFs can be liberated from ECM-
67 bound latent CPLX pools via specific matrix metalloproteinase (MMP) mediated degradation of the
68 alpha2-helix of the PD (42), that blocks access of BMP type II receptors in the closed ring-shape
69 conformation of the CPLX (41). Proteolytic PD degradation was also reported to activate GDF-8
70 (38), GDF-11 (39), and TGF- β (43-45) from the latent state, and in addition integrin mediated
71 mechanical pulling on the TGF- β PD to liberate the GF was demonstrated as activation mechanism
72 (46).

73 However, so far it has not been investigated whether BMP CPLXs are targeted to GAGs and
74 how the presence of the PD may influence the bioavailability of GAG-bound BMP CPLXs. In this
75 study, we show for the first time how BMP CPLXs facilitate interactions with GAGs via their PD

76 and thereby allowing their spatial concentration in bioactive conformation. Further we show for
77 BMP-7 that the bioavailability of BMP CPLXs can be integrated by targeting specific PD binding
78 epitopes for heparin/HS and the microfibril component fibrillin-1 which controls their state of
79 bioactivity.

80 **Results**

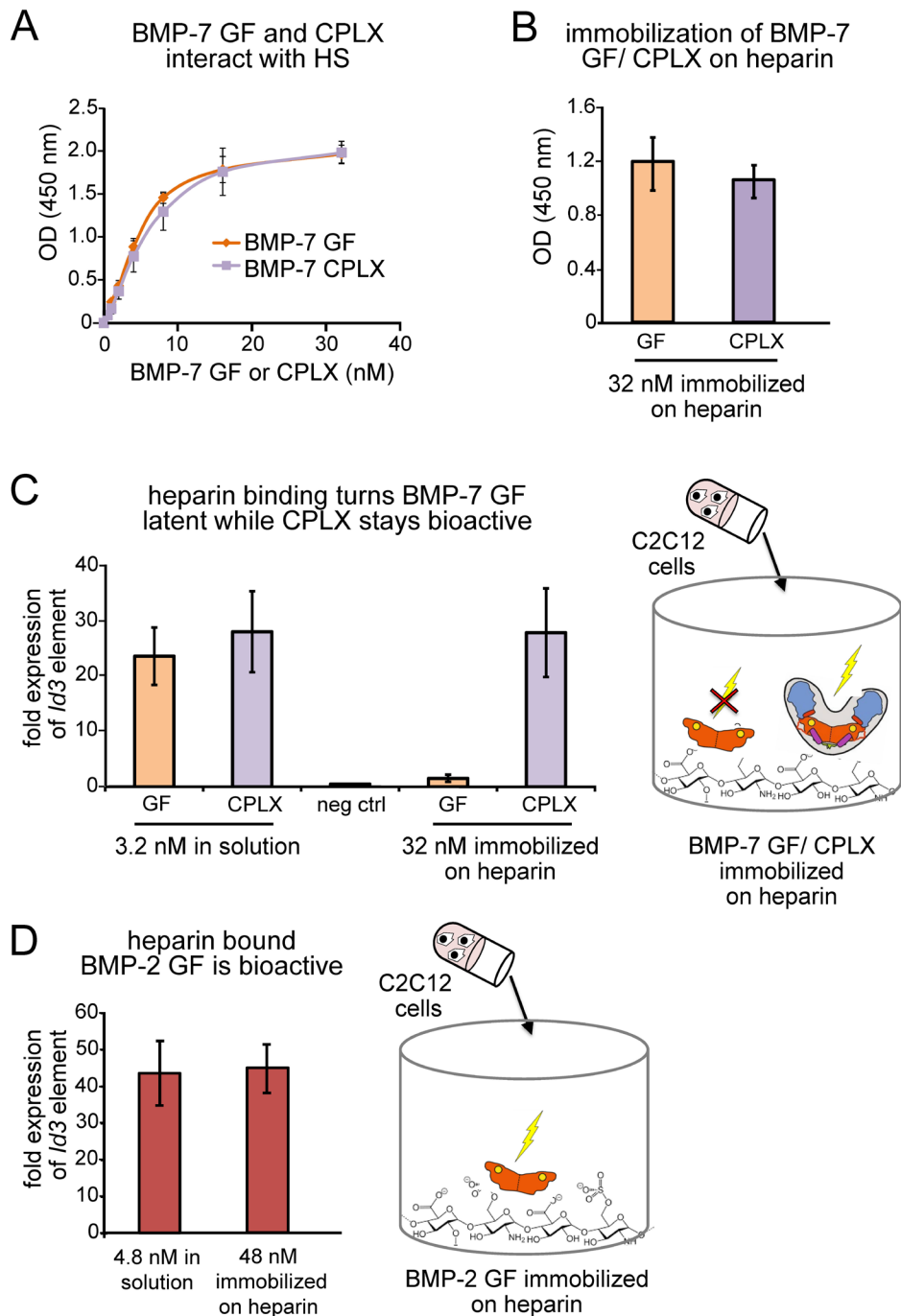
81 *BMP-7 GF and CPLX interact with heparin/ heparan sulfate*

82 Previous data showed that the BMP-7 GF interacts with high affinity with heparin/HS (28, 31) To
83 test whether also the BMP-7 CPLX interacts with sulfated disaccharides that naturally exist in
84 tissues, we subjected BMP-7 CPLX to an ELISA-style binding assay with HS that was isolated from
85 mouse embryo preparations following established protocols (47) and immobilized to solid phase.
86 Our results revealed that both BMP-7 GF and CPLX showed a strong interaction signal with HS that
87 saturated at 15 nM of BMP-7 GF or CPLX (Fig. 1A).

88 *Bioactivity of heparin-bound BMP-7 GF is abolished while it is preserved in heparin-bound CPLX*

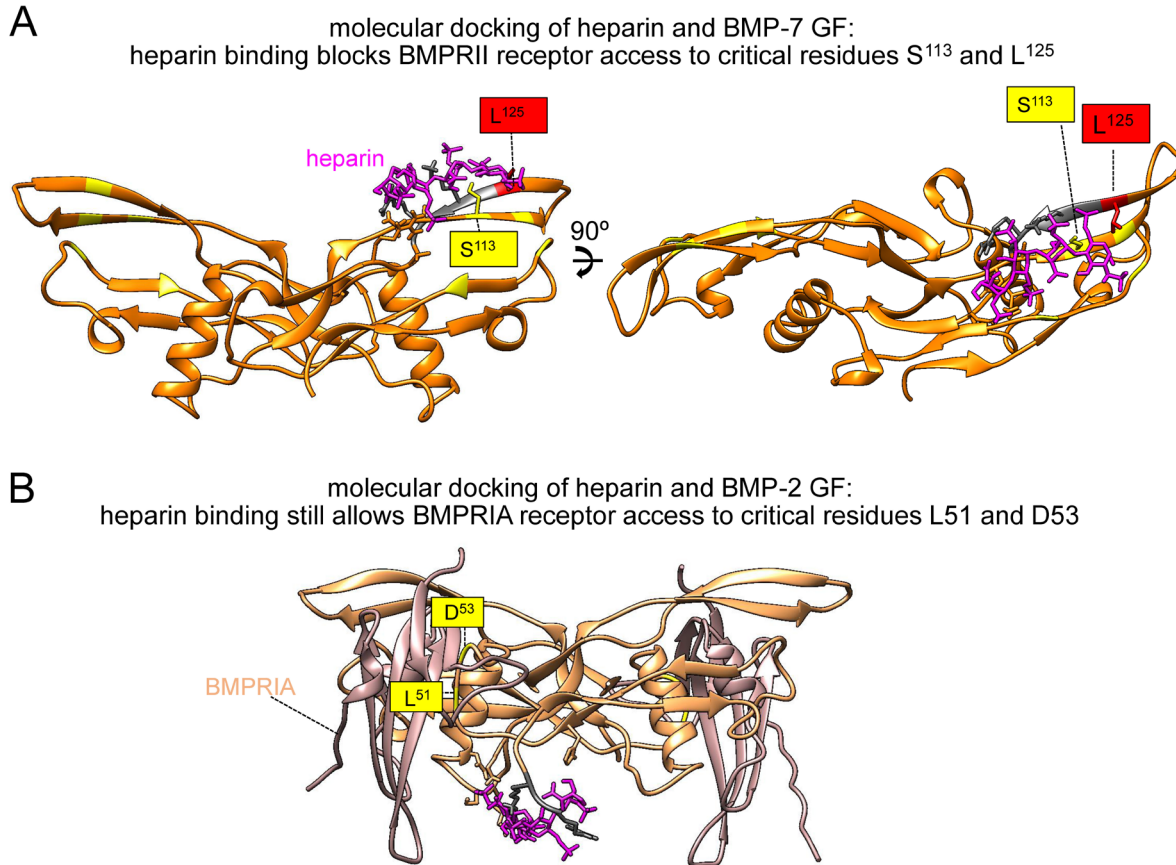
89 To assess the bioactivity of BMP-7 when immobilized to heparin/ HS we used biotinylated heparin
90 in BMP bioactivity assays due to its commercial availability. Biotinylated heparin was immobilized
91 to streptavidin coated wells followed by incubation of BMP-7 GF or CPLX at equal molarity.
92 Comparable immobilization levels of the GF were demonstrated by direct ELISA using a polyclonal
93 anti-BMP-7 GF antibody (Fig. 1B). C2C12 cells were seeded on heparin-immobilized BMP-7 GF
94 and CPLX for 5 h followed by measurement of mRNA levels of the BMP response element *Id3*.
95 Interestingly, BMP-7 GF interaction to heparin resulted in abolished bioactivity while the heparin-
96 bound BMP-7 CPLX showed a comparable bioactivity to the GF administered in solution (Fig. 1C).
97 Molecular docking of the atomic model of the BMP-7 GF dimer (PDB: 1LXI) on heparin indicated
98 that the proposed interaction of heparin chains to the characterized heparin binding epitope of the
99 BMP-7 GF (31) renders crucial residues of the ActRII receptor binding site within the GF (S¹¹³, L¹²⁵)
100 inaccessible (48) (Fig. 2A). This explains the diminished bioactivity observed for the heparin-bound
101 BMP-7 GF since both BMP-7 and TGF- β need to associate with the type II receptor first to trigger

102 the BMP response. In contrast to BMP-7 GF, immobilization of BMP-2 GF to heparin did not confer
 103 latency (Fig. 1D). Molecular docking of heparin to the characterized heparin-binding epitope in the
 104 atomic model of BMP-2 GF (PDB: 6OMN) (31), showed that heparin binding still allows for
 105 receptor engagement since the crucial residues within the BMPRI (L⁵¹ and D⁵³) are still accessible in
 106 the atomic model of the BMP-2/ BMP type I receptor complex (PDB: 1REW) (Fig. 2B) (55).



107 **Figure 1: Heparin/ HS binding confers latency to BMP-7 GF while BMP-7 CPLX and BMP-2**
 108 **GF remain bioactive.** (A) Solid-phase ligand binding assay showed that BMP-7 GF and CPLX
 109 interact with immobilized HS. (B) Direct ELISA using anti-BMP-7 GF as detector antibody

110 indicated that incubation of 32 nM of BMP-7 GF or CPLX with immobilized heparin results in
 111 binding of comparable BMP-7 GF amounts to wells. (C) Bioactivity measurement of heparin-bound
 112 BMP-7 showed that the GF is rendered latent while the CPLX remains bioactive. (D) Bioactivity
 113 measurements revealed that binding to heparin does not affect the bioactivity of BMP-2 GF.

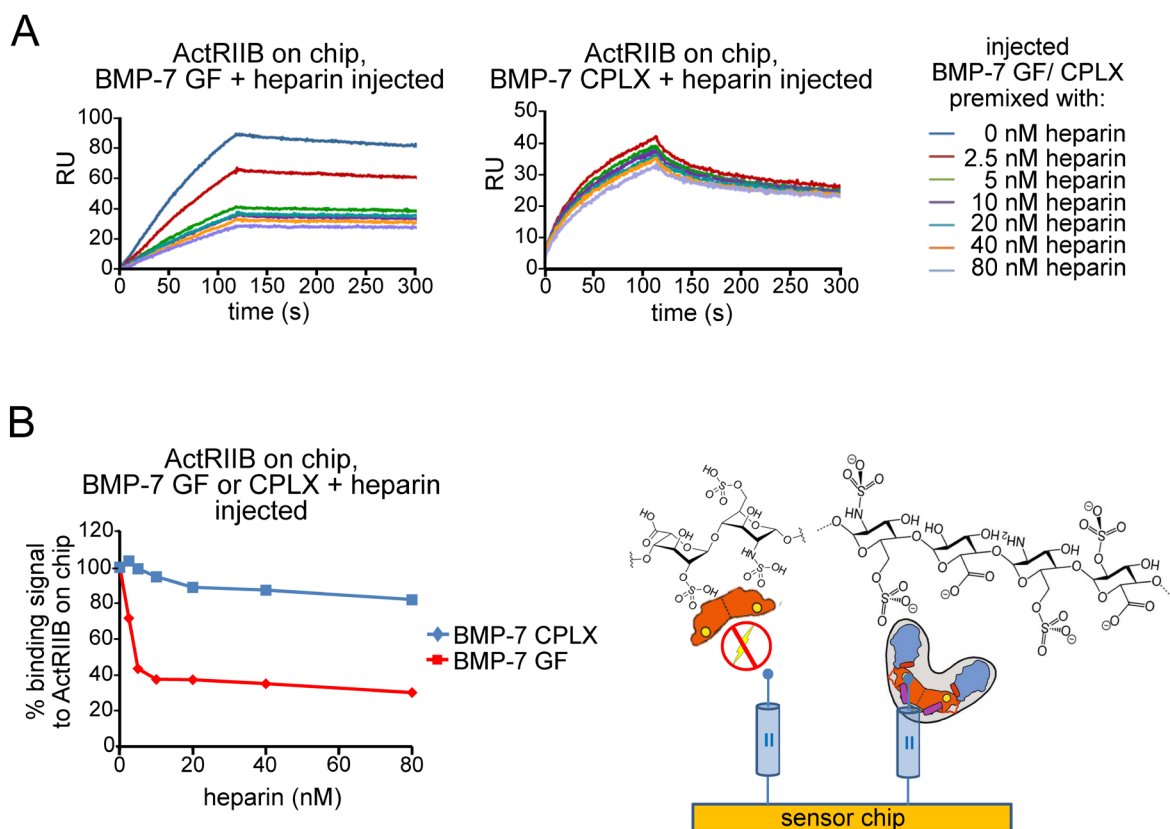


114 **Figure 2: Molecular docking of BMP GF atomic models to heparin shows that heparin blocks**
 115 **BMP receptor binding epitopes in BMP-7 but not in BMP-2.** (A) Molecular docking of heparin
 116 chains to the characterized BMP-7 GF heparin binding site (31). Residue masked by heparin chain
 117 branching is labeled in yellow. Residue participating in the BMP-7 GF heparin binding site (31) is
 118 labeled in red. Both highlighted residues also participate in type II receptor binding (42). (B)
 119 Molecular docking of heparin chains to the characterized BMP-2 GF heparin binding site (31) in
 120 complex with type I receptor (55). Residues utilized by the type I receptor are labeled in yellow.

121 *Heparin binding to BMP-7 GF blocks BMP receptor access while BMP-7 PD protects the GF from*
 122 *heparin inactivation in BMP-7 CPLX*

123 Since we observed that the bioactivity of heparin-bound BMP-7 CPLX was preserved, we wanted to
 124 investigate whether the presence of the PD protects the GF from heparin mediated inactivation and
 125 thereby allowing BMP receptor access. To examine this, we employed surface plasmon resonance

126 and measured the binding activity of BMP-7 GF and CPLX to the immobilized ectodomain of
 127 ActRII after pre-incubation with increasing concentrations of heparin (Fig. 3). Our binding studies
 128 showed that addition of heparin to the BMP-7 GF resulted in a reduction of its interaction signal with
 129 ActRII in a concentration dependent fashion. However, this reduction in binding was not observed
 130 when BMP-7 CPLX was pre-incubated with heparin (Fig. 3), suggesting that the PD protects the GF
 131 from heparin mediated blockage of its type II receptor binding site.

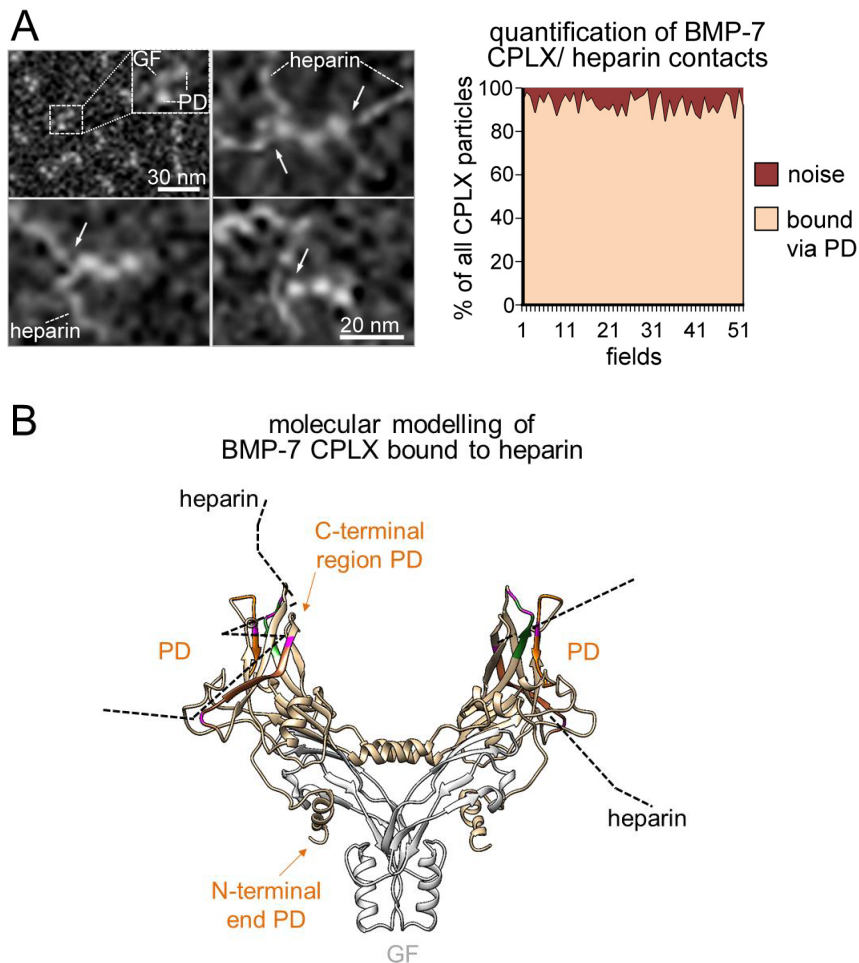


132 **Figure 3: Heparin inhibits BMP-7 GF but not BMP-7 CPLX interaction with ActRIIB.** (A)
 133 BMP-7 GF (20 nM) was premixed with heparin in increasing concentrations (0-80 nM) before flown
 134 over ActRIIB receptor ectodomain immobilized onto a CM5 chip. BMP-7 CPLX (20 nM) was
 135 premixed with the same heparin concentrations as in (A) before flown over immobilized ActRIIB.
 136 (B) (left) Percentage of binding signal for BMP-7 GF and CPLX to ActRIIB in presence of
 137 increasing heparin concentrations. (right) Cartoon illustrating BMP-7 GF and CPLX interaction with
 138 ActRII in presence of heparin.

139 *Mapping of the heparin binding site in BMP-7 CPLX*

140 To investigate the interaction interface of BMP-7 CPLX and heparin, purified CPLX was pre-
 141 incubated with heparin chains and analyzed by transmission electron microscopy (TEM) after

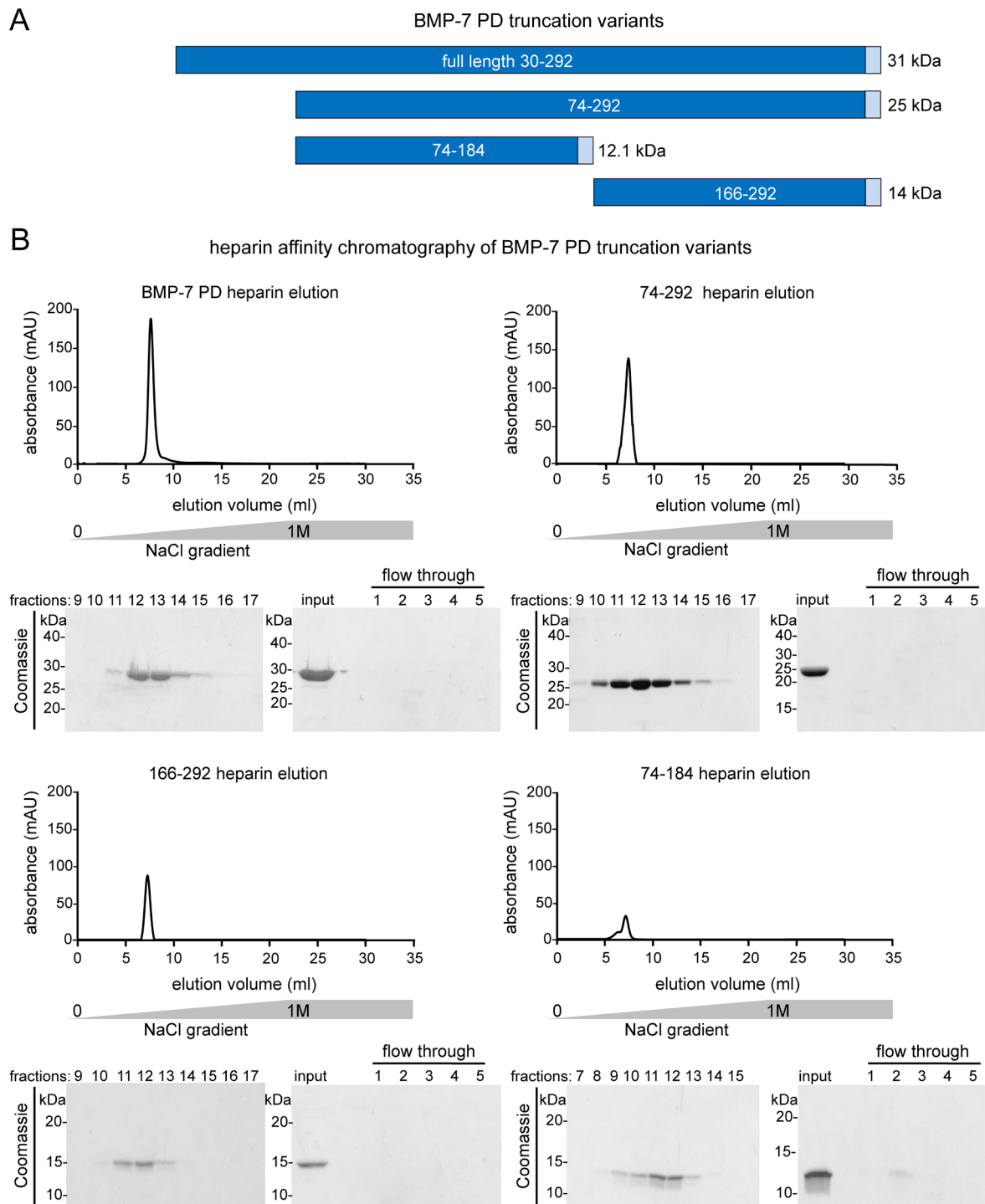
142 negative staining. The quantitative analysis of electron micrographs in 50 different fields revealed
 143 that 95% of all imaged CPLX particles make contact with heparin via the tip of the prodomain
 144 region (Fig. 4A), suggesting that the characterized heparin binding site of the GF moiety (31) is
 145 masked within the CPLX. Molecular modeling of the BMP-7 CPLX using the processed proactivin
 146 CPLX (PDB: 5HLZ) as template provided further insight into the potential heparin/ BMP-7 PD
 147 interaction interface (Fig. 4B).



148 **Figure 4: BMP-7 CPLX binds heparin with the PD arm region.** (A) Negative staining
 149 transmission electron microscopy of BMP-7 CPLX premixed with heparin chains. For the
 150 quantification, 500 BMP-7 CPLX particles were quantified per field in 50 different fields. (B)
 151 Structural model of BMP-7 CPLX built on processed proactivin (PDB: 5HLZ) PD: beige, GF: light
 152 gray, heparin chain: black dotted line, N and C-terminal ends of the modeled BMP-7 PD: orange.

153 Since the residues involved in that interaction interface are predicted to reside predominantly within
 154 the C-terminal part of the BMP-7 PD, we decided to confirm this experimentally. Therefore, BMP-7

155 PD truncation variants were produced in *E.coli* (Fig. 5A) and subjected to heparin affinity
156 chromatography in 8M urea followed by salt gradient elution. We found that N-terminal truncation
157 variants containing the C-terminal region as well as the full length BMP-7 PD showed considerable
158 strong binding to heparin and eluted at 200 mM or 280 mM NaCl respectively under denaturing
159 conditions. The truncation variant lacking the C-terminal region (74-184 aa) was additionally
160 detected in the flow through (Fig. 5B). In addition, when the BMP-7 full length precursor was
161 produced in *E. coli* and subjected to heparin affinity chromatography we detected a small
162 degradation fragment of about 15 kDa that eluted very late in the salt gradient thereby indicating a
163 high binding affinity. Mass spectrometry analysis after SDS-PAGE revealed that the small fragment
164 localized within the C-terminal part of the BMP-7 PD (Fig. S1). These data confirm that the high-
165 affinity heparin binding site in the BMP-7 PD resides within its C-terminal region.

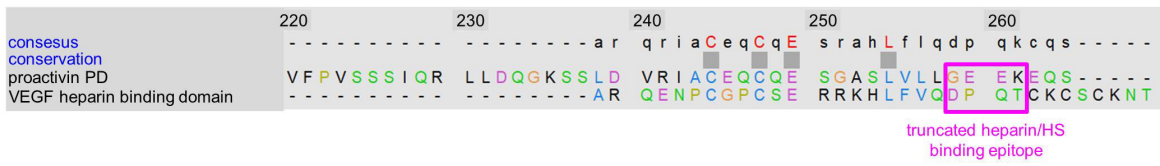


166 **Figure 5: Heparin affinity chromatography of BMP-7 PD and truncation variants showed that**
 167 **the heparin binding site resides towards the C-terminal region of the PD.** (A) Scheme showing
 168 production of full-length BMP-7 PD and truncation variants and their expected molecular weights.
 169 (B) SDS-PAGE and Coomassie staining of elution fractions after heparin affinity chromatography of
 170 full-length and BMP-7 PD truncations followed by gradient elution from 0-1 M NaCl under
 171 denaturing conditions. Heparin flow through was condensed using nickel chelate affinity
 172 chromatography and elution fractions were subjected to SDS-PAGE and Coomassie staining.

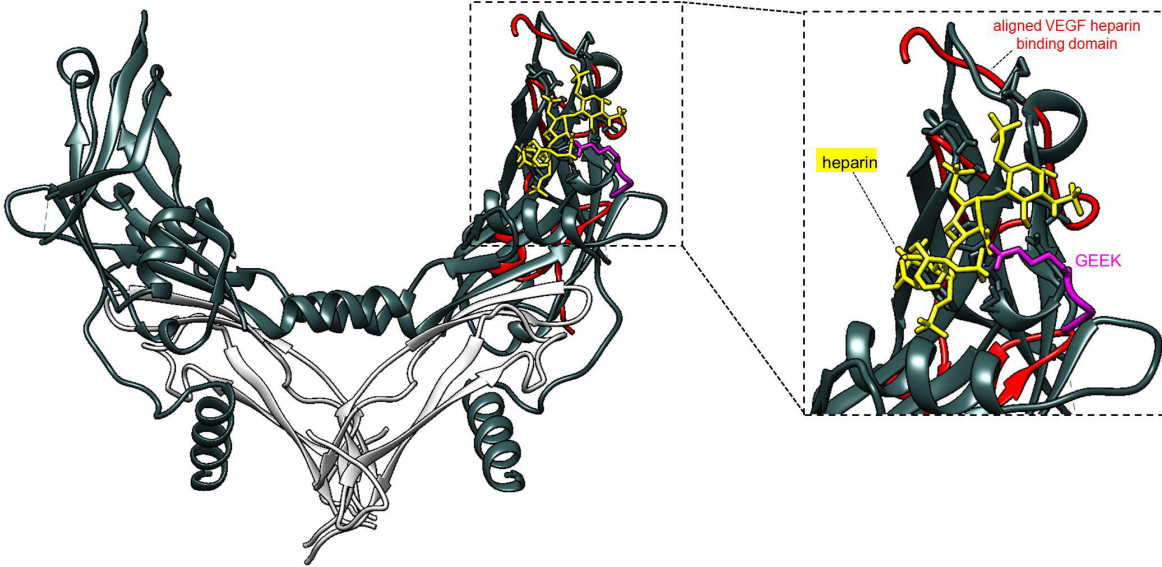
173 To fine map the BMP-7 CPLX heparin binding site within the C-terminal region of the BMP-7 PD,
174 we performed structural and sequence alignments of known GF heparin-binding motifs with TGF- β
175 superfamily members. Of the several growth factors tested, the vascular endothelial growth factor
176 (VEGF) heparin binding domain predicted correctly the characterized heparin/ HS binding site
177 within the activin PD (49). Chain-by-chain sequence alignment of the VEGF heparin binding domain
178 to the activin PD mapped the heparin/HS binding site to the PD arm region. This finding could be
179 supported by molecular docking experiments which also localized the heparin chains to the same site
180 of the proactivin atomic model (PDB: 5HLZ) (Fig. 6A). By applying the same methodology to the
181 BMP-7 CPLX structural model, we aligned the VEGF heparin-binding domain chain-by-chain to the
182 BMP-7 PD (Fig. 6B). This approach led to the identification of specific heparin binding residues
183 within the C-terminal portion of the PD which agrees with the obtained TEM results and mapping
184 data (Fig. 4, 5, 6). Manual positioning of the heparin chains within the PD arm region of the BMP-7
185 CPLX structural model guided by our TEM data, while simultaneously including the predicted
186 heparin binding residues confirmed their possible participation in the PD-heparin interaction
187 interface (Fig. 6B and S2). Furthermore, molecular docking of heparin to the atomic model of GDF-
188 8 (PDB: 5NTU), also suggested heparin binds within the prodomain arm region, which we had
189 previously shown to bind to the GAG chains of heparan sulfate proteoglycan (HSPG) perlecan (Fig.
190 S3) and (34).

A

sequence alignment of VEGF heparin binding domain and proactivin PD

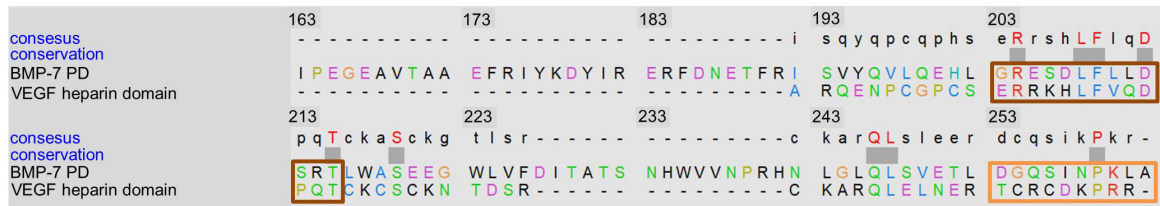


chain-by-chain alignment of the VEGF heparin binding domain to the modeled proactivin PD

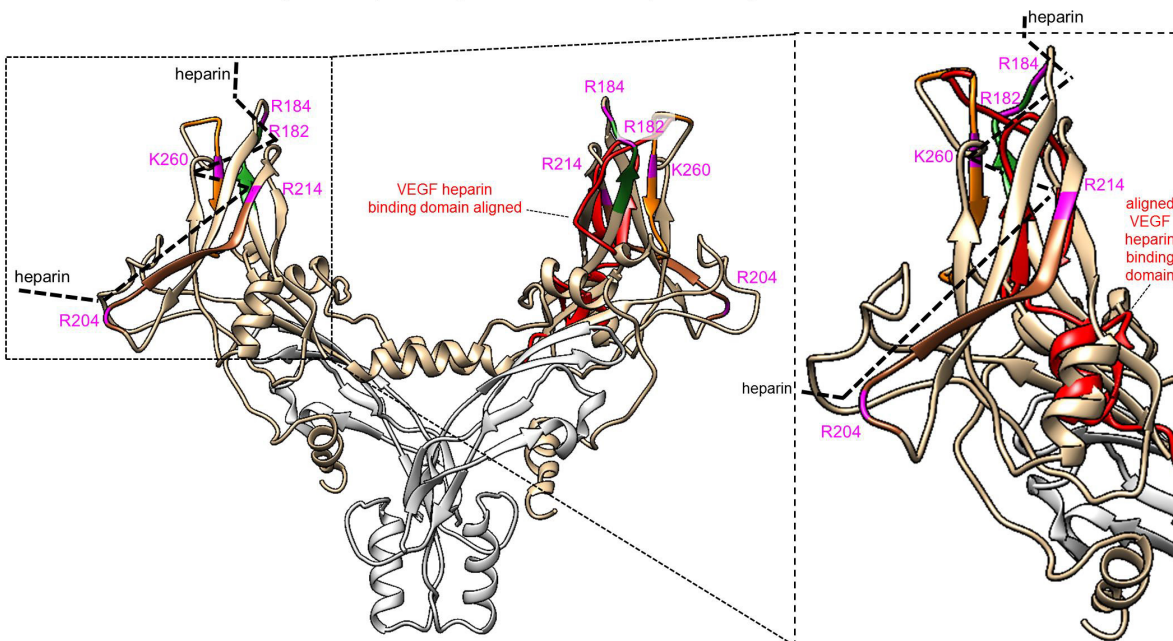


B

sequence alignment of VEGF heparin binding domain and the BMP-7 PD



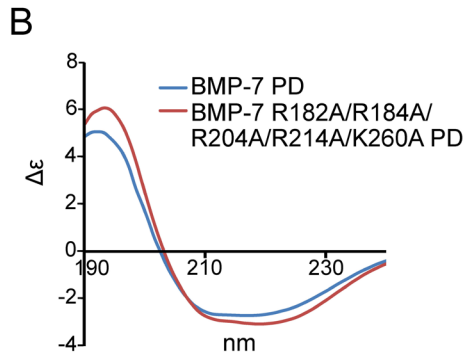
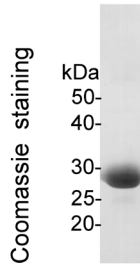
chain-by-chain sequence alignment of the VEGF heparin binding domain to the modeled BMP-7 PD



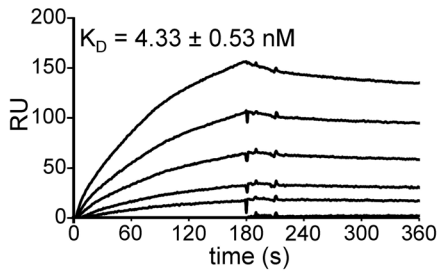
191 **Figure 6: VEGF heparin binding domain sequence alignment to predict the heparin/ HS**
192 **binding epitopes within proactivin and BMP-7 CPLXs.** (A) Chain-by-chain alignment of the
193 VEGF heparin-binding domain and molecular docking of heparin to the atomic model of the
194 processed proactivin (PDB: 5HLZ). (B) Chain-by-chain alignment of VEGF heparin binding domain
195 to BMP-7 PD within the BMP-7 CPLX structural model and identification of specific stretches
196 within the PD arm region.

197 To validate a participation of the identified PD residues in heparin binding we generated a
198 PD variant in which all positively charged residues of the interaction interface were replaced by
199 alanines. Circular dichroism analysis of the resulting BMP-7 R182A/R184A/R204A/R214A/K260A
200 variant showed that the secondary structure remained unaltered by the introduced mutations (Fig.
201 7B). ELISA-style binding studies showed that heparin binding was abolished for the BMP-7
202 R182A/R184A/R204A/R214A/K260A variant (Fig. 7D), while the capability to associate with the
203 BMP-7 GF was preserved (Fig. 7C). In addition, visualization of the BMP-7 CPLX structural model
204 surface indicated that four (R¹⁸², R¹⁸⁴, R²⁰⁴, R²¹⁴) out of five mutated residues are localized on the
205 surface of the PD arms where they are accessible by heparin chains (Fig. 7E), whereas K²⁶⁰ is hidden
206 at the back of the structure and further stabilizes the interaction with penetrating heparin chains.
207 Thereby, this heparin binding interface can be viewed as pocket where R204 and R214 control the
208 entry and R182 and R184 the exit site for the heparin chains (Fig. S2B). However, by examining the
209 sequence of the BMP-7 PD that participates in this pocket P¹⁴⁹-R²⁶⁷ also other positively charged
210 residues flank the identified five residues that may be also involved such as R¹⁵⁰, R¹⁵⁴ and R²⁶⁷.
211 However, when generating double mutants that neutralize the positive charge of the flanking
212 residues R150A/R154A or R260A/R267A, as well as the charge of the predicted entry site
213 R204A/R214A no significant reduction of the heparin binding affinity was observed (Fig. S2C).
214 These results indicate that all identified five residues participate in the heparin interaction interface
215 and contribute equally to the overall affinity of the BMP-7 PD to heparin.

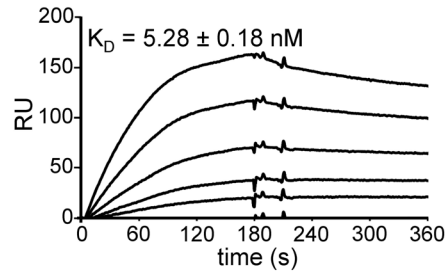
A expression of BMP-7 R182A/R184A/R204A/R214A/K260A PD



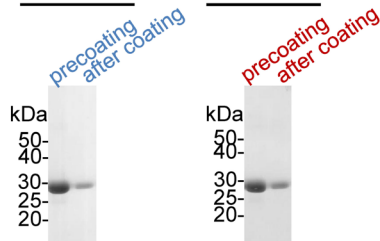
C BMP-7 GF injected onto BMP-7 PD on chip



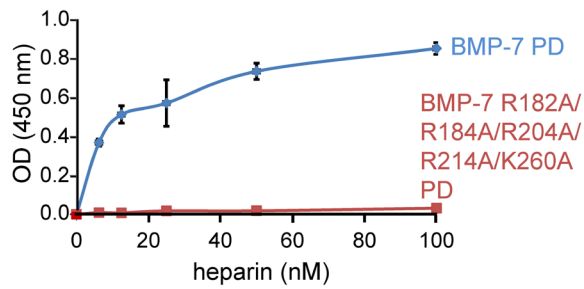
BMP-7 GF injected onto BMP-7 R182A/R184A/R204A/R214A/K260A PD on chip



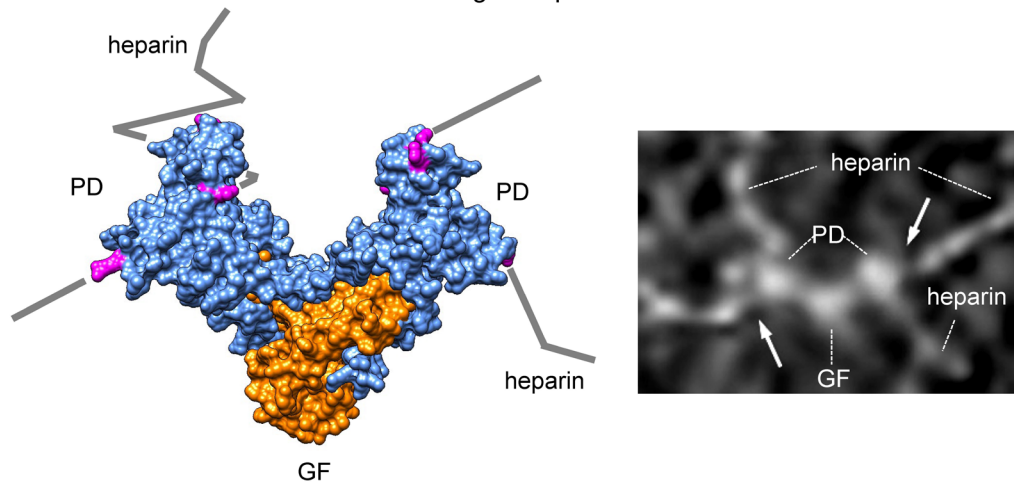
D BMP-7 PD BMP-7 R182A/R184A/R204A/R214A/K260A PD



heparin binding to coated BMP-7 PD



E surface model of BMP-7 CPLX binding to heparin



magenta: positively charged residues interacting with heparin

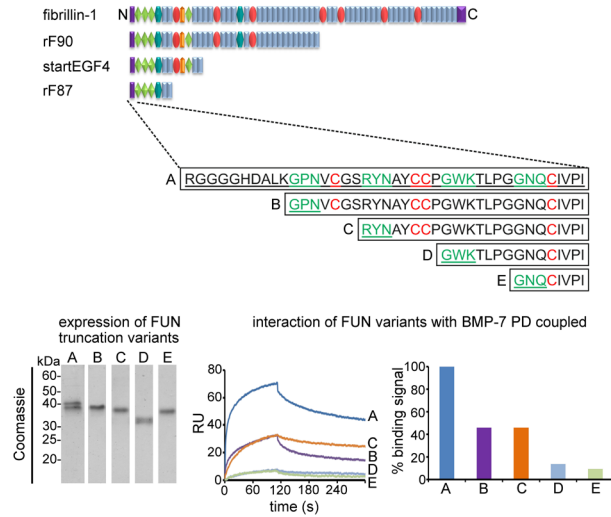
216 **Figure 7: Characterization of the BMP-7 CPLX heparin binding site.** (A) SDS-PAGE and
217 Coomassie staining after purification of the BMP-7 PD R182A/R184A/R204A/R214A/K260A
218 variant. (B) CD analysis showed that the BMP-7 PD R182A/R184A/R204A/R214A/K260A variant
219 folds normally. (C) SPR binding study showed that the immobilized BMP-7 PD
220 R182A/R184A/R204A/R214A/K260A variant has a similar binding affinity to flow over BMP-7
221 GF as wild-type BMP-7 PD. (D) (left) Coating efficiency of mutant and wild-type BMP-7 PD to
222 wells of microtiter plates was comparable as assessed by Coomassie staining of supernatant before
223 and after coating that was subjected to SDS-PAGE. (right) BMP-7 PD
224 R182A/R184A/R204A/R214A/K260A variant does not bind to immobilized heparin in solid-phase
225 ligand binding assay. (E) Surface model of the BMP-7 CPLX interaction with heparin. PD residues
226 are marked in blue, and GF residues are marked in orange. The identified five positively-charged
227 residues within the BMP-7 PD heparin-binding interface are marked in magenta.

228 *Comparison of the BMP-7 PD binding epitopes for heparin and fibrillin-1 suggests a structural*
229 *integration mode to control GF bioavailability*

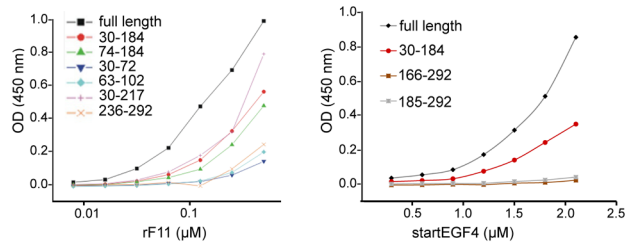
230 In order to better understand how heparin binding and fibrillin-1 binding can be integrated to control
231 BMP-7 CPLX bioavailability, the fibrillin-1/BMP-7 CPLX interaction interface was further
232 characterized (Fig. 8A and B). We therefore further narrowed down the BMP-7 PD binding epitope
233 within the fibrillin unique N-terminal domain (FUN) of fibrillin-1, but also the fibrillin-1 binding
234 epitope with the BMP-7 PD. Previously, we determined via SPR that the fibrillin-1 binding site for
235 the BMP-7 PD resides within Gly⁷⁴-Arg¹⁸⁴ (41), and the BMP-7 PD binding site within the fibrillin-
236 1 unique N-terminal domain (FUN) (33). Further, N-terminal truncation of FUN by 10 residues
237 resulted in 50% reduction of binding activity to the immobilized BMP-7 PD as assessed by SPR
238 binding studies, while the additional deletion of the subsequent 11 residues completely abolished the
239 interaction (Fig. 8A). This suggests that the BMP-7 PD binding site is mostly contained within
240 ⁴⁴RGGGGHDALKGPNVCGSRYNAYCCPGWKTLPG⁷⁶ of fibrillin-1. ELISA-style binding studies
241 with BMP-7 PD truncation variants confirmed the previously characterized fibrillin-1 binding site
242 within BMP-7 PD and further narrowed it down to Gly¹⁰² - Gly¹⁶⁶ (Fig. 8B) (41). The site was further
243 narrowed down by employing molecular docking of the closed-ring BMP-7 CPLX (42) to the NMR
244 solution structure of the FUN domain (PDB: 2M74) (50). After careful examination of 30 docking
245 models generated by the online server, the fibrillin-1 interaction epitope within the BMP-7 PD was

246 mapped to the stretch ¹⁵⁶FRFDLSK¹⁶² (Fig. 8C). Further, in the closed-ring/FUN domain interaction
247 model, the identified heparin-binding epitopes are hidden within the interior of the BMP-7 CPLX
248 closed-ring structure, whereas the fibrillin-1 identified stretch is exposed on the surface (Fig. 8C).
249 However, in the model of the bioactive, V-shape BMP-7 CPLX bound to heparin the identified
250 fibrillin-1 interaction stretch is masked, whereas the heparin-binding motif is available for interaction
251 (Fig. 8D). This suggests that the conformational change of the BMP-7 PD integrates the
252 bioavailability of the GF by restricting access to ECM protein or GAG binding sites.

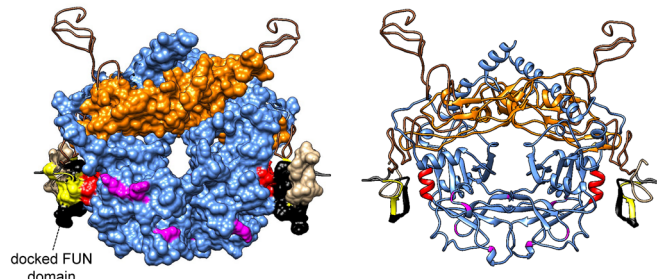
A mapping of BMP-7 PD binding epitope within FUN domain of fibrillin-1



B mapping of the fibrillin-1 binding epitope within BMP-7 PD



C Molecular docking of the closed-ring BMP-7 CPLX to the FUN domain of fibrillin-1



FUN domain epitopes:

SARGGGHDALKGPNVCGSRYNAYCCPGWK

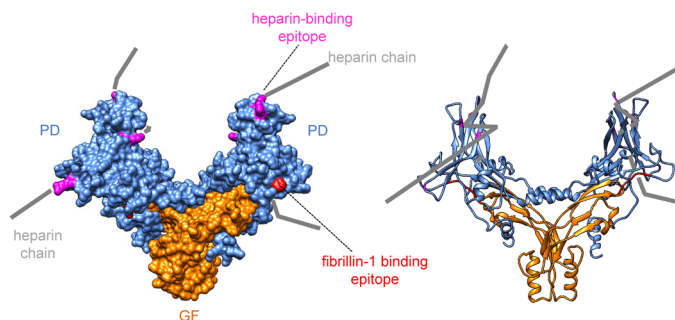
heparin binding residues:

R¹⁸², R¹⁸⁴, R²⁰⁴, R²¹⁴, K²⁶⁰

```

30      74
DFSLDNEVHSSFIHRRRLRSQERREMQRREILSILGLPHRPRPHLGQGHNSAPMFMLDL
      102
YNAMAVEEGGGPGGGGFSYPYKAVFSTQGPPASLQDSHFLTADMDVMSFVNLVE
      156 162 166      184
HDKEFFHPRYHHRFRFDLSKIPEGEAVTAAEFRIYKDYIRERFDNETFRISVYQVLQ
EHLGRESDFLLDSRTLWASEEGWLVFDITATSNHWVWVNRHNLGLQLSVETLDGQ
      292
SINPKLAGLGRHGPQNKQPFMVAFFKATEVHFRSIR
    
```

D Visualization of the fibrillin-1 epitope within the BMP-7 CPLX in open V-shape conformation



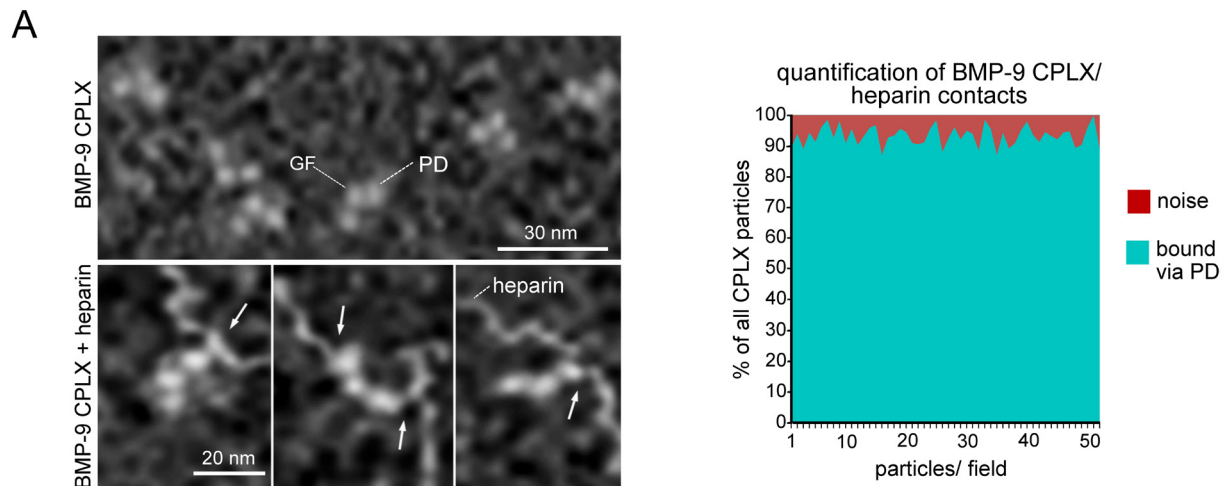
253 **Figure 8: Characterization of the fibrillin-1/ BMP-7 PD interaction epitope.** (A) (top) Domain
 254 structure of used fibrillin-1 proteins spanning the N-terminal region. (bottom, left) SDS-PAGE and
 255 Coomassie staining of rF87 and N-terminal truncation variants after streptavidin affinity
 256 chromatography. (middle) SPR interaction study of rF87 and N-terminal truncation variants with
 257 immobilized BMP-7 PD. (right) Percentage of binding signal detected in shown sensorgrams. (B)
 258 ELISA detection of fibrillin-1 fragments rF11 and startEGF4 incubated in increasing concentrations
 259 with coated BMP-7 PD (full length) and truncation variants. (C) Molecular docking of BMP-7 CPLX
 260 in closed-ring conformation to the NMR solution structure of the FUN domain of fibrillin-1 (PDB:
 261 2M74). Binding epitopes for fibrillin-1 (black/yellow) and heparin (magenta) within the BMP-7 PD
 262 are indicated in surface (left) and ribbon representations (right). (bottom) Residues of the identified
 263 fibrillin-1 binding epitope within BMP-7 PD are highlighted in red within the BMP-7 PD sequence.
 264 (D) Visualization of the fibrillin-1 and heparin binding epitopes within the BMP-7 CPLX open V-
 265 shape conformation in surface (left) and ribbon representations (right). PD: blue, GF: orange, BMP-7
 266 PD interacting epitopes within FUN: black and yellow, FUN domain interacting epitope in BMP-7
 267 PD: red, heparin interacting epitope in BMP-7 PD: magenta.

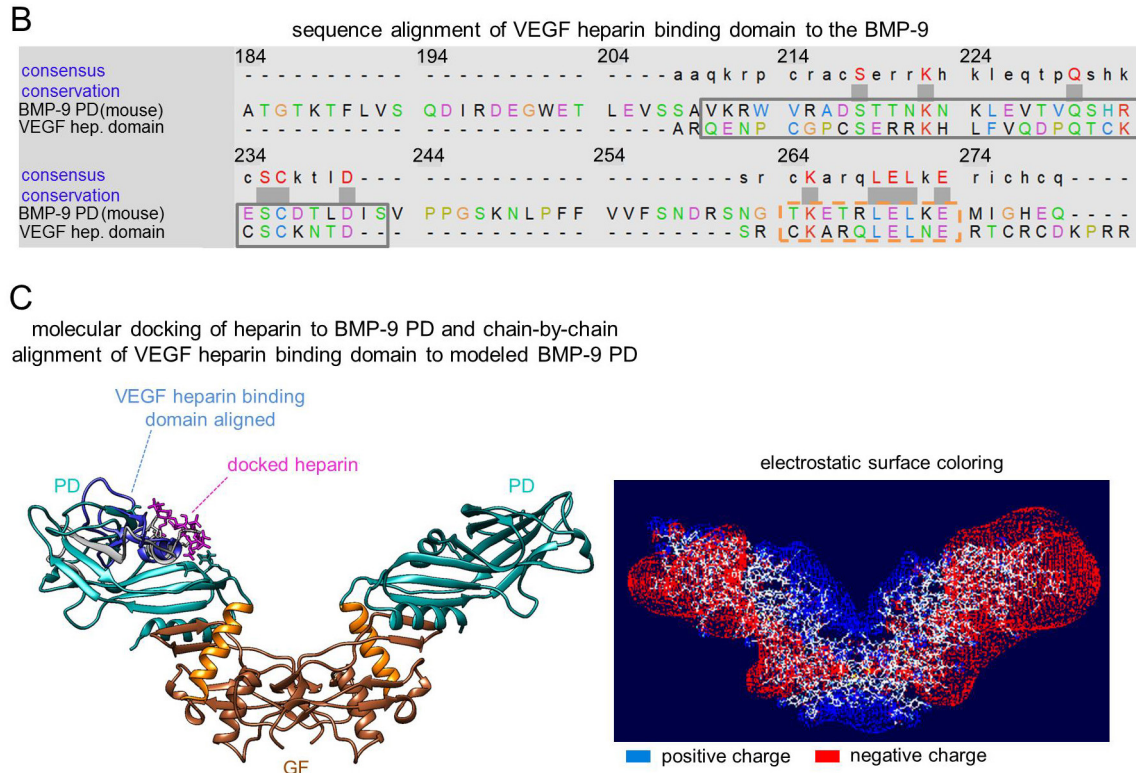
268 *Characterization of the BMP-9 CPLX heparin binding site*

269 Sequence alignments of the BMP-7, BMP-9 and BMP-10 PDs suggest that the identified heparin
 270 binding stretches within the PD arm region of BMP-7 may also be conserved in BMP-9 PD (Fig.
 271 9A). This is in line with the observation that the potentially conserved heparin-binding stretches
 272 between BMP-7 and BMP-9 PDs are absent in the BMP-10 PD where negatively-charged amino
 273 acid insertions are also present (Fig. 9A). In agreement with this finding, heparin affinity
 274 chromatography of the BMP-9 PD under denaturing conditions yielded a clear peak after salt
 275 gradient elution at 227 mM NaCl indicating robust binding (Fig. 9C) similar to the BMP-7 PD (Fig.
 276 5B), whereas BMP-10 PD failed to bind heparin (Fig. 9C). To further test whether the BMP-10
 277 CPLX is capable to interact with heparin, we purified BMP-10 CPLX from overexpressing HEK293
 278 cells and subjected it to heparin affinity chromatography after premixing with BMP-7 CPLX. SDS-
 279 PAGE analysis followed by Coomassie staining of elution fractions and flow through showed that
 280 only BMP-7 CPLX was eluted from the heparin column at 1M NaCl (Fig. S4) whereas BMP-10
 281 CPLX was exclusively detected in the heparin flow through (Fig. 9E). Next, we wanted to
 282 investigate whether the separated BMP-9 and -10 GFs are principally capable to interact with
 283 heparin. Sequence alignment of the BMP-7, -9, and -10 GF sequences suggested that the described

295 BMP-10 CPLX followed by SDS-PAGE and Coomassie staining. In addition, samples before
 296 subjection to the chromatography procedure (input) and the condensed flow through were analyzed.

297 To investigate the BMP-9 CPLX/ heparin interaction interface, commercially available
 298 BMP-9 CPLX was premixed with heparin followed by negative staining TEM. Consistent with the
 299 findings for BMP-7 CPLX (Fig.4A and B), BMP-9 CPLX showed contact with heparin chains via its
 300 PD arm region in 95% of particles examined in 50 different fields (Fig. 10A). Bioactivity
 301 measurements of BMP-9 CPLX when immobilized to heparin, showed that it remains bioactive
 302 similar to BMP-7 CPLX (Fig. S5). To narrow down the heparin binding site of the BMP-9 CPLX,
 303 the VEGF heparin domain was chain-by-chain aligned to the structure of the BMP-9 PD that is
 304 contained in the BMP-9 CPLX atomic model (PDB: 4YCG) (Fig. 10B and S6A and B). By
 305 employing molecular docking of heparin to the BMP-9 CPLX atomic model, it was possible to
 306 narrow-down the BMP-9 CPLX heparin binding site to specific stretches within the PD arm region
 307 (Fig. 10C, left and S6A) that are compatible with electrostatic surface coloring showing presence of
 308 positive charge locally (Fig. 10C, right).

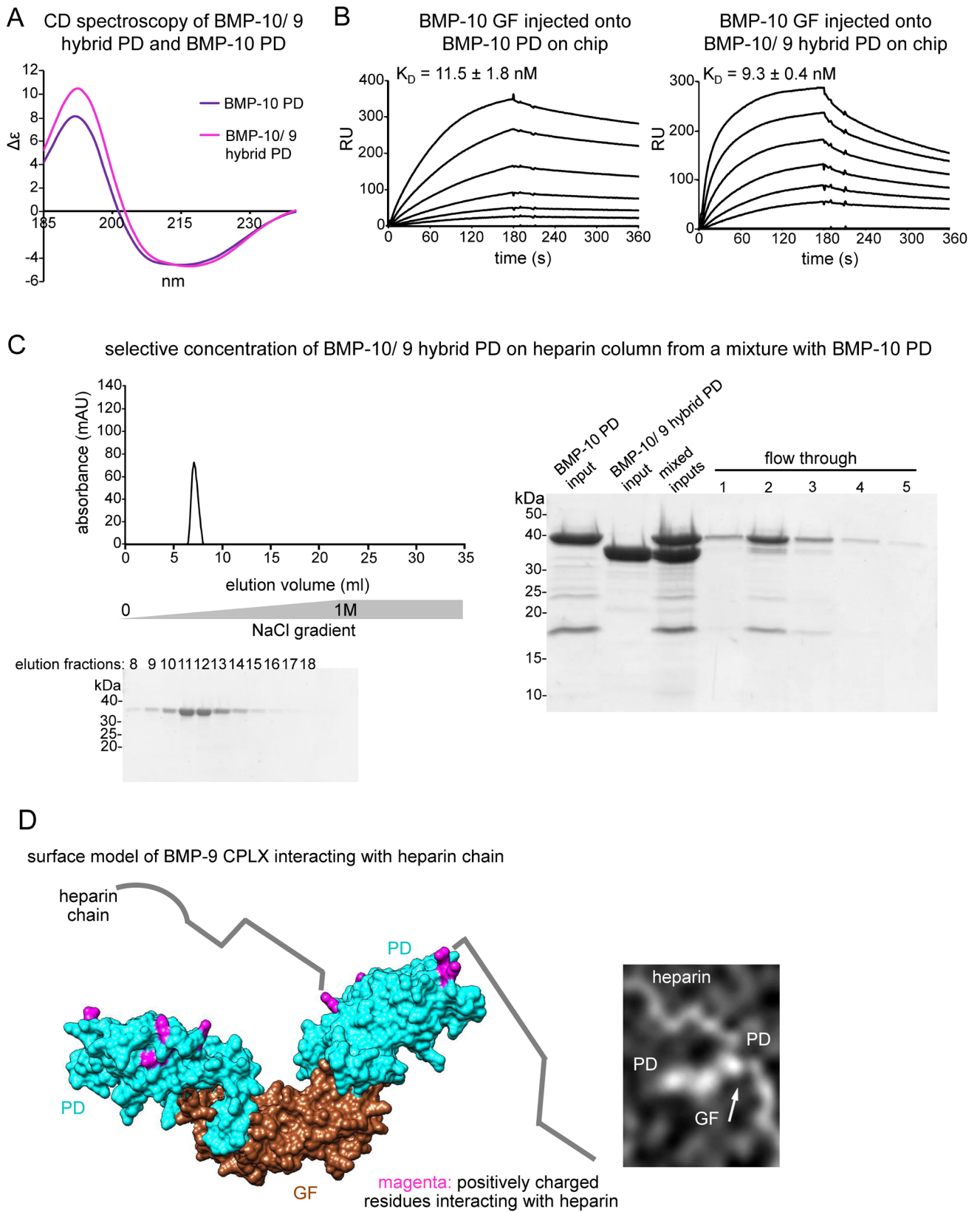




309 **Figure 10: BMP-9 CPLX binds heparin at the PD arm region.** (A) Negative staining transmission
 310 electron microscopy of BMP-9 CPLX premixed with heparin chains. For the quantification, 500
 311 BMP-9 CPLX particles per field were quantified in 50 different fields. (B) Chain-by-chain sequence
 312 alignment of the VEGF heparin binding domain to the BMP-9 PD of the BMP-9 CPLX atomic
 313 model (PDB: 4YCG). (C) (left) Molecular docking of heparin used as a ligand in same structure and
 314 (right) electrostatic surface coloring to identify positively- and negatively-charged patches in BMP-9
 315 CPLX surface model. Positive charge is marked in blue, negative charge is marked in red.

316 To experimentally assess whether these stretches harbor heparin binding potential, we
 317 introduced the predicted heparin-binding stretches of the BMP-9 PD into the BMP-10 PD by
 318 sequence swapping of the corresponding regions. The resulting BMP-10/ 9 hybrid PD was subjected
 319 to heparin affinity chromatography after premixing with the BMP-10 PD. As expected, only the
 320 BMP-10/ 9 hybrid PD was eluted from the heparin column in a salt gradient at 242 mM whereas the
 321 BMP-10 PD was exclusively detected in the flow through (Fig. 11C). CD analysis revealed that the
 322 secondary structure of the BMP-10/ 9 hybrid PD was similar to that of BMP-10 PD (Fig. 11A). Also
 323 SPR analysis showed that the BMP-10/ 9 hybrid PD showed a similar capability to interact with the
 324 BMP-10 GF as the BMP-10 PD (Fig. 11B). In addition, visualizing the surface of the BMP-9 CPLX
 325 atomic model (PDB: 4YCG), confirmed that the positively-charged residues of the identified

326 heparin-binding stretches within the BMP-9 PD are surface-exposed and therefore available for
 327 heparin interaction (Fig. 11D).

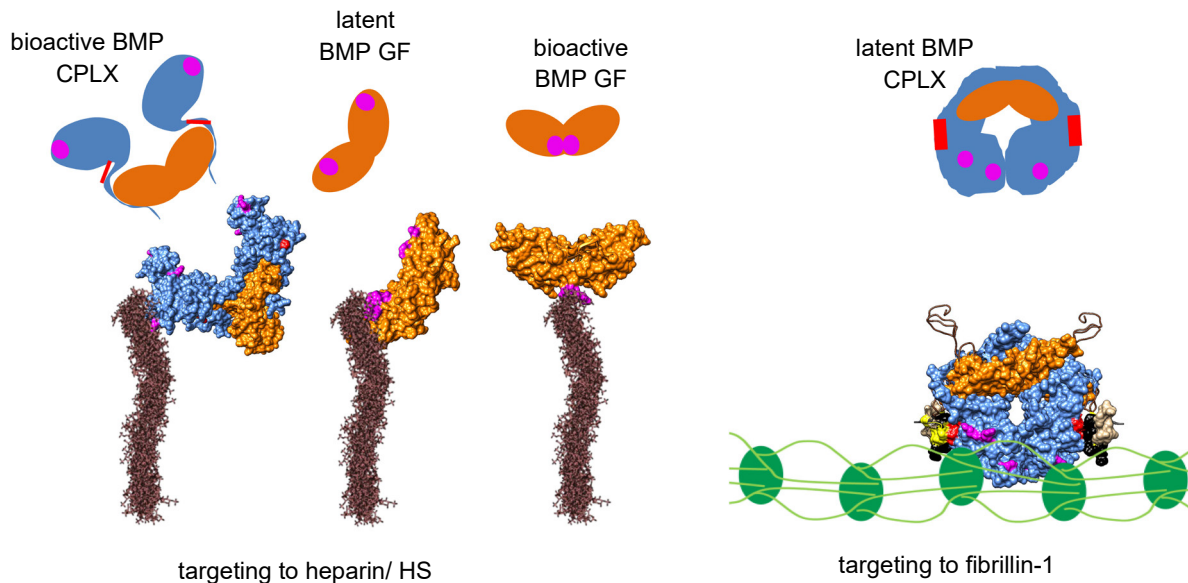


328 **Figure 11: Characterization of the BMP-9 CPLX heparin binding site.** (A) CD analysis of BMP-
329 10/ 9 hybrid PD and BMP-10 PD showed similar secondary structures. (B) SPR interaction study
330 showing that soluble BMP-10 GF has similar affinity to immobilized BMP-10/ 9 hybrid PD and
331 BMP-10 PD. (C) (left) Heparin affinity chromatography of the BMP-10/ 9 hybrid PD premixed with
332 BMP-10 PD under denaturing conditions. Elution was performed in a NaCl gradient, and elution
333 fractions were analyzed by SDS-PAGE followed by Coomassie staining. (right) Flow through of
334 experiment (left) was condensed using nickel chelate affinity chromatography and run on separate
335 SDS-gel together with sample inputs. (D) Surface model of BMP-9 CPLX interacting with heparin
336 chains. PD: cyan, GF: brown. Positively-charged residues of the characterized BMP-9 CPLX heparin
337 binding site are marked in magenta.

338 Discussion

339 In this study, we identified for the first time the heparin/ HS interaction interface of BMP-7 and
340 BMP-9 CPLXs and investigated the molecular requirements for bioactivity and latency of
341 complexed and free GF in presence and absence of heparin. Our results suggest a general mechanism
342 of how BMP CPLXs are targeted and concentrated to the ECM in bioactive, open V-shape
343 conformation to GAGs such as heparin/ HS. Thereby, BMP CPLXs specifically interact with GAGs
344 via positively-charged stretches at the tip of the PD arm region (Figs. 4A, 10A, 12). These heparin/
345 HS-binding stretches appear conserved between the in-solution bioactive proactivin, BMP-7 and
346 BMP-9 CPLXs (Fig. 9A1; S3A) and the latent GDF-8 CPLX (Fig. S3A) that has been shown to bind
347 to the side-chains of the HSPG perlecan (34). Heparin binding of in-solution bioactive BMP CPLXs
348 does not compromise their bioactivity suggesting PD displacement is possible on heparin (Figs. 1, 3,
349 S5, 12) and (37, 41). In addition, the heparin-binding epitope at the PD arm region of the BMP-7
350 CPLX seems to stabilize the bioactive open V-shape conformation and thereby rendering the
351 fibrillin-1 binding epitope in the PD less accessible (Fig. 8D). The opposite is true when the closed-
352 ring BMP-7 CPLX is formed that restricts heparin chain access by maintaining the heparin-binding
353 epitopes towards the interior of the structure (Fig. 8C and Fig. 12). Our results further show that
354 BMP-9 CPLX interacts with heparin in open V-shape conformation (Fig. 10A, 12) and remains
355 bioactive when immobilized to heparin (Fig. S5, 12). Similar to the BMP-7 CPLX (41), a closed-ring
356 shape conformation has been suggested for BMP-9 CPLX by molecular modeling approaches (35)
357 that also renders the conserved BMP-9 heparin binding epitopes inaccessible in that conformation

358 (Fig. 12). Similar to the closed-ring BMP-7 CPLX (41), receptor access to the BMP-9 GF is limited
 359 by the PD within the ring (Fig. 12) and (35).



360 **Figure 12: Heparin/ HS and fibrillin-1 regulate BMP bioactivity and GF receptor access via**
 361 **specific PD epitopes.** Overview model of BMP targeting and sequestration describing how BMP
 362 bioactivity is regulated by different ECM components. Bioactive V-shape BMP CPLXs are
 363 sequestered to fibrillin microfibrils in a closed-ring, latent conformation. In that conformation, PD
 364 binding to fibrillin-1 blocks receptor access to the GF (37, 41). However, when BMP-7 or -9 CPLXs
 365 are targeted to heparin/ HS the bioactive V-shape conformation is retained via specific interaction of
 366 conserved stretches within the PD arm region. In that conformation, GF is accessible and PD
 367 displacement on heparin/ HS upon receptor binding is possible (37, 41). In addition, BMP GFs can
 368 be targeted to heparin/HS in bioactive or latent conformation depending on the epitope that is
 369 utilized for heparin/HS interaction. PD: blue, GF: orange, heparin binding epitopes: magenta,
 370 fibrillin-1 binding epitope: red

371 It is an important question how BMP GF activity is regulated by the ECM in absence of the
 372 PD. Such mechanisms may be relevant for GFs that either do not well associate with their cognate
 373 PDs or that were liberated from ECM-stored pools via proteolytic degradation of their PD (38, 39,
 374 42). Thereby, the direct binding of BMP GFs by GAGs is an important mechanism. BMP GF
 375 binding to GAGs has been studied since years (28), but how these interactions modulate GF
 376 bioactivity is not fully understood. Our finding that immobilization of BMP-2 GF to heparin does not
 377 negatively impact its bioactivity (Fig. 1D, Fig. 12) is in line with previous studies (56, 57). Our

378 molecular docking results showed that heparin interacts with the N-terminal region of BMP-2 (31)
379 and therefore does not block BMPRI receptor binding (Fig. 2B). A similar binding mechanism can
380 be assumed for BMP-4 GF which belongs to the same TGF- β subgroup (Fig. 12).

381 In contrast, utilizing the heparin/HS binding site of BMP-7 GF, which is conserved in
382 members of the same subgroup (also including BMP-5, and -6) (31) confers latency by masking
383 crucial residues required for ActRII receptor engagement (Fig. 2A, Fig. 1C, Fig. 3, Fig. 12). Our
384 binding data also showed that the GFs of the BMP-9 and -10 subgroup do not interact with heparin,
385 which may be due to a conserved negative charge insertion in BMP-9 or -10 GF sequences (E³¹⁹ or
386 E³¹⁴ respectively) thereby replacing R⁴²¹ found in the heparin binding site of BMP-7 GF (Fig. 9A2).
387 Since also the BMP-10 PD was found not to interact with heparin, it can be assumed that only BMP-
388 9 CPLX can be concentrated to heparin/HS via the PD in bioactive conformation. This finding is
389 highly relevant for a better understanding of diseases implicating the involvement of dysregulated
390 BMP-9 and -10 signaling via ALK-1 such as HHT. In the current view, BMP-9 and -10 CPLXs are
391 produced by the liver and circulate with the blood to target endothelial cells of the vasculature (51,
392 52). Our findings suggest that BMP-9 can be preferentially concentrated to the endothelial
393 glycocalyx, which may potentiate its activity and enhance its signaling capability via prolonged
394 contact to co-receptors such as endoglin (53).

395 In the present study, it was possible to identify the heparin binding epitopes of the BMP-7
396 and BMP-9 CPLXs by utilizing chain-by-chain sequence alignments of the VEGF heparin-binding
397 domain to the respective BMP PDs (Fig. 6B, 10B and 10C, S6A and S6B). The same computational
398 method was able to predict correctly the heparin/ HS binding site within the PD arm region of the
399 proactivin CPLX despite part of it being deleted in order to produce the proactivin CPLX crystal
400 (Fig. 6A) and (54). While this method was accurate in identifying the heparin/HS binding sites of the
401 processed BMP-7 CPLX (built on processed proactivin CPLX), BMP-9 CPLX (PDB: 4YCG) and
402 processed proactivin CPLX (PDB: 5HLZ), it failed to map this site within the latent GDF-8
403 unprocessed dimer (PDB: 5NTU) and unprocessed proactivin dimer (PDB: 5HLY). This suggests
404 that lack of PD processing exposes several stretches at the PD-GF interface (Spanou et al., in
405 preparation#1) that mislocalize the VEGF-heparin binding domain away from the PD arm region.

406 Our study provides novel insight into how BMP PD epitopes integrate the bioavailability of
407 their cognate GFs by targeting exquisite sets of epitopes to ECM proteins or GAGs and thereby
408 allowing targeting and spatial concentration of BMP CPLXs to the extracellular microenvironment
409 in bioactive or latent conformation. This information has a high significance for therapeutic
410 interventions that currently rely on optimized BMP based treatments as in the context of non-healing
411 bone fractures, osteoporosis, and connective tissue disease.

412 **Experimental procedures**

413 *Antibodies and proteins*

414 For ELISAs the following antibodies were used: anti-His₆-HRP conjugated (130-092-785, Miltenyi
415 Biotec, Germany), Strep-Tactin HRP conjugated (2-1502-001, IBA, Germany), goat anti-biotin HRP
416 conjugated (ASB-OAIA00064, Biozol, Germany), rabbit anti-human BMP-7 GF (500-P198,
417 PeproTech, Rocky Hill, NJ), mouse anti-human/mouse/primate BMP-9 GF (MAB3209, R&D
418 Systems, Minneapolis, MN), mouse anti-human BMP-10 GF (MAB2926, R&D Systems). The
419 following proteins were commercially obtained: recombinant human BMP-7 GF (354-BP-010/CF,
420 R&D Systems), recombinant human BMP-9 GF (553104, carrier-free, Biolegend, San Diego, CA),
421 recombinant human BMP-9 CPLX (9624-BP-025/CF, R&D Systems), recombinant human BMP-10
422 GF (2926-BP-025/CF, R&D Systems).

423 *Cell culture*

424 HEK293 EBNA (Portland, Oregon, USA) and C2C12 cells (ATCC, Wesel, Germany) were
425 cultivated in high glucose DMEM media (31966047, Thermo Fisher Scientific, Waltham, MA, USA)
426 supplemented with 10% fetal bovine serum (FBS; F7524-500ML, Merck, Germany) and 1%
427 penicillin-streptomycin (Pen/ Strep) (15140-130, Life technologies, Carlsbad, CA, USA). BMP-7
428 CPLX over-expressing HEK293 cells clone 77 (Portland, Oregon, USA) were cultivated as
429 previously described (32) in presence of 250 µgr/ml geneticin without Pen/ Strep. All cells were
430 maintained at 37°C in a 5% CO₂, humidified incubator under sterile conditions.

431 *Transfection*

432 The constructs containing the N-terminal rF87 truncations with a C-terminal double strep-tag were
 433 transfected into HEK293 EBNA cells using FuGENE® transfection reagent (E2312, Promega,
 434 Madison, USA) according to the protocol provided by the manufacturer at a ratio of 3 µl FuGENE®
 435 to 1 µg DNA at 70% confluency. After 24 h of incubation, the FuGENE®/vector-containing medium
 436 was exchanged for high glucose DMEM medium containing 10% v/v FBS, 1% v/v Pen/ Strep, and 1
 437 µg/ml puromycin (P7255, Sigma-Aldrich, St. Luis, USA) to select for positive clones. Then
 438 puromycin concentration was adjusted to 0.5 µg/ml.

439 *Protein expression and purification*

440 The cDNA sequences coding for the human BMP-7 PD variants
 441 R182A/R184A/R204A/R214A/K260A, R150A/R154A, R204A/R214A, R260A/R267A with C-
 442 terminal His₆-tag were generated by gene synthesis as cDNA fragments (Life Technologies,
 443 Carlsbad, California, USA). The expression constructs coding for the human BMP-9 and BMP-10
 444 PDs were generated as previously described (42, 33, 34). The cDNA sequence coding for the BMP-
 445 10/ 9 hybrid PD with C-terminal His₆-tag was generated by gene synthesis (Life Technologies,
 446 Carlsbad, California, USA). More specifically the cDNA sequences encoding for specific human
 447 BMP-10 PD amino acid stretches were substituted for the cDNA sequences encoding for specific
 448 human BMP-9 PD amino acid stretches as shown in the following table:

BMP-10 PD amino acid stretch	BMP-9 PD amino acid stretch
¹⁷⁹ GERNMLVLV ¹⁸⁷	¹⁸⁴ SATETKTFLV ¹⁹³
²¹¹ QKSGSSTHQ ²¹⁹	²¹⁵ VRSDSTKSKNK ²²⁵
²²⁷ KHDEAEDASSGRLEIDTSAQ ²⁴⁶	²³³ HRKGCDTLDISVPPG ²⁴⁷
²⁷⁹ LPELDNLGL ²⁸⁷	²⁸¹ ESVLKKLSK ²⁸⁹

449 The resulting cDNA sequence was cloned via NdeI/ BamHI sites into a pET11a expression vector.
 450 The expression constructs coding for the full length human BMP-7 PD and truncations used in this
 451 study were generated as already described (41). Generation of expression constructs coding for rF11

452 with an N-terminal His₆-tag and startEGF4 with a C-terminal double strep-tag were previously
453 described (33, 34, 41). For the generation of the N-terminal rF87 truncations, the respective human
454 cDNA fragments with a C-terminal double strep-tag were cloned into pCEP-Pu vector that contained
455 the signal peptide of BM40 as described in (41). Processed BMP-7 CPLX with an N-terminal His₆-
456 tag and the untagged processed BMP-10 CPLX were overexpressed and purified in HEK293 cells as
457 previously described (32) and Spanou et al., in preparation#1. The fibrillin-1 fragments: rF11 with an
458 N-terminal His₆-tag , full length rF87 with a C-terminal double strep-tag and startEGF4 with a C-
459 terminal double strep-tag were expressed and purified as described previously (33, 34, 41). The N-
460 terminal rF87 truncations with a C-terminal double strep-tag were expressed and purified as the full
461 length rF87 with a C-terminal double strep-tag as previously described (41). Full length proteins of
462 the human BMP-7 PD and BMP-7 PD mutants as well as the full length proteins of the human BMP-
463 10 PD, BMP-9 PD and the BMP-10/ 9 hybrid PD sequences with a C-terminal his₆-tag were
464 expressed in *E.coli* BL21-CodonPlus Competent Cells (Agilent Technologies, Santa Clara, CA,
465 USA) and purified by Ni-NTA affinity chromatography as previously described (33, 34, 41, 42).

466 *Heparin/HS ELISA and ELISA*

467 For preparing the heparin surface, neutravidin protein (A2666, ThermoFisher Scientific, Waltham,
468 MA) was dissolved in 1 ml 1 × PBS so that a 5 mg/ml stock was obtained and protein was coated at
469 5 µgr/ml in 1 × PBS on Nunc MaxiSorp® flat-bottom 96 well plate (735-0083,VWR, Germany) O/N
470 at 4 °C. Wells were washed 5 × with 1 × TBS and biotinylated heparin was applied at 5 µgr/ml in 1x
471 PBS for 1 h, RT. Wells were washed 5 × with 1 × TBS and blocked with 3% BSA/ 1 × TBS for 1h,
472 RT. After 5 × washes with 1 × TBS, GFs were applied at 160 nM following serial dilution 1:2 in 1 ×
473 TBS supplemented with 0.6 M urea for 2h, RT. After washing 1 × with 1 × TBS/ 0.6 M urea and
474 subsequently 4 × with plain 1 × TBS, primary antibodies were applied in 2% BSA/ 1 × TBS for 1h,
475 RT. Next, 5 × washes with 1 × TBS and secondary antibody incubation in 2% BSA/ 1 × TBS
476 followed for 1h, RT. After 5 × washes with 1 × TBS, signal was developed by addition of 50 µlit 1-
477 Step Ultra TMB-ELISA substrate (34028, Thermo Fisher Scientific,Waltham, MA) and reaction
478 quenched by addition of 50 µlit 10% sulfuric acid. OD was measured at 450 nm using a Sunrise

479 microplate reader (Tecan). For coating BMP-2, BMP-7 GF or CPLX on commercially available
480 biotinylated heparin (HRN1-BN-1, Nanocs, MA, USA), the plate was blocked with 1× animal-free
481 blocker (SP-5030, Vector Labs) and proteins and antibodies were applied in same 1 × animal-free
482 blocker at 48 nM for BMP-2 or 32 nM for BMP-7 proteins. Washing steps were with 1 × TBS and
483 incubations were as previously described.

484 To assess BMP-7 PD and mutants for heparin binding on an ELISA plate, freshly-purified
485 proteins were coated on Nunc MaxiSorp® flat-bottom 96 well plate in 1 × PBS for 24 h at 4 °C. The
486 following day, the supernatant after coating was collected and TCA-precipitated to assess coating
487 efficiency. Plate was washed 5 × with 1 × TBS and blocked with 3% BSA/ 1 × TBS for 1h at RT.
488 Next, 5 × washes of 1 × TBS followed and biotinylated heparin was applied at 100 nM following
489 serial dilution 1:2 in 1 × TBS for 1h, RT. After 5 × washes with 1 × TBS, anti-biotin HRP conjugate
490 was applied at 1: 10000 in 3% BSA/ 1 × TBS for 1h, RT followed by 5 × washes with 1 × TBS and
491 signal development with the ELISA substrate as already described. Biotinylated heparin was
492 provided by T.I and M.K. unless indicated otherwise.

493 For testing BMP-7 proteins on HS, HS was coated on a Nunc MaxiSorp® flat-bottom 96
494 well plate O/N at 5 µgr/ml in 1x PBS. Plate was washed 5 × with 1 × TBS and blocked with 3%
495 BSA/ 1 × TBS for 1h at RT. The plate was washed 5 × with 1 × TBS before applying BMP-7
496 proteins at 32 nM following serial dilution 1:2 in 1x TBS/ 0.6 M urea for 2h at RT. Wells were
497 washed 1 × with 1 × TBS/ 0.6 M urea and then 4 × washes with plain 1 × TBS followed before
498 application of the primary rabbit anti-human BMP-7 GF in 2% BSA/ 1 × TBS for 1h at RT. Next,
499 plate was washed 5 × with 1 × TBS and incubation of anti-rabbit secondary antibody in 2% BSA/ 1
500 × TBS followed for 1h at RT. After 5 × washes of 1 × TBS, signal was developed with the ELISA
501 substrate as already described.

502 To assess BMP-7 PD truncations for binding to fibrillin-1, the truncations were coated at 0.1
503 µM in 1 × PBS, O/N at 4 °C on a Nunc MaxiSorp® flat-bottom 96 well plate. After 5 × washes with
504 1 × TBS-T, plates were blocked with 5% milk in 1 × TBS for 1h, RT and fibrillin fragments
505 containing the FUN domain interaction epitope were applied in 2% milk in 1 × TBS for 2h, RT.
506 After 5 × washes with 1 × TBS-T, the anti-strep or anti-His₆ HRP conjugates were applied at

507 1:10000 or 1:2000 respectively in 2% milk/ 1 × TBS for 1h, RT. Wells were washed 5 × with 1 ×
508 TBS-T and signal was developed with the ELISA substrate.

509 Coating on the ELISA plates was at 100 μlit per well. All washing steps were performed by adding
510 200 μlit of solution per well and all antibody incubation steps were performed by adding 100 μlit of
511 solution per well. BMP proteins were applied at 50 μlit per well. ELISA signal development was by
512 addition of 50 μlit 1-Step Ultra TMB-ELISA substrate (34028, Thermo Fisher Scientific, Waltham,
513 MA) and reaction was quenched by addition of 50 μlit 10% sulfuric acid. OD was measured at 450
514 nm.

515 *Bioactivity assays on heparin*

516 After coating the BMP-2 and BMP-7 proteins on a heparin surface at 48 nM or 32 nM prepared on
517 sterile 96-well plates (3599, Corning Costar, Corning, USA) for 2h at RT as previously described the
518 wells were washed 5 × with 1 × TBS. C2C12 cells in serum-free high glucose DMEM media were
519 seeded at 30000 cells per well (0.1 ml of media with cells per well) and incubated with the coated
520 material for 5 h at a 37 °C humidified incubator with 5% CO₂. Four wells of the 96-well plate were
521 assessed per condition. For coating the BMP-9 CPLX on a heparin surface to measure bioactivity,
522 the heparin surface was blocked with 3% BSA/ 1 × TBS for 1h at RT and after 5 × washes with 1 ×
523 TBS, BMP-9 CPLX was applied at 32 nM in 1 × TBS and allowed to incubate O/N in the coldroom
524 with mild shaking. After 5 × washes with 1 × TBS, C2C12 cells in serum-free high glucose DMEM
525 media were seeded at 30000 cells per well (0.1 ml of media with cells per well) and incubated with
526 the coated material for 5 h at a 37 °C humidified incubator with 5% CO₂. Four wells of the 96-well
527 plate were assessed per condition. After the incubation time had elapsed, serum-free DMEM was
528 discarded and 0.1 ml trizol was added to the adhered C2C12 cells. Material was frozen at -20 °C and
529 RNA extraction, reverse-transcription and qPCR followed on separate day to measure the *Id3* BMP
530 response as previously described (41, 42).

531 *TCA precipitation*

532 To assess the coating efficiency of the BMP-7 PD and mutants in the heparin ELISA experiments
533 after 24 h coating, the supernatants were collected, TCA-precipitated and resuspended in 8M urea, 1
534 M NaCl in 20 mM NaH₂PO₄ × 2H₂O, pH = 7.4 after 2 × ice-cold acetone washes.

535 *Heparin affinity chromatography*

536 BMP-7 PD and truncations, BMP-9 PD, BMP-10 PD and the BMP-10/ 9 hybrid PD were dialyzed
537 into freshly-filtered 8M urea, 20 mM NaH₂PO₄ × 2H₂O, pH = 7.4, by stirring O/N in the cold room
538 using 10 kDa cut-off mini dialysis caps (69572, Thermo Fisher, MA, USA). Heparin column
539 (17040601, Cytiva, Marlborough, MA, USA) was washed with sterile water and calibrated with the
540 calibration buffer: 8M urea, 20 mM NaH₂PO₄ × 2H₂O, pH = 7.4. Each sample was applied at n=9.68
541 nanomoles to ensure equal number of molecules is bound to the heparin column in 10 ml final
542 volume in the calibration buffer and the volume was run × 3 over the heparin column at RT. Column
543 was washed with 10 ml calibration buffer and sample was eluted at RT at a gradient of NaCl from
544 zero to 1 M prepared in the calibration buffer. Detailed NaCl gradient elution protocol used in the
545 AKTA purifier runs is provided in the section “Established protocols to study Bone Morphogenetic
546 proteins” of the materials and methods part of the thesis. Flow through was condensed over a Ni-
547 NTA column (74105, PureCube 100 Ni-NTA Agarose, Cube Biotech, Germany) and eluted in
548 calibration buffer supplemented with 250 mM imidazole at RT.

549 BMP-7 precursor and degradation fragment eluates after nickel affinity chromatography
550 were diluted in 8M urea, 20 mM NaH₂PO₄ × 2H₂O, pH = 7.4 to adjust imidazole concentration to 30
551 mM final. The diluted sample was then subjected to heparin affinity chromatography as described,
552 RT. Next, gradient elution followed at RT from zero to 1M NaCl in 8M urea, 20 mM NaH₂PO₄ ×
553 2H₂O, pH = 7.4 that was prepared using a gradient mixer and peristaltic pump.

554 For the heparin affinity chromatography of the BMP-7/BMP-10 CPLXs in mixture, cell
555 culture-derived CPLXs were dialyzed into 150 mM NaCl, 20 mM NaH₂PO₄ × 2H₂O, pH = 7.4, O/N
556 in the cold room by stirring. After washing with sterile water and calibrating the heparin column with
557 the native calibration buffer: 150 mM NaCl, 20 mM NaH₂PO₄ × 2H₂O, pH = 7.4, CPLXs were

558 applied in 1:1 stoichiometry in the native calibration buffer in 10 ml final volume that was run 3 ×
559 over the heparin column in the cold room. Next the heparin column was washed with native
560 calibration buffer for 10 ml and stepwise elution took place in 20 mM NaH₂PO₄ × 2H₂O, pH = 7.4
561 supplemented with 0.25 M NaCl (eluted for 6 fractions), 0.5 M NaCl (eluted for 7 fractions), 1 M
562 NaCl (eluted for 6 fractions) and 2M NaCl (eluted for 11 fractions) in the cold room. The volume of
563 each fraction was: 0.5 ml. Heparin flow through was condensed over an anion exchanger (29051325,
564 Cytiva, Marlborough, MA, USA) and subsequently over Ni-NTA column in the cold room.

565 *CD spectroscopy*

566 BMP-7 PD, the BMP-7 PD mutant R182A/R184A/R204A/R214A/K260A and BMP-10 PD were
567 dialyzed into 5 mM perchloric acid for 2 overnights in the cold room. BMP-10/ 9 hybrid PD required
568 dialyzation into 20 mM perchloric acid for 2 overnights in the cold room to retain solubility. CD
569 spectra were recorded using a Jasco J-715 spectropolarimeter in a 1-mm path length quartz cell
570 (Hellma, Germany) from 260 to 170 nm at 20 °C. BMP-7 PD and mutant were measured at 0.2
571 mg/ml whereas BMP-10 PD and the BMP-10/ 9 hybrid PD were measured at 0.1 mg/ml. Buffer
572 contribution was subtracted, theta/machine units were converted to Δε and percentage secondary
573 structure was calculated using the CDSSTR algorithm (Dichroweb server).

574 *Surface Plasmon Resonance*

575 CM5 chips (BR100012, Cytiva, Marlborough, MA, USA) were calibrated with the running buffer
576 HBS-EP (BR100188, Cytiva, Marlborough, MA, USA) and BMP-7 PD, the BMP-7 PD mutant
577 R182A/R184A/R204A/R214A/K260A, BMP-10 PD and the BMP-10/ 9 hybrid PD were
578 immobilized on the chips via amine coupling (BR100050, Cytiva, Marlborough, MA, USA) at 400
579 RU for BMP-7 PD, BMP-7 PD mutant and BMP-10 PD. The BMP-10/ 9 hybrid PD was
580 immobilized at 350 RU. The immobilization was accomplished by activating the chip surface for 7
581 min with “1-1” mixture of EDC/NHS at 5 μlit/min flow rate. After the 7-min activation was
582 complete, the PD to be immobilized was injected in 10 mM sodium acetate buffer until the desired
583 response units (RU) was reached. Next, chip surface was inactivated by injection of 1M

584 ethanolamine-HCl, pH=8.5 and further calibrated with the HBS-EP running buffer. BMP-7 GF (at 80
585 nM following serial dilution 1:2) or BMP-10 GF (at 160 nM following serial dilution 1:2) was flown
586 over as analyte in HBS-EP buffer. Measurements were performed using a Biacore® 2000 system
587 (Biacore AB, Uppsala, Sweden). Kinetic constants were calculated as described previously (41).

588 For assessing the effect of heparin interaction for BMP-7 receptor binding, the ActRIIB receptor
589 ectodomain was immobilized via amine coupling as explained previously on a CM5 chip that was
590 pre-calibrated in HBS-EP buffer. 80 nM biotinylated heparin following serial dilution 1:2 was mixed
591 with 20 nM of BMP-7 proteins and subsequently injected to the immobilized receptor.

592 To narrow down the BMP-7 interacting epitope within the FUN domain of fibrillin-1, a CM5 chip
593 was calibrated with HBS-EP buffer and BMP-7 PD was immobilized via amine coupling as
594 explained previously at 1000 RU. Next, the FUN domain N-terminal truncation variants were
595 injected on chip at 100 nM in HBS-EP buffer.

596 For the BMP-7 or BMP-10 GF/ heparin SPR binding study, the Sierra SPR-32 instrument (Bruker,
597 Hamburg, Germany) was employed. PEG chip (Xantec, Düsseldorf, Germany) was calibrated in
598 HBS-EP buffer supplemented with 1M urea (running buffer) and neutravidin was coupled via the
599 amine coupling immobilization technique explained previously. Next, biotinylated heparin
600 (experiment surface) or biotin (control surface) was flown over in 1x PBS. After calibration of the
601 experiment and control surfaces with HBS-EP/ 1M urea buffer, BMP-7 or BMP-10 GFs were
602 injected in the experiment and control surfaces at 60 nM following serial dilution 1:2 in HBS-EP/
603 1M urea buffer. The final NaCl concentration in the HBS-EP/ 1M urea buffer was at 150 mM to
604 mimic the physiological condition. RU of the control surfaces were subtracted from the RU of the
605 experiment surfaces for the BMP-7 or BMP-10 GFs and graphs were plotted using the Sierra
606 Analyser software (Bruker, Hamburg, Germany).

607 *Negative staining transmission electron microscopy and quantification*

608 Purified, cell culture-derived BMP-7 CPLX or purchased BMP-9 CPLX were premixed with heparin
609 chains (B9806, Sigma, St. Luis, USA) and subsequently adsorbed to negative staining EM grids for
610 transmission electron microscopy. To calculate the percentage of molecules binding to heparin

611 chains utilizing the PD arm region, 500 molecules/ field and 50 fields in total were analyzed for
612 BMP-7 or BMP-9 CPLX samples.

613 *Molecular modeling*

614 The structural model of the processed BMP-7 CPLX was built on the processed proactivin atomic
615 model (PDB: 5HLZ) by modeling individual BMP-7 PDs on the proactivin PDs using the phyre2
616 server. Next, the modeled BMP-7 PDs as well as the crystal structure of the BMP-7 GF (PDB: 1LXI)
617 were aligned chain-by-chain to the processed proactivin atomic model using the “Match Maker” tool
618 of the UCSF Chimera software. To visualize the identified heparin-binding BMP-7 PD residues, the
619 surface of the BMP-7 CPLX model was shown and the identified residues were labeled. Similarly, to
620 visualize the identified heparin-binding BMP-9 PD residues, the surface of the BMP-9 CPLX atomic
621 model (PDB: 4YCG) was shown and the identified residues were labeled. All model manipulations
622 were performed with the UCSF Chimera software.

623 *VEGF heparin binding domain predictions*

624 To identify heparin binding epitopes within the processed PDs of BMP CPLXs, the VEGF heparin
625 binding domain NMR solution structure (PDB: 2VGH) was aligned chain-by-chain to the processed
626 PD in question and a sequence alignment of the two was performed using the UCSF chimera
627 software. The method identified stretches within the PD with the highest-homology to the VEGF
628 heparin binding domain.

629 *Molecular docking*

630 BMP-7 PD modeled on processed proactivin PD, the processed proactivin CPLX atomic model
631 (PDB: 5HLZ), the processed BMP-9 CPLX atomic model (PDB: 4YCG), the promyostatin (PDB:
632 5NTU), the BMP-7 GF unified model (PDB: 1LXI) and the BMP-2 GF unified model (PDB:
633 6OMN) were docked to heparin that was used as a ligand. To visualize the docked heparin chains in
634 the BMP-2/BMPRI interaction model (PDB: 1REW), the generated docking model of BMP-2 GF to
635 heparin was overlaid on the BMP-2/BMPRI interaction model using the “Match Maker” tool of the

636 UCSF chimera software. The closed-ring BMP-7 CPLX model (42) was docked to the NMR solution
637 structure of the fibrillin-1 FUN domain (PDB: 2M74) that was used as ligand. All molecular docking
638 experiments were performed by employing the ClusPro 2.0 server. Visualization of the
639 heparin/protein and protein/protein interactions after docking was with the UCSF chimera software.

640 *Electrostatic surface coloring*

641 The atomic models of promyostatin (PDB: 5NTU) and BMP-9 CPLX (PDB: 4YCG) were visualized
642 using the Swiss-PdbViewer 4.1.0 and electrostatic potential was computed by employing the
643 Coulomb method.

644 **Acknowledgments**

645 We thank Marina Tauber and Niklas Sonntag (University of Cologne) for excellent technical
646 assistance. We also thank the CECAD proteomics facility of the University of Cologne for analyzing
647 mass spectrometry data. HS preparations were a generous gift from Prof. Dr. Kay Grobe (University
648 of Münster). Funding for this study was provided by the Deutsche Forschungsgemeinschaft (DFG,
649 German Research Foundation) project number 73111208 (SFB 829/B12 and 397484323
650 TRR259/B09) to G.S. Molecular graphics and analyses were performed with the UCSF Chimera
651 package. Chimera was developed by the Resource for Biocomputing, Visualization, and Informatics
652 at the University of California (San Francisco, CA) (supported by NIGMS, National Institutes of
653 Health, Grant P41-GM103311).

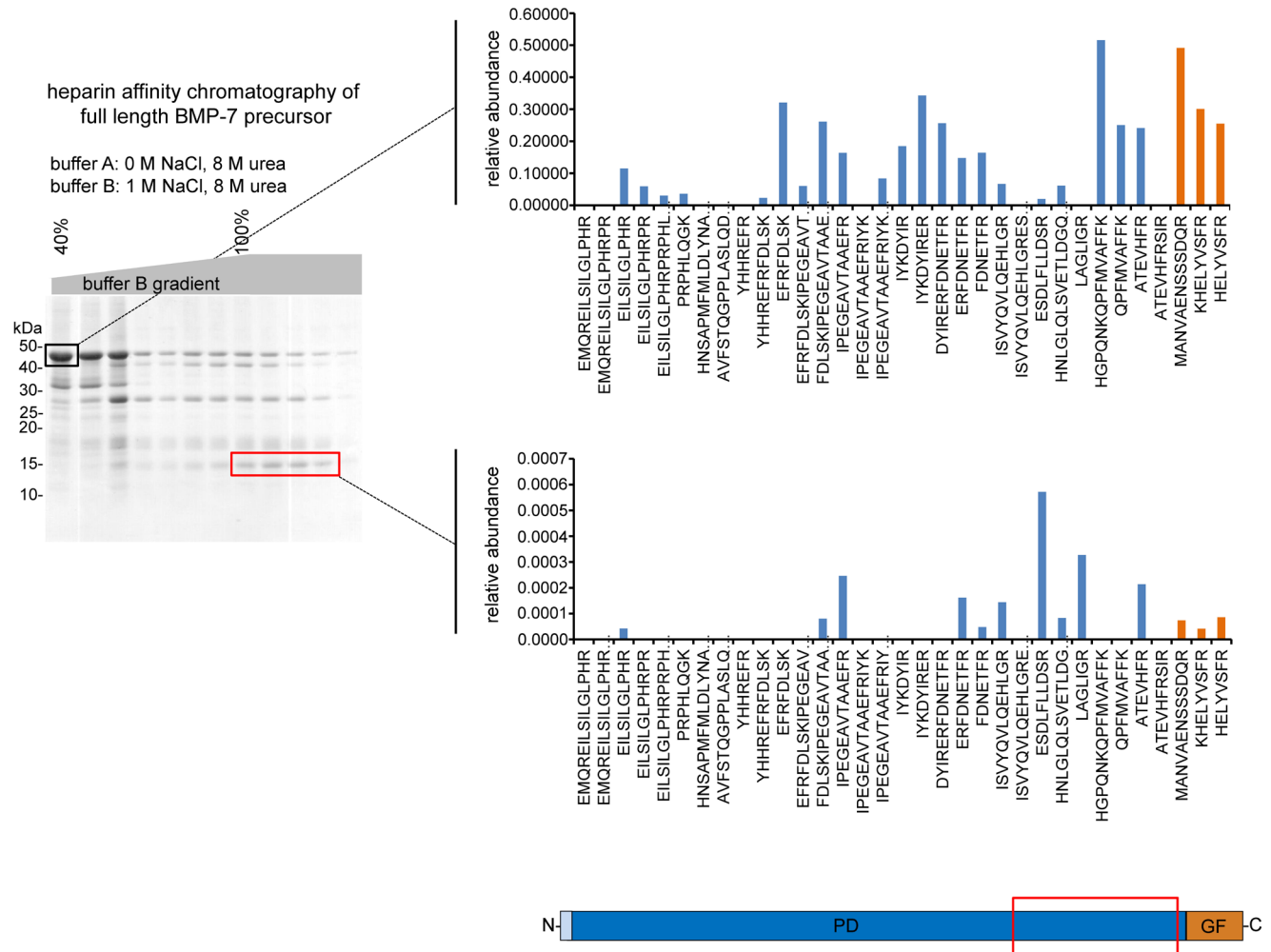
654 **Author contribution statement**

655 C.E.S.S. and G.S. conceived the study. C.E.S.S., A.C., S.D., A.P.W., M.M., S.L. performed research
656 and analyzed data. T.I., and M.K. provided reagents. C.E.S.S., and G.S. wrote and edited the
657 manuscript. G.S. acquired funding for this study.

658 **Conflict of interest**

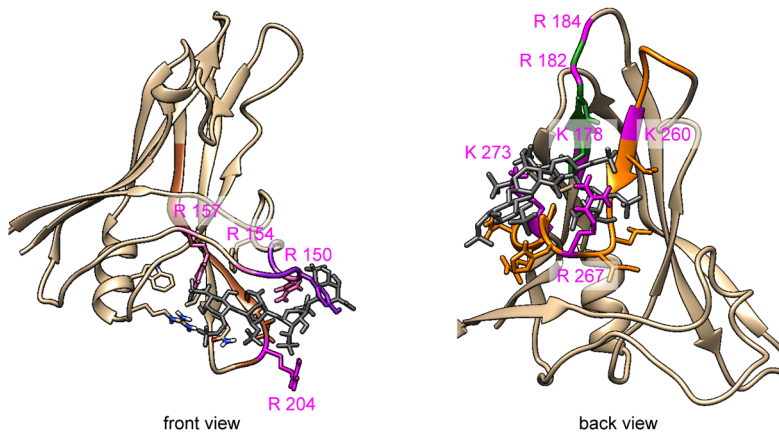
659 The authors declare no conflict of interest.

660 Supplementary material

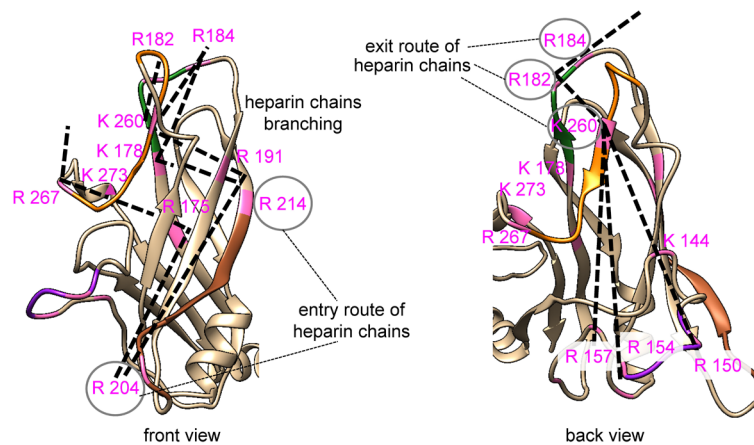


661 **Figure S1: Relative abundance of peptides within the BMP-7 precursor or the strong heparin-**
 662 **binding BMP-7 fragment detected after heparin affinity chromatography followed by mass**
 663 **spectrometry.** BMP-7 precursor and resulting fragments were subjected to heparin affinity
 664 chromatography under denaturing conditions (8M urea) and eluted in a gradient of NaCl from 0-1 M.
 665 The elution fractions were run on SDS-PAGE and respective bands of the BMP-7 precursor or the
 666 strong heparin-binding fragment were gel-excised and then subjected to mass spectrometry. The
 667 relative abundance plotted corresponds to the mass spec signal intensity of individual peptides in the
 668 precursor or the strong heparin-binding fragment divided by the average band intensity of all
 669 peptides detected in the precursor or the strong heparin-binding fragment.

A molecular docking with heparin as ligand to identify the heparin chain entry/ exit points



B positioning of heparin chains within BMP-7 PD arm region

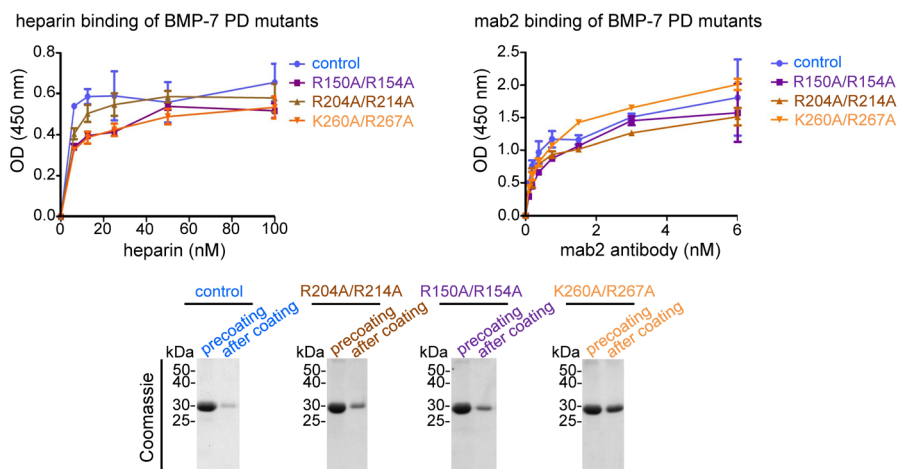


crucial residues controlling heparin binding:
R182, R184, R204, R214, K260

¹⁴⁹PRYHHR¹⁵⁴
¹⁷⁸KDYIRER¹⁸⁴
²⁰³GRESDFLLDSR²¹⁴
²⁵⁶SINPKLAGLIGR²⁶⁷

----- heparin chain

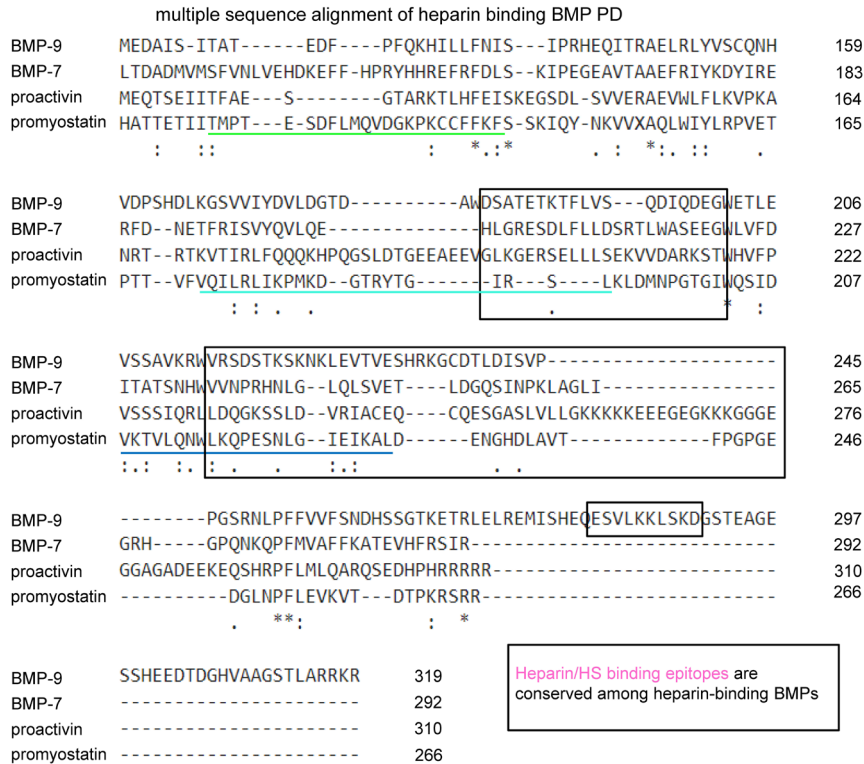
C neutralization of two positive charges within a single stretch does not abolish heparin binding



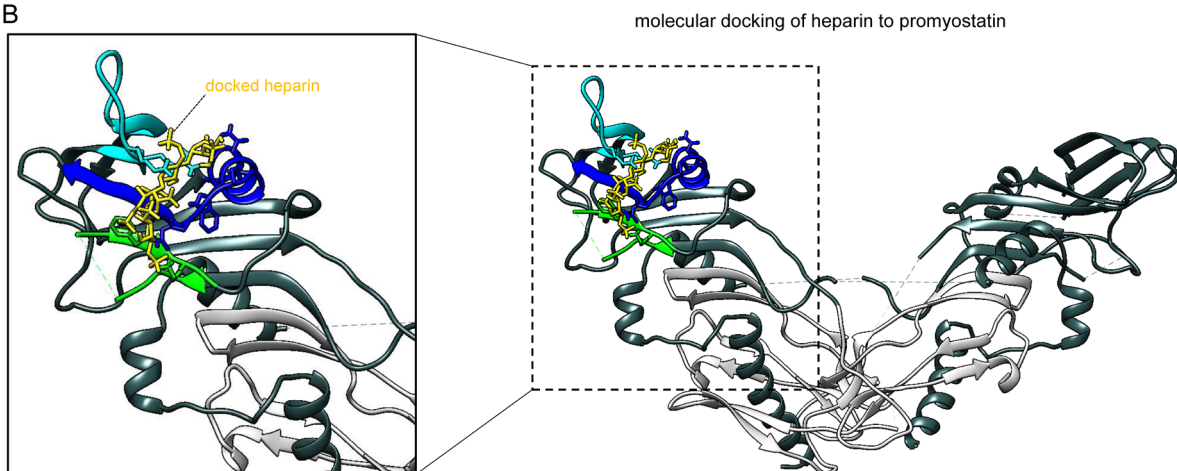
670 **Figure S2: Molecular docking of heparin and positioning of the heparin chains within the**
671 **modeled BMP-7 PD shows involvement of specific residues.** (A) Molecular docking of the heparin
672 chains into the (left) ¹⁴⁹PRYHHR¹⁵⁴, (right) ²⁰³GRESDFLLDSR²¹⁴, (right) ²⁵⁶SINPKLAGLIGR²⁶⁷

673 stretches. (B) Manual positioning of the heparin chains at the stretches identified from (A) and
 674 indication of potential routes heparin chains follow within the BMP-7 PD to penetrate the PD
 675 effectively for robust binding. (C) (top, left) Heparin binding to coated BMP-7 PD and variants. (top,
 676 right) Detection of coated BMP-7 PD and variants by mab2. (bottom) Assessment of coating
 677 efficiency of BMP-7 PD and variants to microtiter wells by SDS-PAGE followed by Coomassie
 678 staining.

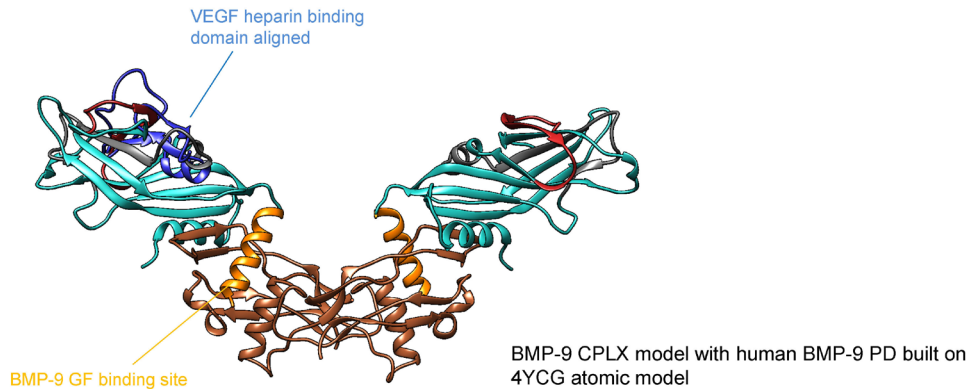
A



B



B. Sequence alignment chain-by-chain of the VEGF heparin binding domain to the modeled human BMP-9 PD built on the atomic model of the BMP-9 CPLX (PDB: 4YCG)



stretch 1 VKRWVRSdstksknkLeVtVESHrKGCdTLdIS
 stretch 2 **DSATETKtFLvsQDIQDEGW**
 stretch 3 ESvLkKlSkD (not covered by atomic model, deduced from sequence alignments using clustal omega)

*Sequence alignment of the VEGF heparin binding domain to the BMP-9 PD (human)

Consensus	183	193	203	213	223
Conservation	d p a s	E r k k h L	f s Q D i Q d c k c	s c k	-----
BMP-9 PD (human)	DSATETKtFLvsQDIQDEGW ETLVSSAVK RWVRSdstks knkLeVtVes				
VEGF hep. domain	GPCSERKHL FVQDPQTCKC SCK-----				
Consensus	233	243	253	263	273
Conservation	-----	-----	-----	d h s	S r c K a r q L E L r E r i s h c
BMP-9 PD (human)	HRKGCdTLdI	SVPPGSRNLP	FFVVFsnDHS	SGTKETRLLEL	REMIshE---
VEGF hep. domain	-----	-----	NTD	SRCKARQLEL	NERTCRCdKP

C. Identified heparin-binding epitopes of BMP-9 PD

BMP-9 PD (human)

KPLQSWGRGSAGGNAHSPLGVPGGGLPEHTFNLMFLENVKVDFLRSLNLSGVPsQDKTRVEPPQYMidLYNRYTSDKSTTPASNIVRSFSMEDAISITATEDFPFQKHILLFNISIPRH
 EQITRAELRLYVSCQNHVDPSHDLKGSVVIYDVLdGTDAWD**SATETKtFLvsQDIQDEGW**ETLEVSSAVKRWVRSdstksknkLeVtVESHrKGCdTLdISVPPGSRNLPFFVVFsnDHS
 SGTKETRLLELREMIshEQ**ESvLkKlSkD**SGTEAGESSHEEDTDGHVAAGSTLARRKR

BMP-10/ 9 hybrid PD (human sequences)

SPIMNLEQSPLEEDMSLFgDVFSEQDgVDFNTLLQSMKDFLkTLNLSDIPTQDSAKVDPPEYMLLYNKfATDRtSMPSANIrsFKNEdLFSQPVsFNGLRKYPLLFNVsIPHHEEVIAMe
 LRlyTLVQRDRMIYDgVDRKITIFeVLESKGDNE**SATETKtFLvs**GEIYGTNSEWETFDVTDAIRRWVRSdstksknkLeVhIEShrKGCdTLdISVPPGNkHNPLLIVfSDDQSSDKERKEELN
 EMISHEQ**ESvLkKlSkD**SfSSGPGEeALLQMRSNIYDSTARIRr

691 **Figure S6: Generation of the BMP-10/ 9 hybrid PD.** (A) Identification of heparin binding epitopes
 692 within BMP-9 PD of the BMP-9 CPLX atomic model by molecular docking of heparin and chain-
 693 by-chain sequence alignment of the VEGF heparin binding domain to the modeled mouse BMP-9
 694 PD. (B) Same as (A) but the VEGF heparin binding domain is now aligned to the modeled human
 695 BMP-9 PD. (C) Identified heparin binding epitopes from (A) and (B) are highlighted in BMP-9 PD

696 and BMP-10/ 9 hybrid PD. Amino acid positions have been adjusted by addition of the N-terminal
697 residues not covered in the atomic model of the BMP-9 CPLX (PDB: 4YCG) and/ or addition of the
698 respective signal peptide sequence for each BMP. The Signal peptide sequence for the BMP-10/ 9
699 hybrid PD is the same as for BMP-10. All sequences can be found in the uniprot database.

700 **References**

- 701 1. Shi, Y., and Massague, J. (2003) Mechanisms of TGF-beta signaling from cell membrane to
702 the nucleus. *Cell* **113**, 685-700
- 703 2. Wu, M. Y., and Hill, C. S. (2009) Tgf-beta superfamily signaling in embryonic development
704 and homeostasis. *Dev Cell* **16**, 329-343
- 705 3. Umulis, D., O'Connor, M. B., and Blair, S. S. (2009) The extracellular regulation of bone
706 morphogenetic protein signaling. *Development* **136**, 3715-3728
- 707 4. Sedlmeier, G., and Sleeman, J. P. (2017) Extracellular regulation of BMP signaling: welcome
708 to the matrix. *Biochem Soc Trans* **45**, 173-181
- 709 5. Zimmermann, L. A., Correns, A., Furlan, A. G., Spanou, C. E. S., and Sengle, G. (2021)
710 Controlling BMP growth factor bioavailability: The extracellular matrix as multi skilled platform. *Cell*
711 *Signal* **85**, 110071
- 712 6. Celeste, A. J., Iannazzi, J. A., Taylor, R. C., Hewick, R. M., Rosen, V., Wang, E. A., and
713 Wozney, J. M. (1990) Identification of transforming growth factor beta family members present in
714 bone-inductive protein purified from bovine bone. *Proc Natl Acad Sci U S A* **87**, 9843-9847
- 715 7. Urist, M. R. (1965) Bone: formation by autoinduction. *Science* **150**, 893-899
- 716 8. Urist, M. R., Mikulski, A., and Lietze, A. (1979) Solubilized and insolubilized bone
717 morphogenetic protein. *Proc Natl Acad Sci U S A* **76**, 1828-1832
- 718 9. Harrison, C. A., Al-Musawi, S. L., and Walton, K. L. (2011) Prodomains regulate the
719 synthesis, extracellular localisation and activity of TGF-beta superfamily ligands. *Growth Factors* **29**,
720 174-186
- 721 10. Sieron, A. L., Louneva, N., and Fertala, A. (2002) Site-specific interaction of bone
722 morphogenetic protein 2 with procollagen II. *Cytokine* **18**, 214-221
- 723 11. Zhu, Y., Ogenesian, A., Keene, D. R., and Sandell, L. J. (1999) Type IIA procollagen containing
724 the cysteine-rich amino propeptide is deposited in the extracellular matrix of prechondrogenic
725 tissue and binds to TGF-beta1 and BMP-2. *J Cell Biol* **144**, 1069-1080

- 726 12. Haudenschild, D. R., Hong, E., Yik, J. H., Chromy, B., Morgelin, M., Snow, K. D., Acharya, C.,
727 Takada, Y., and Di Cesare, P. E. (2011) Enhanced activity of transforming growth factor beta1 (TGF-
728 beta1) bound to cartilage oligomeric matrix protein. *J Biol Chem* **286**, 43250-43258
- 729 13. Hildebrand, A., Romaris, M., Rasmussen, L. M., Heinegard, D., Twardzik, D. R., Border, W.
730 A., and Ruoslahti, E. (1994) Interaction of the small interstitial proteoglycans biglycan, decorin and
731 fibromodulin with transforming growth factor beta. *Biochem J* **302 (Pt 2)**, 527-534
- 732 14. Miura, T., Kishioka, Y., Wakamatsu, J., Hattori, A., Hennebry, A., Berry, C. J., Sharma, M.,
733 Kambadur, R., and Nishimura, T. (2006) Decorin binds myostatin and modulates its activity to
734 muscle cells. *Biochem Biophys Res Commun* **340**, 675-680
- 735 15. Ishida, K., Acharya, C., Christiansen, B. A., Yik, J. H., DiCesare, P. E., and Haudenschild, D. R.
736 (2013) Cartilage oligomeric matrix protein enhances osteogenesis by directly binding and activating
737 bone morphogenetic protein-2. *Bone* **55**, 23-35
- 738 16. Du, Y., Wang, Y., Wang, L., Liu, B., Tian, Q., Liu, C. J., Zhang, T., Xu, Q., Zhu, Y., Ake, O., Qi, Y.,
739 Tang, C., Kong, W., and Wang, X. (2011) Cartilage oligomeric matrix protein inhibits vascular smooth
740 muscle calcification by interacting with bone morphogenetic protein-2. *Circ Res* **108**, 917-928
- 741 17. Brandan, E., Cabello-Verrugio, C., and Vial, C. (2008) Novel regulatory mechanisms for the
742 proteoglycans decorin and biglycan during muscle formation and muscular dystrophy. *Matrix Biol*
743 **27**, 700-708
- 744 18. Zhu, J., Li, Y., Shen, W., Qiao, C., Ambrosio, F., Lavasani, M., Nozaki, M., Branca, M. F., and
745 Huard, J. (2007) Relationships between transforming growth factor-beta1, myostatin, and decorin:
746 implications for skeletal muscle fibrosis. *J Biol Chem* **282**, 25852-25863
- 747 19. Takeuchi, Y., Kodama, Y., and Matsumoto, T. (1994) Bone matrix decorin binds
748 transforming growth factor-beta and enhances its bioactivity. *J Biol Chem* **269**, 32634-32638
- 749 20. Bishop, J. R., Schuksz, M., and Esko, J. D. (2007) Heparan sulphate proteoglycans fine-tune
750 mammalian physiology. *Nature* **446**, 1030-1037

- 751 21. Teran, M., and Nugent, M. A. (2015) Synergistic Binding of Vascular Endothelial Growth
752 Factor-A and Its Receptors to Heparin Selectively Modulates Complex Affinity. *J Biol Chem* **290**,
753 16451-16462
- 754 22. Lin, X., Buff, E. M., Perrimon, N., and Michelson, A. M. (1999) Heparan sulfate
755 proteoglycans are essential for FGF receptor signaling during *Drosophila* embryonic development.
756 *Development* **126**, 3715-3723
- 757 23. Gandhi, N. S., and Mancera, R. L. (2012) Prediction of heparin binding sites in bone
758 morphogenetic proteins (BMPs). *Biochim Biophys Acta* **1824**, 1374-1381
- 759 24. Lindahl, U., Couchman, J., Kimata, K., and Esko, J. D. (2015) Proteoglycans and Sulfated
760 Glycosaminoglycans. In *Essentials of Glycobiology* (rd, Varki, A., Cummings, R. D., Esko, J. D.,
761 Stanley, P., Hart, G. W., Aebi, M., Darvill, A. G., Kinoshita, T., Packer, N. H., Prestegard, J. H.,
762 Schnaar, R. L., and Seeberger, P. H., eds) pp. 207-221, Cold Spring Harbor (NY)
- 763 25. Bornemann, D. J., Park, S., Phin, S., and Warrior, R. (2008) A translational block to HSPG
764 synthesis permits BMP signaling in the early *Drosophila* embryo. *Development* **135**, 1039-1047
- 765 26. Ohkawara, B., Iemura, S., ten Dijke, P., and Ueno, N. (2002) Action range of BMP is defined
766 by its N-terminal basic amino acid core. *Curr Biol* **12**, 205-209
- 767 27. Ruppert, R., Hoffmann, E., and Sebald, W. (1996) Human bone morphogenetic protein 2
768 contains a heparin-binding site which modifies its biological activity. *Eur J Biochem* **237**, 295-302
- 769 28. Rider, C. C. (2006) Heparin/heparan sulphate binding in the TGF-beta cytokine superfamily.
770 *Biochem Soc Trans* **34**, 458-460
- 771 29. Ayerst, B. I., Smith, R. A., Nurcombe, V., Day, A. J., Merry, C. L., and Cool, S. M. (2017)
772 Growth Differentiation Factor 5-Mediated Enhancement of Chondrocyte Phenotype Is Inhibited by
773 Heparin: Implications for the Use of Heparin in the Clinic and in Tissue Engineering Applications.
774 *Tissue Eng Part A* **23**, 275-292

- 775 30. Watson, L. N., Mottershead, D. G., Dunning, K. R., Robker, R. L., Gilchrist, R. B., and Russell,
776 D. L. (2012) Heparan sulfate proteoglycans regulate responses to oocyte paracrine signals in ovarian
777 follicle morphogenesis. *Endocrinology* **153**, 4544-4555
- 778 31. Billings, P. C., Yang, E., Mundy, C., and Pacifici, M. (2018) Domains with highest heparan
779 sulfate-binding affinity reside at opposite ends in BMP2/4 versus BMP5/6/7: Implications for
780 function. *J Biol Chem* **293**, 14371-14383
- 781 32. Gregory, K. E., Ono, R. N., Charbonneau, N. L., Kuo, C. L., Keene, D. R., Bachinger, H. P., and
782 Sakai, L. Y. (2005) The prodomain of BMP-7 targets the BMP-7 complex to the extracellular matrix. *J*
783 *Biol Chem* **280**, 27970-27980
- 784 33. Sengle, G., Charbonneau, N. L., Ono, R. N., Sasaki, T., Alvarez, J., Keene, D. R., Bachinger, H.
785 P., and Sakai, L. Y. (2008) Targeting of bone morphogenetic protein growth factor complexes to
786 fibrillin. *J Biol Chem* **283**, 13874-13888
- 787 34. Sengle, G., Ono, R. N., Sasaki, T., and Sakai, L. Y. (2011) Prodomains of transforming growth
788 factor beta (TGFbeta) superfamily members specify different functions: extracellular matrix
789 interactions and growth factor bioavailability. *J Biol Chem* **286**, 5087-5099
- 790 35. Mi, L. Z., Brown, C. T., Gao, Y., Tian, Y., Le, V. Q., Walz, T., and Springer, T. A. (2015)
791 Structure of bone morphogenetic protein 9 procomplex. *Proc Natl Acad Sci U S A* **112**, 3710-3715
- 792 36. Jiang, H., Salmon, R. M., Upton, P. D., Wei, Z., Lawera, A., Davenport, A. P., Morrell, N. W.,
793 and Li, W. (2016) The Prodomain-bound Form of Bone Morphogenetic Protein 10 Is Biologically
794 Active on Endothelial Cells. *J Biol Chem* **291**, 2954-2966
- 795 37. Sengle, G., Ono, R. N., Lyons, K. M., Bachinger, H. P., and Sakai, L. Y. (2008) A new model for
796 growth factor activation: type II receptors compete with the prodomain for BMP-7. *J Mol Biol* **381**,
797 1025-1039
- 798 38. Wolfman, N. M., McPherron, A. C., Pappano, W. N., Davies, M. V., Song, K., Tomkinson, K.
799 N., Wright, J. F., Zhao, L., Sebald, S. M., Greenspan, D. S., and Lee, S. J. (2003) Activation of latent

- 800 myostatin by the BMP-1/tolloid family of metalloproteinases. *Proc Natl Acad Sci U S A* **100**, 15842-
801 15846
- 802 39. Ge, G., Hopkins, D. R., Ho, W. B., and Greenspan, D. S. (2005) GDF11 forms a bone
803 morphogenetic protein 1-activated latent complex that can modulate nerve growth factor-induced
804 differentiation of PC12 cells. *Mol Cell Biol* **25**, 5846-5858
- 805 40. Shi, M., Zhu, J., Wang, R., Chen, X., Mi, L., Walz, T., and Springer, T. A. (2011) Latent TGF-
806 beta structure and activation. *Nature* **474**, 343-349
- 807 41. Wohl, A. P., Troilo, H., Collins, R. F., Baldock, C., and Sengle, G. (2016) Extracellular
808 Regulation of Bone Morphogenetic Protein Activity by the Microfibril Component Fibrillin-1. *J Biol*
809 *Chem* **291**, 12732-12746
- 810 42. Furlan, A. G., Spanou, C. E. S., Godwin, A. R. F., Wohl, A. P., Zimmermann, L. A., Imhof, T.,
811 Koch, M., Baldock, C., and Sengle, G. (2021) A new MMP-mediated prodomain cleavage mechanism
812 to activate bone morphogenetic proteins from the extracellular matrix. *FASEB J* **35**, e21353
- 813 43. Jenkins, G. (2008) The role of proteases in transforming growth factor-beta activation. *Int J*
814 *Biochem Cell Biol* **40**, 1068-1078
- 815 44. Yu, Q., and Stamenkovic, I. (2000) Cell surface-localized matrix metalloproteinase-9
816 proteolytically activates TGF-beta and promotes tumor invasion and angiogenesis. *Genes Dev* **14**,
817 163-176
- 818 45. Mu, D., Cambier, S., Fjellbirkeland, L., Baron, J. L., Munger, J. S., Kawakatsu, H., Sheppard,
819 D., Broaddus, V. C., and Nishimura, S. L. (2002) The integrin alpha(v)beta8 mediates epithelial
820 homeostasis through MT1-MMP-dependent activation of TGF-beta1. *J Cell Biol* **157**, 493-507
- 821 46. Buscemi, L., Ramonet, D., Klingberg, F., Formey, A., Smith-Clerc, J., Meister, J. J., and Hinz,
822 B. (2011) The single-molecule mechanics of the latent TGF-beta1 complex. *Curr Biol* **21**, 2046-2054
- 823 47. Pallerla, S. R., Lawrence, R., Lewejohann, L., Pan, Y., Fischer, T., Schlomann, U., Zhang, X.,
824 Esko, J. D., and Grobe, K. (2008) Altered heparan sulfate structure in mice with deleted NDST3 gene
825 function. *J Biol Chem* **283**, 16885-16894

- 826 48. Greenwald, J., Groppe, J., Gray, P., Wiater, E., Kwiatkowski, W., Vale, W., and Choe, S.
827 (2003) The BMP7/ActRII extracellular domain complex provides new insights into the cooperative
828 nature of receptor assembly. *Mol Cell* **11**, 605-617
- 829 49. Li, S., Shimono, C., Norioka, N., Nakano, I., Okubo, T., Yagi, Y., Hayashi, M., Sato, Y., Fujisaki,
830 H., Hattori, S., Sugiura, N., Kimata, K., and Sekiguchi, K. (2010) Activin A binds to perlecan through
831 its pro-region that has heparin/heparan sulfate binding activity. *J Biol Chem* **285**, 36645-36655
- 832 50. Yadin, D. A., Robertson, I. B., McNaught-Davis, J., Evans, P., Stoddart, D., Handford, P. A.,
833 Jensen, S. A., and Redfield, C. (2013) Structure of the fibrillin-1 N-terminal domains suggests that
834 heparan sulfate regulates the early stages of microfibril assembly. *Structure* **21**, 1743-1756
- 835 51. Desroches-Castan, A., Tillet, E., Bouvard, C., and Bailly, S. (2022) BMP9 and BMP10: Two
836 close vascular quiescence partners that stand out. *Dev Dyn* **251**, 178-197
- 837 52. Roman, B. L., and Hinck, A. P. (2017) ALK1 signaling in development and disease: new
838 paradigms. *Cell Mol Life Sci* **74**, 4539-4560
- 839 53. Saito, T., Bokhove, M., Croci, R., Zamora-Caballero, S., Han, L., Letarte, M., de Sanctis, D.,
840 and Jovine, L. (2017) Structural Basis of the Human Endoglin-BMP9 Interaction: Insights into BMP
841 Signaling and HHT1. *Cell Rep* **19**, 1917-1928
- 842 54. Wang, X., Fischer, G., and Hyvonen, M. (2016) Structure and activation of pro-activin A. *Nat*
843 *Commun* **7**, 12052
- 844 55. Keller, S., Nickel, J., Zhang, J.-L., Sebald, W., & Mueller, T. D. (2004). Molecular recognition
845 of BMP-2 and BMP Receptor Ia. *Nature Structural & Molecular Biology*, **11**(5), 481–488.
- 846 56. Migliorini, E., Horn, P., Haraszti, T., Wegner, S. V., Hiepen, C., Knaus, P., Richter, R. P., &
847 Cavalcanti-Adam, E. A. (2017). Enhanced biological activity of BMP-2 bound to surface-grafted
848 heparan sulfate. *Advanced Biosystems*, **1**(4), 1600041.
- 849 57. Sefkow-Werner, J., Machillot, P., Sales, A., Castro-Ramirez, E., Degardin, M., Boturyn, D.,
850 Cavalcanti-Adam, E. A., Albiges-Rizo, C., Picart, C., & Migliorini, E. (2020). Heparan sulfate co-

- 851 immobilized with CRGD ligands and BMP2 on biomimetic platforms promotes BMP2-mediated
852 osteogenic differentiation. *Acta Biomaterialia*, **114**, 90–103.

3.4 Activation mechanisms to render fibrillin-bound BMPs bioavailable

Since BMP-7 CPLX assumes a latent, closed-ring conformation once it is bound to microfibril component fibrillin-1 (Wohl et al., 2016), extracellular activation mechanisms should exist that render it again available to surrounding cells. Because BMP-7 GF is rendered inactive by the PD in the fibrillin-1-bound, closed-ring shape conformation, we investigated GF activation mechanisms. Indeed both integrin PD pulling (Shi et al., 2011) and proteolytic PD degradation (Yu et al., 2000; Ge et al., 2006) have been described as mechanisms to activate TGF- β GF from its complexed, LTBP-1-bound, closed-ring form. In the following study, specific proteolytic PD degradation as an activation mechanism to render BMPs bioavailable was investigated.

The following peer-reviewed manuscript was written by Ariane G. Furlan and Gerhard Sengle.

Chara E.S. Spanou expressed and purified BMP prodomains and BMP-7 complex for all *in vitro* cleavage experiments in figures: 3, 4, 9 and S3.

Chara E.S. Spanou established native PAGE conditions for BMP-7 CPLX in figure 9A. Chara E.S. Spanou and Gerhard Sengle conceived the experiments in figure 9C and interpreted the results.

Chara E.S. Spanou studied the mechanism of unfolding by running BMP-7 CPLX on native gels at specific time points post MMP-13 cleavage to confirm results shown in figure 9A. In addition, Chara E.S. Spanou optimized the BMP-7 CPLX yield after size exclusion chromatography (SEC) especially for the needs of the dynamic light scattering (DLS) experiment in S3 since the specific technique requires way higher protein amounts to ensure reliable detection than the transmission electron microscopy with single particle averaging shown in fig. 9C. Chara E.S. Spanou interpreted the DLS results in S3.

Chara E.S. Spanou conceived, performed and analyzed the experiments in figures 6 and 10 and performed the experiments in S1.

RESEARCH ARTICLE

A new MMP-mediated prodomain cleavage mechanism to activate bone morphogenetic proteins from the extracellular matrix

Ariane G. Furlan¹ | Chara E. S. Spanou^{1,2} | Alan R. F. Godwin^{3,4} | Alexander P. Wohl¹ | Laura-Marie A. Zimmermann^{1,2} | Thomas Imhof⁵ | Manuel Koch^{5,6} | Clair Baldock^{3,4} | Gerhard Sengle^{1,2,6,7}

¹Center for Biochemistry, Faculty of Medicine, University Hospital Cologne, University of Cologne, Cologne, Germany

²Department of Pediatrics and Adolescent Medicine, Faculty of Medicine, University Hospital Cologne, University of Cologne, Cologne, Germany

³Wellcome Trust Centre for Cell-Matrix Research, School of Biological Sciences, Faculty of Biology, Medicine and Health, Manchester Academic Health Science Centre, University of Manchester, Manchester, UK

⁴Division of Cell Matrix Biology and Regenerative Medicine, School of Biological Sciences, Faculty of Biology, Medicine and Health, Manchester Academic Health Science Centre, University of Manchester, Manchester, UK

⁵Institute for Dental Research and Oral Musculoskeletal Biology, Faculty of Medicine, University Hospital Cologne, University of Cologne, Cologne, Germany

⁶Center for Molecular Medicine Cologne (CMMC), University of Cologne, Cologne, Germany

⁷Cologne Center for Musculoskeletal Biomechanics (CCMB), Cologne, Germany

Correspondence

Gerhard Sengle, Center for Biochemistry, Faculty of Medicine, University Hospital Cologne, University of Cologne, Joseph-Stelzmann-Street 52, D-50931 Cologne, Germany.

Email: gsengle@uni-koeln.de

Funding information

Deutsche Forschungsgemeinschaft (DFG), Grant/Award Number: 73111208 SFB829/B12, 397484323 TRR259/B09, FOR2722/C2 and FOR2722/B2; MCTI | CNPq | Instituto Nacional de Ciência e Tecnologia da Criosfera (INCT da Criosfera), Grant/Award Number: 231369/2013-1; RCUK | Biotechnology and Biological Sciences Research Council (BBSRC), Grant/Award

Abstract

Since their discovery as pluripotent cytokines extractable from bone matrix, it has been speculated how bone morphogenetic proteins (BMPs) become released and activated from the extracellular matrix (ECM). In contrast to TGF- β s, most investigated BMPs are secreted as bioactive prodomain (PD)–growth factor (GF) complexes (CPLXs). Recently, we demonstrated that PD-dependent targeting of BMP-7 CPLXs to the extracellular fibrillin microfibril (FMF) components fibrillin-1 and -2 represents a BMP sequestration mechanism by rendering the GF latent. Understanding how BMPs become activated from ECM scaffolds such as FMF is crucial to elucidate pathomechanisms characterized by aberrant BMP activation and ECM destruction. Here, we describe a new MMP-dependent BMP-7 activation mechanism from ECM-targeted pools via specific PD degradation. Using Edman sequencing and mutagenesis, we identified a new and conserved MMP-13 cleavage site within the BMP-7

Abbreviations: BMP, bone morphogenetic protein; CD, circular dichroism spectroscopy; CPLX, complex; DPP, decapentaplegic; EBNA, Epstein-Barr virus nuclear antigen; ECM, extracellular matrix; FMF, fibrillin microfibrils; FRET, fluorescence resonance energy transfer; GDF, growth and differentiation factor; GF, growth factor; HEK, human embryonic kidney; LAP, latency-associated peptide; LLC, large latent complex; LTBP, latent TGF- β -binding protein; Mab, monoclonal antibody; MMP, matrix metalloproteinase; PD, prodomain; TEM, transmission electron microscopy; TGF, transforming growth factor; TLL2, tolloid-like protein 2; TMB, tetramethylbenzidine.

This is an open access article under the terms of the Creative Commons Attribution License, which permits use, distribution and reproduction in any medium, provided the original work is properly cited.

© 2021 The Authors. *The FASEB Journal* published by Wiley Periodicals LLC on behalf of Federation of American Societies for Experimental Biology.

Number: BB/S015779/1; Wellcome Trust (Wellcome), Grant/Award Number: 203128/Z/16/Z

PD. A degradation screen with different BMP family PDs and representative MMP family members suggested utilization of the identified site in a general MMP-driven BMP activation mechanism. Furthermore, sandwich ELISA and solid phase cleavage studies in combination with bioactivity assays, single particle TEM, and in silico molecular docking experiments provided evidence that PD cleavage by MMP-13 leads to BMP-7 CPLX disintegration and bioactive GF release.

KEYWORDS

bone morphogenetic protein (BMP), extracellular matrix (ECM), fibrillin, matrix metalloproteinase (MMP), single particle transmission electron microscopy

1 | INTRODUCTION

Bone morphogenetic proteins (BMPs) belong to the TGF- β superfamily of growth factors (GFs) and play a central role in a multitude of cellular processes during embryogenesis and postnatal homeostasis by guiding cell differentiation, proliferation, survival, and apoptosis.^{1,2} Originally, BMPs were discovered as pluripotent cytokines extractable from bone matrix that are capable to induce ectopic bone formation.³ Further studies confirmed that BMPs are stored in embryonic and perinatal connective tissues such as kidney, skin, and blood vessels.⁴⁻⁶ These findings implicate that ECM-bound BMPs serve an important function and that mechanisms for their utilization must exist to control their release at the appropriate time points when their action is required. For instance, the importance of ECM-bound BMPs is not restricted to fetal osteogenesis but also for regeneration of adult bones as illustrated by limb-specific *Bmp2* null mice which presented with irreversible spontaneous fractures.⁷

Among extracellular matrix (ECM) networks collagen fibers were first considered as the primary scaffold responsible for BMP sequestration.^{8,9} Thereby, it was shown that procollagen-2 is able to specifically bind BMP-2 and thereby influencing its bioactivity.¹⁰ In another prominent example it was found that collagen IV controls the bioavailability of the BMP homolog decapentaplegic (*dpp*) in *Drosophila* by binding *dpp* directly or promoting the interaction with its receptor complex.¹¹

Our previous work identified highly specific interactions between the prodomains (PDs) of BMPs and the extracellular glycoproteins fibrillin-1 and -2.^{6,12} In addition, extracellular co-immunostaining of BMPs and fibrillin-1 suggested that fibrillin-1 microfibrils serve as storage platforms for these GFs.⁴⁻⁶ Fibrillins are 350 kDa glycoproteins with a conserved multidomain structure. In tissues, fibrillin-1 and -2 monomers are arranged into supramolecular, beads-on-a-string fibrillin microfibrils (FMF) with a diameter of 10-12 nm.¹³ The importance of FMF integrity becomes evident in congenital connective tissue disorders, caused by mutations in

the fibrillin-1 and -2 coding genes (*FBN1* and *FBN2*), the so-called fibrillinopathies.¹⁴ The fibrillinopathies represent disorders with similar, but also opposing clinical features affecting the musculoskeletal, cardiovascular, ocular, pulmonary, and dermal system.¹⁵ From these clinical features it can be concluded that fibrillins modulate GF-driven growth and differentiation processes in connective tissues. Also, analysis of fibrillin deficient mouse models corroborated this notion. An accelerated maturation of *Fbn1*^{-/-} null osteoblasts was detected due to increased availability of non-ECM-targeted BMPs.¹⁶ Furthermore, genetic ablation of fibrillin-2 resulted in limb patterning and muscle maturation defects caused by dysregulated BMP signaling.^{17,18} Meanwhile it is an established concept that FMF target and sequester TGF- β superfamily GFs and thereby regulate their bioavailability.^{19,20}

TGF- β depends on latent TGF- β -binding proteins (LTBPs) for sufficient secretion and targeting to the ECM in the form of a large latent TGF- β complex (LLC) formed by cysteine bridges of its PD to specialized 8-cysteine LTBP domains.²¹⁻²³ Once secreted, the LLC is targeted to the ECM via LTBP binding to FMF and fibronectin.²⁴⁻²⁷ The mechanisms of TGF- β activation from FMF-bound pools, either by mechanical activation through integrin α v binding to the TGF- β PD (also known as latency-associated peptide: LAP),²⁸⁻³⁰ or upon metalloproteinase cleavage of LAP³¹ have been described. The concept that proteolytic cleavage of LAP leads to the activation of TGF- β -1 GF has been explored in in vitro experiments using MMP-2 and MMP-9.³² Also a combined activation mechanism has been described, where α v β 8 integrin binds to TGF- β -1 via LAP and enables MMP-14 cleavage of LAP and release of TGF- β -1 GF.³³ Another TGF- β -1 GF activation model proposed that BMP-1 cleavage of LTBP-1 at N- and C-terminal sites releases truncated LLC from the ECM which is followed by a second MMP-2-mediated cleavage event of LAP.³⁴ GDF-8 and GDF-11 are activated by BMP-1/Tolloid (TLD) metalloprotease-mediated cleavage of the PD.^{35,36} Recently, tolloid-like protein 2 (TLL2) was also shown to cleave the PD of GDF-8 and thereby activate it from the latent state.³⁷ Similarly, our previous in vitro results

predicted a similar mechanism for BMP-10.¹² Although much work has been undertaken to investigate the mechanisms of TGF- β activation, the regulatory pathways of other TGF- β superfamily members such as BMPs remain largely unknown.

In contrast to TGF- β , most BMPs are secreted as bioactive PD-GF complexes (CPLXs) to the extracellular space.^{12,38-41} Previously, we showed that the BMP-7 PD does not confer latency to the GF in solution, and that BMP type II receptors have free access to their binding sites on the GF. This suggestion arose from velocity sedimentation experiments in sucrose gradients showing that BMP type II receptor binding to the GF results in release of the free PD as a dimer from the CPLX.³⁹ Recently, we could show that upon binding of the BMP-7 PD to the fibrillin-1N-terminal unique domain, a conformational change in the BMP-7 CPLX is induced which renders the GF inactive by locking the α 2-helix of the PD in place, denying access to the BMP type II receptor site.⁴²

However, little is known about how BMPs are released and activated once they are targeted to the ECM. Therefore, the aim of this study was to investigate new BMP activation mechanisms from FMF-targeted pools.

2 | MATERIALS AND METHODS

2.1 | Ethics statement

This study was carried out in strict accordance with German federal law on animal welfare, and the protocols were approved by the "Landesamt für Natur, Umwelt und Verbraucherschutz Nordrhein-Westfalen" (permit no. 84-02.04.2014.A397 for breeding and permit No. 84-02.05.40.14.115 for euthanasia).

2.2 | Antibodies

Previously described monoclonal anti-BMP-7 PD antibodies mab2 and mab33⁴ were kindly provided by Dr Lynn Sakai (Oregon Health and Science University). For western blots, mab33 was either used alone (1:1000 dilution), or in a mixture (1:1 molar ratio) together with mab2 (1:1000 dilution). The generation of polyclonal anti-fibrillin-1 antibody was previously described.⁴³ Polyclonal antibody against BMP-7 GF was purchased from PeproTech (#500-P198, Rocky Hill, NJ).

2.3 | Cell culture

Primary murine skin fibroblasts were isolated from newborn mice.⁴⁴ Primary dermal fibroblasts and HEK 293 cells were cultured in Dulbecco's Modified Eagle's medium (DMEM GlutaMAX, Invitrogen, Carlsbad, CA) supplemented with 10% of fetal bovine serum and penicillin/streptomycin.

2.4 | mRNA expression analysis via quantitative real-time PCR

A total of 1×10^5 HEK 293 cells or primary murine skin fibroblasts cells were grown in 6-well plates prior to BMP GF stimulation at 100 ng/mL. After 24 hours of BMP stimulation, RNA extraction was performed by adding 1 mL of TRIzol Reagent (Thermo Fisher Scientific, Waltham, MA) according to the manufacturer's protocol. A subsequent sample purification step was included using the RNeasy kit (Qiagen, Venlo, The Netherlands), and residual DNA contamination was removed from each sample using the Turbo DNA-free kit (Ambion, Austin, TX). RNA samples were quantified by photospectrometry, and 1.0 μ g of RNA per sample was reverse-transcribed using the Bio-Rad iScript cDNA synthesis kit (Bio-Rad, Hercules, CA). Quantitative PCR was performed using SensiFAST SYBR Hi-ROX Kit in 25 μ L reaction volume (Meridian Bioscience, Cincinnati, OH). PCR was conducted with the StepOnePlus system (Applied Biosystems, Thermo Fisher Scientific). The standard annealing temperature of 60°C was chosen for the selected primer pairs (*Mmp2F*: CAAGTTCCTCCCGCGATGTC, *Mmp2R*: TTCTGGTCAAGGTCACCTGTC; *Mmp3F*: ACATGGAGACTTTGTCCCTTTTG, *Mmp3R*: TTGGCTGAGTGGTAGAGTCCC; *Mmp13F*: TGTTTGCAGAGCACTACTTGAA, *Mmp13R*: CAGTCACCTCTAAGCCAAAGAAA). Analysis of data was performed using the $2^{-\Delta\Delta C_t}$ method⁴⁵ and quantitated relative to the murine *Arbp* or human *GAPDH* gene. Gene expression was normalized to BSA-treated control samples, which provided an arbitrary constant for comparative fold expression. Primer pairs for human *MMP* genes were purchased from Qiagen.

2.5 | Protein expression and purification

BMP-7 CPLX was expressed and purified as described before.⁴ Briefly, the HEK 293 EBNA cell line stably transfected with N-terminally His₆-tagged BMP-7 CPLX was kindly provided by Dr Lynn Sakai (Oregon Health and Science University). Cells were maintained in triple flasks, medium was collected, and affinity purified via nickel chelate affinity chromatography using the Ni-NTA resin (Cube Biotech, Germany). The highest purity fractions of BMP-7 CPLX were eluted with imidazole at a concentration of 50-250 mM. PDs of BMP-4, -5, -7, and -10 were expressed in *E. coli* and purified as previously described.^{6,12} cDNAs encoding for BMP-7 PD mutant variants, PDs of human BMP-9 (K²³-R³¹⁹), human TGF- β -1 (L³⁰-R²⁷⁹), and TGF- β -2 (L²¹-R³³⁰) were generated by gene synthesis (Genewiz, South Plainfield, NJ), cloned into the pET11a vector, overexpressed in *E. coli* with a C-terminally placed His₆-tag, and purified via Ni-NTA.^{6,46} The murine proMMP-2, -7, -8, -9, and -13

(MMP2: NP_032636.1, aa A³⁰-C⁶⁶²; MMP7: NP_034940.2 aa L²¹-L²⁶⁷, MMP8: NP_032637.3, aa F²¹-S⁴⁶⁵; MMP9: NP_038627.1, aa A²⁰-P⁷³⁰; MMP13: NP_032633.1, L¹⁹-C⁴⁷²) were expressed and purified as described previously.⁴⁷ MMP-3, MMP-12, GDF-8 PD, and BMP-7 GF were purchased from R&D Systems (Minneapolis, MN).

2.6 | Proteolytic cleavage assays

MMPs were activated with 250 μ M of amino-phenyl mercuric acetate (APMA) (Sigma-Aldrich, St. Louis, MO) for 2 hours at 37°C. For buffer exchange of solubilized BMP PDs to TC buffer (50 mM of Tris-HCl pH 7.5 and 1 mM of CaCl₂), Amicon ultra 0.5 mL centrifugal filters (Merck Millipore, Burlington, MA) were used. A total of 10 nM of each activated MMP was incubated with 1 μ M of BMP PD in 50 μ L for 2 hours at 25°C. Fragments were analyzed by western blotting and silver staining. For Edman sequencing, 6 μ g of BMP-7 PDs were incubated with 60 ng of MMP-2, MMP-3, or MMP-13. Fragments were separated by 10%-20% SDS-PAGE and transferred to a PVDF membrane. After staining with Ponceau S, the cleavage products were excised, and subjected to N-terminal Edman degradation performed by Proteome Factory AG (Berlin, Germany). MMP activity was assessed through incubation with a quenched Omni-MMP fluorogenic substrate (#BML-P126-0001, Enzo Life Sciences, Lörrach, Germany) in black 96-well plates (Thermo Fisher Scientific, Waltham, MA). Cleavage of the fluorescence resonance energy transfer (FRET)-based substrate (acceptor: MCA, donor: Dpa), led to fluorescence at 400 nm. For each assay, 2 μ M of MMP substrate was incubated with 10 nM of the respective MMP in 100 μ L of TC buffer for 30 minutes, at 25°C, followed by detection of fluorescence emission at 400 nm by an Infinite M1000 spectral photometer (Tecan, Switzerland).

2.7 | Circular dichroism spectroscopy

BMP-7 PD variants were dialyzed into 5 mM of HClO₄. CD spectra were recorded using a Jasco J-715 spectropolarimeter at 260-170 nm in a 0.1-mm path length quartz cell (Hellma, Germany) at 20°C. After subtraction of the buffer contribution, data were converted to $\Delta\epsilon$.

2.8 | ELISA and sandwich ELISA

For ELISA, 100 ng/mL of BMP-7 CPLX was coated to microtiter plates (Nalge Nunc, Rochester, NY) in PBS overnight at 4°C. Wells were blocked with 5% nonfat dry milk/TBS for 1 hour at RT and washed three times with 0.025% TBS-tween, afterwards. Directly coated BMP-7 CPLX was

incubated with MMPs at a molar ratio of 1:100 (MMP:BMP-7 CPLX) for 2 hours at RT in TC buffer. For sandwich ELISA detection, BMP-7 CPLX after MMP-13 cleavage was transferred to anti-BMP-7 GF antibody coated wells (10 μ g/mL, PeproTech) and incubated for 1 hour. Wells were washed three times with 0.025% TBS-tween and incubated with detection antibody against BMP-7 PD (mab33 at 1:1000 dilution) in 2.5% nonfat dry milk/TBS for 2 hours at RT, followed by 1 hour incubation of HRP-conjugated anti-rabbit antibody in 2.5% nonfat dry milk/TBS at RT. Subsequently, wells were washed three times with TBS-tween, and incubated with 50 μ L of 1-Step Ultra TMB-ELISA substrate solution for signal development (Thermo Fisher Scientific, Waltham, MA). OD was read at 450 nm using a Sunrise microplate reader (Tecan).

2.9 | MMP-13 cleavage assays on solid phase

For the generation of an assembled ECM fiber network, 1×10^6 mouse skin fibroblasts were seeded on 6-well plates and cultivated for 4 days, followed by cell removal using deoxycholate.⁴⁸ In brief, cell cultures were washed once with PBS and then, treated twice with 0.5% sodium deoxycholate in 10 mM of Tris-HCl buffer, pH 8.0, at 0°C for 10 minutes. The plates were then allowed to dry overnight at RT. Subsequently, wells were blocked in 5% BSA followed by incubation with BMP-7 CPLX. To assess colocalization between added BMP-7 CPLX and fibrillin-1 fibers by immunofluorescence, cells were grown on 24-well plates. To demonstrate a direct interaction between added BMP-7 CPLX and assembled ECM fibers by ELISA-style solid phase interaction assay, mouse fibroblasts were grown on 96-well plates. For this, 100 ng/mL of BMP-7 CPLX was titrated onto ECM-coated dishes following a 1:2 serial dilution in TBS buffer containing 1% of BSA at RT for 2 hours. BMP-7 CPLX immobilized to ECM fibers was submitted to MMP-13 cleavage (50 ng/mL) in 1 mL of TC buffer for 2 hours at 37°C. Afterwards, the supernatant was collected and subjected to TCA precipitation for western blot analysis or lyophilized to be subjected to BMP bioactivity assays.

2.10 | BMP bioactivity assay

Supernatant from 6-well plates containing GF released from ECM-targeted BMP-7 CPLX after MMP-13 cleavage was collected and dialyzed in mini dialysis tubes with a molecular weight cut-off of 2 kDa into 100 mM acetic acid overnight at 4°C. After dialysis, samples were shock-frozen in liquid nitrogen and lyophilized overnight. Subsequently, samples were resuspended in 10 μ L of 4 mM

HCl and administered to BMP bioactivity assays. To measure BMP bioactivity murine C2C12 myoblasts were utilized as reporter cell line. For each measurement, 3.5×10^4 cells/well were seeded onto 96-well plates. Stimulation was performed in eight wells per concentration in triplicates. Two or three microliters of the obtained supernatant after MMP-13 cleavage of ECM-bound BMP-7 CPLX and 2 or 3 μL of the supernatant without MMP-13 incubation were added for C2C12 cell stimulation. After 5 hours, the total mRNA content of cells was harvested, reverse-transcribed, and subjected to qPCR to measure the mRNA levels of BMP response gene *Id3* (inhibitor of differentiation 3).³⁹ *Id3* mRNA levels were normalized to the mRNA expression of *ARBP* (“acidic ribosomal binding protein”) which served as housekeeping gene. A total of 10 ng/mL of BMP-7 GF (R&D systems) was added to the medium as positive control, and incubation of cells with 0.1% of BSA served as untreated negative control.

2.11 | Transmission electron microscopy (TEM) and single particle analysis

BMP-7 CPLX alone, after dialysis into 1 M urea, or after incubation with MMP-13 for 2 hours was negatively stained as described previously.⁴⁹ BMP-7 CPLX alone and cleaved with MMP-13 data were recorded at $\times 30\,000$ magnification using a FEI Tecnai 12 twin TEM at 120 kV using a Tietz TVIPs F214A CCD camera. Images were recorded with a 1-s exposure at defocus values of -0.5 to $-1.6\ \mu\text{m}$ at $1.5\ \text{\AA}/\text{pixel}$ (Figure 9C). BMP-7 CPLX after dialysis into 1 M urea data were collected on a FEI Tecnai G2 Polara TEM operating at 300 kV equipped with a Gatan K2 summit direct detector. Images were recorded at $\times 23\,000$ magnification with a 1-s exposure in integrating mode at defocus values of -0.5 to $-1.6\ \mu\text{m}$ at $1.67\ \text{\AA}/\text{pixel}$. Single particle analysis was performed using Relion.^{50,51} Particles were selected by a combination of manual and automated picking. The total number of particles selected for BMP-7 CPLX either alone, after MMP-13 incubation, or in the presence of 1 M urea was approximately 900, 6770, or 9600, respectively. Each data set was subjected to two-dimensional classification.

2.12 | Dynamic light scattering

BMP-7 CPLX was dialyzed overnight into TC buffer and cleaved with MMP-13 as described above. DLS measurements of the cleaved and non-cleaved control BMP-7 CPLX were then taken using a Zetasizer Nano-S (Malvern, Herfordshire, UK) at a controlled temperature of 25°C .

2.13 | Molecular docking experiments

The generation of the BMP-7 CPLX closed-ring shape model (Figure 6), based on the TGF- β -1 LAP crystal structure (Protein Data Bank code 3RJR) as a template, with MODELLER⁵² in UCSF Chimera⁵³ was as described.⁴² In this model, a break in the peptide chain was introduced at residue Pro⁸⁰ to allow the PD to be rotated into an open conformation without moving the N-terminal region. Next, using the Chimera software a peptide bond with a phi torsional angle of -60° was introduced at the exact same position in order to re-join the polypeptide chains without moving the N-terminal PD region. The BMP-9 CPLX structure (Protein Data Bank code 4YCI) and the BMP-7 CPLX EM map were used to guide rotation of the PD into an open conformation. To obtain a structural model of BMP-7 PD in the open V-shape conformation, BMP-7 PD was modeled on the proactivin CPLX structure (Protein Data Bank code 5HLZ) using Swiss-model. To gain structural insight into the MMP-13 cleavage mechanism, BMP-7 PD in the open conformation or the closed-ring BMP-7 CPLX, inputted as the “receptors” were docked to the crystal structure of the activated MMP-13 (Protein Data Bank code 4fu4) inputted as the “ligand” in the ClusPro2.0 server⁵⁴ after deleting the structure of the co-crystallized peptide using UCSF chimera software. Subsequently, 30 molecular docking models were screened for each in silico experiment and models 21 and 16 were selected for closed and open BMP-7 PD conformations, respectively, due to excellent alignment of the MMP-13 catalytic site (His²²², His²²⁶, and His²³²) to the prime region ⁸³MLD⁸⁵ of the cleavage site. To obtain a theoretical model of MMP-13 cleaving the BMP-7 CPLX closed-ring, model 21 was structurally aligned to each BMP-7 PD monomer of the closed BMP-7 CPLX model at the ⁸³MLD⁸⁵ site. Images were taken both in ribbon and surface representations. To pinpoint the exact molecular requirements for cleavage in the open BMP-7 PD conformation, model 16 was superimposed to the activated MMP-13 structure (Protein Data Bank code 4fu4) and the positioning of the co-crystallized peptide was compared to the ⁸³MLD⁸⁵ site of BMP-7 PD. Ions and metals were visualized using the 4fu4 template and images were taken in ribbon representation. To generate the open V-shape BMP-7 CPLX model, BMP-7 PD was assembled into a dimer using Swiss-model and the proactivin CPLX was structurally aligned to the BMP-7 PD dimer. Next, the monomers of the BMP-7 GF crystal structure (Protein Data Bank code 1LX5) were structurally aligned to the monomers of the proactivin GF after deleting the structure of the ActRII extracellular domain using UCSF chimera. To understand how MMP-13 is cleaving the open V-shape BMP-7 CPLX, model 16 was structurally aligned to one BMP-7 PD of the CPLX and images were taken both in ribbon and surface representations.

2.14 | Statistical analysis

Data are expressed as mean \pm SD. Statistical analyses were performed using GraphPad Prism software and the significance of differences between groups was determined by applying an unpaired two-tailed Student's test. Values of $P \leq .05$ were considered significant.

3 | RESULTS

3.1 | BMP-7 GF stimulates metalloproteinase activity leading to specific cleavage of BMP-7 PD

Western blot analysis of HEK 293 cells transiently transfected with full length BMP-7 cDNA encoding for the entire BMP-7 PD-GF CPLX showed two bands for BMP-7 PD after 3 days of culture. After 1 day of transfection, only

the expected size of full length BMP-7 PD at approximately 37 kDa was detected, while at day 3 an additional band of about 25 kDa could be observed (Figure 1A). This suggested that after secretion a specific proteolytic event occurred within the BMP-7 PD. To dissect whether BMP-7 PD cleavage may have been initiated by BMP autostimulation or by accumulation of general protease activity in the culture media over time, HEK 293 cells were incubated with BMP-7 GF only for 24 hours and the resulting supernatant was incubated with recombinantly expressed and affinity-purified BMP-7 CPLX protein (Figure 1B). Results from western blot analysis showed that only supernatant obtained from BMP-7 GF stimulated cell layers caused specific BMP-7 PD cleavage. This cleavage was inhibited upon addition of EDTA, suggesting that BMP-7 PD cleavage was caused by metalloproteinase activity (Figure 1B). Based on the findings of previous reports, we hypothesized that BMP-7 stimulation of HEK 293 cells may have induced upregulation of MMPs which in turn led to PD degradation of the BMP-7 CPLX. To

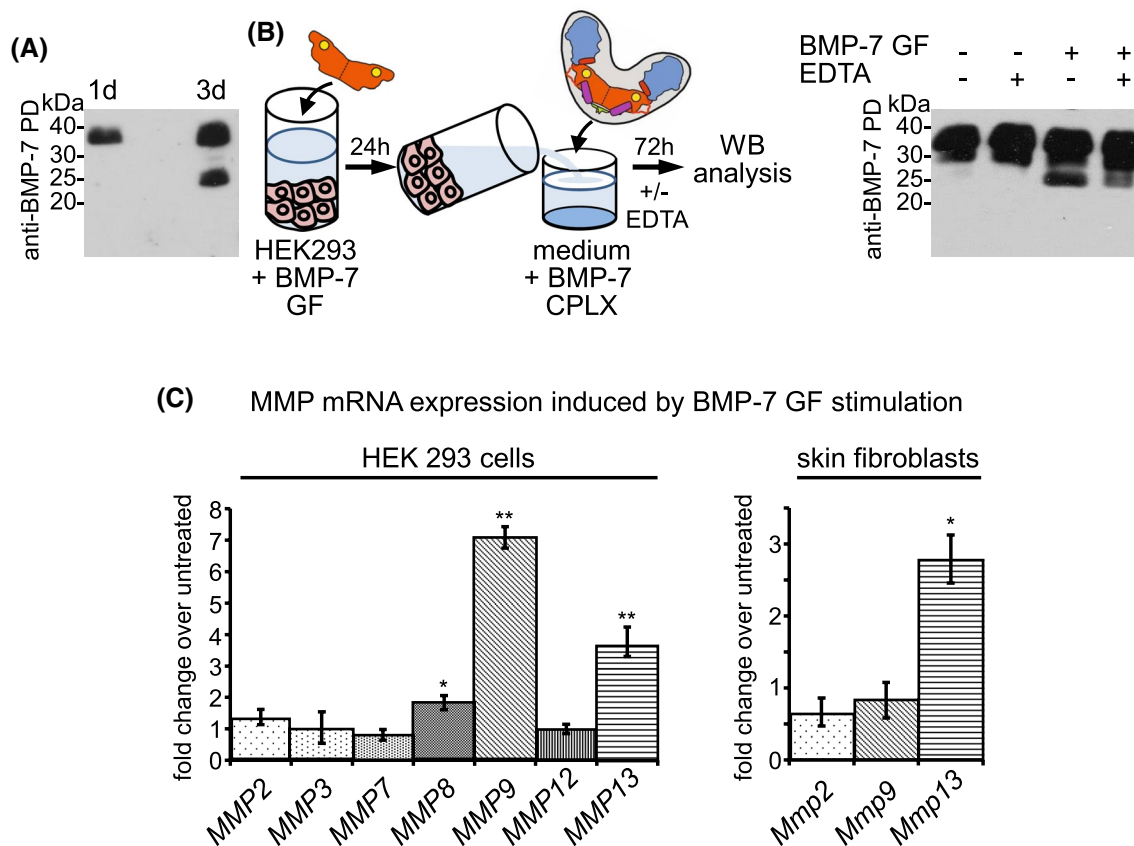


FIGURE 1 Specific cleavage of BMP-7 PD in cell culture medium. A, Cell culture supernatant from HEK 293 cells transiently transfected with BMP-7 cDNA coding for BMP-7 CPLX was monitored via western blot analysis for PD integrity using antibody against BMP-7 PD (mab2/mab33, 1:1 mixture) after 1 and 3 days (d). B, (left) Scheme illustrating experimental design: HEK 293 cells were stimulated with BMP-7 GF (100 ng/mL), and the cell culture supernatant was collected after 24 h. Subsequently, the medium was incubated with recombinant BMP-7 CPLX protein for 72 h in the presence or absence of 10 mM EDTA, followed by western blot analysis using anti-BMP-7 PD antibody (mab2/mab33, 1:1 mixture). C, mRNA expression of MMPs in HEK 293 cells and primary murine dermal fibroblasts measured by qPCR after 24 h of BMP-7 GF stimulation. Error bars show standard deviation of three independent experiments (N = 3). Statistical analysis was by an unpaired two-tailed Student's t test. ** $P \leq .01$, * $P \leq .05$

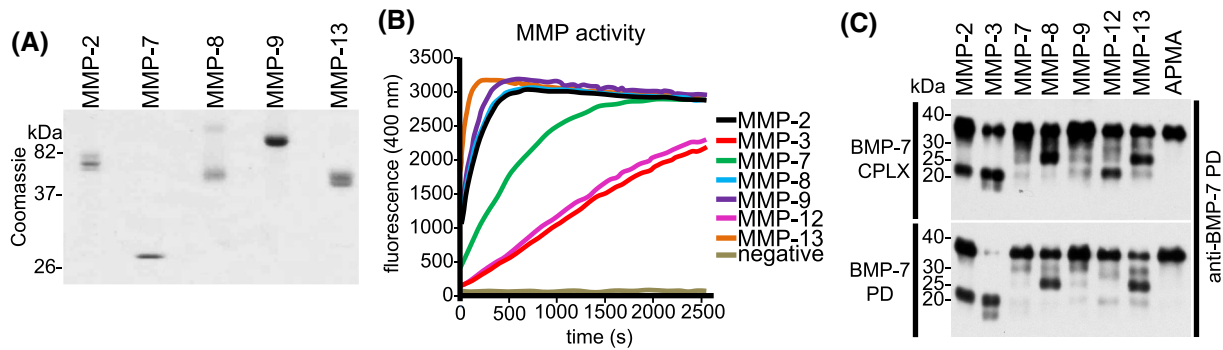


FIGURE 2 Proteolytic processing of BMP-7 PD by representatives of MMP family subgroups. A, Assessment of integrity and purity of recombinantly expressed and affinity-purified MMPs by SDS-PAGE (10% gel) and Coomassie staining. B, Measurement of MMP activity was assessed by fluorescence detected after incubation with a FRET peptide substrate. C, BMP-7 CPLX and separated BMP-7 PD were subjected to cleavage by indicated MMPs. Samples were loaded onto a 10%-20% SDS-PAGE gradient gel, followed by western blot analysis of cleavage products employing antibodies (mab2/mab33, 1:1 mixture) against BMP-7 PD

test this assumption, we measured the mRNA levels of representatives of MMP family subgroups after 24 hours of HEK 293 cell stimulation with BMP-7 GF (Figure 1C). We found that BMP-7 GF administration induced a significant upregulation of MMP-8, -9, and -13 mRNA expression suggesting that the BMP-7 PD was degraded by a BMP-induced MMP activity. Stimulation of ECM resident cells such as skin fibroblasts confirmed that BMP-7 GF is able to induce most robustly MMP-13 mRNA expression (Figure 1C). These experiments suggested that BMP-7 GF is capable to stimulate metalloproteinase expression which in turn leads to specific cleavage of BMP-7 PD.

3.2 | BMP-7 PD as new substrate for MMPs

Previously, it was shown that active TGF- β is able to stimulate matrix metalloproteinase (MMP) expression.⁵⁵ Furthermore, MMP cleavage of the TGF- β PD LAP was proposed as mechanism to release TGF- β GF from the ECM.³¹⁻³³ To evaluate the existence of a potential similar MMP-driven ECM activation mechanism for BMPs, the hypothesis was tested whether the BMP-7 PD also serves as a substrate for MMPs. For this purpose, an in vitro cleavage screening assay was undertaken testing different recombinantly expressed and purified representatives of MMP family subgroups (Figure 2A) and BMP-7 PD and BMP-7 CPLX as substrates. In our screen, MMP-2 and -9 represented the gelatinases, MMP-3 the stromelysins, MMP-7 the matrynsins, MMP-8 and -13 the collagenases, and MMP-12 the elastases.⁵⁶ Prior to BMP-7 PD incubation, MMP activity was assessed through fluorescence increase after incubation with a specific MMP fluorogenic substrate. Cleavage of the substrate resulted in a fluorescence signal at 500 nm (Figure 2B). All tested MMPs were able to cleave the BMP-7 PD, either alone, or when complexed to its cognate GF (Figure 2C). Thereby, we observed varying BMP-7 PD cleavage efficiencies among MMPs, since MMP-7, and -9

only showed moderate activity under the chosen conditions. Interestingly, a considerable number of MMP-mediated cleavage events yielded in BMP-7 PD fragments of similar sizes approximately at 30, 25, and 20 kDa (Figure 2C).

3.3 | Mapping of MMP cleavage site within the BMP-7 PD

To identify specific MMP cleavage sites within the BMP-7 PD, N-terminal Edman sequencing of cleavage products was performed after incubation with MMP-2, MMP-3, and MMP-13. Using this method, the N-terminal sequence of a consensus cleavage product at a size of 20 kDa for MMP-2, MMP-3, and MMP-13 was identified starting with ¹²¹LQDS¹²⁴. In addition, the N-terminal amino acid sequence of two other peptides could be identified after cleavage by MMP-13: ⁸³MLDL⁸⁶, and ¹⁰⁷YKA¹⁰⁹ (Figure 3A). At 0.5 hours incubation time, a higher cleavage efficiency of MMP-13 was observed in comparison to MMP-2 and -3 (Figure 3A). After 0.5 hours incubation in presence of MMP-2 and -3, minor amounts of the first cleavage products could be also detected at 30 kDa similar to the fragment starting with ⁸³MLDL⁸⁶ identified after MMP-13 cleavage. After 2 hours of incubation, quantitative MMP-2 and -3 cleavage was observed yielding the ¹²¹LQDS¹²⁴ fragment at 20 kDa as well as an additional fragment at about 17 kDa with the same N-terminal ¹²¹LQDS¹²⁴ sequence most probably generated by a secondary cleavage event further downstream towards the C-terminus (Figure 3A).

Our assays revealed that MMP-13 cleavage activity was most effective in the presence of 0.05% Triton X-100 (Figure 3B). Therefore, the MMP-13-induced cleavage pattern of BMP-7 PD in the presence or absence of triton was assessed. In the presence of triton, full length BMP-7 PD, as well as the fragment starting with ⁸³MLDL⁸⁶ were not detectable, leading to a more prominent presence of fragments

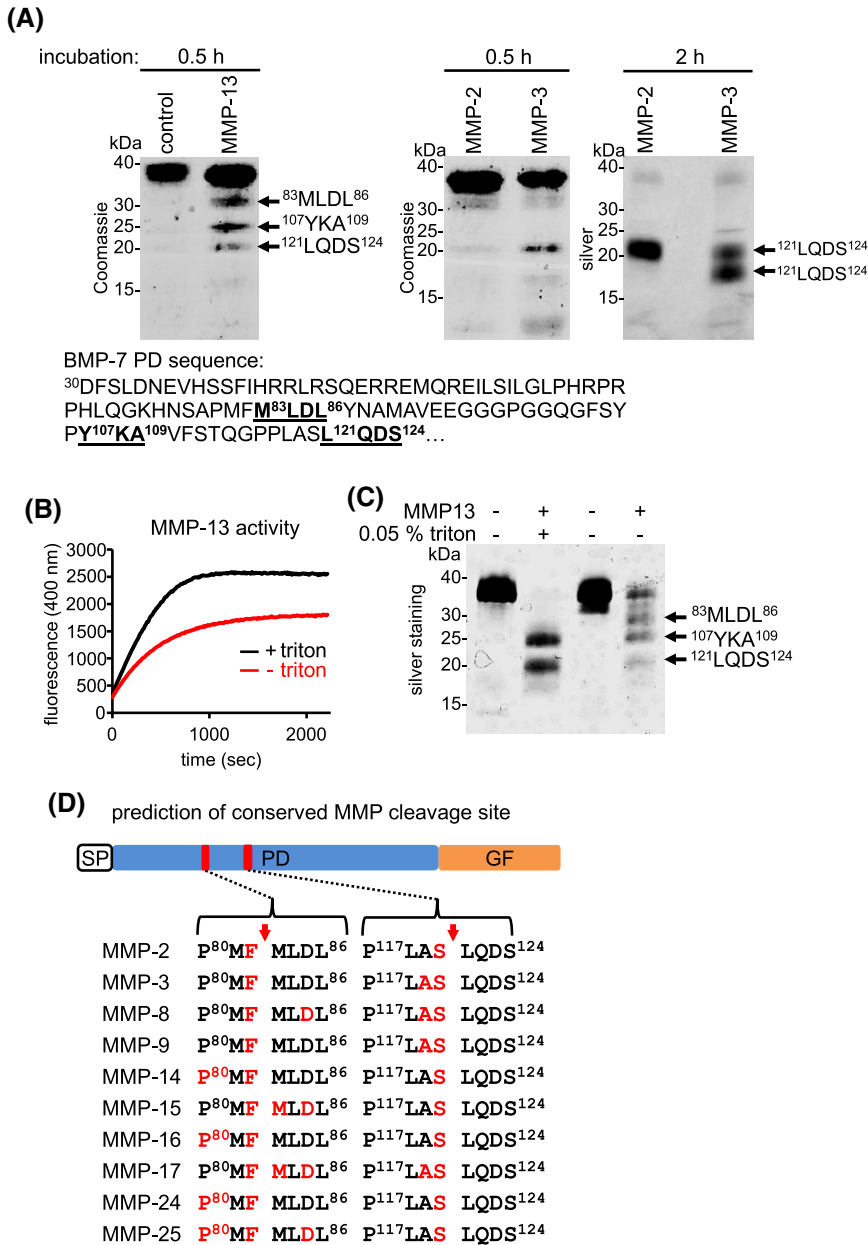


FIGURE 3 Identification of MMP cleavage site within BMP-7 PD. A, (top) N-terminal Edman sequencing of BMP-7 PD fragments generated by MMP-2, MMP-3, and MMP-13 cleavage after indicated incubation times. Resulting BMP-7 PD fragments were separated by SDS-PAGE in a 10%-20% gradient gel followed by Coomassie staining. (bottom) N-terminal amino acid sequences of MMP-13-mediated BMP-7 PD fragments highlighted in black bold and underlined letters. B, MMP-13 activity in the presence or absence of 0.05% Triton X-100 was monitored using a specific substrate. C, BMP-7 PD cleavage (incubation time: 2 h) by MMP-13 in presence or absence of Triton X-100 followed by 10%-20% gradient SDS-PAGE and silver staining. D, MMP cleavage site prediction within BMP-7 PD using the CleavPredict bioinformatics platform. All evaluated MMPs were predicted to cleave BMP-7 PD at the same positions identified by Edman degradation after MMP-13 cleavage. Predicted amino acids located in position 1 (P1) (position right before the cleavage site) are highlighted in red. Arrows indicate position of predicted cleavage sites

starting with ¹²¹LQDS¹²⁴ and ¹⁰⁷YKA¹⁰⁹ (Figure 3C). This finding suggests that fragments starting with ¹²¹LQDS¹²⁴ and ¹⁰⁷YKA¹⁰⁹ are products of a secondary cleavage event derived from the fragment starting with ⁸³MLDL⁸⁶ produced in the primary cleavage event.

Overall, our data led us to the hypothesis that MMP-2, MMP-3, and the other tested MMPs initially process BMP-7 PD at the same cleavage sites as MMP-13. However, the cleavage products may be further processed by different secondary cleavage events. To further explore the possibility of a general MMP cleavage site within BMP-7 PD, the publicly available MMP cleavage prediction platform, CleavPredict,⁵⁷ was utilized. With the help of this software which is based on *Proteomic Identification of Protease Cleavage Sites* (PICS) using human peptide libraries,⁵⁷

potential cleavage sites within the BMP-7 PD for 11 representative MMPs could be predicted. Interestingly, all evaluated MMPs were predicted to cleave BMP-7 PD within the same sites identified by Edman degradation after MMP-13 incubation (Figure 3D).

3.4 | MMPs specifically cleave PDs of TGF- β superfamily members

Sequence alignment of PDs showed that the identified MMP cleavage site ⁸⁰PMFMLD⁸⁵ within the BMP-7 PD is partially conserved among other members of the TGF- β superfamily, except for GDF-8 (Figure 4A). Subjecting PD sequences of BMP subgroup representatives to *in silico* cleavage by

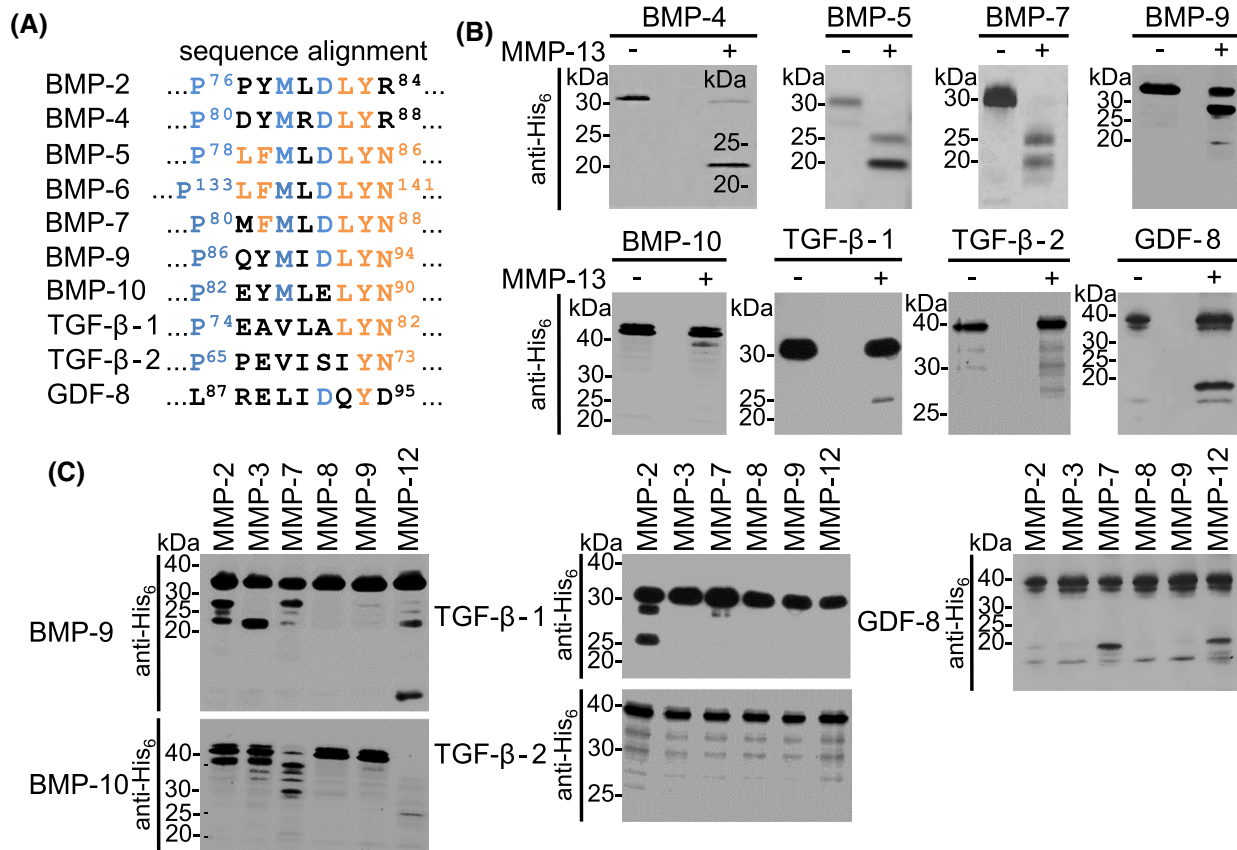


FIGURE 4 Identified MMP cleavage site is conserved among TGF- β superfamily members. A, Sequence alignment of PD sequences of BMP-2, -4, -5, -6, -7, -9, -10, GDF-8, TGF- β -1, and -2 by Clustal Omega showed that the identified MMP cleavage site is partially conserved with the exception of GDF-8. Conserved amino acid residues among evaluated TGF- β superfamily members are highlighted in blue. B, Proteolytic processing of TGF- β superfamily PDs by MMP-13 assessed by western blotting using anti-His₆ antibody. C, TGF- β superfamily PDs subjected to proteolytic cleavage by representative members of the MMP family. Cleavage samples were analyzed by 10%-20% SDS-PAGE followed by western blotting using anti-His₆ antibody

CleavPredict revealed that most MMPs would also utilize this site (Figure S2). Previous studies had shown that Pro in P3 in the non-prime region before the scissile bond of the cleavage site (Figure 5A) is considered the most important amino acid required for MMP-13 recognition, followed by Leu or Met in position P1', and acidic residues in P3' of the prime region.⁵⁸ The alignment showed that the corresponding residues identified in BMP-7 PD P⁸⁰, M⁸³, and D⁸⁵ were conserved among BMP family members (Figure 4A). In addition, we found the motif ⁸⁶LYN⁸⁸ to be conserved for most PDs in positions P4'-P6' after the scissile bond.

To experimentally validate that PDs of TGF- β family members serve as substrates for MMP-13 and other MMPs, an in vitro cleavage screen with representatives of TGF- β and BMP subgroups was performed. Under the chosen conditions, we observed that MMP-13 was able to process all tested PDs with varying efficiencies (Figure 4B). As expected, MMP-13 cleavage of the PD of BMP-5, which belongs to the BMP-5, -6, -7 subgroup, yielded the same cleavage pattern as seen for the BMP-7 PD (Figure 4B). After cleavage of the BMP-4

PD, a representative of the BMP-2, -4 subgroup, only the 20 kDa fragment could be detected (Figure 4B). A cleavage screen of MMP subgroup representatives with PDs of BMP-9 and -10 which both constitute their own BMP subgroup, revealed differences and similarities in resulting fragment patterns and cleavage efficiencies (Figure 4C). Similar cleavage results were observed after MMP-2, -7, and -13 incubation (Figure 4B,C), while BMP-10 PD processing by MMP-12 was more effective than that of BMP-9 PD. Interestingly, MMP-8 and -9 did not process PDs of this subgroup.

TGF- β -1 PD was efficiently cleaved by MMP-2 (Figure 4C) as already described.^{32,59} Also upon MMP-13 cleavage, a fragment at around 25 kDa could be observed in minor amounts (Figure 4B). In contrast, the TGF- β -2 PD was not susceptible to cleavage by the tested MMPs and only a minor degradation was found upon incubation with MMP-2, -12, and -13 (Figure 4B,C).

As GDF-8 lacks most of the residues of the identified, conserved MMP cleavage site, ⁸⁰PMFMLD⁸⁵ (Figure 4A), we expected that GDF-8 might be resistant against MMP

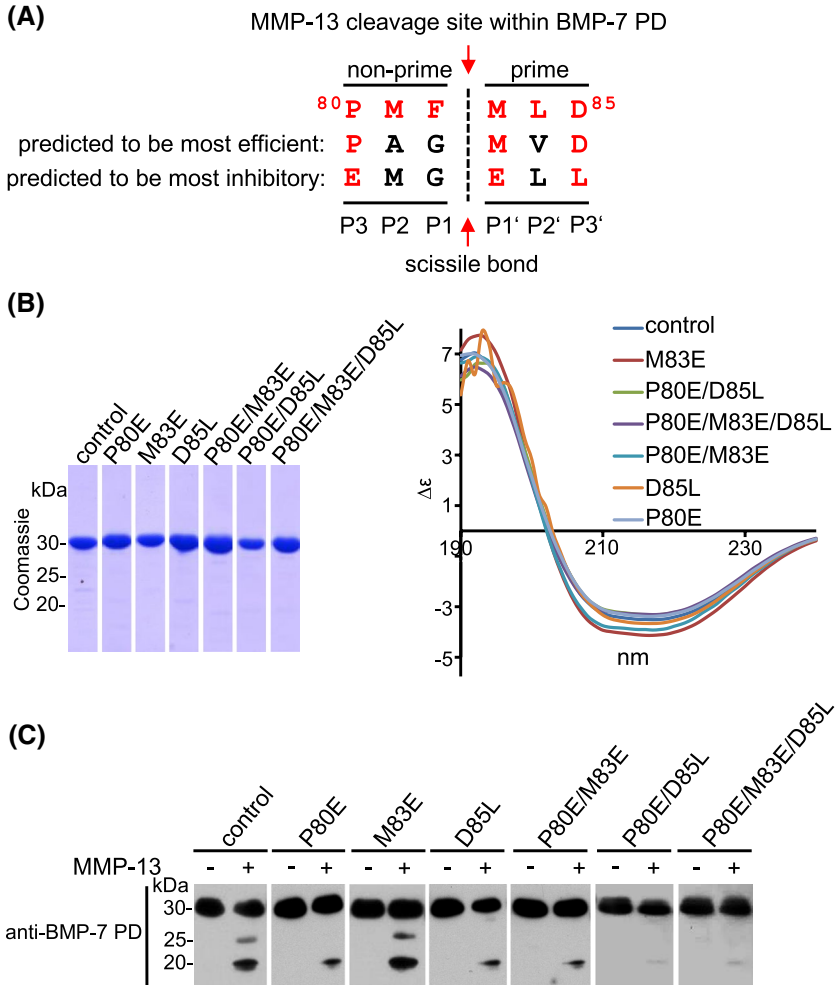


FIGURE 5 Characterization of MMP-13 cleavage site within BMP-7 PD. A, Introduced point mutations within identified MMP-13 cleavage site in BMP-7 PD. Identified MMP-13 cleavage motif within BMP-7 PD is indicated in red. The most efficiently cleaved motif and residues to be most inhibitory for MMP-13 cleavage were previously predicted.⁵⁸ B, Evaluation of integrity, purity, and secondary structure of mutant BMP-7 PD variants by SDS-PAGE (12.5% gel stained with Coomassie), and circular dichroism. C, BMP-7 PD variants carrying point mutations: P80E, M83E, and D85L, double point mutations: P80E/M83E and P80E/D85L, as well as a triple point mutation: P80E/M83E/D85L were subjected to MMP-13 cleavage. Resulting fragments were separated by 10%-20% gradient SDS-PAGE and visualized by western blotting using anti-BMP-7 PD antibody (mab2/mab33, 1:1 mixture)

cleavage. However, in presence of MMP-7, -12 and -13, a cleavage product was detected around 19 kDa (Figure 4B,C).

3.5 | The ⁸⁰PMFMLD⁸⁵ motif is crucial for efficient MMP-13 cleavage of BMP-7 PD

To validate the relevance of the identified ⁸⁰PMFMLD⁸⁵ motif we attempted to inactivate MMP-13 processing of BMP-7 PD by introducing point mutations at critical positions (Figure 5A). Thereby, amino acid substitutions were guided by previous predictions.⁵⁸ BMP-7 PD mutants were overexpressed in *E coli* and affinity purified to more than 95% purity as assessed by SDS-PAGE and Coomassie staining (Figure 5B). The generated BMP-7 PD mutant variants included the single point mutations P80E, M83E, and D85L, the double point mutations P80E/M83E, and P79E/D84L, as well as the triple point mutation P80E/M83E/D85L. All chosen point mutations did not result in secondary structure changes as assessed by circular dichroism (CD) spectroscopy (Figure 5B). All mutated BMP-7 PD variants were subjected to MMP-13 cleavage and the resulting fragments were

analyzed via western blot analysis (Figure 5). In all mutant variants apart from M83E, production of the 25 kDa fragment was abolished and the presence of the 20 kDa fragment was significantly reduced (Figure 5C).

3.6 | Localization of the MMP-13 cleavage site within a three-dimensional structure model of BMP-7 CPLX

Binding of BMP-7 CPLX to fibrillin-1 induces a conformational change of the entire CPLX from an open bioactive V-shape to a closed latent ring-shape.⁴² This inactivation of BMP GF occurs due to a structural re-arrangement of the two PDs leading to blockage of the BMP type II receptor-binding site on the GF by the $\alpha 2$ helix of the PD⁴² (Figure 6A). By localizing the scissile bond of the identified MMP-13 cleavage site (between F⁸² and M⁸³) within the PD in a three-dimensional closed ring-shape structure model of BMP-7 CPLX (Figure 6A), we found that it resides within the $\alpha 2$ helix. Since molecular docking of MMP-13 and the closed BMP-7 CPLX suggested that this site was accessible (Figure 6B),

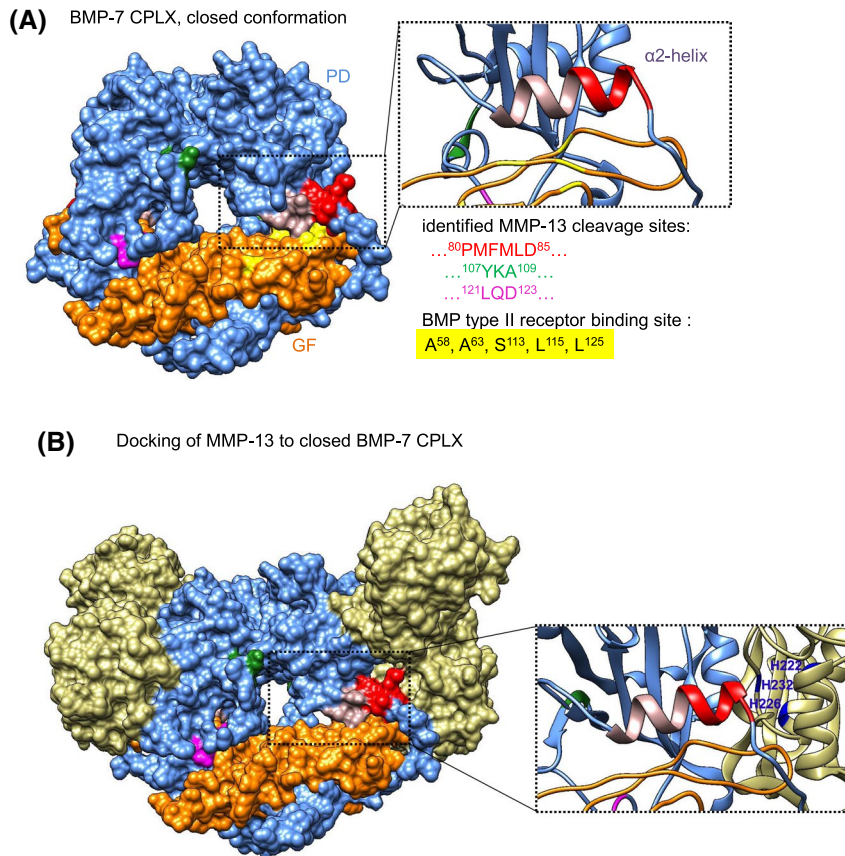


FIGURE 6 Model of MMP-13 cleaving within the inhibitory $\alpha 2$ -helix of the PD in the closed-ring BMP-7 CPLX conformation. A, Localization of the MMP-13 cleavage sites within a three-dimensional structure model of BMP-7 CPLX (surface representation). BMP-7 CPLX is presented in the closed-ring shape conformation, and identified cleavage regions are highlighted: ⁸⁰PMFMLD⁸⁵ (red), ¹⁰⁷YKA¹⁰⁹ (green), ¹²¹LQD¹²³ (magenta). Blue: PD residues, orange: GF residues, inhibitory $\alpha 2$ -helix: light purple, yellow: crucial GF residues interacting with the BMP type II receptors. Area outlined by dashed box is also shown as twofold magnification in ribbon representation. B, Docking of two MMP-13 molecules (beige) to BMP-7 CPLX in closed ring-shape conformation. A twofold magnification of area outlined by dashed box in ribbon representation shows residues of the MMP-13 catalytic site (H²²², H²²⁶, H²³² marked in blue) in proximity to the ⁸⁰PMFMLD⁸⁵ cleavage site (marked in red)

we hypothesized that MMP-13-mediated cleavage of latent fibrillin-1-bound BMP-7 CPLX leads to removal of the $\alpha 2$ -helix resulting in release of bioactive BMP-7 GF.

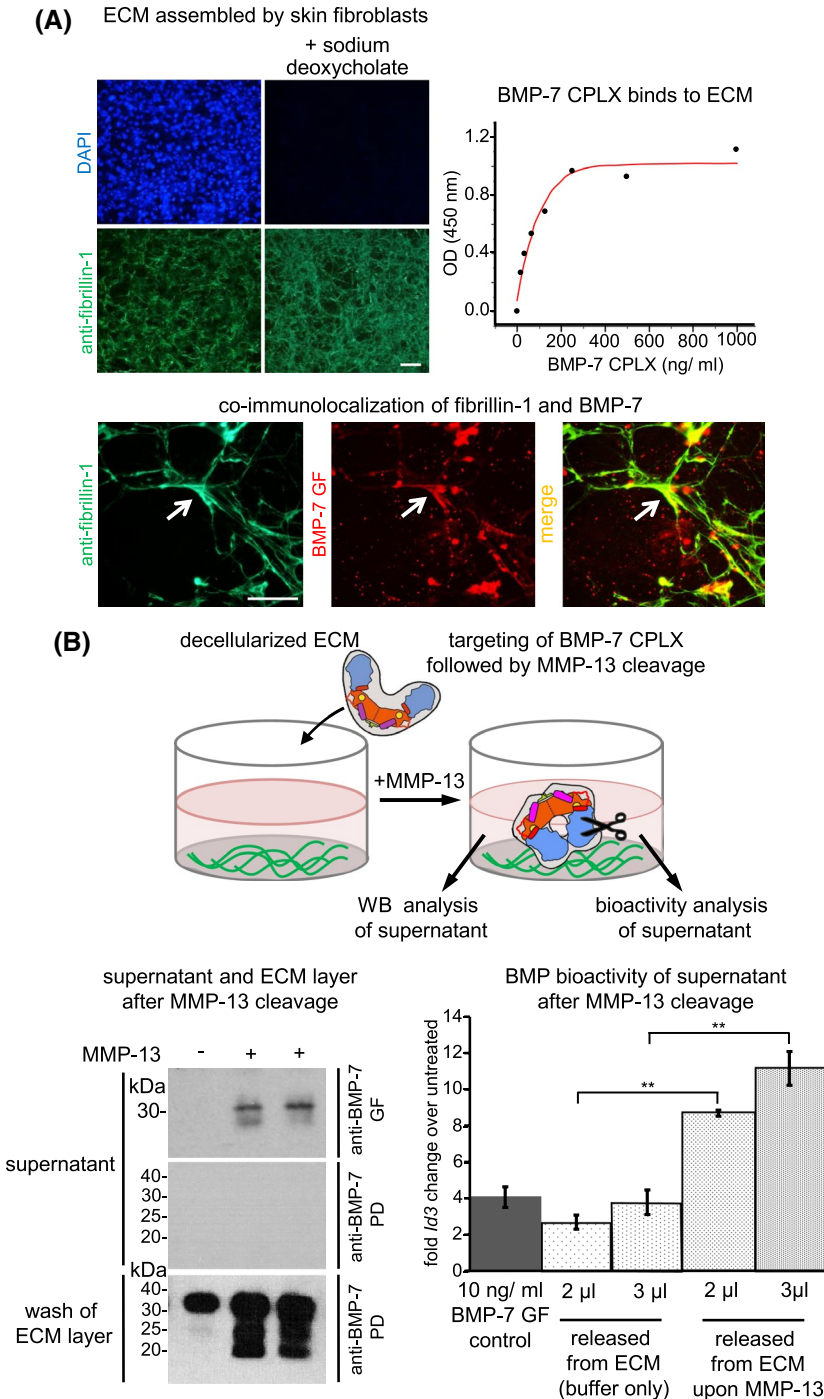
3.7 | MMP-13 cleavage leads to release of active BMP-7 GF from ECM-bound BMP-7 CPLX pools

To test whether MMP-13 is able to cleave and activate BMP-7 CPLX from ECM-bound pools, BMP-7 CPLX was targeted to fibrillin fibers assembled by primary fibroblasts (Figure 7A). Potential release of bioactive GF after MMP-13 cleavage into the supernatant was monitored via western blotting and BMP bioactivity assays. First, efficient binding of BMP-7 CPLX to decellularized fibrillin-1 fibers was demonstrated by detecting co-localizing immunofluorescence signals as well as by ELISA showing a concentration-dependent signal increase (Figure 7A). In a subsequent step, wells with fibrillin fibers decorated with BMP-7 CPLX were incubated

with MMP-13. Western blot analysis showed the presence of released BMP-7 GF into supernatant only when MMP-13 was added (Figure 7B). PD fragments could be only detected in the washed ECM layer, suggesting that upon cleavage they remain attached to the ECM. To assess whether released BMP-7 GF was bioactive, the supernatant was added to C2C12 cells and the mRNA expression of the endogenous BMP response gene *Id3* was measured (Figure 7B). Upon addition of MMP-13, an approximate fourfold increase in BMP activity was detected indicating that the BMP-7 GF was released in bioactive form (Figure 7B).

3.8 | MMP-13 cleavage of BMP-7 PD results in conformational change and CPLX disintegration

To investigate whether MMP-13 cleavage also leads to GF release when the CPLX is immobilized via hydrophobic residues to a non-ECM solid phase, we performed cleavage



studies with plastic-coated CPLX pools. For this purpose, BMP-7 CPLX was coated onto wells of microtiter plates, and was subsequently incubated with MMP-13 for 2 hours at RT in TC buffer (Figure 8). After MMP-13 cleavage, the supernatant was collected and subjected to SDS-PAGE and western blot analysis (Figure 8). In addition, BMP-7 CPLX remaining on the plate was stripped (in 300 mM NaCl, 200 mM acetic acid) and analyzed by western blotting. Similar to the release experiment from fibrillin-1 fibers, it was found that upon MMP-13 cleavage BMP-7 GF was released into the supernatant. However, in contrast to the ECM release experiment

(Figure 7B), BMP-7 PD fragments were simultaneously released into the supernatant. Efficient release of BMP-7 GF could be also confirmed by ELISA detecting less than 40% of BMP-7 GF still immobilized to the plate (Figure 8).

To gain further insight into how BMP-7 PD cleavage by MMP-13 affects BMP-7 CPLX stability, we analyzed samples after in solution cleavage by SDS-PAGE, native-PAGE, sandwich ELISA, and single particle TEM. Interestingly, at 50% BMP-7 PD cleavage, as assessed by Ponceau and western blot analysis, the CPLX signal was not detectable by Coomassie staining on native gels (Figure 9A). To exclude the possibility

FIGURE 7 MMP-13 cleavage of the BMP-7 PD leads to release of bioactive GF from ECM-targeted BMP-7 CPLX. A, Targeting of BMP-7 CPLX to ECM fibers assembled by skin fibroblasts. Top left, Immunofluorescence of assembled ECM fibers by primary mouse skin fibroblasts stained with anti-fibrillin-1 antibody and DAPI before and after decellularization with deoxycholate. Scale bar: 100 µm. Top right, ELISA-style interaction assay of recombinant BMP-7 CPLX with the decellularized ECM layer. Anti-BMP-7 GF antibody was used for detection. Bottom, Co-immunofluorescence analysis using anti-fibrillin-1 and anti-BMP-7 GF antibodies after incubation of recombinant BMP-7 CPLX with decellularized ECM fibers. Arrows point to yellow signals indicating co-localization between fibrillin-1 and BMP-7. Scale bar: 50 µm. B top, Scheme illustrating the design of MMP-13-mediated BMP-7 GF release experiment from ECM-targeted fraction. Bottom left, Supernatant and ECM layer after MMP-13 incubation were analyzed by western blot for BMP-7 presence. Bottom right, Stimulation of C2C12 cells with supernatant after MMP-13 incubation of BMP-7 CPLX bound to decellularized ECM *Id3* transcript levels were used as read-out for BMP-7 bioactivity. Error bars show standard deviation of three independent experiments (N = 3). Statistical analysis was by an unpaired two-tailed Student's t test. ** $P \leq .01$

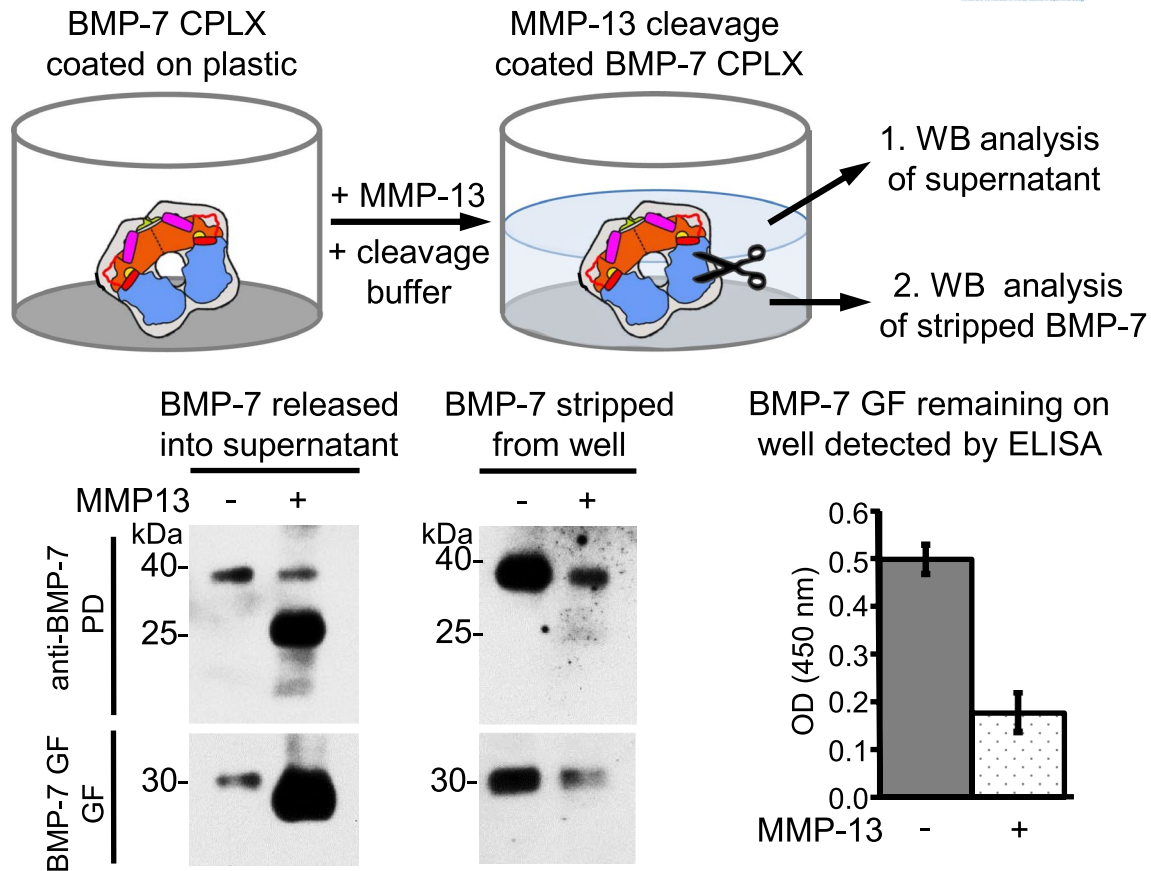


FIGURE 8 MMP-13 cleavage of BMP-7 PD on solid phase leads to BMP-7 CPLX disintegration and GF release. Top, Scheme to illustrate the set-up of the conducted experiment: BMP-7 CPLX was coated to microtiter plate wells and subsequently incubated with MMP-13 in cleavage buffer. The aspirated supernatant after MMP-13 cleavage was TCA precipitated and subjected to 10%-20% SDS-PAGE and western blot analysis using antibodies against BMP-7 PD and BMP-7 GF for detection. In addition, amounts of BMP-7 CPLX remaining on the well surface were stripped (300 mM NaCl and 200 mM acetic acid), TCA precipitated and subjected to western blot analysis. Bottom left, Western blot analysis of BMP-7 PD and GF in supernatant and in fraction stripped from well after MMP-13 incubation in cleavage buffer. Bottom right, Determination of remaining amounts of coated BMP-7 GF on well after MMP-13 incubation by direct ELISA using anti-BMP-7 GF antibody

that the loss of a distinct Coomassie band on native gels was not caused by major aggregation of the BMP-7 CPLX after PD cleavage, we performed dynamic light scattering (DLS) analysis before and after MMP-13 cleavage (Figure S3). Our analysis showed that MMP-13 cleavage did not lead to a decrease of the peak representing monomeric CPLX molecules at a particle size of 10 nm (Figure S3). The peak representing aggregated particles of an average size of 100 nm showed even a slight decrease suggesting that MMP-13-mediated cleavage of the PD led to a decrease rather than an increase of aggregation (Figure S3). To assess CPLX stability after MMP-13 cleavage we performed sandwich ELISA. However, when BMP-7 CPLX after in solution cleavage was transferred to wells pre-coated with anti-BMP-7 GF antibody, followed by incubation with anti-BMP-7 PD detection antibody, still 30% of signal could be detected compared to the non-cleaved control (Figure 9B).

Single particle TEM analysis of MMP-13-cleaved BMP-7 CPLX samples shown in Figure 9A revealed a conformational change of processed CPLX particles. Representative class averages of EM micrographs of the most frequent particles revealed that BMP-7 CPLX cleaved by MMP-13 adopts

a conformational change characterized by a widened angle between the PD arms and a four-subparticle appearance. This appearance was similar to the conformational change induced by the addition of 1 M urea which results in partial CPLX unfolding leading to partial PD displacement from the GF.⁴²

These findings suggested the possibility that processing of one PD per CPLX molecule leads to a conformational change in each molecule and, therefore, to an unfocused migration in native gels. The sandwich ELISA shows that less than 30% CPLX seems to be stable enough for detection. However, the unfolding leads to an unfocused migration in native-PAGE and, therefore, lack of staining intensity at the expected position.

3.9 | Molecular docking suggests that BMP-7 CPLX cleavage by MMP-13 requires PD displacement

To understand how MMP-13 processing of BMP-7 CPLX may occur on a molecular level in silico docking experiments were conducted. The center of the MMP-13 catalytic site is

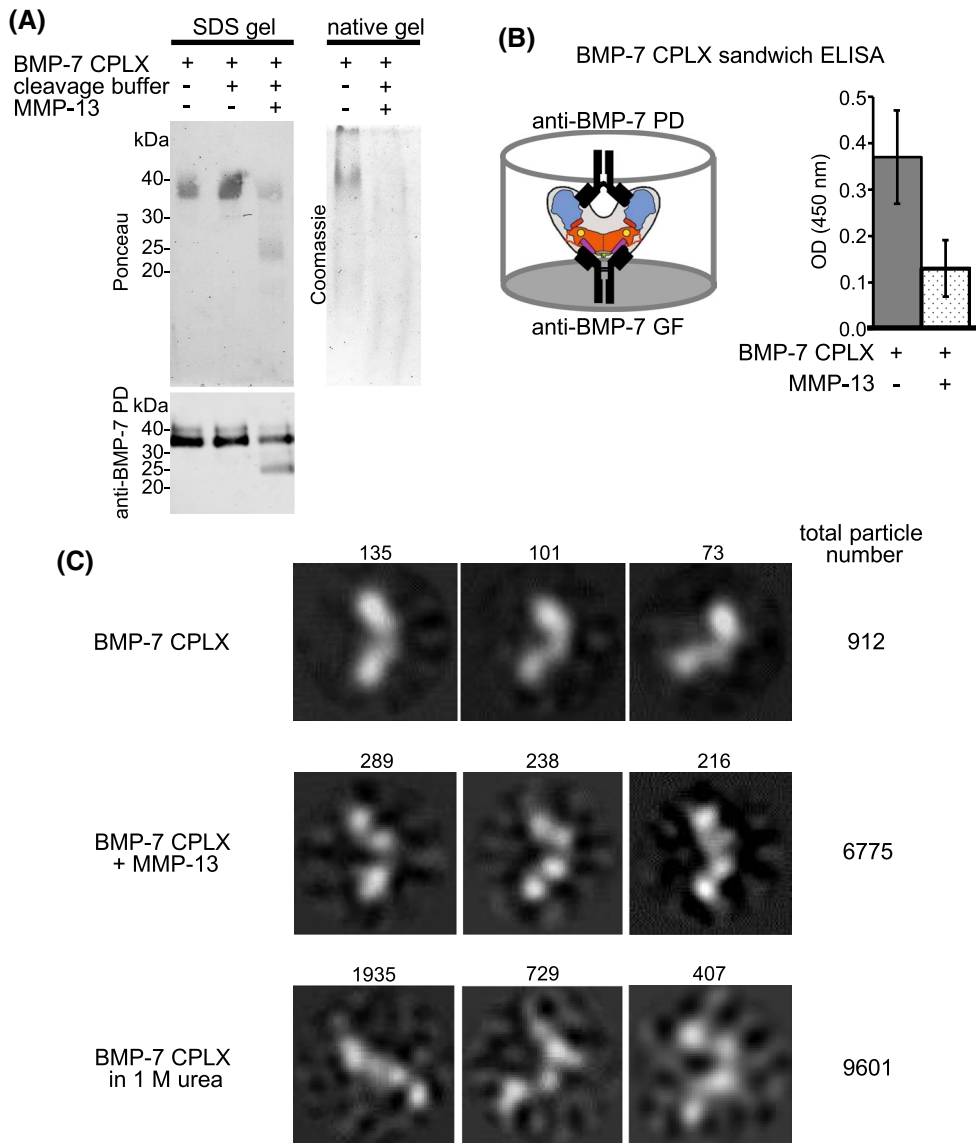
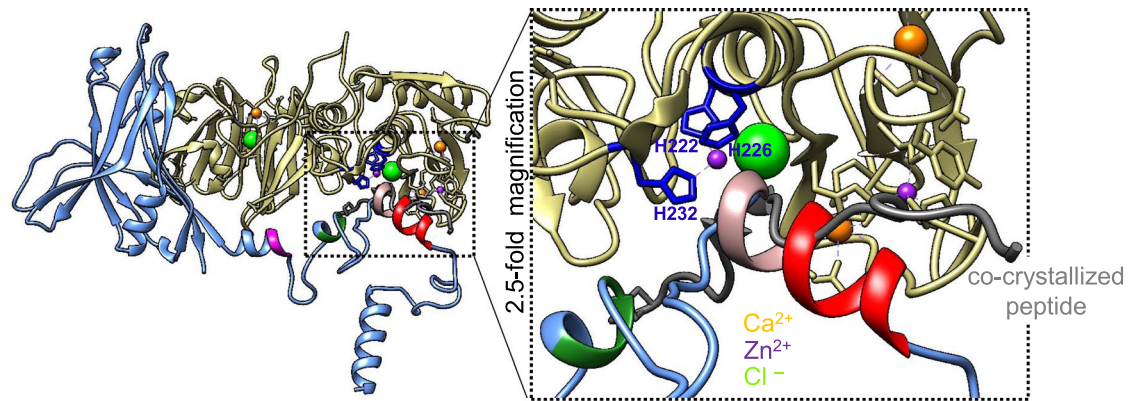
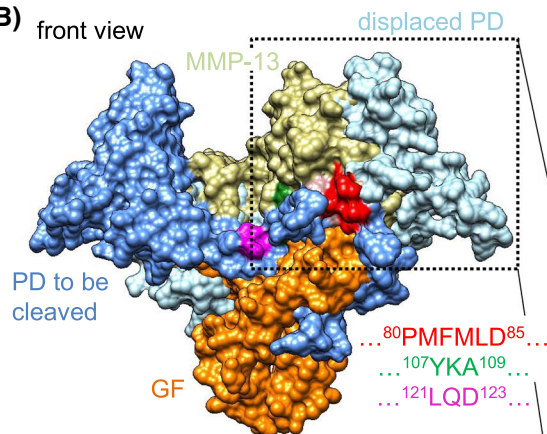


FIGURE 9 BMP-7 PD cleavage by MMP-13 leads to conformational change of BMP-7 CPLX. A, SDS-PAGE, native-PAGE, as well as western blot (mab33) analysis of BMP-7 PD after MMP-13 cleavage. B left, Illustration of sandwich ELISA set-up: anti-BMP-7 GF antibody was immobilized, and anti-BMP-7 PD antibody (mab33) was used for detection. Right, Remaining intact BMP-7 CPLX after MMP-13 incubation was detected by sandwich ELISA. C, Single particle TEM analysis of BMP-7 CPLX after MMP-13 incubation (same samples as shown in [A]), as well as after dialysis into 1 M urea. Depicted images represent class averages of multiple micrographs taken from individual molecules. Number of averaged individual molecules is given above each image (box size = 29.4 × 29.4 nm)

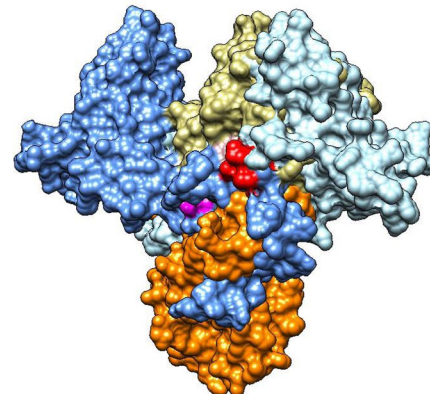
composed of H²²², H²²⁶, and H²³² that capture divalent metal ions with their aromatic rings to polarize water molecules that subsequently attack peptide bonds to perform the proteolysis (Figure 10A). Our docking results revealed that positioning of the ⁸³MLDL⁸⁶ stretch of one PD at the MMP-13 active cleft allows for further processing of the BMP-7 PD at the subsequent cleavage sites ¹⁰⁷YKA¹⁰⁹ and ¹²¹LQD¹²³ due to the interspacing loop regions that allow for flexibility of the PD structure at these sites during the cleavage. To validate the imaging approach, MMP-13 of our in silico cleavage model was aligned to MMP-13 structure co-crystallized with an N-terminal fragment of its activation peptide in its active cleft. Eight such co-crystallized peptides, originating from

the MMP-13 activation peptide after cleavage, consisted of an α -helix or random coil.⁶⁰ This agrees with our experimental data suggesting that the three MMP-13 cleavage sites of BMP-7 PD reside within the second and fourth α -helices at the N-terminal region of the PD (Figure 10A). The ⁸³MLDL⁸⁶ stretch aligns perfectly with the co-crystallized peptide used in this in silico experiment (Figure 10A).

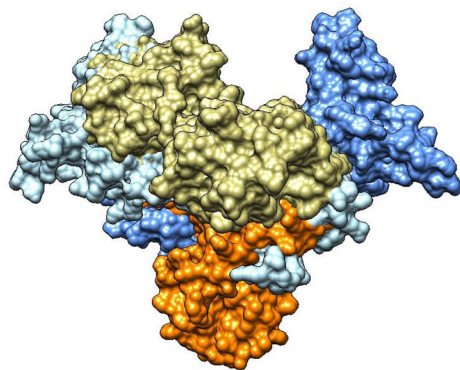
Next, we aligned our generated MMP-13/BMP-7 PD cleavage model (Figure 10A) to PDs of our BMP-7 CPLX model in open V-shape conformation. Thereby, we found that in this open CPLX conformation MMP-13 would need to bend or even displace one PD to gain access for efficient processing of the other PD (Figure 10B).

(A) alignment of co-crystallized peptide with ⁸⁰PMFMLD⁸⁵ at MMP-13 catalytic site**(B)** front view

side view



back view



front view, two-fold magnification

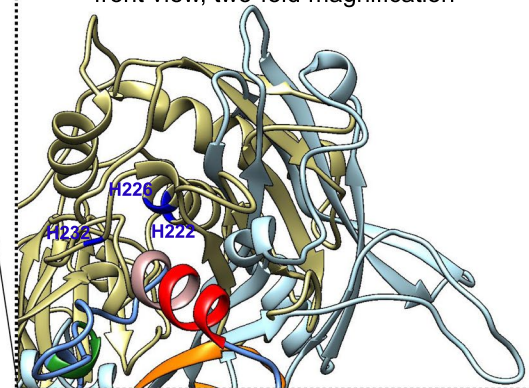


FIGURE 10 MMP-13 co-localizes with one BMP-7 PD to accomplish cleavage of the other PD in the open CPLX conformation. A, Docking of one BMP-7 PD in open conformation to the MMP-13 catalytic site. Residues of the catalytic site: H²²², H²²⁶, H²³² (all in blue), as well as cleavage regions ⁸⁰PMFMLD⁸⁵ (red), ¹⁰⁷YKA¹⁰⁹ (green), and ¹²¹LQD¹²³ (magenta) are marked. The magnified dashed box shows co-localization of the α 2-helix (light purple) carrying the cleavage site ⁸⁰PMFMLD⁸⁵ with the co-crystallized peptide (gray) of the MMP-13 crystal structure serving as positive control. B, Surface models of MMP-13 (beige) and BMP-7 CPLX in open V-shape conformation suggesting MMP-13 needs to bend one PD (light blue) to cleave the other (blue). Magnified (twofold) dashed box shows co-localization of MMP-13 and BMP-7 PD in ribbon representation. GF residues: orange

4 | DISCUSSION

Although many studies addressed the mechanisms of TGF- β activation,^{29,30,32,34,59,61,62} the required pathways for cellular utilization of other TGF- β superfamily members such as BMPs remain largely unknown. Since the discovery of BMPs as pluripotent cytokines extractable from bone matrix, it has

been speculated how BMPs targeted to the ECM become released and activated.

In this study, we uncovered a new proteolytic PD cleavage mechanism involving MMPs to release BMP GFs from FMF-stored ECM pools. In this context, BMP PDs not only mediate efficient targeting and sequestration of BMP GFs upon ECM binding, but also allow controlled release of bioactive

GF upon specific cleavage by MMPs. Our previous studies showed that binding of BMP-7 CPLX to fibrillin-1 induces a conformational change of the entire CPLX from an open bioactive V-shape to a closed latent ring-shape (Figure 6A). In this closed conformation, a structural re-arrangement of the two PDs leads to blockage of the BMP type II receptor-binding sites on the GF by the α 2-helix of the PD (Figure 6).⁴² Here, in our proposed MMP-13-mediated BMP-7 activation mechanism, recognition of the ⁸⁰PMFMLD⁸⁵ motif followed by PD processing of the scissile bond between F⁸² and M⁸³ leads to unfolding and disintegration of the entire CPLX resulting in release of the active GF dimer.

Our investigations revealed interesting molecular aspects of this BMP activation mechanism. Molecular docking experiments (Figure 6B) suggested the potential necessity of two MMP-13 monomers for efficient PD processing in the closed BMP-7 CPLX ring-shape conformation, to effectively release the active GF dimer. However, in the open V-shape CPLX, efficient scissile bond cleavage by MMP-13 at the ⁸⁰PMFMLD⁸⁵ site in one PD requires partial displacement of the other PD, suggesting a 1:1 stoichiometry (Figure 10).

Our in solution data suggest that cleavage of potentially only one PD is sufficient to result in unfolding and disintegration of the entire CPLX (Figure 6A). A possible explanation for this observation is that PD self-interaction contributes significantly to CPLX stability.⁴² Previously, we had also shown that BMP-7 PDs compete with BMP type II receptors for the same binding site on the GF, and that upon type II receptor binding, both PDs are displaced as a dimer.³⁹ PD dimers could be also detected in solution when the CPLX was step by step separated into its components by dialysis into increasing concentrations of urea.⁴² This suggests that PD dimers serve as a molecular clamp only exerting tight complexation of the GF dimer, when the dimer is intact. Our previous in solution data also showed that CPLX unfolding and disintegration takes place upon dialysis into increasing concentrations of urea (1-4 M).⁴² Here, our EM data showed partial unfolding of the CPLX already at a concentration of 1 M urea (Figure 9C), which we previously demonstrated is accompanied by PD displacement as dimer.⁴² This poses the possibility that the analyzed molecules with widened angle and four-subparticle appearance represent GF dimers from which PD dimers are about to be displaced in the 1 M urea sample. The similar appearance between BMP-7 CPLX molecules after dialysis into 1 M urea and MMP-13 cleavage further support our notion that PD cleavage leads to CPLX unfolding and release of the PD dimer clamp.

In the BMP PD cleavage assays conducted, we found that presence of 0.05% Triton X-100 served as an optimal concentration for efficient MMP-13 cleavage (Figure 3B,C). It is known that MMP activity is dependent on the detergent concentration used. To avoid adverse effects, it is crucial to

determine the optimal detergent concentration. At low concentrations, detergents act as monomers that may stabilize and activate MMPs. However, at high concentrations they form micelles that might sequester and inhibit MMP activity.^{35,63} In absence of Triton, BMP-7 PD processing by MMP-13 occurred with a reduced turn-over rate yielding three fragments starting with ⁸³MLDL⁸⁶, ¹²¹LQDS¹²⁴, and ¹⁰⁷YKA¹⁰⁹ (Figure 3C). However, in presence of Triton the ⁸³MLDL⁸⁶ fragment disappeared leading to an increased presence of the other two fragments (Figure 3B). This finding suggests that the fragment starting with ⁸³MLDL⁸⁶ is produced during the primary cleavage event and ¹²¹LQDS¹²⁴ and ¹⁰⁷YKA¹⁰⁹ are products of subsequent cleavage events. These experimental data are also in line with our in silico docking results which showed that the F⁸²-M⁸³ scissile bond was most surface accessible in comparison to P¹⁰⁶-Y¹⁰⁷, or S¹²⁰-L¹²¹ in the closed ring-shape BMP-7 CPLX conformation. Our experimental data also suggest that the S¹²⁰-L¹²¹ scissile bond is less accessible in absence of Triton in solid phase cleavage assays indicated by a less pronounced presence of the PD cleavage product at 20 kDa (Figures 8 and 9).

Using CleavPredict,⁵⁸ a cleavage site composed of six amino acid residues was predicted, three non-prime (amino acids downstream to the cleaved scissile bond) and three prime (amino acids upstream to the cleaved scissile bond) (Figure 5A). For most efficient MMP-13 cleavage, a general cleavage site was proposed based on a pronounced presence of a rigid Pro in P3 (non-prime), and Leu, Ile, or Met in P1' (prime), followed by small or acidic residues in P3' in the identified substrates.⁵⁸ In all mutated BMP-7 PD variants, apart from M83E, production of the fragment starting with ⁸³MLDL⁸⁶ was abolished and the fragments starting with ¹²¹LQDS¹²⁴ and ¹⁰⁷YKA¹⁰⁹ were significantly reduced (Figure 5C). This result is supportive of the hypothesis that P⁸⁰ and D⁸⁵ are required for PD cleavage by MMP-13 but disagrees with the assumption that M⁸³ is crucial for MMP-13 processing, since mutation of this residue did not affect the cleavage pattern (Figure 5C).

Our sequence alignment analysis showed that the identified ⁸⁰PMFMLD⁸⁵ motif in the BMP-7 PD was conserved among other BMP PDs (Figure 4A, Figure S2), suggesting a general MMP-mediated BMP PD cleavage mechanism. Our BMP PD cleavage screen revealed similarities but also differences to BMP-7 PD processing. BMP-5 and -7 belong to the same BMP subgroup and showed an identical cleavage pattern for MMP-13 (Figure 4B). However, BMP-4 PD processing did not yield the band at 25 kDa suggesting more efficient secondary cleavage. This may be due to different amino acid residues present in the P1 and P2 positions of the non-prime region of the cleavage site. Also, in BMP-9 and 10 PDs the most significant changes of the cleavage motif are within this region resulting in less efficient processing

by MMP-13. More specifically, BMP-10 PD lacks an Asp (D) in the P3' position of the prime region that is predicted to be required for efficient cleavage (Figure 5A).⁵⁸ This may explain the almost diminished MMP-13 cleavage of BMP-10 PD compared to BMP-9 PD (Figure 4B). However, our results also showed that most likely these changes protect BMP-9 and -10 PD from MMP-8 and -9 cleavage but make them more susceptible to MMP-12 processing in comparison to BMP-7 (Figure 4C). It is also conceivable that the different conformations of the BMP PDs impact MMP cleavage efficiency in the conducted assays. Based on the sequence homology, it can be assumed that BMP-9 and -10 PDs fold similarly but differently than BMP-7 PD.

In TGF- β -1 and -2 most critical residues of the identified MMP motif in BMP-7 PD are altered. However, maintaining a Pro in P3 and some conserved residues in the P4'-P6' prime region most probably allows MMP-13 processing of both TGF PDs to a minor extent. Interestingly, we observed only very limited MMP-2 cleavage of TGF- β -2 PD in comparison to TGF- β -1 (Figure 4C). This suggests that the presence of a second proline at the P2 position of the non-prime region is inhibitory for efficient MMP processing (Figure 4A). As GDF-8 lacks most residues predicted to be critical for MMP recognition and processing, we expected it to be inert against MMP cleavage. However, we observed that after MMP-7, -12, and -13 incubation, a cleavage product at around 19 kDa was detected. According to our predictions using CleavPredict, substitution of Pro to Leu in P1 which is found in the GDF-8 PD sequence, is not sufficient to block MMP-13 cleavage. Based on the alignment shown in Figure 4A, the GDF-8 PD sequence still contains a conserved Asp (D) residue in P3' of the ⁸⁰PMFMLD⁸⁵ motif. Also, Leu in P1' and Ile in P2' were found suitable for MMP cleavage using trypsin-generated human peptide libraries.⁵⁸ Furthermore, a degradation product of about 19 kDa is also obtained upon cleavage of GDF-8 PD by TLL2. The TLL2 cleavage site ⁹⁹DDSSDGSLE¹⁰⁷ was identified to be located three amino acids further downstream to the identified MMP cleavage site.³⁷ Based on the similar sizes, we can speculate that this region may be also prone to proteolytic degradation by MMPs. Since TLL2 cleavage at this site showed to weaken critical PD-GF interactions leading to activation of the GF from its latent CPLX form,³⁷ the newly found proteolytic susceptibility of GDF-8 PD opens up further investigation to study similar activation mechanisms mediated by MMPs.

The investigated MMP-mediated cleavage events yielded in BMP-7 PD fragments of similar sizes approximately at 30, 25, and 20 kDa (Figure 2C) which remain attached to the ECM layer (Figure 7B). Previously, we reported that the BMP-7 CPLX binds to fibrillin-1 via a specific epitope residing within Gly⁷⁴ - Arg¹⁸⁴ of the PD. Therefore, it is possible that all three PD cleavage products (starting with M⁸³, Y¹⁰⁷, or L¹²¹) generated by MMP-13 cleavage still contain the high

affinity binding site for fibrillin-1 and are, therefore, not released from FMF under the chosen buffer conditions. This may suggest that PD fragments remaining on the FMF may block targeting of freshly produced BMP CPLXs. However, it is certainly possible that further degradation reactions occur in vivo to finally clear the remaining PD fragments. The fate of PD fragments has to be viewed in a context-dependent manner. In situations with little ECM present such as during embryogenesis, PD fragments may be released freely to exert their own functional role. It was already reported that certain BMP-7 PD fragments called bone forming peptide 1 and 2 (BFP-1 and -2) can induce osteogenesis more potently than BMP-7 GF in in vitro and in vivo experiments.^{64,65} However, the underlying mechanism remains unclear. A possible explanation is that these PD fragments promote GF interactions with its receptor complex. BFP-1 (G¹⁰⁰-Q¹¹⁴) resides within the ⁸³MLD⁸⁵ and ¹²¹LQD¹²³ cleavage sites.⁶⁴ The sequence giving rise to the BFP-2 fragment (V¹⁴⁰-R¹⁵⁴) lies further downstream beyond the ¹²¹LQD¹²³ cleavage site.⁶⁵ Interestingly, cleavage at the ¹⁰⁷YKA¹⁰⁹ site would split the BFP-1 peptide in two halves potentially leading to its inactivation. Our data suggest that MMP-13 processes BMP-7 PD first at the ⁸³MLD⁸⁵ site, followed by a secondary cleavage event at ¹⁰⁷YKA¹⁰⁹, which is succeeded by cleavage at the ¹²¹LQD¹²³ site that will split BFP-1 into two smaller fragments. MMP-2 and MMP-3 seem to follow a different cleavage sequence that does not utilize the ¹⁰⁷YKA¹⁰⁹ cleavage site (Figure 3A). This implies that despite most MMP cleavage events yielded BMP-7 PD fragments of similar sizes, it is likely that PD processing by different MMPs yields PD fragments with different functional activity, which may add another layer of regulation of BMP activity in certain physiological conditions. For instance, in differentiation processes such as chondrogenic or osteogenic differentiation, where MMPs are known to play an important role,^{66,67} BMP bioactivity may be further modulated by the generation of functionally active PD fragments.

The concept that proteases serve as specific activators of TGF- β superfamily members through PD cleavage has been previously explored. TGF- β -1 PD could be cleaved in in vitro experiments by MMP-2 and MMP-9.^{32,59} In addition, MMP-14 activity, which depends on integrins, can promote TGF- β -1 activation.³³ Furthermore, MMP cleavage of the TGF- β PD was proposed as a mechanism to release TGF- β GF from the ECM.^{27,31} In addition, it could be shown that the metalloproteinase BMP-1, a procollagen endopeptidase removing C-terminal collagen propeptides, serves as GF activating enzyme by PD cleavage of several TGF- β superfamily members. BMP-1 is capable to process the PDs of GDF-8, GDF-11, and BMP-10 PDs and thereby rendering the GF from latent to bioactive.^{12,35,36} Interestingly, in a previous cleavage screen with BMP-1 and PDs of BMP-4, -5, -7 no processing was observed,¹² suggesting that

different TGF- β superfamily members are activated by different sets of metalloproteinases. This is probably reflecting the different cellular circumstances requiring activation of specific GFs. In the early stages of development where little ECM is present, active GFs are regulated by complexation to BMP antagonists such as chordin,⁶⁸ which need to be also cleaved by BMP-1/tolloid-related metalloproteases to liberate the active GF.⁶⁸⁻⁷⁰ At later stages of development and certainly with the beginning of postnatal life when increasingly more ECM is present, PD-ECM interactions facilitate GF targeting and sequestration. In this phase, MMPs start to regulate the bioavailability of tissue resident BMPs such as BMP-7. However, for soluble BMPs such as BMP-10 it could be shown that the PD complexation facilitates GF specificity toward cellular surfaces. While the BMP-10 CPLX appeared to be latent toward C2C12 mouse myoblasts,¹² it proved to be bioactive toward endothelial cells.⁴⁰ BMP-9 and -10 have been suggested to have redundant functions and also form hetero GF dimers.^{71,72} Until now, the complex interplay of BMP-9 and -10 functions in development and disease are not fully understood. As MMPs are also present in blood, controlled MMP cleavage of BMP-9 and -10 PDs may represent a new mechanism to orchestrate their bioactivity under normal physiological or endothelial stress/disease conditions.

Our observation of BMP-dependent induction of MMP expression (Figure 1B,C) was also found to be implicated in developmental or disease mechanisms accompanied by ECM degradation. For instance, BMP-2 stimulation of the mouse myoblast cell line C2C12 initiated strong expression of MMP-13.⁷³ Also, BMP-2 and -4 stimulation of primary human fibroblast led to MMP-1, -2, -3, and -13 upregulation which was suggested to be a mechanism in melanoma invasion.⁷⁴ Furthermore, other studies have shown that BMPs are drivers of tumor metastasis by inducing MMP expression and activity.⁷⁵ For instance, BMP-stimulated MMP-2 and -9 activity was shown to be a relevant mechanism in breast cancer cell migration and invasion.⁷⁶ Previous studies could associate BMP-7 expression with early bone metastasis development in breast cancer.^{77,78} MMP-13 was described to be overexpressed at the tumor-bone interface and abrogation of MMP-13 in this area inhibited bone metastasis.⁷⁹ As cancer often times recapitulates embryonic programs, it is not surprising that similar mechanisms occur during cartilage development. During chondrogenesis, BMPs control terminal differentiation where chondrocytes become hypertrophic and remove the collagen matrix through the upregulation of MMP-13.²⁷ Interestingly, during OA, chondrocytes in articular cartilage behave again as terminally differentiating chondrocytes. There, elevated BMP levels in damaged cartilage not only contribute to tissue repair by stimulating

ECM synthesis but also promote cartilage degeneration by stimulating MMP-13 expression.⁸⁰

Overall, BMP-stimulated MMP production appears to be an established mechanism during development and disease with the goal to rapidly remodel ECM architecture. Thereby, a fine-tuned balance between BMP and MMP activity is crucial. In disease situations such as cancer or OA, small amounts of active BMP or MMP may initiate a vicious feed-forward cycle where MMP-mediated BMP release from ECM-targeted pools further promotes MMP production ultimately resulting in severe ECM destruction. Similarly, in connective tissue disorders such as Marfan syndrome, failed BMP sequestration due to ECM deficiency may also trigger MMP-mediated destruction cascade in tissues.

This study provides evidence for the existence of an MMP-dependent mechanism for BMP activation from ECM-targeted pools by PD cleavage. This knowledge may open up new therapeutic avenues, to impede pathomechanisms characterized by dysregulated BMP GF activity and ECM destruction.

ACKNOWLEDGMENTS

The authors thank Marina Tauber and Niklas Sonntag for excellent technical assistance. The authors also thank Dr Thomas Jowitt of the University of Manchester Biomolecular analysis facility for collecting the DLS data. Funding for this study was provided by the Deutsche Forschungsgemeinschaft (DFG, German Research Foundation) project numbers 73111208 (SFB 829/B12), 397484323 (TRR 259/B09), as well as FOR2722/C2 to G.S. DFG funding was also provided to M.K. (FOR2722/B2). In addition, this study was supported in part by a Brazilian National Council for Scientific and Technological Development (CNPq-Brazil) fellowship to A.G.F. [process number: 231369/2013-1]. The Wellcome Centre for Cell-Matrix Research is supported by funding from the Wellcome Trust (203128/Z/16/Z). A.R.F.G. is supported by BBSRC funding (Ref: BB/S015779/1).

CONFLICT OF INTEREST

The authors declare no conflict of interest.

AUTHOR CONTRIBUTIONS

G. Sengle designed the research. A.G. Furlan, C.E.S. Spanou, A.R.F. Godwin, A.P. Wohl, and L.M.A. Zimmermann performed the research. T. Imhof and M. Koch contributed new reagents. A.G. Furlan, C.E.S. Spanou, A.R.F. Godwin, A.P. Wohl, L.M.A. Zimmermann, and C. Baldock analyzed the data. A.G. Furlan and G. Sengle wrote the manuscript.

REFERENCES

1. Shi Y, Massague J. Mechanisms of TGF-beta signaling from cell membrane to the nucleus. *Cell*. 2003;113:685-700.

2. Wu MY, Hill CS. Tgf-beta superfamily signaling in embryonic development and homeostasis. *Dev Cell*. 2009;16:329-343.
3. Wang EA, Rosen V, D'Alessandro JS, et al. Recombinant human bone morphogenetic protein induces bone formation. *Proc Natl Acad Sci U S A*. 1990;87:2220-2224.
4. Gregory KE, Ono RN, Charbonneau NL, et al. The prodomain of BMP-7 targets the BMP-7 complex to the extracellular matrix. *J Biol Chem*. 2005;280:27970-27980.
5. Charbonneau NL, Ono RN, Corson GM, Keene DR, Sakai LY. Fine tuning of growth factor signals depends on fibrillin microfibril networks. *Birth Defects Res C Embryo Today*. 2004;72:37-50.
6. Sengle G, Charbonneau NL, Ono RN, et al. Targeting of bone morphogenetic protein growth factor complexes to fibrillin. *J Biol Chem*. 2008;283:13874-13888.
7. Tsuji K, Bandyopadhyay A, Harfe BD, et al. BMP2 activity, although dispensable for bone formation, is required for the initiation of fracture healing. *Nat Genet*. 2006;38:1424-1429.
8. Paralkar VM, Weeks BS, Yu YM, Kleinman HK, Reddi AH. Recombinant human bone morphogenetic protein 2B stimulates PC12 cell differentiation: potentiation and binding to type IV collagen. *J Cell Biol*. 1992;119:1721-1728.
9. Suzawa M, Takeuchi Y, Fukumoto S, et al. Extracellular matrix-associated bone morphogenetic proteins are essential for differentiation of murine osteoblastic cells in vitro. *Endocrinology*. 1999;140:2125-2133.
10. Sieron AL, Louneva N, Fertala A. Site-specific interaction of bone morphogenetic protein 2 with procollagen II. *Cytokine*. 2002;18:214-221.
11. Wang X, Harris RE, Bayston LJ, Ashe HL. Type IV collagens regulate BMP signalling in Drosophila. *Nature*. 2008;455:72-77.
12. Sengle G, Ono RN, Sasaki T, Sakai LY. Prodomains of transforming growth factor beta (TGFbeta) superfamily members specify different functions: extracellular matrix interactions and growth factor bioavailability. *J Biol Chem*. 2011;286:5087-5099.
13. Sakai LY, Keene DR, Engvall E. Fibrillin, a new 350-kD glycoprotein, is a component of extracellular microfibrils. *J Cell Biol*. 1986;103:2499-2509.
14. Sakai LY, Keene DR, Renard M, De Backer J. FBN1: the disease-causing gene for Marfan syndrome and other genetic disorders. *Gene*. 2016;591:279-291.
15. Loeys BL, Matthys DM, de Paepe AM. Genetic fibrillinopathies: new insights in molecular diagnosis and clinical management. *Acta Clin Belg*. 2003;58:3-11.
16. Nistala H, Lee-Arteaga S, Smaldone S, et al. Fibrillin-1 and -2 differentially modulate endogenous TGF-beta and BMP bioavailability during bone formation. *J Cell Biol*. 2010;190:1107-1121.
17. Arteaga-Solis E, Gayraud B, Lee SY, Shum L, Sakai L, Ramirez F. Regulation of limb patterning by extracellular microfibrils. *J Cell Biol*. 2001;154:275-281.
18. Sengle G, Carlberg V, Tufa SF, et al. Abnormal activation of BMP signaling causes myopathy in Fbn2 null mice. *PLoS Genet*. 2015;11:e1005340.
19. Ramirez F, Rifkin DB. Extracellular microfibrils: contextual platforms for TGFbeta and BMP signaling. *Curr Opin Cell Biol*. 2009;21:616-622.
20. Sengle G, Sakai LY. The fibrillin microfibril scaffold: a niche for growth factors and mechanosensation? *Matrix Biol*. 2015;47:3-12.
21. Miyazono K, Hellman U, Wernstedt C, Heldin CH. Latent high molecular weight complex of transforming growth factor beta 1. Purification from human platelets and structural characterization. *J Biol Chem*. 1988;263:6407-6415.
22. Unsold C, Hyytiainen M, Bruckner-Tuderman L, Keski-Oja J. Latent TGF-beta binding protein LTBP-1 contains three potential extracellular matrix interacting domains. *J Cell Sci*. 2001;114:187-197.
23. Saharinen J, Keski-Oja J. Specific sequence motif of 8-Cys repeats of TGF-beta binding proteins, LTBPs, creates a hydrophobic interaction surface for binding of small latent TGF-beta. *Mol Biol Cell*. 2000;11:2691-2704.
24. Dallas SL, Sivakumar P, Jones CJ, et al. Fibronectin regulates latent transforming growth factor-beta (TGF beta) by controlling matrix assembly of latent TGF beta-binding protein-1. *J Biol Chem*. 2005;280:18871-18880.
25. Isogai Z, Ono RN, Ushiro S, et al. Latent transforming growth factor beta-binding protein 1 interacts with fibrillin and is a microfibril-associated protein. *J Biol Chem*. 2003;278:2750-2757.
26. Ono RN, Sengle G, Charbonneau NL, et al. Latent transforming growth factor beta-binding proteins and fibulins compete for fibrillin-1 and exhibit exquisite specificities in binding sites. *J Biol Chem*. 2009;284:16872-16881.
27. Dangelo M, Sarment DP, Billings PC, Pacifici M. Activation of transforming growth factor beta in chondrocytes undergoing endochondral ossification. *J Bone Miner Res*. 2001;16:2339-2347.
28. Fontana L, Chen Y, Prijatelj P, et al. Fibronectin is required for integrin alphavbeta6-mediated activation of latent TGF-beta complexes containing LTBP-1. *FASEB J*. 2005;19:1798-1808.
29. Shi M, Zhu J, Wang R, et al. Latent TGF-beta structure and activation. *Nature*. 2011;474:343-349.
30. Buscemi L, Ramonet D, Klingberg F, et al. The single-molecule mechanics of the latent TGF-beta1 complex. *Curr Biol*. 2011;21:2046-2054.
31. Jenkins G. The role of proteases in transforming growth factor-beta activation. *Int J Biochem Cell Biol*. 2008;40:1068-1078.
32. Yu Q, Stamenkovic I. Cell surface-localized matrix metalloproteinase-9 proteolytically activates TGF-beta and promotes tumor invasion and angiogenesis. *Genes Dev*. 2000;14:163-176.
33. Mu D, Cambier S, Fjellbirkeland L, et al. The integrin alpha(v)beta8 mediates epithelial homeostasis through MT1-MMP-dependent activation of TGF-beta1. *J Cell Biol*. 2002;157:493-507.
34. Ge G, Greenspan DS. BMP1 controls TGFbeta1 activation via cleavage of latent TGFbeta-binding protein. *J Cell Biol*. 2006;175:111-120.
35. Wolfman NM, McPherron AC, Pappano WN, et al. Activation of latent myostatin by the BMP-1/tolloid family of metalloproteinases. *Proc Natl Acad Sci U S A*. 2003;100:15842-15846.
36. Ge G, Hopkins DR, Ho WB, Greenspan DS. GDF11 forms a bone morphogenetic protein 1-activated latent complex that can modulate nerve growth factor-induced differentiation of PC12 cells. *Mol Cell Biol*. 2005;25:5846-5858.
37. Le VQ, Iacob RE, Tian Y, et al. Tolloid cleavage activates latent GDF8 by priming the pro-complex for dissociation. *EMBO J*. 2018;37:384-397.
38. Brown MA, Zhao Q, Baker KA, et al. Crystal structure of BMP-9 and functional interactions with pro-region and receptors. *J Biol Chem*. 2005;280:25111-25118.
39. Sengle G, Ono RN, Lyons KM, Bachinger HP, Sakai LY. A new model for growth factor activation: type II receptors compete with the prodomain for BMP-7. *J Mol Biol*. 2008;381:1025-1039.

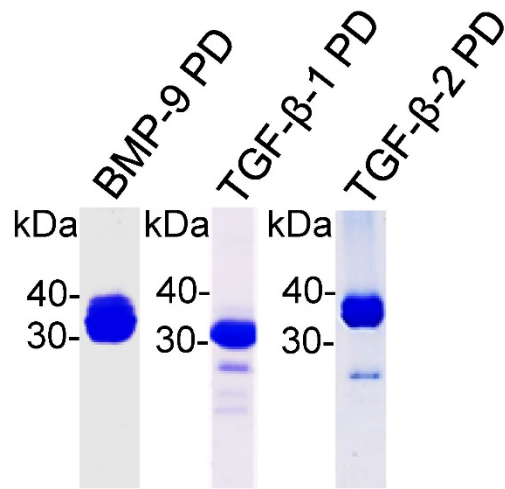
40. Jiang H, Salmon RM, Upton PD, et al. The prodomain-bound form of bone morphogenetic protein 10 is biologically active on endothelial cells. *J Biol Chem.* 2016;291:2954-2966.
41. Kienast Y, Jucknischke U, Scheiblich S, et al. Rapid activation of bone morphogenetic protein 9 by receptor-mediated displacement of Pro-domains. *J Biol Chem.* 2016;291:3395-3410.
42. Wohl AP, Troilo H, Collins RF, Baldock C, Sengle G. extracellular regulation of bone morphogenetic protein activity by the microfibril component fibrillin-1. *J Biol Chem.* 2016;291:12732-12746.
43. Hiepen C, Jatzlau J, Hildebrandt S, et al. BMPR2 acts as a gatekeeper to protect endothelial cells from increased TGFbeta responses and altered cell mechanics. *PLoS Biol.* 2019;17:e3000557.
44. Lichti U, Anders J, Yuspa SH. Isolation and short-term culture of primary keratinocytes, hair follicle populations and dermal cells from newborn mice and keratinocytes from adult mice for in vitro analysis and for grafting to immunodeficient mice. *Nat Protoc.* 2008;3:799-810.
45. Livak KJ, Schmittgen TD. Analysis of relative gene expression data using real-time quantitative PCR and the 2^{-Delta Delta C(T)} Method. *Methods.* 2001;25:402-408.
46. Kuo CL, Isogai Z, Keene DR, et al. Effects of fibrillin-1 degradation on microfibril ultrastructure. *J Biol Chem.* 2007;282:4007-4020.
47. Koch M, Veit G, Stricker S, et al. Expression of type XXIII collagen mRNA and protein. *J Biol Chem.* 2006;281:21546-21557.
48. Hedman K, Kurkinen M, Alitalo K, Vaheri A, Johansson S, Hook M. Isolation of the pericellular matrix of human fibroblast cultures. *J Cell Biol.* 1979;81:83-91.
49. Berry R, Jowitt TA, Ferrand J, et al. Role of dimerization and substrate exclusion in the regulation of bone morphogenetic protein-1 and mammalian tolloid. *Proc Natl Acad Sci U S A.* 2009;106:8561-8566.
50. Kimanius D, Forsberg BO, Scheres SHW, Lindahl E. Accelerated cryo-EM structure determination with parallelisation using GPUs in RELION-2. *eLife.* 2016;5:e18722.
51. Tang G, Peng L, Baldwin PR, et al. EMAN2: an extensible image processing suite for electron microscopy. *J Struct Biol.* 2007;157:38-46.
52. Sali A, Blundell TL. Comparative protein modelling by satisfaction of spatial restraints. *J Mol Biol.* 1993;234:779-815.
53. Pettersen EF, Goddard TD, Huang CC, et al. UCSF Chimera—a visualization system for exploratory research and analysis. *J Comput Chem.* 2004;25:1605-1612.
54. Kozakov D, Hall DR, Xia B, et al. The ClusPro web server for protein-protein docking. *Nat Protoc.* 2017;12:255-278.
55. Liu Y, Li Y, Li N, et al. TGF-beta1 promotes scar fibroblasts proliferation and transdifferentiation via up-regulating MicroRNA-21. *Sci Rep.* 2016;6:32231.
56. Nagase H, Visse R, Murphy G. Structure and function of matrix metalloproteinases and TIMPs. *Cardiovasc Res.* 2006;69:562-573.
57. Kumar S, Ratnikov BI, Kazanov MD, Smith JW, Cieplak P. CleavPredict: a platform for reasoning about matrix metalloproteinases proteolytic events. *PLoS One.* 2015;10:e0127877.
58. Eckhard U, Huesgen PF, Schilling O, et al. Active site specificity profiling of the matrix metalloproteinase family: proteomic identification of 4300 cleavage sites by nine MMPs explored with structural and synthetic peptide cleavage analyses. *Matrix Biol.* 2016;49:37-60.
59. Wang M, Zhao D, Spinetti G, et al. Matrix metalloproteinase 2 activation of transforming growth factor-beta1 (TGF-beta1) and TGF-beta1-type II receptor signaling within the aged arterial wall. *Arterioscler Thromb Vasc Biol.* 2006;26:1503-1509.
60. Stura EA, Visse R, Cuniasso P, Dive V, Nagase H. Crystal structure of full-length human collagenase 3 (MMP-13) with peptides in the active site defines exosites in the catalytic domain. *FASEB J.* 2013;27:4395-4405.
61. Lyons RM, Gentry LE, Purchio AF, Moses HL. Mechanism of activation of latent recombinant transforming growth factor beta 1 by plasmin. *J Cell Biol.* 1990;110:1361-1367.
62. Ribeiro SM, Poczatek M, Schultz-Cherry S, Villain M, Murphy-Ullrich JE. The activation sequence of thrombospondin-1 interacts with the latency-associated peptide to regulate activation of latent transforming growth factor-beta. *J Biol Chem.* 1999;274:13586-13593.
63. Park HI, Lee S, Ullah A, Cao Q, Sang QX. Effects of detergents on catalytic activity of human endometase/matrilysin 2, a putative cancer biomarker. *Anal Biochem.* 2010;396:262-268.
64. Kim HK, Kim JH, Park DS, et al. Osteogenesis induced by a bone forming peptide from the prodomain region of BMP-7. *Biomaterials.* 2012;33:7057-7063.
65. Kim HK, Lee JS, Kim JH, et al. Bone-forming peptide-2 derived from BMP-7 enhances osteoblast differentiation from multipotent bone marrow stromal cells and bone formation. *Exp Mol Med.* 2017;49:e328.
66. Assis-Ribas T, Forni MF, Winnischofer SMB, Sogayar MC, Trombetta-Lima M. Extracellular matrix dynamics during mesenchymal stem cells differentiation. *Dev Biol.* 2018;437:63-74.
67. Almalki SG, Agrawal DK. Effects of matrix metalloproteinases on the fate of mesenchymal stem cells. *Stem Cell Res Ther.* 2016;7:129.
68. Troilo H, Zuk AV, Tunnicliffe RB, et al. Nanoscale structure of the BMP antagonist chordin supports cooperative BMP binding. *Proc Natl Acad Sci U S A.* 2014;111:13063-13068.
69. Scott IC, Blitz IL, Pappano WN, et al. Mammalian BMP-1/Tolloid-related metalloproteinases, including novel family member mammalian Tolloid-like 2, have differential enzymatic activities and distributions of expression relevant to patterning and skeletogenesis. *Dev Biol.* 1999;213:283-300.
70. Piccolo S, Agius E, Lu B, Goodman S, Dale L, De Robertis EM. Cleavage of Chordin by Xolloid metalloprotease suggests a role for proteolytic processing in the regulation of Spemann organizer activity. *Cell.* 1997;91:407-416.
71. Ricard N, Ciais D, Levet S, et al. BMP9 and BMP10 are critical for postnatal retinal vascular remodeling. *Blood.* 2012;119:6162-6171.
72. Tillet E, Ouarne M, Desroches-Castan A, et al. A heterodimer formed by bone morphogenetic protein 9 (BMP9) and BMP10 provides most BMP biological activity in plasma. *J Biol Chem.* 2018;293:10963-10974.
73. Nakashima A, Tamura M. Regulation of matrix metalloproteinase-13 and tissue inhibitor of matrix metalloproteinase-1 gene expression by WNT3A and bone morphogenetic protein-2 in osteoblastic differentiation. *Front Biosci.* 2006;11:1667-1678.
74. Rothhammer T, Braig S, Bosserhoff AK. Bone morphogenetic proteins induce expression of metalloproteinases in melanoma cells and fibroblasts. *Eur J Cancer.* 2008;44:2526-2534.
75. Bach DH, Park HJ, Lee SK. The dual role of bone morphogenetic proteins in cancer. *Mol Ther Oncolytics.* 2018;8:1-13.
76. Cyr-Depauw C, Northey JJ, Tabaries S, et al. Chordin-Like 1 suppresses bone morphogenetic protein 4-induced breast cancer cell migration and invasion. *Mol Cell Biol.* 2016;36:1509-1525.

77. Alarmo EL, Parssinen J, Ketolainen JM, Savinainen K, Karhu R, Kallioniemi A. BMP7 influences proliferation, migration, and invasion of breast cancer cells. *Cancer Lett.* 2009;275:35-43.
78. Sakai H, Furihata M, Matsuda C, et al. Augmented autocrine bone morphogenic protein (BMP) 7 signaling increases the metastatic potential of mouse breast cancer cells. *Clin Exp Metastasis.* 2012;29:327-338.
79. Nannuru KC, Futakuchi M, Varney ML, Vincent TM, Marcusson EG, Singh RK. Matrix metalloproteinase (MMP)-13 regulates mammary tumor-induced osteolysis by activating MMP9 and transforming growth factor-beta signaling at the tumor-bone interface. *Cancer Res.* 2010;70:3494-3504.
80. van der Kraan PM, Blaney Davidson EN, van den Berg WB. Bone morphogenetic proteins and articular cartilage: to serve and protect or a wolf in sheep clothing's? *Osteoarthritis Cartilage.* 2010;18:735-741.

SUPPORTING INFORMATION

Additional Supporting Information may be found online in the Supporting Information section.

How to cite this article: Furlan AG, Spanou CES, Godwin ARF, et al. A new MMP-mediated prodomain cleavage mechanism to activate bone morphogenetic proteins from the extracellular matrix. *The FASEB Journal.* 2021;35:e21353. <https://doi.org/10.1096/fj.202001264R>

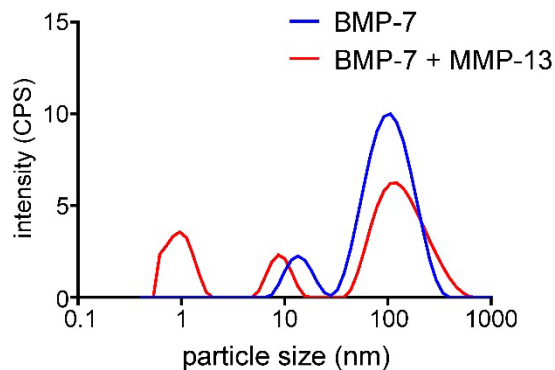


Supplementary Figure S1: Affinity purification of recombinant TGF- β superfamily PDs used in this study. Coomassie Brilliant Blue-stained SDS-PAGE quality control gels of recombinantly expressed and affinity-purified PDs.

BMP-4 PD										BMP-9 PD																	
scissile bond										scissile bond																	
non-prime					prime					non-prime					prime												
P3 P2 P1			↓		P1' P2' P3'			P3 P2 P1			↓		P1' P2' P3'														
MMP-2	S	A	V	I	P	D	Y	M	R	D	L	Y	R	MMP-2	R	V	E	P	P	Q	Y	M	I	D	L	Y	N
MMP-8	S	A	V	I	P	D	Y	M	R	D	L	Y	R	MMP-3	R	V	E	P	P	Q	Y	M	I	D	L	Y	N
MMP-9	S	A	V	I	P	D	Y	M	R	D	L	Y	R	MMP-8	R	V	E	P	P	Q	Y	M	I	D	L	Y	N
MMP-15	S	A	V	I	P	D	Y	M	R	D	L	Y	R	MMP-9	R	V	E	P	P	Q	Y	M	I	D	L	Y	N
MMP-16	S	A	V	I	P	D	Y	M	R	D	L	Y	R	MMP-10	R	V	E	P	P	Q	Y	M	I	D	L	Y	N
MMP-17	S	A	V	I	P	D	Y	M	R	D	L	Y	R	MMP-14	R	V	E	P	P	Q	Y	M	I	D	L	Y	N
MMP-24	S	A	V	I	P	D	Y	M	R	D	L	Y	R	MMP-15	R	V	E	P	P	Q	Y	M	I	D	L	Y	N
MMP-25	S	A	V	I	P	D	Y	M	R	D	L	Y	R	MMP-16	R	V	E	P	P	Q	Y	M	I	D	L	Y	N
MMP-3	S	A	V	I	P	D	Y	M	R	D	L	Y	R	MMP-17	R	V	E	P	P	Q	Y	M	I	D	L	Y	N
MMP-10	S	A	V	I	P	D	Y	M	R	D	L	Y	R	MMP-25	R	V	E	P	P	Q	Y	M	I	D	L	Y	N
MMP-14	S	A	V	I	P	D	Y	M	R	D	L	Y	R	MMP-24	R	V	E	P	P	Q	Y	M	I	D	L	Y	N

BMP-10 PD													
scissile bond													
non-prime					prime								
P3 P2 P1			↓		P1' P2' P3'								
MMP-8	K	V	D	P	P	E	Y	M	L	E	L	Y	N
MMP-10	K	V	D	P	P	E	Y	M	L	E	L	Y	N
MMP-14	K	V	D	P	P	E	Y	M	L	E	L	Y	N
MMP-15	K	V	D	P	P	E	Y	M	L	E	L	Y	N
MMP-16	K	V	D	P	P	E	Y	M	L	E	L	Y	N
MMP-17	K	V	D	P	P	E	Y	M	L	E	L	Y	N
MMP-24	K	V	D	P	P	E	Y	M	L	E	L	Y	N
MMP-25	K	V	D	P	P	E	Y	M	L	E	L	Y	N
MMP-2	K	V	D	P	P	E	Y	M	L	E	L	Y	N
MMP-3	K	V	D	P	P	E	Y	M	L	E	L	Y	N
MMP-9	K	V	D	P	P	E	Y	M	L	E	L	Y	N

Supplementary Figure S2: Predicted MMP cleavage sites in BMP-4, -9, and 10 PDs using the CleavPredict platform. P1 cleavage positions before the predicted scissile bond (red arrow) are indicated in red. Six residues of each predicted cleavage site in non-prime (P3, P2, P1) and prime (P1', P2', P3') region are marked in yellow.



Supplementary Figure S3: Dynamic light scattering (DLS) of BMP-7 CPLX after MMP-13 cleavage. Intensity size distribution of BMP-7 CPLX incubated in the presence or absence of MMP-13. The y-axis represents counts per second (CPS) and the x-axis represents particle size in nm.

4. Discussion

4.1 Mechanisms controlling BMP bioavailability within the ECM

In this thesis the molecular mechanisms controlling the bioavailability of BMPs within extracellular tissue microenvironments were investigated. This is important for a better understanding of how extracellular microenvironments control BMP activity in a contextual manner such as in development, tissue homeostasis, and disease. BMPs can be targeted to the ECM as free GFs or as PD-GF CPLXs. BMPs were reported to get targeted and sequestered to FMF or extracellular heparin/ HS GAGs. Targeting to these two ECM scaffolds differently impacts their conformation which defines the status of their bioactivity. More specifically, it was found that heparin/ HS allows binding of BMP CPLXs in bioactive V-shape conformation, while targeting to fibrillin-1 induces a conformational change into a latent ring-shape. From ECM-bound pools BMPs may be utilized via proteolytic cleavage mechanisms. Such cleavage mechanisms can play an activating role either by releasing fibrillin-bound BMPs or converting latent BMP single-chain precursors into bioactive CPLXs. Overall, extracellular microenvironments are capable to spatially concentrate BMPs in specific bioactivity states depending on the cellular context. Any disturbance in these mechanisms leads to disbalanced ECM-cell communication that is responsible for disease causing pathogenic mechanisms.

4.1.1 PPC processing impacts BMP bioavailability

BMPs are produced as single chain precursors encompassing a PD and a GF moiety. Subsequent to PD folding, disulfide-bridging between the GF moieties of two BMP precursors leads to the formation of an unprocessed BMP dimer (Gray and Mason et al., 1990). This dimer is then subjected to proteolytic cleavage at the C-terminal PD ends to produce a non-covalently associated PD-GF CPLX. This processing step is performed by intra- or extracellular PPCs depending on the ligand and tissue. For example, GDF-8 and TGF- β can both be processed intra- or extracellularly (Cotton et al., 2018; Shi et al., 2011; Zacchigna et al., 2006; Anderson et al., 2008) with GDF-8 detected in unprocessed form in skeletal muscle but in processed form in serum (Anderson et al., 2008).

Similar extracellular activation mechanisms could exist for other BMPs such as BMP-10 that is known to circulate in human plasma in unprocessed form (Hodgson et al., 2020). However, BMP-7 was shown to be exclusively processed extracellularly (Gregory et al., 2005; Spanou et al., in preparation#1, Fig. S2A). The data of this thesis suggests that PPC processing of the BMP-10 dimer results in an angle difference between the PD arms. This conformational change allows type I receptor access to the GF moiety and PD displacement that is required for type II receptor access (Fig. 4.1 and Jiang et al., 2016 and Spanou et al., in preparation#1, Figs. 6, 7A, 7B and S8B). The previous suggests that BMP-10 may be transported in inactive form to target cells in different vascular beds where its specific activation depends on the presence of available PPCs (Spanou et al., in preparation#1).

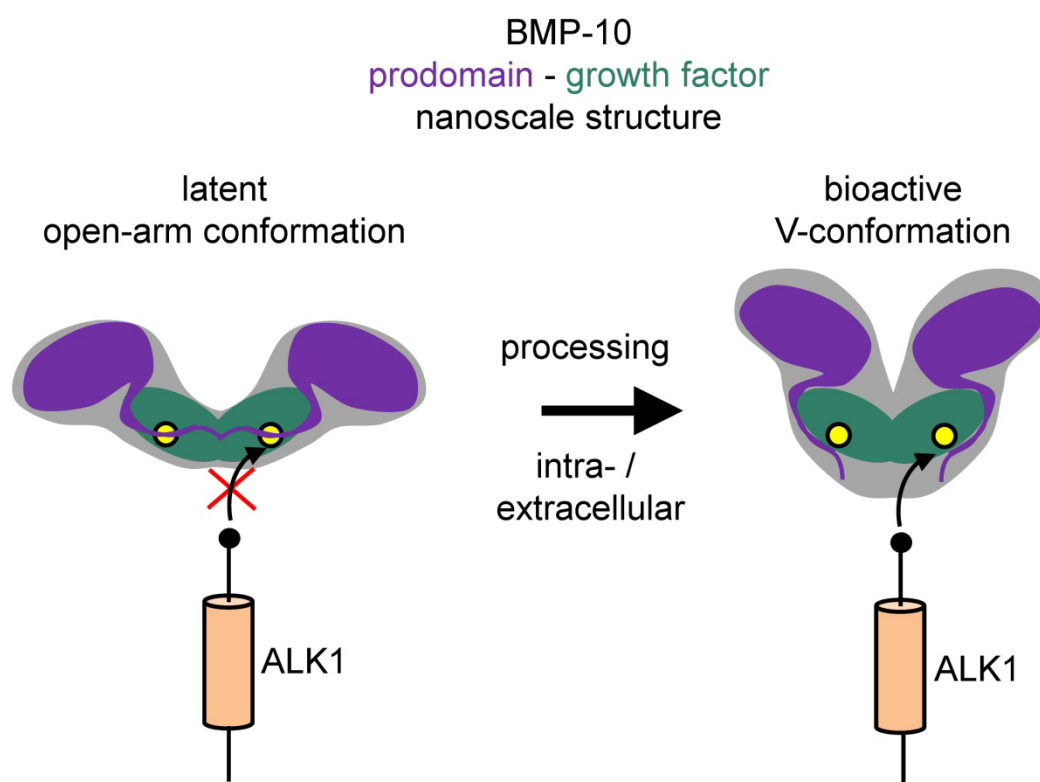


Figure 4.1: PPC processing renders BMP-10 into a V-shape, bioactive conformation. Unprocessed BMP-10 assumes an open-arm conformation with a wide angle. In that conformation, secondary structure elements such as the inhibitory $\alpha 1$ helix mask BMP-10 GF thus interfering with ALK-1 receptor binding to the GF and rendering BMP-10 latent. Upon PPC processing, a conformational change is induced with a tighter angle between PD arms that rearranges the structure of the CPLX so that BMP-10 GF is accessible by the ALK-1 receptor to trigger BMP signaling.

4.1.2 MMP cleavage regulates the bioavailability of BMPs

It is an open question how closed-ring BMP CPLXs become activated from FMF latent pools. Previous studies on the closed-ring, latent TGF- β CPLX showed that TGF- β GF can be rendered available to receptors by integrin pulling or proteolytic degradation of the TGF- β PD called LAP (Yu et al., 2000; Ge et al., 2006; Shi et al., 2011). Preliminary experiments showed that integrin pulling does not seem to be a major activation mechanism for BMPs (Zimmermann et al., 2021). To that end, proteolytic PD cleavage by matrix metalloproteinases as an activation mechanism of fibrillin-targeted BMPs was further investigated.

Our results identified a new MMP-driven activation mechanism that releases bioactive BMP GF from fibrillin-bound pools. Since bioactive BMPs can trigger the expression of MMPs leading to tissue-specific ECM remodeling (Furlan, Spanou et al., 2021, Zimmermann et al., 2021), a de-activating mechanism would be necessary to limit BMP activity and balance homeostasis. Indeed, targeting of BMP-7 GF to heparin/ HS blunts its bioactivity (Spanou et al., in preparation#2, and Fig. 4.2), suggesting an effective way to turn off BMP GF activity. MMP-13 mediated cleavage of BMP-7 PD also occurs when BMP-7 CPLX is heparin-bound leading to GF release (Furlan et al., unpublished results). Such a mechanism allows BMP GFs to diffuse to other cellular microenvironments thus removing them locally.

4.1.3 Targeting of BMPs to glycosaminoglycans

Overall, heparin/HS and fibrillin can differentially regulate the bioactivity of complexed and uncomplexed GFs within the ECM. When BMP-7 CPLX is targeted to fibrillin-1, it assumes a latent, closed-ring conformation (Wohl et al., 2016, and Fig. 4.2). When the in-solution bioactive, processed BMP CPLXs are targeted to heparin/ HS, their bioactive state is maintained (Spanou et al., in preparation#2, Figs 1 and S5). MMPs could be cleaving heparin-bound CPLXs to render them latent and stop the BMP response when required (Fig. 4.2). In addition to this, unprocessed, latent BMPs could be targeted to heparin/ HS where heparin-bound PPCs such as PACE4 or PC5A (Tsuji et al., 2003; Mayer et al., 2008) may convert them into signaling competent BMPs or render them more available for further proteolytic

activating processing. Such a mechanism could not only exist for the heparin-binding BMP-7 CPLX (Gregory et al., 2005; Spanou et al., in preparation#1) but also for the GDF-8 CPLX (Sengle et al., 2011) (Anderson et al., 2008). This may explain the low extracellular processing rate observed for BMP-10 (~more than a week required to obtain 50% processing when the BMP-7 PPC site is utilized) since BMP-10 does not bind heparin (Spanou et al., in preparation#1, Fig. 1D and 2A2) and hence cannot be concentrated locally on the cell layer where the HSPG-bound PPCs, PACE4 and PC5A process their substrates (Tsuji et al., 2003; Mayer et al., 2008).

Furthermore, BMPs can be targeted to extracellular heparin/ HS via different epitopes within the GF that control their bioactivity. BMPs that form unstable CPLXs, such as BMP-2, may be mostly targeted to heparin/ HS as GFs. Interestingly, BMP-2 GF utilizes a different epitope for heparin/ HS interaction than BMP-7 GF that does not affect its bioactivity (Spanou et al., in preparation#2, Figs. 1 and 2, and Fig. 4.2). It remains to be further investigated how the bioactivity of BMP GFs and CPLXs are regulated upon GAG binding.

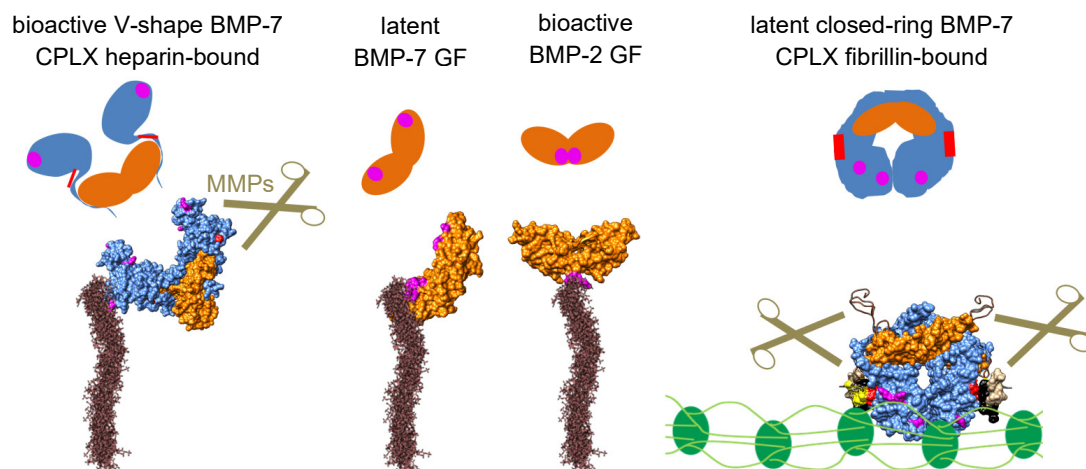


Figure 4.2: Graphical overview of the identified mechanisms regulating BMP bioavailability within the ECM. BMPs are targeted to fibrillin-1 in a closed-ring latent conformation requiring MMP proteolytic processing for activation (Furlan, Spanou et al., 2021). However, when BMPs are targeted to heparin/ HS their V-shape conformation is maintained thus prolonging their bioactive state (Spanou et al., in preparation#2). To that end, MMPs could be cleaving heparin-bound, bioactive BMP CPLXs to trigger CPLX unfolding and block BMP signaling when it is biologically required (Furlan, Spanou et al., 2021). In addition, uncomplexed BMPs can be targeted to heparin/ HS in a bioactive or latent conformation depending on the GF epitope utilized for the interaction (Spanou et al., in preparation#2) (modified after Spanou et al., in preparation#2).

4.1.4 Dysregulated ECM bioavailability mechanisms in disease onset and progression

In the previous three chapters new mechanisms to regulate BMP bioavailability utilized by the ECM were discussed and analyzed. These mechanisms seem to function differently even between members of the same BMP subgroup suggesting intricate folding and unique biochemical properties for each BMP. In the context of the diverse ECM microenvironments within the same or different tissues this translates into different signaling outputs that are orchestrated in a tissue-specific or systemic fashion to balance organismal homeostasis. To that end, several diseases can stem from dysregulated BMP signaling depending on the tissue, organ or system examined.

4.1.4.1 BMPs in HHT

Hereditary hemorrhagic telangiectasia (HHT) is an autosomal dominant disease that is caused by mutations in the BMP-9 ligand or its signaling receptors ALK-1 and ENG. The disease is characterized by arteriovenous malformations (AVMs) that are abnormal connections between arteries and veins found in place of normal capillary beds. Without the function of capillary beds to lower arterial blood pressure, AVMs lead to vascular rupture and internal bleeding (Roman et al., 2017). Recently it was discovered that concurrent deletion of *bmp-10* and *bmp-10-like* in zebrafish leads to formation of similar AVMs observed in *acvr1l* mutants that do not express the ALK-1 receptor (Capasso et al., 2020). The previous finding strongly suggested that dysregulated BMP-10 signaling alone is responsible for the severe form of HHT since *bmp-9* zebrafish and mice mutants showed no severe phenotype similarly to a milder clinical phenotype reported in patients with BMP-9 mutations (Roman et al., 2017; Capasso et al., 2020). Hence, the absence of BMP-10 interaction with heparin may better explain why lack of BMP-10 signaling leads to high HHT disease penetrance. BMP-9 and BMP-10 are TGF- β superfamily ligands with partially overlapping functions (Roman et al., 2017). In this thesis it was discovered that BMP-9 CPLX but not BMP-10 CPLX interacts with heparin (Spanou et al., in preparation#2). Hence, BMP-9 CPLX could be lingering on the glycocalyx of the endothelial cell surface and thereby facilitate prolonged signaling via ALK-1 or its co-

receptor ENG even in haploinsufficiency of ALK-1 or ENG. However, due to its inability to interact with the glycocalyx, BMP-10 cannot establish similar continuous signaling events in haploinsufficiency of receptors. This may then lead to the characteristic HHT clinical phenotype suggesting that BMP targeting to the ECM in bioactive state may control disease penetrance. In addition, the presence of BMP-9 in processed form in human plasma where most BMP-10 was detected in unprocessed form may further differentially contribute to disease progression (Hodgson et al., 2020). Since results from this thesis and previous studies showed that unprocessed BMPs are latent (Plöger et al., 2008; Wang et al., 2016; Spanou et al., in preparation#1) and that processing can also take place extracellularly (Zacchigna et al., 2006; Anderson et al., 2008, Spanou et al., in preparation#1) the availability and activity of PPCs in distinct tissues could be locally controlling AVM onset and progression by regulating BMP-10 bioactivity and hence HHT disease penetrance.

4.1.4.2 BMPs in cancer

In a different disease context, BMP-10 was reported to have tumor-suppressive functions thereby serving as “oncogene” that promotes cancer patient survival (Ye et al., 2010; Yuan et al., 2019). Interestingly, both MMP-13 (Yamada et al., 2010; Nannuru et al., 2010) and the metalloproteinase bone morphogenetic protein 1 (BMP-1) (Hsieh et al., 2018) are involved in cancer metastasis. It is known that BMP-10 PD is cleaved very efficiently by BMP-1 (Sengle et al., 2011) but remains almost intact when incubated with MMP-13 (Furlan, Spanou et al., 2021). Since in this thesis it was discovered that BMP-10 PD does not inhibit signaling to endothelial cells or myoblasts, BMP-1 cleavage of bioactive V-shape BMP-10 CPLX (Spanou et al., in preparation#1) will likely trigger unfolding events (Furlan, Spanou et al., 2021) that compromise BMP-10 signaling competency. In addition, since pathological overexpression of MMPs in malignancies triggers ECM remodeling that can also lead to chronic fibrosis (Giannandrea and Parks et al., 2014), and fibrotic tissue is known to promote tumor progression (Piersma et al., 2020), BMP-10 CPLX could be targeted to the fibrotic ECM in a closed-ring, latent conformation (Spanou et al., in preparation#1) thus promoting tumor progression and metastasis. Since BMP-10 CPLX does not bind heparin/HS (Spanou et al., in preparation#1; Spanou et al., in preparation#2), mechanisms to target BMP-10 CPLX to the ECM in bioactive V-shape, remain to be identified.

In addition, furin inactivation is considered a promising cancer therapy approach (He et al., 2020). However, anti-furin therapy should be considered in a tissue specific context. For instance, furin inactivation in the liver was shown to promote hepatocellular carcinoma (Declercq et al., 2015) whereas furin overexpression hindered hepatic tumor growth (Huang et al., 2012). These findings are in line with reports demonstrating that BMP-10 is expressed by hepatic stellate cells (HSCs) and that its activation by intracellular furin is necessary in order to exert liver-specific functions (Desroches-Castan et al., 2021). Indeed, BMP-10 overexpression in human hepatic cancer cell lines hindered their growth, size and weight to a remarkable extent both *in vitro* and *in vivo* (Yuan et al., 2019). Interestingly, since BMP-10 circulates in unprocessed form in human plasma (Hodgson et al., 2020) and extracellular processing of BMP-10 is possible (Spanou et al., in preparation#1), the availability of extracellular PPCs may define the activation status of circulating, unprocessed BMP-10 to protect tissues against tumor invasion and metastasis. Indeed, *in vitro* overexpression of BMP-10 in prostate cancer cells decreased their growth, migration and invasion (Ye et al., 2009). The tumor-suppressive properties of BMP-10 might be regulated by the presence of fibrotic tissue in the surrounding area that could sequester BMP-10 CPLX in closed-ring shape (Spanou et al., in preparation#1).

4.1.4.3 BMPs in connective tissue disorders

Opposing clinical features are caused by distinct fibrillin-1 mutations (Sengle and Sakai, 2015). MFS is caused by mutations in almost all *FBNI* exons and is characterized by tall stature, thin, translucent, hyperelastic skin and aortic aneurysms (Lee et al., 1991). In contrast, WMS is characterized by short stature, hypermuscularity, stiff, fibrotic skin, stiff joints and brachydactyly (Faivre et al., 2003). Our current understanding is that fibrillin-1 mutations differently affect the structural integrity of FMF and thereby the activation status of targeted and sequestered growth factors of the TGF- β superfamily (Zigrino and Sengle, 2019). This in turn may lead to aberrant TGF- β and BMP signaling events which activate different downstream cascades that promote tissue remodeling, ECM destruction or fibrosis (Sengle et al., 2012; Sengle et al., 2015).

Aberrant BMP activation due to insufficient sequestration to FMF can in turn trigger enhanced MMP expression thus fueling a feed-forward cycle that ultimately

leads to ECM destruction (Fig. 4.3). To that end, blocking BMP activation by inhibiting MMP activity has been proposed as a promising strategy against MFS aneurysm progression (Furlan, doctoral dissertation, 2018, p. 91).

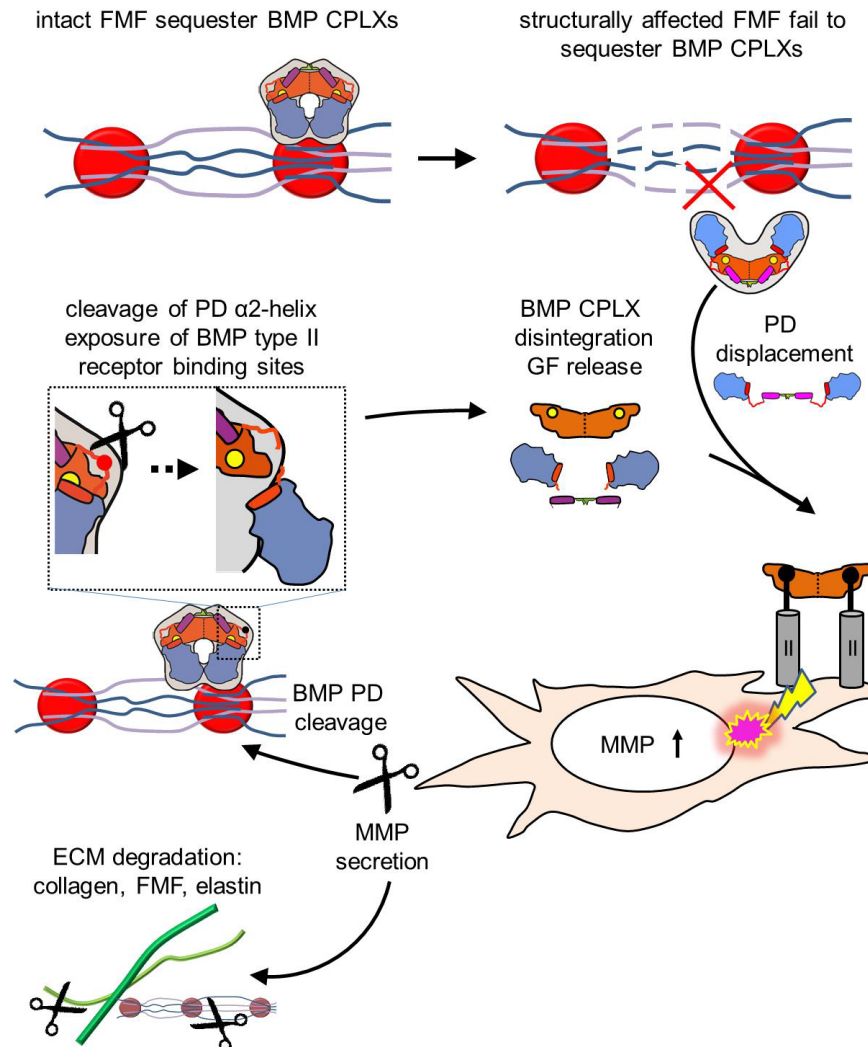


Figure 4.3: Aberrant BMP activation results in MMP overexpression and ECM remodeling. In a physiological context, BMPs are sequestered to intact FMF in a closed-ring, latent conformation. Insufficient sequestration of BMPs due to structurally affected FMF renders these ligands more prone to activation by on-site available MMPs that release bioactive GF via PD cleavage (Furlan, Spanou et al., 2021). The released GF can then trigger MMP overexpression (Furlan, Spanou et al., 2021) leading to ECM degradation to fuel a feed-forward cycle of BMP activation and ECM destruction (from Zimmermann et al., 2021).

In WMS on the other hand, the causative mutations within fibrillin-1 are very well-characterized. These mutations include the three-domain WMS deletion site (TB1, proline rich, and EGF4-like domains) and point mutations within the TB5 domain. Within the FMF ultrastructure, these domains are thought to reside in very

close proximity to each other near the bead region (Fig. 1.5). Indeed, either deletion of these three domains or point mutations within the TB5 domain, are sufficient to manifest the WMS clinical phenotype suggesting these fibrillin-1 domains participate in cooperating growth factor targeting and activation mechanisms within the FMF ultrastructure (Cain et al., 2012; Zigrino and Sengle, 2019). More specifically, it is thought that lack of ADAMTS enzyme targeting to fibrillin-1 due to the deletion of these three domains would result in lack of BMP or TGF- β proteolytic activation since these enzymes similarly to MMPs cleave BMP-7 PD and CPLX (Sengle et al., 2012; Furlan, doctoral dissertation, 2018, p. 75; Furlan, Spanou et al., 2021). In addition, the point mutations within TB5 that are causative for WMS also abolish heparin/HS binding to that region (Cain et al., 2012). Therefore, lack of local heparin binding would inhibit targeting of BMPs in bioactive conformation (Spanou et al., in preparation#2). Overall, the identified mechanisms regulating BMP bioavailability within the ECM can control the onset and progression of diseases characterized by dysregulated BMP signaling.

4.2 Outlook

In this work new mechanisms were identified that regulate the bioavailability of BMP growth factors within the ECM. These mechanisms can control BMP biosynthesis, targeting and activation from the ECM thus providing better insights into disease mechanisms characterized by dysregulated BMP signaling.

In the context of MFS, BMPs may still be targeted but insufficiently sequestered by mutant fibrillin. It remains still an open question whether the presence of mutant FMF affects BMP utilization by tissue resident cells.

In addition, further activation mechanisms from the matrix could be investigated by assessing BMP and TGF- β PDs for ADAMTS cleavage. What is more, bioactivity measurements after ADAMTS cleavage of fibrillin-bound BMP CPLXs would allow a better understanding of the nature of this activation mechanism.

Further, since heparin/ HS is abundantly found on the cell surface it may affect BMP internalization as an additional mechanism to regulate BMP bioavailability.

5. References

- ❖ Allen, B. L., & Rapraeger, A. C. (2003). Spatial and temporal expression of heparan sulfate in mouse development regulates FGF and FGF receptor assembly. *Journal of Cell Biology*, *163*(3), 637–648. <https://doi.org/10.1083/jcb.200307053>
- ❖ Allendorph, G. P., Vale, W. W., & Choe, S. (2006). Structure of the ternary signaling complex of a TGF- β superfamily member. *Proceedings of the National Academy of Sciences*, *103*(20), 7643–7648. <https://doi.org/10.1073/pnas.0602558103>
- ❖ Anderson, S. B., Goldberg, A. L., & Whitman, M. (2008). Identification of a novel pool of extracellular pro-myostatin in skeletal muscle. *Journal of Biological Chemistry*, *283*(11), 7027–7035. <https://doi.org/10.1074/jbc.m706678200>
- ❖ Barry, A. E., Baldeosingh, R., Lamm, R., Patel, K., Zhang, K., Dominguez, D. A., Kirton, K. J., Shah, A. P., & Dang, H. (2020). Hepatic stellate cells and hepatocarcinogenesis. *Frontiers in Cell and Developmental Biology*, *8*. <https://doi.org/10.3389/fcell.2020.00709>
- ❖ Bertoli-Avella, A. M., Gillis, E., Morisaki, H., Verhagen, J. M. A., de Graaf, B. M., van de Beek, G., Gallo, E., Kruithof, B. P. T., Venselaar, H., Myers, L. A., Laga, S., Doyle, A. J., Oswald, G., van Cappellen, G. W. A., Yamanaka, I., van der Helm, R. M., Beverloo, B., de Klein, A., Pardo, L., ... Loeys, B. L. (2015). Mutations in a TGF- β ligand, TGFB3, cause syndromic aortic aneurysms and dissections. *Journal of the American College of Cardiology*, *65*(13), 1324–1336. <https://doi.org/10.1016/j.jacc.2015.01.040>
- ❖ Billings, P. C., Yang, E., Mundy, C., & Pacifici, M. (2018). Domains with highest heparan sulfate-binding affinity reside at opposite ends in BMP2/4 versus BMP5/6/7: Implications for function. *Journal of Biological Chemistry*, *293*(37), 14371–14383. <https://doi.org/10.1074/jbc.ra118.003191>

- ❖ Bishop, J. R., Schuksz, M., & Esko, J. D. (2007). Heparan sulphate proteoglycans fine-tune mammalian physiology. *Nature*, *446*(7139), 1030–1037.
<https://doi.org/10.1038/nature05817>
- ❖ Bramlage, C. P., Tampe, B., Koziolok, M., Maatouk, I., Bevanda, J., Bramlage, P., Ahrens, K., Lange, K., Schmid, H., Cohen, C. D., Kretzler, M., & Müller, G. A. (2010). Bone morphogenetic protein (BMP)-7 expression is decreased in human hypertensive nephrosclerosis. *BMC Nephrology*, *11*(1). <https://doi.org/10.1186/1471-2369-11-31>
- ❖ Buscemi, L., Ramonet, D., Klingberg, F., Formey, A., Smith-Clerc, J., Meister, J.-J., & Hinz, B. (2011). The single-molecule mechanics of the latent TGF- β 1 complex. *Current Biology*, *21*(24), 2046–2054. <https://doi.org/10.1016/j.cub.2011.11.037>
- ❖ Cain, S. A., Baldock, C., Gallagher, J., Morgan, A., Bax, D. V., Weiss, A. S., Shuttleworth, C. A., & Kielty, C. M. (2005). Fibrillin-1 interactions with heparin. *Journal of Biological Chemistry*, *280*(34), 30526–30537.
<https://doi.org/10.1074/jbc.m501390200>
- ❖ Cain, S. A., McGovern, A., Baldwin, A. K., Baldock, C., & Kielty, C. M. (2012). Fibrillin-1 mutations causing Weill-Marchesani syndrome and acromicric and geleophysic dysplasias disrupt heparan sulfate interactions. *PLoS ONE*, *7*(11).
<https://doi.org/10.1371/journal.pone.0048634>
- ❖ Capasso, T. L., Li, B., Volek, H. J., Khalid, W., Rochon, E. R., Anbalagan, A., Herdman, C., Yost, H. J., Villanueva, F. S., Kim, K., & Roman, B. L. (2020). BMP10-mediated ALK1 signaling is continuously required for vascular development and maintenance. *Angiogenesis*, *23*(2), 203–220. <https://doi.org/10.1007/s10456-019-09701-0>

- ❖ Cash, J. N., Rejon, C. A., McPherron, A. C., Bernard, D. J., & Thompson, T. B. (2009). The structure of myostatin:Follistatin 288: Insights into receptor utilization and heparin binding. *The EMBO Journal*, *28*(17), 2662–2676.
<https://doi.org/10.1038/emboj.2009.205>
- ❖ Chen, H., Shi, S., Acosta, L., Li, W., Lu, J., Bao, S., Chen, Z., Yang, Z., Schneider, M. D., Chien, K. R., Conway, S. J., Yoder, M. C., Haneline, L. S., Franco, D., & Shou, W. (2004). BMP10 is essential for maintaining cardiac growth during murine cardiogenesis. *Development*, *131*(9), 2219–2231. <https://doi.org/10.1242/dev.01094>
- ❖ Constam, D. B., & Robertson, E. J. (1999). Regulation of bone morphogenetic protein activity by prodomains and proprotein convertases. *Journal of Cell Biology*, *144*(1), 139–149. <https://doi.org/10.1083/jcb.144.1.139>
- ❖ Cotton, T. R., Fischer, G., Wang, X., McCoy, J. C., Czepnik, M., Thompson, T. B., & Hyvönen, M. (2018). Structure of the human myostatin precursor and determinants of growth factor latency. *The EMBO Journal*, *37*(3), 367–383.
<https://doi.org/10.15252/emboj.201797883>
- ❖ Dagoneau, N., Benoist-Lasselin, C., Huber, C., Faivre, L., Mégarbané, A., Alswaid, A., Dollfus, H., Alembik, Y., Munnich, A., Legeai-Mallet, L., & Cormier-Daire, V. (2004). ADAMTS10 mutations in autosomal recessive Weill-Marchesani syndrome. *The American Journal of Human Genetics*, *75*(5), 801–806.
<https://doi.org/10.1086/425231>
- ❖ Declercq, J., Brouwers, B., Pruniau, V. P., Stijnen, P., Tuand, K., Meulemans, S., Prat, A., Seidah, N. G., Khatib, A.-M., & Creemers, J. W. (2015). Liver-specific inactivation of the proprotein convertase furin leads to increased hepatocellular carcinoma growth. *BioMed Research International*, *2015*, 1–8.
<https://doi.org/10.1155/2015/148651>

- ❖ Desroches-Castan, A., Tillet, E., Bouvard, C., & Bailly, S. (2021). BMP9 and BMP10: Two close vascular quiescence partners that stand out. *Developmental Dynamics*. <https://doi.org/10.1002/dvdy.395>
- ❖ Dietz, H. C., Cutting, C. R., Pyeritz, R. E., Maslen, C. L., Sakai, L. Y., Corson, G. M., Puffenberger, E., Hamosh, A., Nanthakumar, E. J., Curristin, S. M., Stetten, G., Meyers, D. A., & Francomano, C. A. (1991). Marfan syndrome caused by a recurrent de novo missense mutation in the fibrillin gene. *Nature*, *352*(6333), 337–339. <https://doi.org/10.1038/352337a0>
- ❖ Diwan, A. D., Leong, A., Appleyard, R., Bhargav, D., Fang, Z. M., & Wei, A. (2013). Bone morphogenetic protein-7 accelerates fracture healing in osteoporotic rats. *Indian Journal of Orthopaedics*, *47*(6), 540–546. <https://doi.org/10.4103/0019-5413.121569>
- ❖ El-Hallous, E., Sasaki, T., Hubmacher, D., Getie, M., Tiedemann, K., Brinckmann, J., Bätge, B., Davis, E. C., & Reinhardt, D. P. (2007). Fibrillin-1 interactions with fibulins depend on the first hybrid domain and provide an adaptor function to tropoelastin. *Journal of Biological Chemistry*, *282*(12), 8935–8946. <https://doi.org/10.1074/jbc.m608204200>
- ❖ Faivre, L. (2003). In frame fibrillin-1 gene deletion in autosomal dominant Weill-Marchesani syndrome. *Journal of Medical Genetics*, *40*(1), 34–36. <https://doi.org/10.1136/jmg.40.1.34>
- ❖ Farooq, M., Nakai, H., Fujimoto, A., Fujikawa, H., Kjaer, K. W., Baig, S. M., & Shimomura, Y. (2013). Characterization of a novel missense mutation in the prodomain of GDF5, which underlies brachydactyly type C and mild Grebe type chondrodysplasia in a large Pakistani family. *Human Genetics*, *132*(11), 1253–1264. <https://doi.org/10.1007/s00439-013-1330-3>

- ❖ Fontana, L., Chen, Y., Prijatelj, P., Sakai, T., Fässler, R., Sakai, L. Y., & Rifkin, D. B. (2005). Fibronectin is required for integrin $\alpha 5\beta 1$ -mediated activation of latent TGF- β complexes containing LTBP-1. *The FASEB Journal*, *19*(13), 1798–1808.
<https://doi.org/10.1096/fj.05-4134com>
- ❖ Furlan, A. G., Spanou, C. E. S., Godwin, A. R., Wohl, A. P., Zimmermann, L. M. A., Imhof, T., Koch, M., Baldock, C., & Sengle, G. (2021). A new MMP-mediated prodomain cleavage mechanism to activate bone morphogenetic proteins from the extracellular matrix. *The FASEB Journal*, *35*(3).
<https://doi.org/10.1096/fj.202001264r>
- ❖ Furlan, A. G. (2018). New mechanisms involved in aortic aneurysm formation due to fibrillin-1 deficiency [doctoral dissertation]. University of Cologne
- ❖ Gandhi, N. S., & Mancera, R. L. (2012). Prediction of heparin binding sites in bone morphogenetic proteins (BMPs). *Biochimica Et Biophysica Acta (BBA) - Proteins and Proteomics*, *1824*(12), 1374–1381. <https://doi.org/10.1016/j.bbapap.2012.07.002>
- ❖ Gao, L., Chen, L., Fan, L., Gao, D., Liang, Z., Wang, R., & Lu, W. (2016). The effect of losartan on progressive aortic dilatation in patients with Marfan's syndrome: A meta-analysis of prospective randomized clinical trials. *International Journal of Cardiology*, *217*, 190–194. <https://doi.org/10.1016/j.ijcard.2016.04.186>
- ❖ Ge, G., & Greenspan, D. S. (2006). BMP1 controls TGFB1 activation via cleavage of latent TGFB-binding protein. *Journal of Cell Biology*, *175*(1), 111–120.
<https://doi.org/10.1083/jcb.200606058>
- ❖ Giannandrea, M., & Parks, W. C. (2014). Diverse functions of matrix metalloproteinases during fibrosis. *Disease Models & Mechanisms*, *7*(2), 193–203.
<https://doi.org/10.1242/dmm.012062>

- ❖ Gray, A. M., & Mason, A. J. (1990). Requirement for activin A and transforming growth factor-- β 1 pro-regions in homodimer assembly. *Science*, *247*(4948), 1328–1330. <https://doi.org/10.1126/science.2315700>
- ❖ Greenwald, J., Groppe, J., Gray, P., Wiater, E., Kwiatkowski, W., Vale, W., & Choe, S. (2003). The BMP7/ActRII extracellular domain complex provides new insights into the cooperative nature of receptor assembly. *Molecular Cell*, *11*(3), 605–617. [https://doi.org/10.1016/s1097-2765\(03\)00094-7](https://doi.org/10.1016/s1097-2765(03)00094-7)
- ❖ Gregory, K. E., Ono, R. N., Charbonneau, N. L., Kuo, C.-L., Keene, D. R., Bächinger, H. P., & Sakai, L. Y. (2005). The prodomain of BMP-7 targets the BMP-7 complex to the extracellular matrix. *Journal of Biological Chemistry*, *280*(30), 27970–27980. <https://doi.org/10.1074/jbc.m504270200>
- ❖ Griffith, D. L., Keck, P. C., Sampath, T. K., Rueger, D. C., & Carlson, W. D. (1996). Three-dimensional structure of recombinant human osteogenic protein 1: Structural paradigm for the transforming growth factor beta superfamily. *Proceedings of the National Academy of Sciences*, *93*(2), 878–883. <https://doi.org/10.1073/pnas.93.2.878>
- ❖ Grobet, L., Royo Martin, L. J., Poncelet, D., Pirottin, D., Brouwers, B., Riquet, J., Schoeberlein, A., Dunner, S., Ménissier, F., Massabanda, J., Fries, R., Hanset, R., & Georges, M. (1997). A deletion in the bovine myostatin gene causes the double-muscling phenotype in cattle. *Nature Genetics*, *17*(1), 71–74. <https://doi.org/10.1038/ng0997-71>
- ❖ Guex, N., & Peitsch, M. C. (1997). Swiss-model and the Swiss-PDB viewer: An environment for comparative protein modeling. *Electrophoresis*, *18*(15), 2714–2723. <https://doi.org/10.1002/elps.1150181505>
- ❖ Harges, K., Becker, G. L., Lu, Y., Dahms, S. O., Köhler, S., Beyer, W., Sandvig, K., Yamamoto, H., Lindberg, I., Walz, L., von Messling, V., Than, M. E., Garten, W., &

- Steinmetzer, T. (2015). Novel furin inhibitors with potent anti-infectious activity. *ChemMedChem*, *10*(7), 1218–1231. <https://doi.org/10.1002/cmdc.201500103>
- ❖ He, Z., Thorrez, L., Siegfried, G., Meulemans, S., Evrard, S., Tejpar, S., Khatib, A.-M., & Creemers, J. W. (2020). The proprotein convertase furin is a pro-oncogenic driver in Kras and BRAF driven colorectal cancer. *Oncogene*, *39*(17), 3571–3587. <https://doi.org/10.1038/s41388-020-1238-z>
 - ❖ Henrich, S., Cameron, A., Bourenkov, G. P., Kiefersauer, R., Huber, R., Lindberg, I., Bode, W., & Than, M. E. (2003). The crystal structure of the proprotein processing proteinase furin explains its stringent specificity. *Nature Structural & Molecular Biology*, *10*(7), 520–526. <https://doi.org/10.1038/nsb941>
 - ❖ Hodgson, J., Swietlik, E. M., Salmon, R. M., Hadinnapola, C., Nikolic, I., Wharton, J., Guo, J., Liley, J., Haimel, M., Bleda, M., Southgate, L., Machado, R. D., Martin, J. M., Treacy, C. M., Yates, K., Daugherty, L. C., Shamardina, O., Whitehorn, D., Holden, S., ... Morrell, N. W. (2020). Characterization of GDF2 mutations and levels of BMP9 and BMP10 in pulmonary arterial hypertension. *American Journal of Respiratory and Critical Care Medicine*, *201*(5), 575–585. <https://doi.org/10.1164/rccm.201906-1141oc>
 - ❖ Horbelt, D., Denkis, A., & Knaus, P. (2012). A portrait of transforming growth factor β superfamily signalling: Background matters. *The International Journal of Biochemistry & Cell Biology*, *44*(3), 469–474. <https://doi.org/10.1016/j.biocel.2011.12.013>
 - ❖ Hosaka, M., Nagahama, M., Kim, W. S., Watanabe, T., Hatsuzawa, K., Ikemizu, J., Murakami, K., & Nakayama, K. (1991). ARG-x-lys/ARG-ARG motif as a signal for precursor cleavage catalyzed by furin within the constitutive secretory pathway.

Journal of Biological Chemistry, 266(19), 12127–12130.

[https://doi.org/10.1016/s0021-9258\(18\)98867-8](https://doi.org/10.1016/s0021-9258(18)98867-8)

- ❖ Hsieh, Y.-Y., Tung, S.-Y., Pan, H.-Y., Yen, C.-W., Xu, H.-W., Deng, Y.-F., Lin, Y.-J., Hsu, W.-T., Wu, C.-S., & Li, C. (2018). Upregulation of bone morphogenetic protein 1 is associated with poor prognosis of late-stage gastric cancer patients. *BMC Cancer*, 18(1). <https://doi.org/10.1186/s12885-018-4383-9>
- ❖ Huang, Y.-H., Lin, K.-H., Liao, C.-H., Lai, M.-W., Tseng, Y.-H., & Yeh, C.-T. (2012). Furin overexpression suppresses tumor growth and predicts a better post-operative disease-free survival in hepatocellular carcinoma. *PLoS ONE*, 7(7). <https://doi.org/10.1371/journal.pone.0040738>
- ❖ Hubmacher, D., El-Hallous, E. I., Nelea, V., Kaartinen, M. T., Lee, E. R., & Reinhardt, D. P. (2008). Biogenesis of extracellular microfibrils: Multimerization of the fibrillin-1 C-terminus into bead-like structures enables self-assembly. *Proceedings of the National Academy of Sciences*, 105(18), 6548–6553. <https://doi.org/10.1073/pnas.0706335105>
- ❖ Isogai, Z., Ono, R. N., Ushiro, S., Keene, D. R., Chen, Y., Mazzieri, R., Charbonneau, N. L., Reinhardt, D. P., Rifkin, D. B., & Sakai, L. Y. (2003). Latent transforming growth factor β -binding protein 1 interacts with fibrillin and is a microfibril-associated protein. *Journal of Biological Chemistry*, 278(4), 2750–2757. <https://doi.org/10.1074/jbc.m209256200>
- ❖ Jaaks, P., D'Alessandro, V., Grob, N., Büel, S., Hajdin, K., Schäfer, B. W., & Bernasconi, M. (2016). The proprotein convertase furin contributes to rhabdomyosarcoma malignancy by promoting vascularization, migration and invasion. *PLOS ONE*, 11(8). <https://doi.org/10.1371/journal.pone.0161396>

- ❖ Jiang, H., Salmon, R. M., Upton, P. D., Wei, Z., Lawera, A., Davenport, A. P., Morrell, N. W., & Li, W. (2016). The prodomain-bound form of bone morphogenetic protein 10 is biologically active on endothelial cells. *Journal of Biological Chemistry*, *291*(6), 2954–2966. <https://doi.org/10.1074/jbc.m115.683292>
- ❖ Jin, Y., Zheng, W., Li, L., Huang, G., Liu, Y., Jiang, H., Zhang, Y., & Tang, C. (2019). Loss of BMP-10 is correlated with poor survival in ovarian cancer. *Pathology - Research and Practice*, *215*(1), 121–126. <https://doi.org/10.1016/j.prp.2018.10.025>
- ❖ Kaltcheva, M. M., Anderson, M. J., Harfe, B. D., & Lewandoski, M. (2016). BMPs are direct triggers of interdigital programmed cell death. *Developmental Biology*, *411*(2), 266–276. <https://doi.org/10.1016/j.ydbio.2015.12.016>
- ❖ Kambadur, R., Sharma, M., Smith, T. P. L., & Bass, J. J. (1997). Mutations in myostatin (GDF8) in double-muscled Belgian blue and Piedmontese cattle. *Genome Research*, *7*(9), 910–915. <https://doi.org/10.1101/gr.7.9.910>
- ❖ Keller, S., Nickel, J., Zhang, J.-L., Sebald, W., & Mueller, T. D. (2004). Molecular recognition of BMP-2 and BMP receptor IA. *Nature Structural & Molecular Biology*, *11*(5), 481–488. <https://doi.org/10.1038/nsmb756>
- ❖ Kienast, Y., Jucknischke, U., Scheiblich, S., Thier, M., de Wouters, M., Haas, A., Lehmann, C., Brand, V., Bernicke, D., Honold, K., & Lorenz, S. (2016). Rapid activation of bone morphogenetic protein 9 by receptor-mediated displacement of prodomains. *Journal of Biological Chemistry*, *291*(7), 3395–3410. <https://doi.org/10.1074/jbc.m115.680009>
- ❖ Kim, R. Y., Robertson, E. J., & Solloway, M. J. (2001). BMP6 and BMP7 are required for cushion formation and septation in the developing mouse heart. *Developmental Biology*, *235*(2), 449–466. <https://doi.org/10.1006/dbio.2001.0284>

- ❖ Kjaer, K. W. (2006). A mutation in the receptor binding site of GDF5 causes Mohr-wriedt brachydactyly type A2. *Journal of Medical Genetics*, 43(3), 225–231.
<https://doi.org/10.1136/jmg.2005.034058>
- ❖ Kozakov, D., Hall, D. R., Xia, B., Porter, K. A., Padhorny, D., Yueh, C., Beglov, D., & Vajda, S. (2017). The ClusPro web server for protein–protein docking. *Nature Protocols*, 12(2), 255–278. <https://doi.org/10.1038/nprot.2016.169>
- ❖ Kuo, C.-L., Isogai, Z., Keene, D. R., Hazeki, N., Ono, R. N., Sengle, G., Peter Bächinger, H., & Sakai, L. Y. (2007). Effects of fibrillin-1 degradation on microfibril ultrastructure. *Journal of Biological Chemistry*, 282(6), 4007–4020.
<https://doi.org/10.1074/jbc.m606370200>
- ❖ Le Goff, C., Morice-Picard, F., Dagoneau, N., Wang, L. W., Perrot, C., Crow, Y. J., Bauer, F., Flori, E., Prost-Squarcioni, C., Krakow, D., Ge, G., Greenspan, D. S., Bonnet, D., Le Merrer, M., Munnich, A., Apte, S. S., & Cormier-Daire, V. (2008). ADAMTSL2 mutations in geleophysic dysplasia demonstrate a role for ADAMTS-like proteins in TGF- β bioavailability regulation. *Nature Genetics*, 40(9), 1119–1123.
<https://doi.org/10.1038/ng.199>
- ❖ Le, V. Q., Iacob, R. E., Tian, Y., McConaughy, W., Jackson, J., Su, Y., Zhao, B., Engen, J. R., Pirruccello-Straub, M., & Springer, T. A. (2018). Tolloid cleavage activates latent GDF8 by priming the pro-complex for dissociation. *The EMBO Journal*, 37(3), 384–397. <https://doi.org/10.15252/emj.201797931>
- ❖ Le, V. Q., Iacob, R. E., Zhao, B., Su, Y., Tian, Y., Toohey, C., Engen, J. R., & Springer, T. A. (2022). Protection of the prodomain α 1-helix correlates with latency in the transforming growth factor- β family. *Journal of Molecular Biology*, 434(5), 167439. <https://doi.org/10.1016/j.jmb.2021.167439>

- ❖ Lee, B., Godfrey, M., Vitale, E., Hori, H., Mattei, M.-G., Sarfarazi, M., Tsipouras, P., Ramirez, F., & Hollister, D. W. (1991). Linkage of Marfan syndrome and a phenotypically related disorder to two different fibrillin genes. *Nature*, *352*(6333), 330–334. <https://doi.org/10.1038/352330a0>
- ❖ Lee, S. S. J., Knott, V., Jovanović, J., Harlos, K., Grimes, J. M., Choulier, L., Mardon, H. J., Stuart, D. I., & Handford, P. A. (2004). Structure of the integrin binding fragment from fibrillin-1 gives new insights into microfibril organization. *Structure*, *12*(4), 717–729. <https://doi.org/10.1016/j.str.2004.02.023>
- ❖ Livak, K. J., & Schmittgen, T. D. (2001). Analysis of relative gene expression data using real-time quantitative PCR and the $2^{-\Delta\Delta CT}$ method. *Methods*, *25*(4), 402–408. <https://doi.org/10.1006/meth.2001.1262>
- ❖ Li, S., Shimono, C., Norioka, N., Nakano, I., Okubo, T., Yagi, Y., Hayashi, M., Sato, Y., Fujisaki, H., Hattori, S., Sugiura, N., Kimata, K., & Sekiguchi, K. (2010). Activin A binds to perlecan through its pro-region that has heparin/heparan sulfate binding activity. *Journal of Biological Chemistry*, *285*(47), 36645–36655. <https://doi.org/10.1074/jbc.m110.177865>
- ❖ Loeys, B. L., Chen, J., Neptune, E. R., Judge, D. P., Podowski, M., Holm, T., Meyers, J., Leitch, C. C., Katsanis, N., Sharifi, N., Xu, F. L., Myers, L. A., Spevak, P. J., Cameron, D. E., Backer, J. D., Hellemans, J., Chen, Y., Davis, E. C., Webb, C. L., ... Dietz, H. C. (2005). A syndrome of altered cardiovascular, craniofacial, neurocognitive and skeletal development caused by mutations in TGFBR1 or TGFBR2. *Nature Genetics*, *37*(3), 275–281. <https://doi.org/10.1038/ng1511>
- ❖ Mayer, G., Hamelin, J., Asselin, M.-C., Pasquato, A., Marcinkiewicz, E., Tang, M., Tabibzadeh, S., & Seidah, N. G. (2008). The regulated cell surface zymogen activation of the proprotein convertase PC5A directs the processing of its secretory

- substrates. *Journal of Biological Chemistry*, 283(4), 2373–2384.
<https://doi.org/10.1074/jbc.m708763200>
- ❖ McCroskery, S., Thomas, M., Maxwell, L., Sharma, M., & Kambadur, R. (2003). Myostatin negatively regulates satellite cell activation and self-renewal. *Journal of Cell Biology*, 162(6), 1135–1147. <https://doi.org/10.1083/jcb.200207056>
 - ❖ McDonald, J., Wooderchak-Donahue, W., VanSant Webb, C., Whitehead, K., Stevenson, D. A., & Bayrak-Toydemir, P. (2015). Hereditary hemorrhagic telangiectasia: Genetics and molecular diagnostics in a new era. *Frontiers in Genetics*, 6. <https://doi.org/10.3389/fgene.2015.00001>
 - ❖ McPherron, A. C., & Lee, S.-J. (1997). Double muscling in cattle due to mutations in the myostatin gene. *Proceedings of the National Academy of Sciences*, 94(23), 12457–12461. <https://doi.org/10.1073/pnas.94.23.12457>
 - ❖ McPherron, A. C., Lawler, A. M., & Lee, S.-J. (1997). Regulation of skeletal muscle mass in mice by a new TGF- β superfamily member. *Nature*, 387(6628), 83–90. <https://doi.org/10.1038/387083a0>
 - ❖ Mi, L.-Z., Brown, C. T., Gao, Y., Tian, Y., Le, V. Q., Walz, T., & Springer, T. A. (2015). Structure of bone morphogenetic protein 9 procomplex. *Proceedings of the National Academy of Sciences*, 112(12), 3710–3715. <https://doi.org/10.1073/pnas.1501303112>
 - ❖ Migliorini, E., Horn, P., Haraszti, T., Wegner, S. V., Hiepen, C., Knaus, P., Richter, R. P., & Cavalcanti-Adam, E. A. (2017). Enhanced biological activity of BMP-2 bound to surface-grafted heparan sulfate. *Advanced Biosystems*, 1(4), 1600041. <https://doi.org/10.1002/adbi.201600041>

- ❖ Mitu, G. M., Wang, S., & Hirschberg, R. (2007). BMP7 is a podocyte survival factor and rescues podocytes from diabetic injury. *American Journal of Physiology-Renal Physiology*, 293(5). <https://doi.org/10.1152/ajprenal.00179.2007>
- ❖ Mu, D., Cambier, S., Fjellbirkeland, L., Baron, J. L., Munger, J. S., Kawakatsu, H., Sheppard, D., Broaddus, V. C., & Nishimura, S. L. (2002). The integrin $\alpha\beta 8$ mediates epithelial homeostasis through MT1-MMP-dependent activation of TGF- $\beta 1$. *Journal of Cell Biology*, 157(3), 493–507. <https://doi.org/10.1083/jcb.200109100>
- ❖ Nannuru, K. C., Futakuchi, M., Varney, M. L., Vincent, T. M., Marcusson, E. G., & Singh, R. K. (2010). Matrix metalloproteinase (MMP)-13 regulates mammary tumor-induced osteolysis by activating MMP9 and transforming growth factor- β signaling at the tumor-bone interface. *Cancer Research*, 70(9), 3494–3504. <https://doi.org/10.1158/0008-5472.can-09-3251>
- ❖ Nogami, H., & Urist, M. R. (1970). A morphogenetic matrix for differentiation of cartilage in tissue culture. *Experimental Biology and Medicine*, 134(2), 530–535. <https://doi.org/10.3181/00379727-134-34829>
- ❖ Ohkawara, B., Iemura, S.-ichiro, ten Dijke, P., & Ueno, N. (2002). Action range of BMP is defined by its N-terminal basic amino acid core. *Current Biology*, 12(3), 205–209. [https://doi.org/10.1016/s0960-9822\(01\)00684-4](https://doi.org/10.1016/s0960-9822(01)00684-4)
- ❖ Olivieri, J., Smaldone, S., & Ramirez, F. (2010). Fibrillin assemblies: Extracellular determinants of tissue formation and fibrosis. *Fibrogenesis & Tissue Repair*, 3(1). <https://doi.org/10.1186/1755-1536-3-24>
- ❖ Ono, R. N., Sengle, G., Charbonneau, N. L., Carlberg, V., Bächinger, H. P., Sasaki, T., Lee-Arteaga, S., Zilberberg, L., Rifkin, D. B., Ramirez, F., Chu, M.-L., & Sakai, L. Y. (2009). Latent transforming growth factor β -binding proteins and fibulins compete for fibrillin-1 and exhibit exquisite specificities in binding sites. *Journal of*

- Biological Chemistry*, 284(25), 16872–16881.
<https://doi.org/10.1074/jbc.m809348200>
- ❖ Pettersen, E. F., Goddard, T. D., Huang, C. C., Couch, G. S., Greenblatt, D. M., Meng, E. C., & Ferrin, T. E. (2004). UCSF chimera-A visualization system for exploratory research and analysis. *Journal of Computational Chemistry*, 25(13), 1605–1612. <https://doi.org/10.1002/jcc.20084>
 - ❖ Piersma, B., Hayward, M. K., & Weaver, V. M. (2020). Fibrosis and cancer: A strained relationship. *Biochimica Et Biophysica Acta (BBA) - Reviews on Cancer*, 1873(2), 188356. <https://doi.org/10.1016/j.bbcan.2020.188356>
 - ❖ Piha-Gossack, A., Sossin, W., & Reinhardt, D. P. (2012). The evolution of extracellular fibrillins and their functional domains. *PLoS ONE*, 7(3). <https://doi.org/10.1371/journal.pone.0033560>
 - ❖ Plöger, F., Seemann, P., Schmidt-von Kegler, M., Lehmann, K., Seidel, J., Kjaer, K. W., Pohl, J., & Mundlos, S. (2008). Brachydactyly Type A2 associated with a defect in proGDF5 processing. *Human Molecular Genetics*, 17(9), 1222–1233. <https://doi.org/10.1093/hmg/ddn012>
 - ❖ Punjani, A., Rubinstein, J. L., Fleet, D. J., & Brubaker, M. A. (2017). CryoSPARC: Algorithms for rapid unsupervised cryo-EM structure determination. *Nature Methods*, 14(3), 290–296. <https://doi.org/10.1038/nmeth.4169>
 - ❖ Quadros, R. M., Miura, H., Harms, D. W., Akatsuka, H., Sato, T., Aida, T., Redder, R., Richardson, G. P., Inagaki, Y., Sakai, D., Buckley, S. M., Seshacharyulu, P., Batra, S. K., Behlke, M. A., Zeiner, S. A., Jacobi, A. M., Izu, Y., Thoreson, W. B., Urness, L. D., ... Gurumurthy, C. B. (2017). Easi-CRISPR: A robust method for one-step generation of mice carrying conditional and insertion alleles using long ssDNA

- donors and CRISPR ribonucleoproteins. *Genome Biology*, 18(1).
<https://doi.org/10.1186/s13059-017-1220-4>
- ❖ Ribeiro, S. M. F., Poczatek, M., Schultz-Cherry, S., Villain, M., & Murphy-Ullrich, J. E. (1999). The activation sequence of thrombospondin-1 interacts with the latency-associated peptide to regulate activation of latent transforming growth factor- β . *Journal of Biological Chemistry*, 274(19), 13586–13593.
<https://doi.org/10.1074/jbc.274.19.13586>
 - ❖ Rider, C., & Mulloy, B. (2017). Heparin, heparan sulphate and the TGF- β cytokine superfamily. *Molecules*, 22(5), 713. <https://doi.org/10.3390/molecules22050713>
 - ❖ Roman, B. L., & Hinck, A. P. (2017). ALK1 signaling in development and disease: New paradigms. *Cellular and Molecular Life Sciences*, 74(24), 4539–4560.
<https://doi.org/10.1007/s00018-017-2636-4>
 - ❖ Rosen, V. (2009). BMP2 signaling in bone development and repair. *Cytokine & Growth Factor Reviews*, 20(5-6), 475–480.
<https://doi.org/10.1016/j.cytogfr.2009.10.018>
 - ❖ Saito, T., Bokhove, M., Croci, R., Zamora-Caballero, S., Han, L., Letarte, M., de Sanctis, D., & Jovine, L. (2017). Structural basis of the human endoglin-BMP9 interaction: Insights into BMP signaling and HHT1. *Cell Reports*, 19(9), 1917–1928.
<https://doi.org/10.1016/j.celrep.2017.05.011>
 - ❖ Sakai, L. Y., Keene, D. R., Glanville, R. W., & Bächinger, H. P. (1991). Purification and partial characterization of fibrillin, a cysteine-rich structural component of connective tissue microfibrils. *Journal of Biological Chemistry*, 266(22), 14763–14770. [https://doi.org/10.1016/s0021-9258\(18\)98752-1](https://doi.org/10.1016/s0021-9258(18)98752-1)
 - ❖ Salmon, R. M., Guo, J., Wood, J. H., Tong, Z., Beech, J. S., Lawera, A., Yu, M., Grainger, D. J., Reckless, J., Morrell, N. W., & Li, W. (2020). Molecular basis of

- ALK1-mediated signalling by BMP9/BMP10 and their prodomain-bound forms.
Nature Communications, 11(1). <https://doi.org/10.1038/s41467-020-15425-3>
- ❖ Schuelke, M., Wagner, K. R., Stolz, L. E., Hübner, C., Riebel, T., Kömen, W., Braun, T., Tobin, J. F., & Lee, S.-J. (2004). Myostatin mutation associated with gross muscle hypertrophy in a child. *New England Journal of Medicine*, 350(26), 2682–2688.
<https://doi.org/10.1056/nejmoa040933>
 - ❖ Selamet Tierney, E. S., Levine, J. C., Sleeper, L. A., Roman, M. J., Bradley, T. J., Colan, S. D., Chen, S., Campbell, M. J., Cohen, M. S., De Backer, J., Heydarian, H., Hoskoppal, A., Lai, W. W., Liou, A., Marcus, E., Nutting, A., Olson, A. K., Parra, D. A., Pearson, G. D., ... Lacro, R. V. (2018). Influence of aortic stiffness on aortic-root growth rate and outcome in patients with the Marfan syndrome. *The American Journal of Cardiology*, 121(9), 1094–1101.
<https://doi.org/10.1016/j.amjcard.2018.01.016>
 - ❖ Sengle, G., & Sakai, L. Y. (2015). The fibrillin microfibril scaffold: A niche for growth factors and mechanosensation? *Matrix Biology*, 47, 3–12.
<https://doi.org/10.1016/j.matbio.2015.05.002>
 - ❖ Sengle, G., Charbonneau, N. L., Ono, R. N., Sasaki, T., Alvarez, J., Keene, D. R., Bächinger, H. P., & Sakai, L. Y. (2008). Targeting of bone morphogenetic protein growth factor complexes to fibrillin. *Journal of Biological Chemistry*, 283(20), 13874–13888. <https://doi.org/10.1074/jbc.m707820200>
 - ❖ Sengle, G., Ono, R. N., Lyons, K. M., Bächinger, H. P., & Sakai, L. Y. (2008). A new model for growth factor activation: Type II receptors compete with the prodomain for BMP-7. *Journal of Molecular Biology*, 381(4), 1025–1039.
<https://doi.org/10.1016/j.jmb.2008.06.074>

- ❖ Sengle, G., Ono, R. N., Sasaki, T., & Sakai, L. Y. (2011). Prodomains of transforming growth factor β (TGFB) superfamily members specify different functions. *Journal of Biological Chemistry*, 286(7), 5087–5099. <https://doi.org/10.1074/jbc.m110.188615>
- ❖ Sengle, G., Tsutsui, K., Keene, D. R., Tufa, S. F., Carlson, E. J., Charbonneau, N. L., Ono, R. N., Sasaki, T., Wirtz, M. K., Samples, J. R., Fessler, L. I., Fessler, J. H., Sekiguchi, K., Hayflick, S. J., & Sakai, L. Y. (2012). Microenvironmental regulation by fibrillin-1. *PLoS Genetics*, 8(1). <https://doi.org/10.1371/journal.pgen.1002425>
- ❖ Shi, M., Zhu, J., Wang, R., Chen, X., Mi, L., Walz, T., & Springer, T. A. (2011). Latent TGF- β structure and activation. *Nature*, 474(7351), 343–349. <https://doi.org/10.1038/nature10152>
- ❖ Shi, M., Zhu, J., Wang, R., Chen, X., Mi, L., Walz, T., & Springer, T. A. (2011). Latent TGF- β structure and activation. *Nature*, 474(7351), 343–349. <https://doi.org/10.1038/nature10152>
- ❖ Stura, E. A., Visse, R., Cuniasse, P., Dive, V., & Nagase, H. (2013). Crystal structure of full-length human collagenase 3 (MMP-13) with peptides in the active site defines exosites in the catalytic domain. *The FASEB Journal*, 27(11), 4395–4405. <https://doi.org/10.1096/fj.13-233601>
- ❖ Susan-Resiga, D., Essalmani, R., Hamelin, J., Asselin, M.-C., Benjannet, S., Chamberland, A., Day, R., Szumska, D., Constam, D., Bhattacharya, S., Prat, A., & Seidah, N. G. (2011). Furin is the major processing enzyme of the cardiac-specific growth factor bone morphogenetic protein 10. *Journal of Biological Chemistry*, 286(26), 22785–22794. <https://doi.org/10.1074/jbc.m111.233577>
- ❖ Tan, K., & Lawler, J. (2009). The interaction of thrombospondins with extracellular matrix proteins. *Journal of Cell Communication and Signaling*, 3(3-4), 177–187. <https://doi.org/10.1007/s12079-009-0074-2>

- ❖ Teran, M., & Nugent, M. A. (2015). Synergistic binding of vascular endothelial growth factor-A and its receptors to heparin selectively modulates complex affinity. *Journal of Biological Chemistry*, *290*(26), 16451–16462.
<https://doi.org/10.1074/jbc.m114.627372>
- ❖ Tiedemann, K., Sasaki, T., Gustafsson, E., Göhring, W., Bätge, B., Notbohm, H., Timpl, R., Wedel, T., Schlötzer-Schrehardt, U., & Reinhardt, D. P. (2005). Microfibrils at basement membrane zones interact with perlecan via fibrillin-1. *Journal of Biological Chemistry*, *280*(12), 11404–11412.
<https://doi.org/10.1074/jbc.m409882200>
- ❖ Tsuji, A., Sakurai, K., Kiyokage, E., Yamazaki, T., Koide, S., Toida, K., Ishimura, K., & Matsuda, Y. (2003). Secretory proprotein convertases PACE4 and PC6A are heparin-binding proteins which are localized in the extracellular matrix. *Biochimica Et Biophysica Acta (BBA) - Proteins and Proteomics*, *1645*(1), 95–104.
[https://doi.org/10.1016/s1570-9639\(02\)00532-0](https://doi.org/10.1016/s1570-9639(02)00532-0)
- ❖ Urist, M. R. (1965). Bone: Formation by autoinduction. *Science*, *150*(3698), 893–899.
<https://doi.org/10.1126/science.150.3698.893>
- ❖ Urist, M. R., & Strates, B. S. (1971). Bone morphogenetic protein. *Journal of Dental Research*, *50*(6), 1392–1406. <https://doi.org/10.1177/00220345710500060601>
- ❖ Vlodaysky, I., & Friedmann, Y. (2001). Molecular properties and involvement of heparanase in cancer metastasis and angiogenesis. *Journal of Clinical Investigation*, *108*(3), 341–347. <https://doi.org/10.1172/jci13662>
- ❖ Vukicevic, S., Basic, V., Rogic, D., Basic, N., Shih, M. S., Shepard, A., Jin, D., Dattatreyamurty, B., Jones, W., Dorai, H., Ryan, S., Griffiths, D., Maliakal, J., Jelic, M., Pastorcic, M., Stavljenic, A., & Sampath, T. K. (1998). Osteogenic protein-1 (bone morphogenetic protein-7) reduces severity of injury after ischemic acute renal

- failure in rat. *Journal of Clinical Investigation*, *102*(1), 202–214.
<https://doi.org/10.1172/jci2237>
- ❖ Wagner, K. R., McPherron, A. C., Winik, N., & Lee, S.-J. (2002). Loss of myostatin attenuates severity of muscular dystrophy in mdx mice. *Annals of Neurology*, *52*(6), 832–836. <https://doi.org/10.1002/ana.10385>
 - ❖ Wang, R. N., Green, J., Wang, Z., Deng, Y., Qiao, M., Peabody, M., Zhang, Q., Ye, J., Yan, Z., Denduluri, S., Idowu, O., Li, M., Shen, C., Hu, A., Haydon, R. C., Kang, R., Mok, J., Lee, M. J., Luu, H. L., & Shi, L. L. (2014). Bone morphogenetic protein (BMP) signaling in development and human diseases. *Genes & Diseases*, *1*(1), 87–105. <https://doi.org/10.1016/j.gendis.2014.07.005>
 - ❖ Wang, X., Fischer, G., & Hyvönen, M. (2016). Structure and activation of pro-activin A. *Nature Communications*, *7*(1). <https://doi.org/10.1038/ncomms12052>
 - ❖ Weiskirchen, R. (2009). BMP-7 as antagonist of organ fibrosis. *Frontiers in Bioscience*, *14*(1), 4992. <https://doi.org/10.2741/3583>
 - ❖ Wohl, A. P., Troilo, H., Collins, R. F., Baldock, C., & Sengle, G. (2016). Extracellular regulation of bone morphogenetic protein activity by the microfibril component fibrillin-1. *Journal of Biological Chemistry*, *291*(24), 12732–12746. <https://doi.org/10.1074/jbc.m115.704734>
 - ❖ Yadin, D. A., Robertson, I. B., McNaught-Davis, J., Evans, P., Stoddart, D., Handford, P. A., Jensen, S. A., & Redfield, C. (2013). Structure of the fibrillin-1 N-terminal domains suggests that heparan sulfate regulates the early stages of microfibril assembly. *Structure*, *21*(10), 1743–1756. <https://doi.org/10.1016/j.str.2013.08.004>
 - ❖ Yamada, T., Imada, T., Masuda, M., Tanaka, K., Rino, Y., Akaike, M., Morinaga, S., Shiozawa, M., Kunisaki, C., Numata, K., Fujii, S., Sato, T., Yamamoto, N., Inagaki,

- D., Kanazawa, A., Tamura, S., Yoshihara, K., & Oshima, T. (2010). Overexpression of MMP-13 gene in colorectal cancer with liver metastasis. *Anticancer Research*, *30*(7), 2693–2699.
- ❖ Ye, L., Bokobza, S., Li, J., Moazzam, M., Chen, J., Mansel, R. E., & Jiang, W. G. (2010). Bone morphogenetic protein-10 (BMP-10) inhibits aggressiveness of breast cancer cells and correlates with poor prognosis in breast cancer. *Cancer Science*, *101*(10), 2137–2144. <https://doi.org/10.1111/j.1349-7006.2010.01648.x>
 - ❖ Ye, L., Kynaston, H., & Jiang, W. G. (2009). Bone morphogenetic protein-10 suppresses the growth and aggressiveness of prostate cancer cells through a Smad independent pathway. *Journal of Urology*, *181*(6), 2749–2759. <https://doi.org/10.1016/j.juro.2009.01.098>
 - ❖ Yu, Q., & Stamenkovic, I. (2000). Cell surface-localized matrix metalloproteinase-9 proteolytically activates TGF- β and promotes tumor invasion and angiogenesis. *Genes & Development*, *14*(2), 163–176. <https://doi.org/10.1101/gad.14.2.163>
 - ❖ Yuan, Y.-M., Ma, N., Zhang, E.-B., Chen, T.-W., Jiang, H., Yin, F.-F., Wang, J.-J., Zhang, F.-K., Ni, Q.-Z., Wang, X., Bao, Y., Wang, K., Cheng, S.-Q., Zhang, X.-L., Wang, X.-F., Li, J.-J., & Xie, D. (2019). BMP10 suppresses hepatocellular carcinoma progression via PTPRS–STAT3 axis. *Oncogene*, *38*(48), 7281–7293. <https://doi.org/10.1038/s41388-019-0943-y>
 - ❖ Zacchigna, L., Vecchione, C., Notte, A., Cordenonsi, M., Dupont, S., Maretto, S., Cifelli, G., Ferrari, A., Maffei, A., Fabbro, C., Braghetta, P., Marino, G., Selvetella, G., Aretini, A., Colonnese, C., Bettarini, U., Russo, G., Soligo, S., Adorno, M., ... Bressan, G. M. (2006). Emilin1 links TGF- β maturation to blood pressure homeostasis. *Cell*, *124*(5), 929–942. <https://doi.org/10.1016/j.cell.2005.12.035>

- ❖ Zebedin, E., Mille, M., Speiser, M., Zarrabi, T., Sandtner, W., Latzenhofer, B., Todt, H., & Hilber, K. (2007). C2C12 skeletal muscle cells adopt cardiac-like sodium current properties in a cardiac cell environment. *American Journal of Physiology-Heart and Circulatory Physiology*, 292(1).
<https://doi.org/10.1152/ajpheart.00119.2006>
- ❖ Zeisberg, M., & Kalluri, R. (2008). Reversal of experimental renal fibrosis by BMP7 provides insights into novel therapeutic strategies for chronic kidney disease. *Pediatric Nephrology*, 23(9), 1395–1398. <https://doi.org/10.1007/s00467-008-0818-x>
- ❖ Zeisberg, M., Hanai, J.-ichi, Sugimoto, H., Mammoto, T., Charytan, D., Strutz, F., & Kalluri, R. (2003). BMP-7 counteracts TGF- β 1–induced epithelial-to-mesenchymal transition and reverses chronic renal injury. *Nature Medicine*, 9(7), 964–968.
<https://doi.org/10.1038/nm888>
- ❖ Zhang, H., & Bradley, A. (1996). Mice deficient for BMP2 are non-viable and have defects in amnion/chorion and cardiac development. *Development*, 122(10), 2977–2986. <https://doi.org/10.1242/dev.122.10.2977>
- ❖ Zigrino, P., & Sengle, G. (2019). Fibrillin microfibrils and proteases, key integrators of fibrotic pathways. *Advanced Drug Delivery Reviews*, 146, 3–16.
<https://doi.org/10.1016/j.addr.2018.04.019>
- ❖ Zimmermann, L.-M. A., Correns, A., Furlan, A. G., Spanou, C. E. S., & Sengle, G. (2021). Controlling BMP growth factor bioavailability: The extracellular matrix as multi skilled platform. *Cellular Signalling*, 85, 110071.
<https://doi.org/10.1016/j.cellsig.2021.110071>

6. Abbreviations

A	Ampere
Å	Angström
aa	amino acid
ActR	activin receptor
ADAMTS	a disintegrin and metalloproteinase with thrombospondin motifs
ADAMTSL	a disintegrin and metalloproteinase with thrombospondin motifs)-like
ALK-1	activin receptor-like kinase-1
APMA	amino-phenyl mercuric acetate
APS	ammonium persulfate
AU	absorbance unit
AVM	arteriovenous malformation
BCA	bicinchoninic acid
BMP	bone morphogenetic protein
BMPR	bone morphogenetic protein receptor
BSA	bovine serum albumin
cbEGF	calcium binding epidermal growth factor-like domain
CD	circular dichroism
CM	carboxymethylated dextran
CPLX	complex
Da	Dalton
DLS	dynamic light scattering
DMEM	Dulbecco's Modified Eagle Medium

DMSO	dimethyl sulfoxide
DNA	deoxyribonucleic acid
DTT	dithiothreitol
ECM	extracellular matrix
EDC	1-Ethyl-3-(3-dimethylaminopropyl)carbodiimide
EDTA	Ethylenediaminetetraacetic acid
EGF	epidermal growth factor
ELISA	enzyme-linked immunosorbent assay
EM	electron microscopy
EMILIN-1	Elastin microfibril interfacier 1
ENG	endoglin
FBN	fibrillin
FBS	fetal bovine serum
FGF	fibroblast growth factor
FMF	fibrillin microfibrils
FUN	fibrillin unique N-terminal domain
GAG	glycosaminoglycan
GDNF	growth and differentiation factor
GF	growth factor
h	hour
HHT	hereditary hemorrhagic telangiectasia
his ₆ -tag	six-histidine-tag
HRP	horseradish peroxidase
HS	heparan sulfate
HSC	hepatic stellate cell

HSPG	heparan sulfate proteoglycan
<i>Id3</i>	inhibitor of differentiation 3
IPTG	Isopropyl β -D-1-thiogalactopyranoside
ITC	isothermal titration calorimetry
LAP	latency-associated peptide
LDS	Loeys-Dietz syndrome
LLC	large latent complex
LTBP	latent TGF- β binding protein
MFS	Marfan syndrome
min	minute
MMP	matrix metalloproteinase
NHS	N-Hydroxysuccinimide
Ni-NTA	nickel-nitrilotriacetic acid
nM	nanomolar
nm	nanometer
NMR	nuclear magnetic resonance
OD	optical density
O/N	overnight
PACE4	paired basic amino acid-cleaving enzyme 4
PAGE	polyacrylamide gel electrophoresis
PBS	phosphate-buffered saline
PC5A	proprotein convertase 5A
PCR	polymerase chain reaction
PDB	protein data bank
PD	prodomain

pen/strep	penicillin-streptomycin
PMSF	phenylmethanesulfonyl fluoride
PPC	proprotein convertase
qPCR	quantitative PCR
rF	recombinant fibrillin fragment
RGD	Integrin binding motif Arg-Gly-Asp
RT	room temperature
RU	response units
s	seconds
SDS	sodium dodecyl sulfate
SEC	size exclusion chromatography
SLC	small latent complex
SPR	surface plasmon resonance
strep-tag	streptavidin tag
TB	TGF β -binding protein-like domain
TBS	Tris-buffered saline
TBS-T	Tris-buffered saline with tween 20
TCA	Trichloroacetic acid
TEM	transmission electron microscopy
TEMED	N,N,N',N'-Tetramethyl ethylenediamine
TGF- β	transforming growth factor beta
TGF β R	transforming growth factor beta receptor
TLL2	tolloid-like protein 2
TMB	3,3',5,5'-Tetramethylbenzidine
TC	Tris-HCl with CaCl ₂

UV	ultraviolet
V	Volts
VEGF	vascular endothelial growth factor
WMS	Weill-Marchesani syndrome
$\Delta\varepsilon$	delta epsilon

7. Acknowledgments

Firstly and foremost I would like to thank both Gerhard and Mats for giving me the opportunity to work in this institute, in the exciting topic of growth factor biology and for believing in my potential. All projects were difficult but also very intellectually challenging. To reach reasonable conclusions, very often I had to think outside the box and look for solutions that were very unconventional and not so obvious.

To that end, I am very grateful to the attitude that Gerhard showed as my primary supervisor: He was very supportive and encouraged independent thinking. The outcome of this attitude led to the establishment of several wet and dry lab techniques that we can now use in the lab to study better the structure of BMPs and proteins in general.

This institute has the unique advantage that many research groups exchange ideas, work together and hold common meetings. Hence, I wouldn't go very far without the established Wednesday seminars. To that end I would like to thank a lot Mats, Raimund and Gerhard for their highly informed feedback. Heparin is a strange molecule but calculating surface charges and assuming heparin chains as straight lines were life-savers. To that end, I also would like to thank my tutors, Ulrich Baumann and Mario Fabri for providing valuable feedback in the tutor meetings. In addition, I would like to thank Gerhard, Ulrich Baumann and Siegfried Roth for taking over as first and second reviewers and chair in the defense.

Substantial credit goes to Alexander Wohl. Throughout the years I obtained invaluable feedback for designing experiments and interpreting results. I particularly valued his technical expertise and welcomed his ability to debate and criticize scientific observations and results since this sharpened my critical skill.

Next, I would like to thank all my colleagues in Sengle Lab and Zentrum Biochemie for the nice working atmosphere and for experimental help. I would also like to express my thanks to all technicians in Zentrum Biochemie for ordering reagents, providing protocols and technical help. Ich danke dem gesamten Zentrum Biochemie für alles.

The remaining credit goes to my family for providing support, understanding and for making my vacation days shiny and unforgettable. Throughout the years they were my most ardent supporters that encouraged my scientific endeavors. Thank you so much for constantly supporting my efforts.



Charikleia (Chara) Spanou
Gleueler Str.147 • 50931 Cologne, Germany
Mobile: +49(0)15738806210
cspanou1@smail.uni-koeln.de
Born: September 25th, 1991
Research gate:
https://www.researchgate.net/profile/Chara_Spanou

University education:

- 04/2017 – present PhD Student in Biochemistry, Graduate School for Biological Sciences (GSfBS), University of Cologne, Faculty of Mathematics and Natural Sciences, Cologne, Germany

Supervisor: Prof. Dr. Sengle
- 10/2013 – 01/2016 Master of Science in Molecular Biology and Biomedicine (MBB)
Grade: 9.62/10 (Excellent)
University of Crete and Institute for Molecular Biology and Biotechnology (IMBB), Crete, Greece

Master's thesis at IMBB

Supervisor: Dr. Siden-Kiamos

Title: *Dissecting a stress-induced mechanism in anopheline midgut epithelium after infection with the rodent malaria parasite P.berghei*
- 9/2009 – 10/2013 Bachelor of Science in Biology
Grade: 8.15/10 (Very Good)
University of Crete, Greece

Bachelor's thesis at University of Crete, Department of Biology

Supervisor: Prof. Dr. Gizeli

Title: *Biophysical study of the activation state of the human cytoskeletal proteins ezrin and moesin using an acoustic biosensor*

Work experience:

- 02/2016-02/2017 Bench scientist at Cellular Stress Responses in Aging-Associated Diseases (CECAD), Cluster of Excellence of the University of Cologne, Germany

Awards and Memberships:

- 12/2013-12/2014 IMBB scholarship for distinguished admission to MBB graduate program
- 09/2009 scholarship for distinguished admission to the Department of Biology, University of Crete, Greece

Member of the German Society for Matrix Biology

Publications:

Furlan, A. G., **Spanou, C. E. S.**, Godwin, A. R. F., Wohl, A. P., Zimmermann, L. M. A., Imhof, T., Koch, M., Baldock, C., & Sengle, G. (2021). A new MMP-mediated prodomain cleavage mechanism to activate bone morphogenetic proteins from the extracellular matrix. *The FASEB Journal*, 35(3). <https://doi.org/10.1096/fj.202001264r>

Oral presentations:

- 05/2021 "Structural requirements for the regulation of BMP bioactivity by heparin", German and French Societies for Matrix Biology, Annual Meeting held online
- 11/2019 "New molecular insight into the regulation of BMP activity by heparin", 10th SFB829 PhD and Postdoc retreat, Schwelm, Germany
- 08/2018 "New molecular insight into the regulation of BMP activity by heparin", 9th SFB829 PhD and Postdoc retreat, Kürten-Hungenbach, Germany
- 03/2018 "New molecular insight into the regulation of BMP activity by heparin", German Society for Matrix Biology, Annual Meeting, Fraunhofer Institutszentrum Stuttgart (IZS), Germany

Poster presentations:

- 03/2019 "New molecular insight into the regulation of BMP activity by heparin" German Society for Matrix Biology, Annual Meeting, Regensburg, Germany
- 11/2018 "New mechanisms of fibrillin-dependent fibrosis" SFB829 International Symposium: "Molecular mechanisms regulating skin homeostasis", Max Planck Institute for Biology of Aging, Cologne, Germany.
- 03/2018 "New molecular insight into the regulation of BMP activity by heparin" German Society for Matrix Biology, Annual Meeting, Fraunhofer IZS, Stuttgart, Germany

Workshops:

- 10/2021 "Scientific Misconduct" by Prof. Langmann
- 10/2020 "Good Scientific Conduct: Biases in Science" by Prof. Gehring
- 11/2019 "Getting Funded-Writing an Individual Fellowship" by Dr. Willmott
- 06/2019 "Advanced Scientific Writing: Writing Publishable Research Articles" by Dr. Willmott
- 05/2019 "Statistics for Experimental Life Scientists" by Prof. Michel



Erklärung zur Dissertation
gemäß der Promotionsordnung vom 12. März 2020

***Diese Erklärung muss in der Dissertation enthalten sein.
(This version must be included in the doctoral thesis)***

„Hiermit versichere ich an Eides statt, dass ich die vorliegende Dissertation selbstständig und ohne die Benutzung anderer als der angegebenen Hilfsmittel und Literatur angefertigt habe. Alle Stellen, die wörtlich oder sinngemäß aus veröffentlichten und nicht veröffentlichten Werken dem Wortlaut oder dem Sinn nach entnommen wurden, sind als solche kenntlich gemacht. Ich versichere an Eides statt, dass diese Dissertation noch keiner anderen Fakultät oder Universität zur Prüfung vorgelegen hat; dass sie - abgesehen von unten angegebenen Teilpublikationen und eingebundenen Artikeln und Manuskripten - noch nicht veröffentlicht worden ist sowie, dass ich eine Veröffentlichung der Dissertation vor Abschluss der Promotion nicht ohne Genehmigung des Promotionsausschusses vornehmen werde. Die Bestimmungen dieser Ordnung sind mir bekannt. Darüber hinaus erkläre ich hiermit, dass ich die Ordnung zur Sicherung guter wissenschaftlicher Praxis und zum Umgang mit wissenschaftlichem Fehlverhalten der Universität zu Köln gelesen und sie bei der Durchführung der Dissertation zugrundeliegenden Arbeiten und der schriftlich verfassten Dissertation beachtet habe und verpflichte mich hiermit, die dort genannten Vorgaben bei allen wissenschaftlichen Tätigkeiten zu beachten und umzusetzen. Ich versichere, dass die eingereichte elektronische Fassung der eingereichten Druckfassung vollständig entspricht.“

Teilpublikationen:

Furlan, A. G., Spanou, C. E. S., Godwin, A. R. F., Wohl, A. P., Zimmermann, L. M. A., Imhof, T., Koch, M., Baldock, C., & Sengle, G. (2021). A new MMP - mediated prodomain cleavage mechanism to activate bone morphogenetic proteins from the extracellular matrix. The FASEB Journal, 35(3). <https://doi.org/10.1096/fj.202001264r>

Köln, den 02.04.22

Charikleia (Chara) Spanou

